

# **Multi-photon microscopy of cartilage**

---

**Submitted by Jessica Claire Mansfield, to the University of Exeter as a thesis for the degree of Doctor of Philosophy in Physics, September 2008**

**Supervised by:**

**Professor Peter Winlove**

**Dr Steve Matcher†**

**Dr Julian Moger**

**Dr Karen Knapp**

**This thesis is available for Library use on the understanding that it is copyright material and that no quotation from the thesis may be published without proper acknowledgement.**

**I certify that all material in this thesis which is not my own work has been identified and that no material has previously been submitted and approved for the award of a degree by this or any other University.**

**Jessica Mansfield**

† Currently at: The Kroto Institute, University of Sheffield

## **Abstract**

Articular cartilage has been imaged using the following multi-photon modalities: Second Harmonic Generation (SHG), Two-photon Fluorescence (TPF) and Coherent Anti-Stokes Raman Scattering (CARS). A simple epi detection microscope was constructed for SHG and TPF imaging in the early stages of this research. Later the imaging was transferred to a new microscope system which allowed simultaneous forwards and epi detection and combined CARS imaging with TPF and SHG.

Multiphoton spectroscopic studies were conducted on both intact tissue samples and the major components of the extracellular matrix, in order to identify sources of TPF. Fluorescence was detected from type II collagen, elastin and samples of purified collagen and elastin crosslinks. Age related glycation crosslinks of collagen may be a significant source of TPF. No fluorescence was detected from proteoglycans.

In intact, unfixed healthy articular cartilage the cells were observed via CARS, surrounded in their pericellular matrix which is characterised by an increase in TPF. The collagen of the extra cellular matrix showed up clearly in the SHG images. Diseased cartilage was also imaged revealing microscopic lesion at the articular surface in early osteoarthritis and highly fibrous collagen structures and cell clusters in more advanced degeneration.

In young healthy cartilage a network of elastin fibres were found lying parallel to the articular surface in the most superficial 50µm of the tissue. Regional variations in these fibres were also investigated. The fibres appeared mainly long and straight suggesting that they may be under tension, further work is needed to identify whether they have a mechanical function.

The polarization sensitivity of the SHG from collagen has been investigated for both cartilage and tendon. In the most superficial tissue these measurements can be used directly to determine the collagen fibre orientation. However at increasing depths the effects of biattenuation and birefringence must be considered. Healthy cartilage has a characteristic

pattern of polarization sensitivity with depth and this changes at lesions indicating a disruption of the normal collagen architecture.

The methods developed in this thesis demonstrate the use of non-linear microscopy to visualise the structure of the extracellular matrix and cells in intact unstained tissue. They should also be appropriate in many areas of cell and matrix biology.

## **Acknowledgements**

I would like to thank Professor Peter Winlove for his excellent supervision he has been a constant source of encouragement and ideas, helping both in the laboratory and with all the written work and presentations produced over the past 4 years. With the optics in this thesis I would like to acknowledge the following: Dr Steve Matcher for his contribution to the design and construction of microscope 1 and Dr Julian Moger for setting up the new multi-photon laboratory. I would also like to thank the staff of the mechanical workshop who have made multiple parts for the microscope always to the highest level of precision.

During the past 4 years I have been lucky to work in a lively and friendly group and therefore I would like to thank the members of biophysics past and present for their support and for making our laboratory a pleasant place to work. I would especially like to thank Ellen Green and Dave Colridge for their assistance and John Hale for this patient help with ImageJ.

I would like to thank Don Attenburrow who has provided me with funding via the Coote Bequest to carry on my research for a year after the first 3 years of my thesis. Not only has he provided funding he has also been a source of insightful conversations and ideas for future work.

Lastly I would like to thank my family who have been very supportive during the completion of my thesis.

## Table of Contents

|          |  |           |
|----------|--|-----------|
| <b>1</b> | <b>Background.....</b>                           | <b>13</b> |
| 1.1      | Introduction .....                               | 13        |
| 1.2      | The Non-linear Microscope.....                   | 14        |
| 1.3      | Second Harmonic Generation.....                  | 19        |
| 1.3.1    | General theory .....                             | 19        |
| 1.3.2    | Phase mismatch and propagation direction .....   | 21        |
| 1.3.3    | SHG in Tissues.....                              | 23        |
| 1.4      | Two-Photon Fluorescence.....                     | 31        |
| 1.4.1    | General Theory.....                              | 31        |
| 1.4.2    | Biological TPF .....                             | 35        |
| 1.5      | Coherent Anti-Stokes Raman Scattering CARS ..... | 38        |
| 1.5.1    | General Theory.....                              | 38        |
| 1.5.2    | Raman Selection Rules.....                       | 44        |
| 1.5.3    | Biological applications of CARS .....            | 45        |
| 1.6      | Extracellular Matrix Biology.....                | 47        |
| 1.6.1    | Cartilage Biology .....                          | 51        |
| 1.6.2    | Intervertebral disc.....                         | 58        |
| 1.6.3    | Elastic cartilage .....                          | 61        |
| <b>2</b> | <b>Experimental.....</b>                         | <b>62</b> |
| 2.1      | Introduction .....                               | 62        |
| 2.2      | Microscope 1 .....                               | 63        |
| 2.2.1    | Microscope design.....                           | 63        |
| 2.2.2    | Microscope testing .....                         | 67        |
| 2.3      | Microscope 2 .....                               | 70        |
| 2.4      | Spectrometer Set-up .....                        | 76        |
| 2.5      | Sample source and Preparation .....              | 85        |
| 2.5.1    | Articular Cartilage.....                         | 85        |
| 2.5.2    | Elastic Cartilage .....                          | 88        |
| 2.5.3    | Intervertebral Disc.....                         | 88        |
| 2.5.4    | Tendon.....                                      | 89        |
| 2.5.5    | Histology .....                                  | 89        |
| <b>3</b> | <b>Sources of Multiphoton contrast.....</b>      | <b>90</b> |
| 3.1      | Introduction .....                               | 90        |

|          |   |            |
|----------|---|------------|
| 3.2      | Experimental Procedure .....  | 91         |
| 3.2.1    | Power curves .....  | 91         |
| 3.2.2    | Spectra .....   | 91         |
| 3.3      | Sources of TPF in the extra cellular matrix .....                           | 92         |
| 3.3.1    | Purified Extra Cellular Matrix Proteins .....                               | 92         |
| 3.3.2    | Elastin and Collagen Crosslinks .....                                       | 96         |
| 3.3.3    | Proteoglycans .....   | 102        |
| 3.3.4    | Hydroxylapatite .....   | 104        |
| 3.4      | Intact tissue samples .....   | 105        |
| 3.5      | Discussion .....  | 111        |
| <b>4</b> | <b>Imaging cartilage .....</b>  | <b>116</b> |
| 4.1      | Introduction .....  | 116        |
| 4.2      | Healthy Cartilage .....   | 117        |
| 4.2.1    | Enface cartilage samples .....  | 117        |
| 4.2.2    | Cartilage Sections .....  | 128        |
| 4.3      | Lesions .....   | 137        |
| 4.3.1    | Butterfly lesions .....   | 138        |
| 4.3.2    | Early superficial lesions .....   | 140        |
| 4.3.3    | Highly degenerate tissue .....  | 144        |
| 4.4      | Discussion .....  | 149        |
| <b>5</b> | <b>Imaging Elastin Networks .....</b>                                       | <b>151</b> |
| 5.1      | Introduction .....  | 151        |
| 5.2      | Elastin in articular cartilage .....  | 152        |
| 5.2.1    | Confirmation of the identity of elastin fibres using immuno-staining<br>152 |            |
| 5.2.2    | Transverse Sections .....   | 154        |
| 5.3      | Distribution of elastin fibres across the joint surface .....               | 155        |
| 5.3.1    | Fibre properties .....  | 158        |
| 5.3.2    | Elastin fibre variations with age .....                                     | 161        |
| 5.4      | Elastin in the intervertebral disc .....                                    | 163        |
| 5.5      | Elastic Cartilage .....   | 168        |
| 5.6      | Discussion .....  | 177        |
| <b>6</b> | <b>Polarization sensitive non-linear microscopy .....</b>                   | <b>179</b> |
| 6.1      | Introduction .....  | 179        |

|          |  |            |
|----------|--|------------|
| 6.2      | Polarization Sensitive Measurements.....   | 179        |
| 6.2.1    | Validation of Polarization Sensitive Microscope Set-up .....                               | 180        |
| 6.2.2    | Polarization Sensitivity Curves in the Superficial Layers of<br>Cartilage and Tendon ..... | 182        |
| 6.2.3    | Polarization Sensitivity relative to Split Lines .....                                     | 187        |
| 6.2.4    | Ratio Images of Polarization Sensitive Measurements .....                                  | 189        |
| 6.3      | Variations in Polarization Sensitivity with Depth .....                                    | 190        |
| 6.3.1    | Tendon.....  | 190        |
| 6.3.2    | Cartilage .....  | 195        |
| 6.3.3    | Polarization Sensitivity in Degenerate Lesions.....  | 198        |
| 6.4      | Discussion.....  | 203        |
| <b>7</b> | <b>Conclusions and Future Work.....</b>  | <b>207</b> |
| <b>8</b> | <b>Appendix:.....</b>  | <b>214</b> |
|          | Polarization sensitivity of collagen fibres at an angle to the imaging plane .....         | 214        |
| <b>9</b> | <b>References .....</b>  | <b>214</b> |

## Table of Figures

|  |    |
|--|----|
| Figure 1-1 Energy level diagram for SHG.....   | 19 |
| Figure 1-2 phase diagrams for forward and epi SHG .....  | 21 |
| Figure 1-3 The orientation of the collagen fibril w.r.t. the laser beam. ....                            | 26 |
| Figure 1-4 The energy level diagram for two-photon fluorescence.....                                     | 31 |
| Figure 1-5 The energy level diagrams for three CARS processes;.....                                      | 39 |
| Figure 1-6 CARS signal as a function of the detuning $\Delta$ .....                                      | 41 |
| Figure 1-7 Dependence of the CARS signal on the size D of the scatter. ....                              | 44 |
| Figure 1-8 A schematic diagram of the ECM.....   | 47 |
| Figure 1-9 A schematic diagram of collagen structure up to the microfibrillar level.....                 | 48 |
| Figure 1-10 The structure of a proteoglycan aggregate as found in cartilage.....                         | 50 |
| Figure 1-11 A schematic diagram of the zonal structure of cartilage. ....                                | 53 |
| Figure 1-12 A schematic diagram of the intervertebral disc.....  | 59 |
| Figure 1-13 A schematic diagram of the elastin fibres within the intervertebral disc .....               | 60 |
| Figure 2-1 The optical setup for microscope 1. ....  | 64 |
| Figure 2-2 A schematic diagram of the optical set-up of our home built microscope.....                   | 65 |
| Figure 2-3 The relationship between the voltage and scan size for microscope 1.....                      | 68 |
| Figure 2-4 A schematic diagram of the optical table layout in the new laser lab.....                     | 71 |
| Figure 2-5 A schematic diagram of the FluoView 300 scan unit. ....                                       | 73 |
| Figure 2-6 A schematic diagram of the IX71 microscope head.....  | 75 |
| Figure 2-7 The relationship between the voltage and scan size.....                                       | 77 |
| Figure 2-8 Scanners, microscope head and spectrometer;.....  | 79 |
| Figure 2-9 Transmission across the dichroic and coloured glass filter.....                               | 80 |
| Figure 2-10 The efficiency curves for the 3 gratings used in the spectrometer.....                       | 81 |
| Figure 2-11 A composite spectrum taken of cartilage using grating 3 .....                                | 82 |
| Figure 2-12 standard and measured spectra of 4 fluorophores used for calibration. ....                   | 83 |
| Figure 2-13 The correction factor for grating 1 calculated from the standard spectra. ....               | 84 |
| Figure 2-14 A cross section of the lower end of a equine forelimb.....                                   | 87 |
| Figure 2-15 A section of the distal end of the 3 <sup>rd</sup> metacarpal showing the cortical ridge. .. | 87 |
| Figure 3-1 Multiphoton spectra of two purified elastin samples excited at 800nm.....                     | 93 |
| Figure 3-2 multi-photon spectra taken of collagen samples .....  | 94 |
| Figure 3-3 the power curves taken for the 4 extra cellular matrix hydrolysates.....                      | 97 |
| Figure 3-4 Spectra of the four hydrolysate cross-link samples.....                                       | 98 |

|   |     |
|---|-----|
| Figure 3-5 A comparison between spectra from elastin and crosslink sample A .....         | 99  |
| Figure 3-6 A comparison between equine tendon and cross link sample B spectra. ....       | 100 |
| Figure 3-7 The spectra of desmosine and isodesmosine cross-links.....                     | 101 |
| Figure 3-8 The power curves for different extra-cellular matrix proteoglycans.....        | 102 |
| Figure 3-9 The power curve for hydroxylapaptite .....                                     | 104 |
| Figure 3-10 Spectra of articular cartilage at different areas within a given sample. .... | 106 |
| Figure 3-11 The sample variance in the fluorescent spectra of articular cartilage .....   | 107 |
| Figure 3-12 The spectra of different regions of section of articular cartilage. ....      | 108 |
| Figure 3-13. A comparison of the spectra of type collagen II and cartilage.....           | 109 |
| Figure 3-14 Images of the purified type II collagen, compared to intact cartilage. ....   | 109 |
| Figure 3-15 Spectra of the intervertebral disc annulus and nucleus .....                  | 110 |
| Figure 4-1 A TPF image of articular cartilage.....  | 118 |
| Figure 4-2 An SHG image of cartilage. ....  | 119 |
| Figure 4-3 Forwards CARS images taken of chondrocytes in the superficial zone. ....       | 121 |
| Figure 4-4 “Shadows” of cells in the CARS images. ....                                    | 123 |
| Figure 4-5 SHG, TPF and CARS images from the superficial zone .....                       | 125 |
| Figure 4-6 The SHG, TPF and CARS intensity profiles across a pair of cells. ....          | 126 |
| Figure 4-7 A reconstruction of the surface of the articular cartilage. ....               | 127 |
| Figure 4-8 A full depth section of articular cartilage.....                               | 129 |
| Figure 4-10 SHG and TPF images of the radial zone. ....                                   | 132 |
| Figure 4-11 TPF and SHG intensity profiles taken across the tidemark. ....                | 134 |
| Figure 4-12 The interface between bone and calcified cartilage .....                      | 136 |
| Figure 4-13 A schematic diagram of the distal end of the 3 <sup>rd</sup> metacarpal. .... | 138 |
| Figure 4-14 Multi-photon imaging on a sample containing a butterfly lesion. ....          | 139 |
| Figure 4-15: A 3D reconstruction of a microlesion. ....                                   | 140 |
| Figure 4-16 histological sections of the sample imaged for figure 4-15. ....              | 141 |
| Figure 4-17 A SHG and TPF images showing splitting of the collagen matrix. ....           | 142 |
| Figure 4-18 A reconstruction of fibrillated collagen at the articular surface.....        | 143 |
| Figure 4-19 Histology of the region shown in figure 4-18. ....                            | 144 |
| Figure 4-20 Highly degenerated tissue showing a very fibrous structure.....               | 145 |
| Figure 4-21 Cell clusters seen on the sagital ridge of a sample with advanced OA. ....    | 146 |
| Figure 4-22 Cell clusters at the with a surrounding fibrous capsule.....                  | 147 |
| Figure 4-23 histology carried out on the cortical ridge sample from figure 4-22.....      | 148 |
| Figure 5-1 Multi-photon imaging and immuo-staining of elastin fibres. ....                | 153 |

|  |     |
|--|-----|
| Figure 5-2 TPF and SHG imaging on a transverse section.....                                  | 154 |
| Figure 5-3 Areas imaged for elastin fibres within the metacarpophanageal joint. ....         | 155 |
| Figure 5-4 Elastin fibre arrangements from different regions. ....                           | 156 |
| Figure 5-5 A schematic diagram of elastin fibre orientations in different regions. ....      | 157 |
| Figure 5-6 The number of elastin fibres as a function of depth. ....                         | 158 |
| Figure 5-7 Montage of TPF images showing branching elastin fibres. ....                      | 159 |
| Figure 5-8 Profile across a thick elastin fibre. ....  | 160 |
| Figure 5-9 Profile across a thin elastin fibre. ....   | 160 |
| Figure 5-10 Age dependence of elastin fibre density.....                                     | 161 |
| Figure 5-11 TPF image showing broken elastin fibres at the articular surface .....           | 162 |
| Figure 5-12 Multi-photon microscopy of the intervertebral disc annulus. ....                 | 164 |
| Figure 5-13 A 3D reconstruction of the disc annulus. ....                                    | 165 |
| Figure 5-14 Multi-photon images of the rats tail annulus.....                                | 166 |
| Figure 5-15 Multi-photon images from the nucleus of the equine disc. ....                    | 167 |
| Figure 5-16 enface imaging of the inner portion of the elastic cartilage of the ear. ....    | 169 |
| Figure 5-17 3D reconstruction of the inner portion of the elastic cartilage.....             | 170 |
| Figure 5-18 Profiles across elatin in elastic cartilage.....                                 | 171 |
| Figure 5-19 The perichondrium layer of elastic cartilage viewed enface.....                  | 173 |
| Figure 5-20 SHG and TPF images from a transverse section of elastic cartilage. ....          | 174 |
| Figure 5-21 Elastic cartilage stained with orcein.....                                       | 176 |
| Figure 6-1 The polarization sensitivity of TPF from fluorescein. ....                        | 180 |
| Figure 6-2 Fibre orientations found from imaging and polarization sensitivity.....           | 181 |
| Figure 6-3 TPF and SHG polarization sensitivity in cartilage and tendon. ....                | 182 |
| Figure 6-4 Polarization sensitivity curve fitting. ....                                      | 184 |
| Figure 6-5 The effect of the objective on polarization.....                                  | 186 |
| Figure 6-6 Split lines in articular cartilage.....   | 188 |
| Figure 6-7 Ratio images taken in cartilage. ....   | 189 |
| Figure 6-8 Polarization dependence with depth in tendon.....                                 | 191 |
| Figure 6-9 Polarization sensitivity with depth in cartilage. ....                            | 197 |
| Figure 6-10 Histology of the lesion investigated for figure 6-11.....                        | 199 |
| Figure 6-11 The polarization dependence of TPF and SHG at a lesion.....                      | 200 |
| Figure 6-12 Histology of the lesion investigated for figure 6-13.....                        | 201 |
| Figure 6-13 Polarization dependence of SHG with depth at a lesion. ....                      | 202 |
| Figure 0-1 Polarization sensitivity for collagen fibres at an angle to the imaging plane:... | 216 |

### **Table of Tables**

|   |     |
|---|-----|
| Table 1.1 A comparison between non-linear microscopy and other imaging techniques ...         | 16  |
| Table 1.2 A summary of biological sources of SHG. ....  | 23  |
| Table 1.3 SHG signal dependence on polarization of the incident light. ....                   | 25  |
| Table 1.4 A summary of known two photon fluorophores. ....                                    | 36  |
| Table 1.5 CARS vibrational modes in biological tissues. ....                                  | 45  |
| Table 3.1 A summary of the TPF and SHG from the samples investigated in this chapter<br>..... | 112 |
| Table 6.1 The visibility of the polarization sensitivity of SHG and TPF. ....                 | 183 |
| Table 6.2 A comparison of split line and polarization sensitivity results. ....               | 187 |

## Publications

*“Analysis of collagen fibre arrangement in normal and diseased cartilage using Polarization Sensitive Non-linear Microscopy”* (J C Mansfield, C P Winlove, J Moger and S Matcher) – **journal of biomedical optics** – 13 (4) July / August **2008**

## Conferences and Proceedings

**5<sup>th</sup> Elastin European Meeting (2008)** *“Elastic Fibre Organisation in articular cartilage”* (J Yu, J C Mansfield, J Urban, J Moger, C P Winlove) Poster Presentation (Paper relating to this work currently in draft)

**IOP- 2nd Annual Biophotonics: Technology and Applications meeting (2007)**  
*“Collagen fibre arrangement in normal and diseased cartilage using non-linear microscopy”* (J C Mansfield, C.P. Winlove, J. Moger and S. Matcher) Oral Presentation

**SPIE Photonics West (2007):** *“Second-harmonic and two-Photon imaging and polarimetry of articular cartilage”* (J C Mansfield, C P Winlove, J Moger, K Knapp and S Matcher ) Poster presentation and conference proceedings

**5<sup>th</sup> World Congress of Biomechanics (2006):** *“imaging articular cartilage using non-linear microscopy”* (J C Mansfield, C P Winlove, K Knapp and S Matcher) Oral presentation

**SPIE Photonics West (2006):** *“Imaging articular cartilage using second harmonic generation microscopy”* (J C Mansfield, C P Winlove, K Knapp and S Matcher ) Poster presentation and conference proceedings

# 1 Background

---

## 1.1 Introduction

In this study multi-photon microscopy has been used to investigate articular cartilage. The aim of this work was to characterise the appearance of healthy tissue with this technique and then investigate degenerate tissue with the aim of observing changes for osteoarthritis research. In this chapter the structure of the extra cellular matrix and healthy articular cartilage is described in section 1.6 along with some of the characteristics of osteoarthritic degeneration. The multi-photon imaging in this thesis relied on the following three imaging modalities: second harmonic generation (SHG), two photon fluorescence (TPF) and coherent anti-Stokes Raman scattering (CARS). These processes are described here along with the different contrasts they provide in biological imaging. There are two main advantages of multi-photon microscopy; firstly the images produced through multi-photon microscopy have submicron resolutions and also 3Dimensional data sets can be generated and secondly the non-linear optical process rely on endogenous contrast and therefore the technique can be used to provide detailed structural data intact unstained samples.

Non-linear optical processes occur in high electric fields where the electric polarization vector  $\vec{P}$  is no longer linearly proportional to the electric field strength  $\vec{E}$ . In this case the approximation for low electric field

$$\vec{P} = \varepsilon_0 \chi \vec{E} \quad (1)$$

must be replaced by the following polynomial expression where  $\chi^{(n)}$  are  $(n+1)^{\text{th}}$  order tensors<sup>1,2</sup>

$$\vec{P} = \varepsilon_0 \left( \chi^{(1)} \cdot \vec{E} + \chi^{(2)} : \vec{E}\vec{E} + \chi^{(3)} :: \vec{E}\vec{E}\vec{E} + \dots \right). \quad (2)$$

Second order processes, for example TPF and SHG, are described by the second order non-linear susceptibility tensor  $\chi^{(2)}$ . Third order processes, for example CARS and third harmonic generation (THG) are described by the third order non-linear susceptibility tensor  $\chi^{(3)}$ . For non-linear effects to occur the electric field strength typically needs to be greater

than about  $100\text{kV/m}^{-1}$  and for this reason they normally are observed in focused laser beams.

## **1.2 The Non-linear Microscope**

Non-linear microscopy is a laser scanning microscopy technique which is built on the principles of confocal microscopy<sup>3</sup>. In both these techniques the focal point of a laser is scanned through the sample and the image is generated from the signal produced at each point in the scan. Non-linear optical processes have a very small interaction cross sections as they rely on multiple photons interacting with a molecule and also they are dependent on the square of the laser power for second order interactions or the cube of the laser power for third order interactions (as shown in equation 2). The consequence of this is that the non-linear processes will only occur within the focal point of the laser beam. This makes the process inherently con-focal and removes the need for a pinhole to exclude off focus light.

All the multi-photon processes produce light at different wavelengths allowing the different signals to be separated from each other and the laser fundamental. SHG and TPF are excited by infra red laser sources but produce light in the visible range (with TPF having a longer wavelength than SHG). CARS requires infra red laser excitation sources and the signal is again in the infra red but at a shorter wavelength.

With multi-photon microscopy it is possible to achieve submicron resolution in the imaging plane and approximately micron resolution in the axial direction. This good axial resolution makes non-linear microscopy an ideal technique for obtaining 3D data sets; this is achieved by taking a series of images of the sample where the sample is moved towards the objective on a motor stage between each image<sup>4</sup>.

The non-linear optical processes used in this thesis do not require the use of exogenous contrast agents. The TPF signal comes from endogenous fluorophores<sup>5</sup>, SHG comes from biological structures lacking inversion symmetry<sup>6</sup> and the CARS contrast is derived from intrinsic molecular vibrations<sup>7</sup>. Typically IR laser excitation sources are used for multi-photon microscopy and these have a greater penetration depth into tissues than UV or

visible light which is used in confocal microscopy<sup>8</sup>, and therefore enable images to be taken at greater depths. For example Campagnola et al were able to image with SHG a sample of mouse muscle tissue that was 550 $\mu$ m thick<sup>6</sup>. The combination of the reasonable depth penetration and lack of staining means these techniques can be used on intact tissue samples. This reduced the risk of artefacts caused by sample preparation and opens the possibility for non-linear microscopy to be developed into an in-vivo imaging technique in the future.

In non-linear microscopy there are also reduced problems due to photo-bleaching compared to confocal microscopy. SHG images are unaffected by photo-bleaching as SHG is an elastic process and no energy is absorbed by the sample during the process and TPF photo-bleaching effects are limited to the focal spot of the laser excitation beam.

Multi-photon microscopy is compared to other techniques which are used to investigate tissues at a similar level in table 1.1. These include optical coherence tomography (OCT), con-focal microscopy, transmission light microscopy (Differential Interference Contrast (DIC), phase contrast), scanning electron microscopy and transmission electron microscopy.

|                            | OCT <sup>9</sup>                                      | X-ray scattering <sup>10-12</sup>                    | Confocal <sup>13</sup>   | Electron microscopy                     |                                 | Transmitted light  |  | Non-linear microscopy                             |  |  |
|----------------------------|---|--|--|---|---------------------------------|--|--|---|--|--|
|                            |   |  |  | scanning                                | transmission                    | DIC  | Phase contrast   | SHG   | TPF  | CARS   |
| <b>Lateral Resolution</b>  | 1-15 $\mu$ m  | 2-6 $\mu$ m  | 0.15 $\mu$ m <sup>14</sup>                                       | nm                                      | nm                              | $\approx$ 0.5 $\mu$ m  | $\approx$ 0.5 $\mu$ m  | $\frac{0.61\lambda_0}{\sqrt{2}NA}$                | $\frac{0.61\lambda_0}{\sqrt{2}NA}$                     | $\frac{0.61\lambda_0}{\sqrt{3}NA}$ <sup>15</sup> |
| <b>Axial resolution</b>    | 1-15 $\mu$ m  | Dependent on sample thickness                        | 0.22 $\mu$ m <sup>14</sup>                                       | N/A                                     | N/A                             | <0.5 $\mu$ m if thin sections are used <sup>13</sup>                                       |  | $\frac{2n\lambda_0}{\sqrt{2}(NA)^2}$ <sup>1</sup> | $\frac{2n\lambda_0}{\sqrt{2}(NA)^2}$ <sup>15</sup>     | $\frac{2n\lambda_0}{3(NA)^2}$ <sup>15</sup>      |
| <b>Depth penetration</b>   | Up to 2-3mm   | N/A  | Typically 50-100 $\mu$ m but up to 150-200 $\mu$ m <sup>16</sup> | none                                    | Ultra-thin slices needed        | Thin samples are needed to minimize contribution of out of focus light from rest of sample | Dependent on the scattering of the tissue and the laser power used can be up to about 500 $\mu$ m <sup>6</sup> |   |  |  |
| <b>Contrast</b>            | Reflection off interfaces between refractive indices  | x-ray scattering off periodic structures             | Fluorescently labeled molecules                                  | Metal coating on surface of sample      | Density of embedded medium      | Variations in refractive index of the sample   | Molecules lacking inversion symmetry   | Endogenous fluorophores                           | Molecular bond vibrations<br>E.g. CH <sub>2</sub> bond |  |
| <b>Tissue preparation</b>  | Intact tissue samples                                 | Sections wrapped in mylar                            | Staining with a fluorescent dye                                  | Metal coating surface                   | Fixing, dehydrating & embedding | Unstained thin histological sections   | Intact tissue samples can be used  |   |  |  |
| <b>General limitations</b> | Less resolution possible compared to other techniques | Imaging time, image reconstruction and sample damage | Needs staining photo-bleaching and damage may be a problem       | Artifacts due to preparation technique, |                                 | Need thin sections, therefore unable to image the 3D structure of tissues                  | Expensive set-up requiring high powered lasers   |   |  |  |

Table 1.1 A comparison between non-linear microscopy and other imaging techniques

Non-linear microscopy was first developed in 1971 by Fine and Hansen<sup>17</sup> but did not become a very practical technique for biological samples until the development of ultra short pulsed mode locked lasers<sup>3, 18</sup>. This is because the non-linear processes have a very small absorption cross-section and therefore need high instantaneous laser powers to excite them. Ultra short pulsed lasers are needed as they enable a lower average power to be used in order to produce the same amount of non-linear signal. Equation (3) shows the relationship between the powers of a pulsed and continuous wave laser producing the same amount of signal<sup>3</sup>.

$$P_{CW} = (\tau f_p)^{-1/2} P_{Pulsed} \quad (3)$$

Where  $\tau$  is the pulse duration time and  $f_p$  is the repetition rate of the pulses. The lower average powers used by pulsed lasers avoid the problems of tissue damage due to excessive heating, which was occurring when samples were illuminated with the high powered continuous wave lasers<sup>3, 18, 19</sup>. Typically non-linear microscopes use a Ti:Sapphire laser which produces IR light with a wavelength tuneable between 700 and 900nm in 100fs pulses, for SHG and TPF imaging. For CARS two different excitation wavelengths are needed with the difference between the two wavelengths being tuneable; this excitation beam is provided by an Optical Parametric Oscillator (OPO).

Although non-linear microscopy relies on longer wavelength excitation light, it is still able to produce images with a sub-micron resolution. This is because the intensity of the signal depends on the square of the incident intensity for two-photon processes (SHG and TPF) which improves the possible resolution of a non-linear microscope. In the focal plane the effective focal spot size within which the SHG or TPF light is produced is smaller by a factor of  $1/\sqrt{2}$  compared to the effective focal spot in confocal fluorescence microscopy. For a non-linear microscope the Rayleigh criterion for the minimum resolvable distance  $|x_{min}|$  can be written as follows, with equation 4a being for a 2 photon process and equation 4b for a 3 photon process<sup>20</sup>.

$$|x_{min}| = \frac{0.61\lambda}{NA} \cdot \frac{1}{\sqrt{2}} = \frac{0.46\lambda}{NA} \quad (4a)$$

$$|x_{min}| = \frac{0.61\lambda}{NA} \cdot \frac{1}{\sqrt{3}} = \frac{0.35\lambda}{NA} \quad (4b)$$

In these equations NA is the numerical aperture of the objective and  $\lambda$  is the wavelength of the excitation light. Equation (4) shows that the longer wavelengths used for non-linear microscopy decrease the resolution but even so lateral resolutions of less than 300nm have been achieved<sup>6</sup>. This resolution is adequate to image cells and some of their cellular contents, and also see individual fibres within connective tissues. The axial resolution for non-linear microscopy is also improved by the dependence on the square of the incident power. In the axial direction the incident laser power is proportional to  $1/d^2$  where  $d$  is the axial distance from the focal point and consequently TPF and SHG production is proportional to  $(1/d^4)^8$ .

## 1.3 Second Harmonic Generation

### 1.3.1 General theory

The first non-linear optical process discussed in this chapter is second Harmonic Generation (SHG) or frequency doubling. This is a coherent elastic process where two excitation photons are simultaneously absorbed in an optically non-linear medium to create a SHG photon with a wavelength exactly half that of the excitation wavelength. This process is summarized in the energy level diagram shown in figure 1-1.

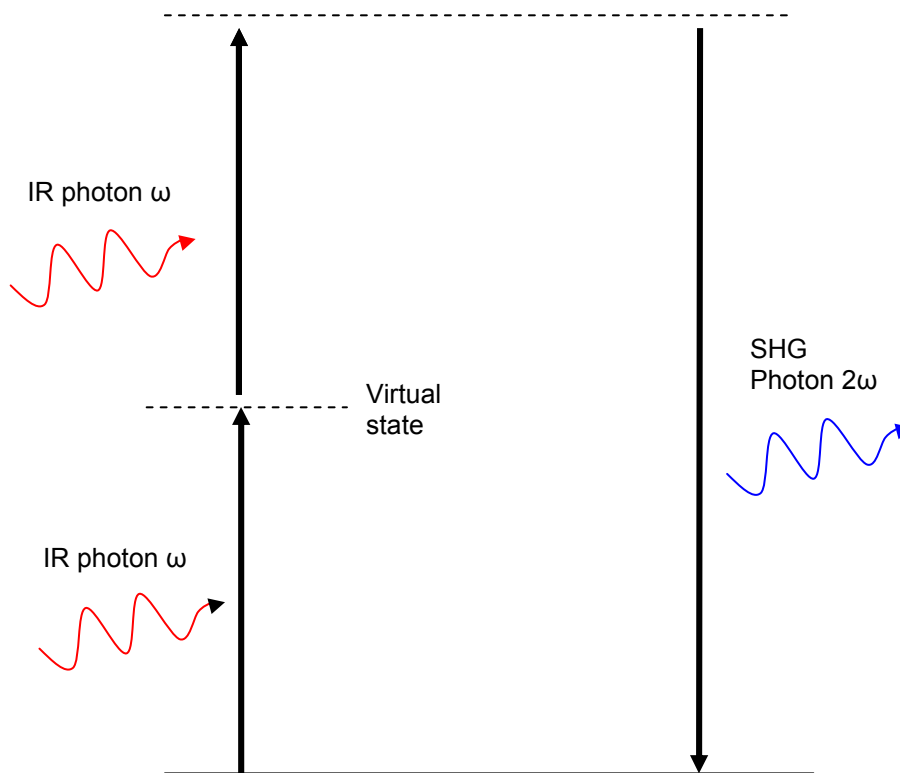


Figure 1-1 Energy level diagram for SHG

Second harmonic generation is described in the second term in the non-linear polarization polynomial (equation 2). When the exciting field is a linearly polarized sine wave and the medium is isotropic then equation (2) simplifies to:

$$P = \varepsilon_0 (\chi^{(1)} E_0 \sin \omega t + \chi^{(2)} E_0^2 \sin^2 \omega t + \chi^{(3)} E_0^3 \sin^3 \omega t + \dots) \quad (5)$$

Where  $\chi_1$  etc. are scalar dielectric susceptibility coefficients. Using standard trigonometric identities we can rearrange to give<sup>21</sup>.

$$P = \epsilon_0 \chi^{(1)} E_0 \sin \omega t + \frac{\epsilon_0 \chi^{(2)}}{2} E_0^2 (1 - \cos 2\omega t) + \frac{\epsilon_0 \chi^{(3)}}{4} E_0^3 (3 \sin \omega t - \sin 3\omega t) + \dots (6)$$

In equation (6) the  $\cos 2\omega t$  term represents the second harmonic generation and the  $\sin 3\omega t$  term represents third harmonic generation. The process can also be viewed quantum mechanically as the combination of two photons with energy  $\hbar\omega$  forming a single photon with energy  $2\hbar\omega$ . Second harmonic generation cannot take place in an isotropic medium i.e. where there are no preferred directions. This is because in an isotropic medium a reversal of the direction of the electric field causes a reversal in the direction of the polarization, in other words polarization is an odd function of electric field. For this to be the case the terms in  $E^2$  would have to be zero ruling out the possibility of second harmonic generation<sup>21</sup>. Therefore a necessary condition for generation of second harmonic light is for a medium to be non-isotropic on the scale of the wavelength of light, and to lack inversion symmetry<sup>19</sup>.

There are several factors affecting the magnitude of second harmonic generation. It depends quadratically on the intensity of the excitation light and will also be affected by the polarization and wavelength of the excitation light. It will also depend on the properties of the material: the non-linear susceptibility, the phase mismatch between the SHG and the excitation light and the distribution and orientation of the SHG sources within the focal volume.

### 1.3.2 Phase mismatch and propagation direction

As SHG is a coherent process it is affected by interference effects and the phase mismatch within the sample. The phase mismatch is the value  $\vec{q} = 2\vec{k}_1 - \vec{k}_2$ , where  $\vec{k}_2$  is the wave-vector of the SHG light and  $\vec{k}_1$  is the wave-vector of the incident laser light<sup>18</sup>. The differences in phase mismatch for SHG generated in the forwards and backwards direction are shown in figure 1-2. For SHG generated in the epi direction the phase mismatch is large and for forwards SHG the phase mismatch is much less.

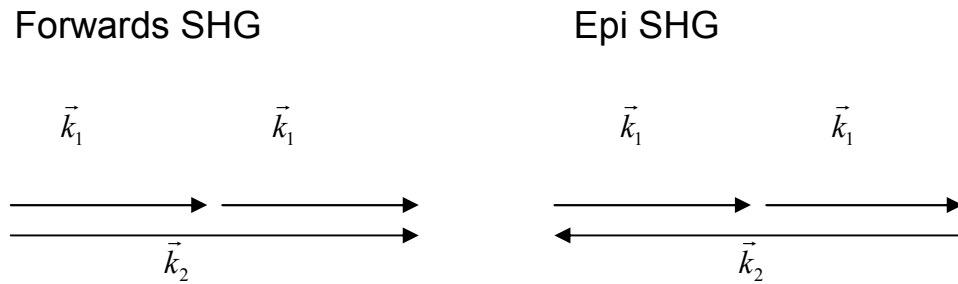


Figure 1-2 phase diagrams for forward and epi SHG

The SHG signal will be greatest when the phase mismatch is zero, because in this case the SHG generated throughout the sample will be in phase with the incident driving electric field and will interfere constructively. However in real materials the phases will not be matched due to dispersion (the wavelength dependence of the refractive index). This means that there will be some destructive interference between some of the SHG produced at different depths within the sample resulting in reduced intensity. The length over which the forwards SHG will interfere constructively is called the coherence length and is given by the following equation<sup>1</sup>,

$$L_c = \frac{\lambda_1}{4|n_2 - n_1|} \quad (7)$$

where  $\lambda_1$  is the incident wavelength of the laser and  $n_1$  and  $n_2$  are the refractive indexes of the material for the incident light and the SHG respectively<sup>1</sup>. Even in low dispersion materials there is a large phase mismatch in the epi direction and therefore the signal in this direction will be low due to destructive inference and the SHG will be predominantly generated propagating in the forwards direction.

For a linearly propagating laser source in a non-linear crystal all the SHG will be generated in the forwards direction. However in many systems excited with a focused laser beam SHG may be generated in both the forwards and epi directions. In this case the propagation angle and power of the SHG will be dependent on the excitation light distribution and on the spatial arrangement of the SHG sources within the focal volume<sup>22</sup>. Assuming that the beam has a Gaussian profile and is polarized in the y direction then the electric field in the focal volume can be described by the equation 8 in Cartesian co-ordinates:<sup>22-24</sup>

$$\vec{E}_\omega(x, y, z) = -iE_{\omega 0} \exp\left(-\frac{(x^2 + y^2)}{w^2} - \frac{z^2}{w_z^2} + i\xi\vec{k}_\omega z\right) \hat{y} \quad (8)$$

where  $w$  and  $w_z$  are the radii of the beam widths in the radial and axial direction respectively,  $k_\omega$  is the wave-vector of the excitation light and  $\xi$  is the reduction in wave-vector caused by the phase anomaly or Gouy shift. The beam waists are dependent on the NA of the objective and on the wavelength of the excitation light, with the values decreasing for higher NA and shorter wavelengths. The parameter  $\xi$  is also determined by the NA of the objective, with its significance increasing for higher NA objectives.

The total second harmonic electric field in a given direction is given by the integral over the focal volume of the electric field in that direction produced by the SHG sources at every point. Mertz et al<sup>22, 24</sup> determined the results for different distributions of SHG sources. In the case of a completely uniform distribution of sources over the focal volume their model predicted that the SHG light would propagate as a forward directed hollow cone, with the angle of the cone being dependent on  $\xi$ . This angular distribution is due to the requirement of phase matching in a coherent process. The second harmonic photons have a wave-vector  $\vec{k}_{2\omega} = 2\vec{k}_\omega$ , but due to the Gouy phase shift the excitation photons have an effective wave-vector of  $\xi\vec{k}_\omega$  and therefore to allow phase matching the SHG light must be generated at an angle  $\theta$  from the z axis where  $\theta \approx \cos^{-1} \xi$ . For more complex distributions of SHG sources within the focal volume SHG light was found to also be generated in the backwards direction. An example is a sinusoidal variation in density of SHG sources of appropriate periodicity in the axial direction. The proportion of the focal volume occupied by SHG sources was also found to affect the ratio of light generated in the forward/ backward direction.

### 1.3.3 SHG in Tissues

#### 1.3.3.1 Sources of SHG

In biological samples there are many structures giving them a high non-linear susceptibility through a lack of inversion symmetry and/or chirality. The structures and locations of known biological sources of SHG are summarised in table 1.2

| Source of SHG                    | Structure   | Location              |
|----------------------------------|---|-----------------------|
| Fibrillar collagen <sup>25</sup> | Rod shaped protein molecules with a triple helix structure. | Extracellular matrix. |
| Tubulin <sup>6</sup>             | Rod shaped protein  | Cytoskeleton          |
| Microtubules <sup>26</sup>       | Rod shaped protein  | Cytoskeleton          |
| Actin/ myosin <sup>27, 28</sup>  | Rod shaped proteins   | Muscle fibres         |
| Starch <sup>29, 30</sup>         | Strings of polysaccharides chiral structure                 | Food store in plants  |

**Table 1.2 A summary of biological sources of SHG.**

In this project we mainly focus on the second harmonic generation from collagen, as it has been the most widely characterised and also is the most abundant structural protein in the body<sup>19</sup>. Collagen structure is highly anisotropic: the collagen molecules consist of 3 peptide chains arranged in a triple helix to form long rod shaped proteins. These are then organised to form fibrils, and therefore provides a strong source of second harmonic generation<sup>19</sup>. The second harmonic generation from collagen is enhanced by the chiral properties of the triple helix. This is because chiral structures are inherently non-centrosymmetric.<sup>31</sup>

Cox et al carried out experiments to determine whether the SHG signal intensity depended on the type of collagen present. In tissue samples there were large differences between the SHG signal from types I, II and III collagen, but when these collagens were extracted to produce amorphous samples of each collagen type, the SHG signals were similar. This led them to the conclusion that the differences in the signals were due to different degrees of order in the different types of collagen in various tissues rather than a difference in the intrinsic SHG producing properties of the different collagen molecules<sup>32</sup>.

### **1.3.3.2 Polarization effects**

For many sources of second harmonic generation the amount of signal produced is dependent on the polarization state of the incident laser light with which the sample is excited. In this section we will focus on the polarization sensitivity of SHG from collagen as this has been the focus of most previous polarization sensitive studies<sup>18, 19, 23, 25, 33, 34</sup>, although other sources of SHG also have polarization sensitivity for example myosin and actin structures have been investigated by Chu et al<sup>27</sup> and by Plotnikov et al<sup>28</sup>. Most studies on the polarization sensitivity of collagen have been carried out on tendon which is composed of highly ordered parallel collagen I fibres.

The intensity of the second harmonic signal produced from a collagen sample is dependent on the orientation and polarisation state of the laser excitation light with respect to the fibre axis. For a linearly polarized laser beam incident on a collagen fibril the amount of second harmonic signal produced at different polarization orientations is summarised in table 1.3.. For fibrils lying in the plane perpendicular to the direction of laser light propagation the amount of SHG produced depends on the angle between the fibre axis and the laser polarization. If the light is polarised along the fibre axis the maximum SHG signal will be observed whereas if it is polarized perpendicular to the fibre axis the weakest SHG signal will be observed<sup>35</sup>. This means that the polarization dependence of the SHG signal can be measured in order to find the orientation of the collagen fibrils within a tissue. This technique was used by Yasui et al in 2004 to find the orientation of collagen fibrils in various tissue samples<sup>35</sup> and this will be pursued in Chapter 6 of this thesis. The intensity of the SHG signal also depends on the angle between the collagen fibre and the imaging plane. The intensity of the SHG is maximum when the collagen fibre is in the imaging plane and very low when the fibre is perpendicular to the imaging plane. (This effect is discussed in more detail in the appendix.)

| Polarization of incident light | Collagen fibre orientation                 |  |
|--------------------------------|--|--|
|                                | Parallel to direction of light propagation | In the plane perpendicular to direction of light propagation |
| Parallel to fibre axis         | N/A  | Strong SHG signal  |
| Perpendicular to fibre axis    | V. Weak SHG signal                         | Weak SHG signal  |

**Table 1.3 SHG signal dependence on polarization of the incident light. (adapted from Yasui et al<sup>35</sup>)**

To quantify how the SHG signal varies with fibril orientation and laser polarization let us consider the non-linear susceptibility tensor  $\chi_2$ . This tensor is third order and contains 27 elements. The components of the polarization are from <sup>1</sup>.

$$P_i = \sum_{jk} \epsilon_0 \chi_{ijk} E_j E_k \quad (9)$$

The components of  $\chi_2$  can be written as follows <sup>19</sup>,

$$\chi_{ijk} = a s_i s_j s_k + b s_i \delta_{jk} + \frac{c}{2} (s_j \delta_{ik} + s_k \delta_{ij}) \quad (10)$$

where  $s_i$ ,  $s_j$  and  $s_k$  are components of  $\hat{s}$ , a unit vector pointing along the axis of the collagen fibre, and  $a$ ,  $b$  and  $c$  are constants, which depend on the optical properties of the material and must be found experimentally.

These expressions can be simplified through the use of ‘‘Kleinmann symmetry’’ which states that the elements of the second order susceptibility tensor that are related by permutations of the indices are equal, ie  $\chi_{ijk} = \chi_{ikj} = \chi_{jik} = \chi_{jki} = \chi_{kij} = \chi_{kji}$ . By requiring this symmetry of equation 6 one can see that this implies that  $b = c/2$ . Therefore the 27 elements of the  $3 \times 3 \times 3$  non-linear susceptibility tensor can be contracted into a  $6 \times 3$  Kleinmann D tensor. This assumption of Kleinmann symmetry can be used because second harmonic generation is an elastic scattering process and does not involve the excitement of electrons into a higher energy state and therefore the polarization can be written as follows <sup>18, 19</sup>,

$$\vec{P} = a \hat{s} (\hat{s} \cdot \vec{E})^2 + b \hat{s} (\vec{E} \cdot \vec{E}) + 2b \vec{E} (\hat{s} \cdot \vec{E}). \quad (11)$$

A number of experiments have been carried out on rats tail tendon in order to characterise the polarization sensitivity of type I collagen. The first experiments were carried out by Freund et al<sup>25, 33</sup> with further work by Stoller et al<sup>18, 19, 34</sup> and Williams et al<sup>23</sup>. The majority of this work has been carried out for the simplest case where the collagen fibres are in the plane perpendicular to the laser propagation and for this discussion we take the collagen fibril axis  $\hat{s}$  to be pointing along the x-axis. This arrangement is shown in figure 1-3.

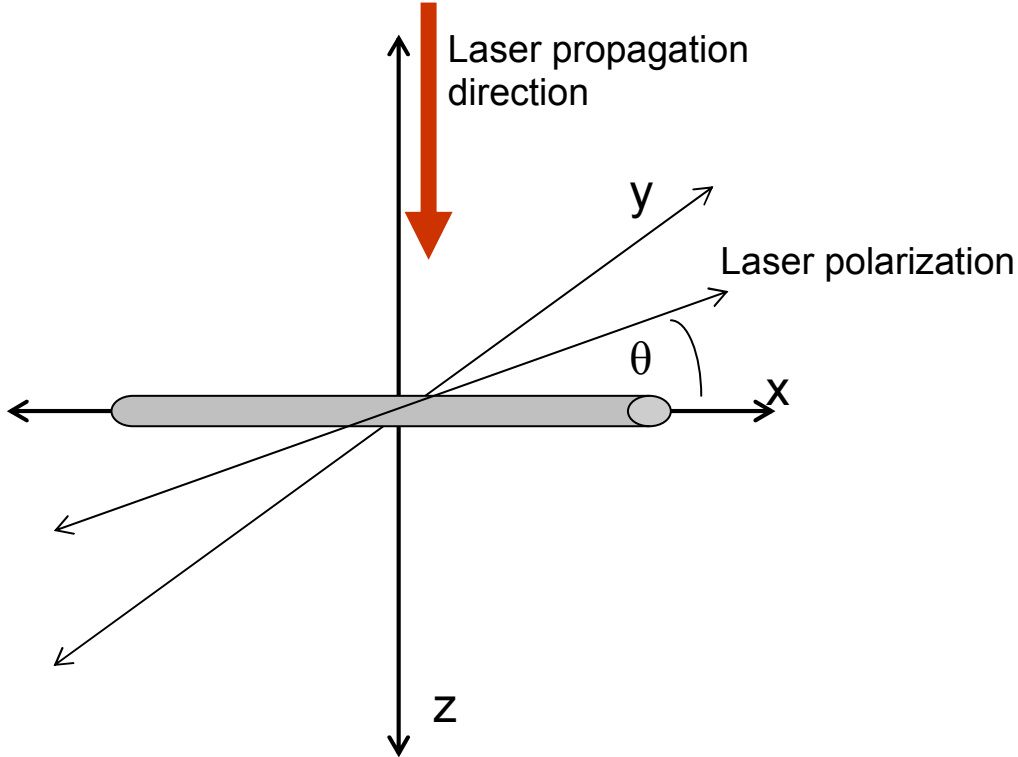


**Figure 1-3 The orientation of the collagen fibril w.r.t. the laser beam.** This is the arrangement assumed by Freund et al<sup>25</sup> in their analysis. The collagen fibre is along the z-axis and the laser beam is propagating in the z direction and is linearly polarized at an angle  $\theta$  w.r.t the collagen fibril.

In this case the SHG light can be split into 2 components polarized parallel and perpendicular to the fibre axis:

$$P_{(2\omega)x} = \chi_{xxx} E_{(\omega)x}^2 + \chi_{xyy} E_{(\omega)y}^2 \quad (12a)$$

$$P_{(2\omega)y} = 2\chi_{xyy} E_{(\omega)x} E_{(\omega)y} \quad , \quad (12b)$$

where the coefficients  $\chi_{xxx}$  and  $\chi_{xyy}$  can be calculated from equation 10, and  $E_{(\omega)x}$  and  $E_{(\omega)y}$  are the components of the laser electric field in the x and y directions respectively. Taking absolute measurements of the SHG intensity is challenging and therefore most polarization

sensitivity measurements calculate either the ratio  $\rho = \chi_{xxx} / \chi_{xyy}$  or the ratio  $\gamma = a / b$ , both of which can be estimated without absolute intensity measurements. The two ratios are related via the equation  $\rho = \frac{1+3\gamma}{\gamma}$ . The intensity of the SHG in each of the polarization states as a function of angle  $\theta$  between the fibres and the laser polarization is given by the equations<sup>25</sup>

$$I_x(\theta) = [\rho \cos^2 \theta + \sin^2 \theta]^2 \quad (13a)$$

$$I_y(\theta) = [\sin 2\theta]^2 \quad (13b)$$

The values of  $\rho$  found by curve fitting these equations 13a and 13b in the literature range from 1.3 to 2.6. The highest value was from Williams et al<sup>23</sup> and the lowest value is from Freund et al<sup>25</sup>. The difference between the values is thought to arise from the differences in imaging area in the experiments. The higher values are obtained when the imaging area is small whereas low values are obtained when whole fibres are imaged, as here multiple fibre orientations exist in the imaging area due to the crimp of the rats tail tendon.

To find the actual values of the coefficients of  $\chi^{(2)}$ , the laser focal point must be characterised. Due to the quadratic dependence of the SHG intensity on the input power the production of SHG light depends strongly on the dimensions of the focal point. Also phase mismatching within the focal volume needs to be known as this will reduce SHG yield. Stoller et al<sup>34</sup> characterised this by measuring the SHG from a quartz sample (known non-linear susceptibility tensor) and then using this value in calculations of the second order non-linear susceptibility for collagen. For a collagen fibre aligned along the  $x$  axis they found that  $\chi_{xxx} = 0.4$  pm/V and that the other non-zero components  $\chi_{xyy} = \chi_{yyx} = \chi_{yxx}$  were  $0.68\chi_{xxx}$ .

The anisotropic structure of collagen means that it is birefringent, i.e. light of different polarizations experiences different refractive indices. The optic axis of collagen lies along the axis of the collagen molecules. The refractive index for light polarized along the optic axis (extraordinary rays) ( $n_e$ ) is greater than the refractive index of light polarized perpendicular to it (ordinary rays) ( $n_o$ ) and the difference in these refractive indices  $\Delta n = (n_e - n_o)$  is the birefringence. The birefringence of collagen based tissues is a combination

of intrinsic birefringence (caused by the optical anisotropy of individual fibres) and form birefringence (caused by the difference between the refractive index of medium and the anisotropically arranged collagen fibres)<sup>36</sup>. The overall birefringence is tissue dependent and has been measured to be about 0.003 for rats tail tendon<sup>19, 34</sup> and  $6.0 \pm 0.6 \times 10^{-3}$  for bovine intervertebral disc<sup>37</sup>. The consequence of birefringence is that the polarization of the light changes as it passes through the sample of collagen. Generally linearly polarized light will become elliptically polarized and the angle of polarisation will rotate with the distance travelled. Birefringence will affect the polarization dependence of the SHG; this will be different at different depths in the sample as the polarization of both the incident laser light and the exiting SHG will have been rotated by different amounts. The magnitude of the effect will depend on the degree of order of the collagen fibrils in the sample. In less ordered samples the effects will be less as the direction of the optic axis will vary throughout the sample<sup>19</sup>. Polarization sensitivity in tissues is discussed in more detail in chapter 6.

### 1.3.3.3 Phase mismatch

In order to investigate whether phase mismatch is an important factor to consider in non-linear microscopy of biological tissues we consider the magnitude of the effect in type I collagen fibres. To generate SHG light from collagen an incident wavelength of 800nm is normally used giving a SHG signal at 400nm. The dispersion relation for collagen at these wavelengths gives  $\Delta n = -0.03$ , this gives a coherence length of  $7\mu\text{m}$ <sup>34</sup>. Biological tissues will not be 100% collagen, but instead will consist of water, collagen and many other organic molecules. The dispersion for the relevant wavelengths of light in water is less and therefore it has a longer coherence length of  $28\mu\text{m}$ . This means that the coherence length in a tissue sample will depend on its composition and has been estimated to be between  $5\mu\text{m}$  and  $13\mu\text{m}$ <sup>38</sup>. In SHG microscopy the focal area in which the SHG light is generated is of sub-micron dimensions, which is much less than the coherence length in collagen and therefore the SHG signal should not be significantly reduced by destructive interference.

### 1.3.3.4 Wavelength dependence

At least four different experiments have been carried out to measure the wavelength dependence of SHG from various collagen samples over the tuneable wavelength range of a Ti:sapphire laser (720-980nm).<sup>39-42</sup> There is little agreement between the spectra reported in

the various papers and this suggests that there may be a significant dependence on the sample source from which the collagen is taken, or the purification of the sample and the solution it is immersed in. Theoretically the intensity as a function of excitation wavelength, the interaction length  $L$  and the dispersion within the tissue, is expressed in the following equation,<sup>38-41</sup>

$$I_{2\omega} \propto \frac{|\chi^{(2)}|^2 L^2 I_{\omega}^2}{n_{\omega}^2 n_{2\omega} \lambda_{ex}^2} \times \frac{\sin^2(2\pi\lambda^{-1}L\Delta n)}{(2\pi\lambda^{-1}L\Delta n)^2} \quad (14)$$

This equation is for plane waves and therefore will not be a complete description of the more complicated case of SHG within the tight focal point of a high numerical aperture objective which is typically used for multi-photon microscopy. Substituting known values for the dispersion in biological samples and the focal point size of a high NA objective into the equation gives a steady decrease in intensity with wavelength over Ti:sapphire wavelength range. This qualitatively fits with the data presented by Zipfel et al<sup>42</sup> but can not explain the series of peaks presented in the other papers. A complicating factor is that the value of the non-linear susceptibility may change as a function of wavelength as it can be increased by a resonant contribution when the energy of the SHG emission overlaps with an electronic absorption band within the tissue.<sup>43</sup> The most extensive study of the SHG excitation spectra for collagen was carried out by Theodossiou et al<sup>39</sup>, who found the SHG excitation spectrum was different in the forwards and backscattered directions. They also observed that changing the medium in which the sample was placed to a refractive index matching medium also altered the spectrum.

### 1.3.3.5 Propagation Direction of SHG from collagen

SHG from collagen has been detected in both the forwards and epi direction. A study of SHG from tendon and fascia collagen by Légaré et al<sup>44</sup> revealed that the forwards and epi images from thin sections showed different features. The fibrous structure was evident in the forwards images and the epi images showed submicron heterogeneities. In thick tissue samples a considerable proportion of the SHG generated in the forwards direction will be backscattered towards the epi detector. This results in the epi SHG images from thick tissues showing similar structural features to the forwards SHG images.

The proportion of forward and backward scattered SHG generated by collagen fibril of different diameters is discussed by Williams et al <sup>23</sup>. They found that the diameter of the collagen fibrils had little effect on the ratio of forwards to backwards SHG, and suggested that this behaviour was in better agreement with a model based on the work of Mertz et al in which SHG is generated on the surface of a cylindrical collagen fibril rather than from the entire volume of a solid cylinder. Also the effect of the environment on the ratio of forward to backward scattered light, was investigated and was found to be dependent on the salt concentration with a larger proportion of backwards SHG at higher salt concentrations. They hypothesised that the SHG is only generated in the cylindrical outer-shell of the collagen fibril and that changing the salt concentration changes the thickness of this shell. Hence the distribution of the SHG sources within the focal volume is changed and therefore the ratio of forwards to backwards SHG<sup>23</sup>.

## 1.4 Two-Photon Fluorescence

### 1.4.1 General Theory

Two Photon Fluorescence (TPF) involves the simultaneous absorption (i.e. as a single quantum event in a time period of around 0.1fs, given by the uncertainty principle) of two photons. The energy from the photons excites an electron into a higher state, the excited electron then returns back to its ground state via thermal relaxation followed by the emission of a single fluorescent photon<sup>3</sup>. The excitation photons are typically in the near infra red and each have approximately half the energy needed to raise an electron into the excited electronic state. The process is summarised in the following energy level diagram, figure 1-4.

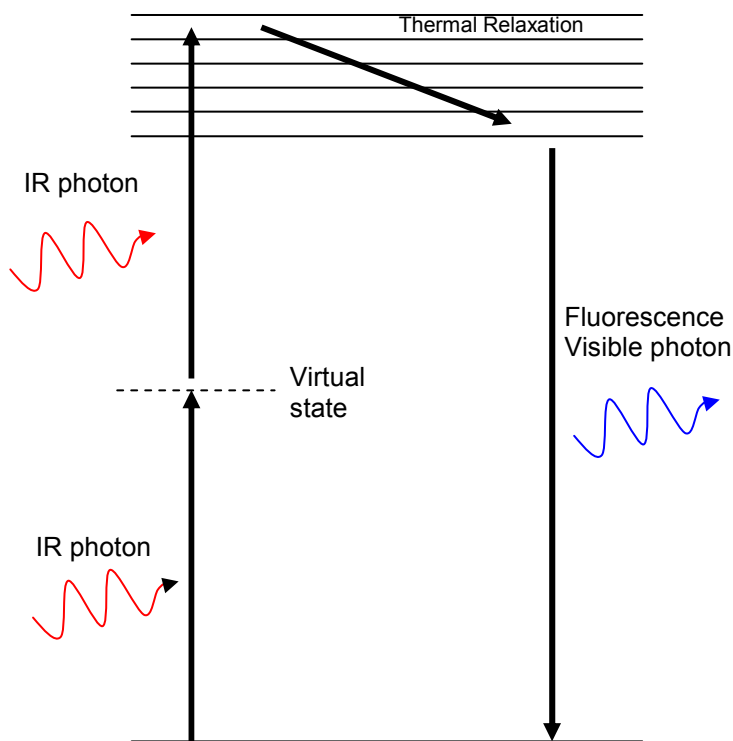


**Figure 1-4 The energy level diagram for two-photon fluorescence**

TPF photons can be distinguished from SHG photons, as TPF is an inelastic process compared to the elastic process of SHG. Therefore the TPF will always be produced with a longer wave-length than SHG which will always be at a wavelength half that of the laser

excitation wavelength. The wavelength of the TPF light is longer because some of the excitation energy is lost through non radiative dissipation.

Unlike SHG and CARS, TPF is an incoherent process. This means that we do not have to consider the phase mismatch between the TPF and the laser excitation light as the TPF is generated out of phase and therefore there are no effects of constructive or destructive interference within the focal volume to consider.

The requirement for simultaneous absorption of two photons means that TPF cross-sections are very small, and are measured in units of Göppert Meyers (GM)<sup>3</sup>. The unit is named after the person to first predict TPF and is defined as,  $1\text{GM} = 10^{-58}\text{m}^4\text{s}$ .

As the electron in TPF is excited to a real excited energy state it can remain in this state for a finite time (typically a few nanoseconds, dependent on the fluorophore) before returning to its original energy state via fluorescence. This means that fluorescent processes become saturated when the probability  $n_a$  that a fluorophore simultaneously absorbs two photons during a single laser pulse approaches 1. This probability is given by:

$$n_a \propto \frac{\delta_2 P_{ave}^2}{\tau_p f_p^2} \left( \frac{NA^2}{2\hbar c \lambda} \right)^2 \quad (15)$$

where  $\delta_2$  is the interaction cross section,  $P_{ave}$  is the time averaged power output of the laser,  $\tau_p$  and  $f_p$  are the pulse width and repetition rate respectively,  $NA$  is the numerical aperture of the objective and  $\lambda$  is the excitation wavelength.<sup>3, 45</sup> When using a Ti:sapphire laser with 100fs pulses at a typical power of 1-50mW and a high numerical aperture lens, a fluorophore with a typical cross section of 10GM will be approaching saturation.<sup>3</sup> For efficient TPF the time between pulses of the laser needs to be comparable with the relaxation rate of the fluorophores, and the 84MHz repetition rate of a Ti:sapphire lasers is of the right order of magnitude. The cross-sections for endogenous fluorophores are much less than those for fluorescent dyes and therefore for studies based on the intrinsic fluorescent properties of tissues, such as those reported in this thesis, the effects of saturation will be less significant.

TPF cross-sections can not be quantitatively predicted from the single photon cross-sections for the same fluorophore, but generally the peak in the TPF cross-section is found at about twice the wavelength of the peak in the single photon cross-section<sup>3</sup>. The TPF wavelength peak is never red shifted from the value of twice the single photon excitation peak but is often blue shifted from this value<sup>46</sup>.

Typically the emission spectrum for a given fluorophore is the same for two-photon excitation as for single photon excitation<sup>46, 47</sup>. Both are also usually independent of the excitation wavelength used<sup>48</sup>. This is due to Kasha's rule which states that the electron usually decays to the bottom of the energy level (via thermal relaxation) before decaying to the ground state via the emission of a fluorescent photon<sup>49</sup>. However the spectrum of some endogenous fluorophores (for example collagen fluorescence<sup>50</sup>) has been found to be dependent on excitation wavelength, with the peak of the fluorescence shifting to shorter wavelengths as the excitation wavelength is decreased. This is the case when the excitation wavelength used is longer than the peak excitation wavelength. This effect has to be considered for fluorophores which have a shorter peak excitation wavelength than the range of the Ti:sapphire laser typically used for TPF<sup>51</sup>.

Many fluorescent samples exhibit fluorescence anisotropy if excited with polarized light resulting in the fluorescent signal being partially polarized. This effect results from the existence of transition moments for absorption and emission which lie along specific directions within the molecule structure. Even in a homogeneous solution where all the fluorophores are randomly orientated the TPF may be polarized as the molecules with their fluorescent dipoles orientated parallel with the electric field vector will be preferentially excited. This effect is greater for multi-photon excitation than for single photon fluorescence as the probability of a fluorophore being excited is proportional to  $\cos^2 \theta$  for single photon fluorescence and  $\cos^4 \theta$  for two-photon fluorescence, where  $\theta$  is the angle between the excitation light polarization and the absorption transition dipole. Therefore the population of excited fluorophores is not randomly orientated, but instead has a higher population of molecules with their transition moment parallel with the electric field. When a fluorescent molecule emits the fluorescence it acts like a radiating dipole aligned along the emission transition moment. The intensity of the radiation is proportional to

$\cos^2 \xi$  where  $\xi$  is the angle from the plane perpendicular to the fluorescent dipole moment. This means that for samples with polarization anisotropy there will also be a preferred direction of the fluorescence signal with most light being generated in the plane perpendicular to the dipole.

The light is emitted polarized along the emission dipole moment, which is not always parallel with the absorption dipole. When measuring the fluorescence polarization anisotropy of a fluorescent sample the anisotropy parameter  $r$  is usually calculated. This parameter is defined as

$$r = \frac{I_{\parallel} - I_{\perp}}{I_{\parallel} + 2I_{\perp}} \quad , \quad (16)$$

where  $I_{\perp}$  is the intensity of the fluorescence polarized perpendicular to the laser polarization and  $I_{\parallel}$  is the intensity of the fluorescence polarized parallel to the laser polarization. This equation assumes a homogeneous distribution of fluorescent molecules, for example a solution, in a fibrous material there will be a fixed frame of reference and the anisotropy will depend on the laser polarization with respect to the fibres.

The maximum fundamental anisotropy  $r_0$  for an isotropic distribution of fluorophores is 0.4 for single photon fluorescence and 0.57 for two-photon fluorescence. These values are for fluorophores where the absorption and emission transition moments are perfectly aligned. For many fluorophores this is not the case and there is an angle  $\beta$  between the absorption and emission moments. In this case the value of  $r_0$  depends on the angle  $\beta$  as follows

$$r_0 = \frac{2}{5} \left( \frac{3 \cos^2 \beta - 1}{2} \right) \quad . \quad (17)$$

A cause of low anisotropy from a sample is rotational diffusion of the fluorophores. For small fluorophores in a low viscosity fluid (e.g. fluorescein in water) the rate of rotation is typically faster than the fluorescent life-time of the molecule and therefore this results in a loss of anisotropy. For larger fluorophores in a viscous solution the rotation is slower and therefore there is still some anisotropy. Therefore for fluorophores in the extracellular

matrix fluorescence anisotropy is unlikely to be completely lost through rotation diffusion.<sup>49</sup>

### **1.4.2 Biological TPF**

To interpret the TPF images taken of tissues it is important to have some knowledge of which molecules are producing the TPF. Known endogenous two-photon fluorophores are NAD(P)H, flavins, lipofuscin, porphyrins, collagen and elastin, these fluorophores and their excitation properties are summarised in table 1.4<sup>45</sup>. Most proteins exhibit single-photon fluorescence due to the amino acids tryptophan and tyrosine, but in two-photon fluorescence these amino acids cannot be excited by the 800nm IR laser pulse typically used as their one-photon absorption lies in the UV between (250-300nm) and they would typically need excitation light between 500-600nm to excite two-photon fluorescence<sup>4</sup>, although fluorescence may possibly be generated by three-photon excitation. Within the cells the most important sources of TPF are NAD(P)H and the flavins, and both of these may be excited by the 800nm excitation beam<sup>4,5</sup>.

| Fluorophore                                 | Excitation Wavelength (peak) | TPF cross-section (GM)      |
|---|------------------------------|-----------------------------|
| Endogenous fluorophores                     |                              |                             |
| NAD(P)H <sup>42</sup>                       | 690-730                      | $9 \times 10^{-2}$          |
| Flavoproteins (flavins) <sup>42</sup>       | 700-730                      | 0.1-0.8                     |
| Lipofuscin <sup>42</sup>                    | 700-850                      | high                        |
| Retinol <sup>42</sup>                       | 700-830                      | $7 \times 10^{-2}$          |
| Pyridoxine (vitamin b6) <sup>42</sup>       | 690-710                      | $8 \times 10^{-3}$          |
| Folic acid <sup>42</sup>                    | 700-770                      | $7 \times 10^{-3}$          |
| Cholecalciferol <sup>42</sup>               | <700                         | $6 \times 10^{-4}$          |
| NFT (neurofibrillary tangles) <sup>42</sup> | 700-780                      | unknown                     |
| Collagen                                    | $\leq 750$ <sup>41</sup>     | unknown                     |
| Keratin <sup>51</sup>                       | ~720                         | $2.5 \times 10^{-3}$        |
| Elastin <sup>42</sup>                       | 700-740                      | unknown                     |
| Commonly used Fluorescent dyes              |                              |                             |
| Flourescein                                 | 780nm <sup>52</sup>          | 38 (at 780nm) <sup>48</sup> |

**Table 1.4 A summary of known two photon fluorophores.**

The fluorescence of certain molecules such as NAD(P)H and flavoproteins is dependent on their external environment, for example the oxidative state. NAD(P)H is only fluorescent in its reduced state and flavoproteins are only fluorescent when oxidised. This makes it possible to investigate the metabolism of cells through studies of their TPF. In many tissues some of the sources of TPF have not yet been identified, for example little is known about the source of the TPF in the extra-cellular matrix of cartilage. In this thesis we attempt to identify the sources of TPF from the extra-cellular matrix.

In contrast to SHG, photo-bleaching and photo-damage will occur with the TPF. This is because TPF is an inelastic process with energy being absorbed by the fluorophores. Understanding and minimising these effects is clearly important if non-linear microscopy is to be developed as an in-vivo technique and it is important also to consider them when carrying out experiments in-vitro as these processes are likely to impact on the

quantifiability of the experiments. Measurements of photo-damage on tissues have found that the amount of damage depends quadratically on the excitation power and therefore the primary damage mechanism is via two-photon absorption.<sup>4, 53</sup> Some studies have measured a higher power law for the dependence of photo-bleaching and damage on power, indicating that higher order processes (three and four photon absorption) may also be causing photo-bleaching and damage<sup>54</sup>. The photo-bleaching mechanism affects the selection of laser powers and pulse widths to minimise it. For a two-photon damage mechanism the amount of photo-damage relative to the fluorescence intensity is independent on pulse width, whereas for a three-photon process shorter pulse widths will cause a larger increase in bleaching relative to the increase in fluorescence<sup>53</sup>.

## 1.5 Coherent Anti-Stokes Raman Scattering CARS

### 1.5.1 General Theory

The third non-linear optical process which is used in this thesis is Coherent Anti-stokes Raman Scattering (CARS). This is a process, in which the contrast mechanism relying on the vibrational properties of the sample. CARS enables the extremely weak Raman scattering effect to be enhanced by pumping the sample with two laser beams. Raman scattering is an inelastic scattering process involving the vibrational modes of the scattering molecules. There are two types of scattering: Stokes Raman scattering and anti-Stokes Raman scattering. In Stokes Raman scattering part of the energy of the scattered photon is transferred to a bond vibration in the scattering molecule and the scattered photon consequently has less energy and a longer wavelength. In anti-Stokes Raman scattering the scattered photon gains energy from a bond vibration within the scattering molecule and consequently has a shorter wavelength. The anti-Stokes Raman scattering process has a much smaller cross-section than Stokes Raman scattering. Raman spectroscopy has been developed as an analytical technique allowing different molecules to be identified by their specific vibrational frequencies. Characteristic peaks occur in the Raman spectra at Raman shifts which correspond to the energy of specific bond vibrations.<sup>7</sup>

To produce a CARS signal two laser beams must be focused on the sample. These are the Stokes laser beam ( $\omega_s$ ) and the pump laser beam ( $\omega_p$ ). The CARS signal is generated with a frequency  $\omega_{AS} = 2\omega_p - \omega_s$ . If the difference between the frequency of the Stokes beam and the pump beam ( $\omega_p - \omega_s$ ) corresponds to the frequency of a vibration of a molecular bond within the sample the CARS signal is strongly enhanced. The energy level diagram for the CARS process is shown in figure 1-5a.

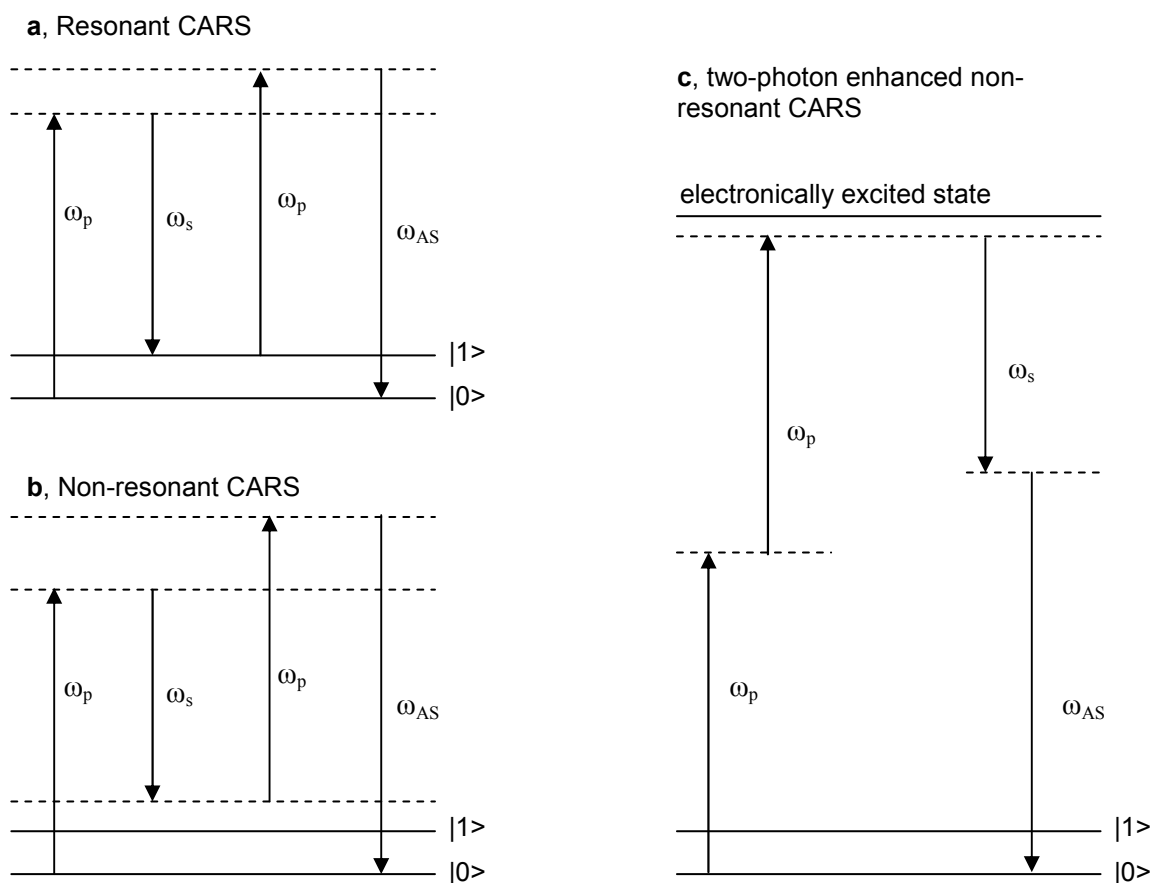


**Figure 1-5** The energy level diagrams for three CARS processes; resonant CARS (a), non-resonant CARS (b) and two-photon enhanced non-resonant CARS (c).  $|0\rangle$  and  $|1\rangle$  represent the ground vibrational state and the excited vibrational state respectively. Resonant CARS occurs when  $(\omega_p - \omega_s)$  is tuned to the energy difference between these two vibrational states. (modified from a figure by Cheng et al 2001<sup>55</sup>)

The major advantage of CARS microscopy is that it can be used without staining to image many molecules within the sample which have no intrinsic fluorescence and do not exhibit second harmonic generation. To produce contrast for a specific molecule the frequency of the pump and Stokes laser beams are tuned so that the difference between them corresponds to a bond vibration which occurs within the molecule (this would be represented by a peak in the single photon Raman spectrum). For example for imaging the lipids within a sample the lasers are tuned so that  $(\omega_p - \omega_s)$  corresponds the vibrational frequency of the C-H bonds which exist in large numbers in the hydrocarbon chains of the lipids.

CARS is a third order non-linear process and is therefore governed by terms within the third order non-linear susceptibility tensor  $\chi^{(3)}$ . The intensity of the CARS signal is

dependent quadratically on the intensity of the pump beam and linearly on the intensity of the stokes beam

$$I_{CARS} \propto I_S I_P^2 |\chi^{(3)}|^2. \quad (18)$$

As the CARS intensity is proportional to  $|\chi^{(3)}|^2$  it is dependent on the square of the number of vibrational modes within the excitation volume. This is due to the coherent nature of the process with all the vibrational modes oscillating in phase and interfering constructively. This increases the specificity of CARS when imaging lipids via the CH<sub>2</sub> bond vibrations. CH<sub>2</sub> bonds occur within most organic molecules but are at a very high density within the hydrocarbon tails of lipid molecules.

There are three terms in  $\chi^{(3)}$  and these are shown in equation 19. The first term is the resonant  $\chi_R^{(3)}(\Delta)$  which corresponds to enhanced CARS signal where  $(\omega_p - \omega_s)$  corresponds to a bond vibration, the second term is a non-resonant term  $\chi_{NR}^{(3)}$  which corresponds to the bulk electronic vibrations and the third term corresponds to the two-photon enhanced non-resonant contribution.

$$\chi^{(3)} = \frac{A_R}{\Delta - i\Gamma_R} + \chi_{NR}^{(3)} + \frac{A_T}{\omega_T - 2\omega_p - i\Gamma_T} \quad (19)$$

In equation (19)  $\Delta = \omega_p - \omega_s - \Omega_R$  (this is referred to as the detuning), with  $\Omega_R$  corresponding to the central frequency of the Raman spectral line of the bond vibration being excited with a band width of  $\Gamma_R$ <sup>7</sup>.  $\omega_T$  corresponds to the frequency of an electronic transition and  $\Gamma_T$  is the band width of this transition.  $A_R$  and  $A_T$  are constants representing the cross-sections for the Raman scattering and two-photon absorption respectively.<sup>56</sup> The non-resonant term is largely independent of  $(\omega_p - \omega_s)$ , whereas the contribution of the non-resonant term is dependent of the tuning of the laser frequencies. The contribution of the two-photon enhanced term can be minimised if the laser pump beam is tuned to wavelengths away from those that can excite electronic transitions via two-photon excitation and this is generally true when it is tuned to longer wavelengths<sup>55</sup>. The nonresonant CARS process is shown in figure 1-5b If the pump wavelength corresponds to

a peak in the two-photon fluorescence absorption the non-resonant CARS is enhanced, this process is shown in figure 1-5c<sup>55</sup>.

Expanding the expression for  $|\chi^{(3)}|^2$  shows that the CARS signal is dependent of three terms. When  $\omega_p$  is tuned away from two-photon electronic transitions so that the two-photon enhanced term may be ignored,

$$I_{CARS}(\Delta) \propto |\chi_{NR}^{(3)}|^2 + |\chi_R^{(3)}(\Delta)|^2 + 2\chi_{NR}^{(3)} \text{Re} \chi_R^{(3)}(\Delta). \quad (20)$$

The first term in this expression represents the non-resonant background and the second term represents the resonant contribution and hence provides information on the concentration of the resonant scatters within the sample. The final term is a mix of contributions of the resonant and non-resonant terms. In figure 1-6 a plot of this function is shown. The non-resonant background remains constant as a function of the detuning, and the resonant term peaks at  $\Delta = 0$ . The mixed term is negative for when the  $(\omega_p - \omega_s) > \Omega_R$ , this results in a decrease in Raman intensity at Raman shifts which are blue shifted with respect to centre of the Raman peak. In imaging, this results in a negative contrast with the areas containing a large number of resonant scatters appearing as dark spots with respect to a brighter non-resonant background<sup>7</sup>.

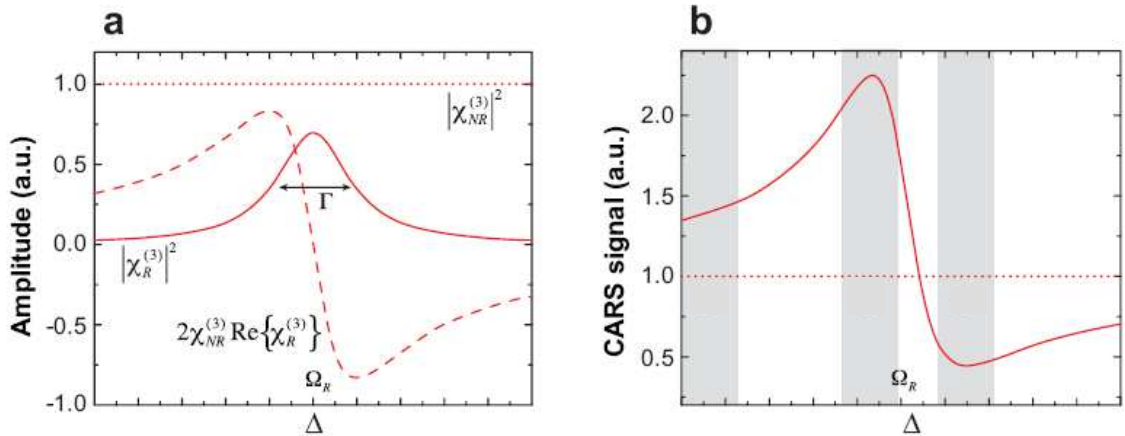


**Figure 1-6 CARS signal as a function of the detuning  $\Delta$**

**A plot of the components of the CARS signal as a function of the detuning  $\Delta$  (a) and a plot of the overall CARS intensity as a function of  $\Delta$  (b) (reproduced from a figure in Evans et al 2008<sup>7</sup>)**

The non-resonant background limits the contrast in CARS microscopy. The solvent in which the sample is contained often contributes to the resonant background. For example water produces a strong resonant signal with a broad spectral range. In order to be able to

distinguish between the non-resonant background and the resonant CARS signal images need to be taken at different values of  $(\omega_p - \omega_s)$ . The first image will be taken with  $(\omega_p - \omega_s)$  tuned to the vibrational frequency of the bonds of interest, a second image will be taken with  $(\omega_p - \omega_s)$  tuned to a frequency which corresponds to the dip in CARS intensity shown in figure 1-6, and finally another image taken with  $(\omega_p - \omega_s)$  tuned far away from the bond resonance. The areas of high concentration of bond vibrations will only show up as high intensity features in the first image, dark negative contrast features in the second image and will be absent from the third image.<sup>7,57</sup>

For CARS imaging picosecond pulses have been found to be preferable to femtosecond pulses. Although, with shorter pulse widths, the overall CARS intensity is greatest due to the higher instantaneous laser power, the resonant CARS signal is overwhelmed by the non-resonant background. This is because the resonant CARS signal is saturated at the shorter pulse durations as the spectral width of the laser excitation beam is greater than the Raman line width. The ratio of resonant CARS to the total CARS intensity increases with pulse duration over the femtosecond range and plateaus at a pulse duration of approximately 2ps. For CARS imaging, the ratio of resonant to non-resonant background signal is more important than the overall signal intensity as the chemical specific data is all contained within the resonant signal. Consequently picosecond laser excitation sources are best suited to CARS imaging<sup>58</sup>.

CARS is a coherent process and therefore the direction of the signal is determined by the phase matching conditions. This is important for understanding the differences between the CARS signal detected in the forwards and backwards directions. A qualitative description of the effect of phase matching on the signal in the forwards and backwards directions can be obtained from the equation for the CARS signal for plane waves propagating through a slab of thickness D:

$$I_{AS(D)} = \frac{\pi}{2n_{AS}c} \omega_{AS}^2 D^2 |\vec{P}^{(3)}|^2 \sin c^2 \left( \frac{|\Delta k|D}{2} \right) \quad (21)$$

Where  $n_{AS}$  is the refractive index for the anti-Stokes light,  $c$  is the speed of light in a vacuum,  $\omega_{AS}$  is the angular frequency of the anti-Stokes light and  $\vec{P}^{(3)}$  is the third order

polarization of the sample. The phase mismatch  $\Delta\vec{k}$  is given by  $\Delta\vec{k} = \vec{k}_{AS} - (2\vec{k}_p - \vec{k}_s)$ , where  $\vec{k}_p$ ,  $\vec{k}_s$  and  $\vec{k}_{AS}$  are the wave-vectors of the pump, Stokes and anti-Stokes photons. Assuming that the dispersion in the refractive index for these wavelengths is negligible (i.e.  $n \approx n_{AS} \approx n_s \approx n_p$ ) then there will be no phase mismatch in the forwards direction ( $|\Delta\vec{k}| = 0$ ). This means that there will be constructive interference and the signal in the forwards direction will increase quadratically with D as  $\sin^2\left(\frac{|\Delta k|D}{2}\right) \approx 1$ . In the epi direction there will not be phase matching as  $\vec{k}_{AS}$  is in the opposite direction to  $\vec{k}_p$  and  $\vec{k}_s$  and this gives ( $|\Delta\vec{k}| \approx 4n\pi/\lambda_{AS}$ ) and therefore there is destructive interference, which results in the CARS intensity oscillating as a function of D. Volkmer et al<sup>59</sup> calculated the epi and forwards signal for scatters of different diameters D within the focal point of a high numerical aperture objective and their results are shown in figure 1-7. Their results showed that the epi CARS signal drops dramatically for larger scatterers, while the forwards CARS signal increases and starts to plateau when the scatterers approach the size of the focal volume. Water will be present throughout the focal volume and will therefore act as a large scatter generating non-resonant CARS. In the forwards direction its effect will be large, however it is negligible in the epi direction. This makes epi CARS more efficient for imaging small features which are smaller than the wavelength of the pump laser. The forward CARS efficiency on the other hand increases with the size of the objects being imaged with the upper limit of the amount of signal generated being imposed by the size of the focal volume from which the signal can be generated.<sup>59</sup>

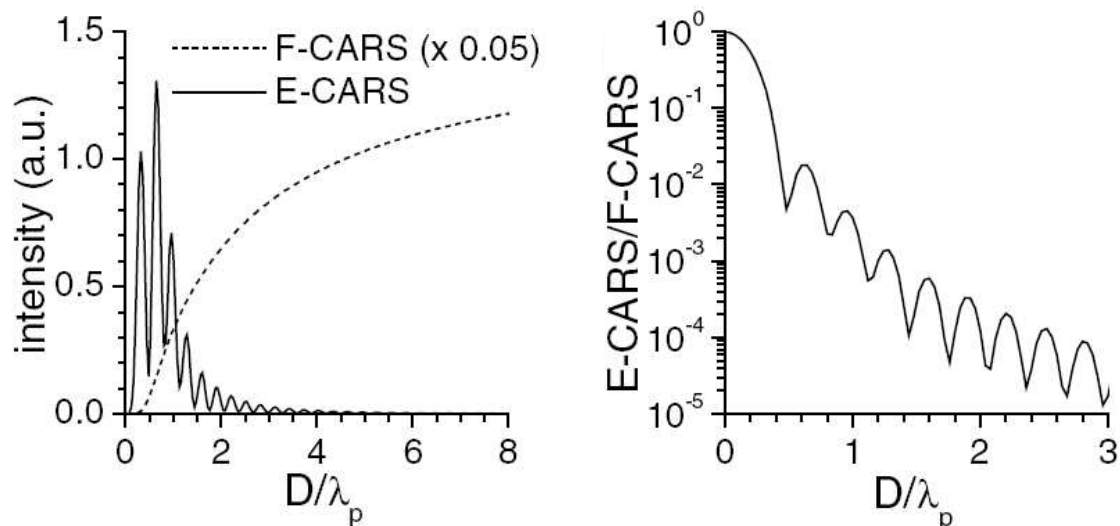


**Figure 1-7** Dependence of the CARS signal on the size  $D$  of the scatter. Data for the forwards and epi direction (from a figure in Volkmer et al<sup>59</sup>)

### 1.5.2 Raman Selection Rules

Not all bond vibrations can be investigated through Raman and CARS spectroscopy. For a vibration to be Raman active the polarizability of the molecules must change during the vibration. To determine whether this is the case the polarizability ellipsoid can be plotted for the centre and the extremes of the vibration. If the shape, size or orientation of the ellipsoid changes then the vibration will be Raman active. For simple molecules with a centre of symmetry (for example  $\text{CO}_2$ ) the mutual exclusion principle applies. This states that vibrations which are symmetric with respect to the centre of symmetry (for example symmetric stretching) are Raman active, whereas vibrations which are anti-symmetric with respect to the centre of symmetry (for example anti-symmetric stretching and symmetric bending) are not Raman active.<sup>60</sup> For larger more complex molecules this principle is relaxed due to less symmetry within the molecule.

### 1.5.3 Biological applications of CARS

CARS imaging is well suited for biological research as it allows the investigation of unstained samples. The majority of CARS imaging to date has been done using the CH bond resonance which provides good contrast for lipids, however different bond vibrations have also been investigated for imaging the DNA and proteins. The bond vibrations and the structures they provide contrast for are summarised in table 1.5.

| Bond Vibration  | $(\omega_p - \omega_s)$   | Provides contrast for:                       | Cell structures images                                   |
|---|---|--|--|
| CH <sub>2</sub> symmetric stretching vibration                            | 2845 cm <sup>-1</sup> <sup>7</sup><br>2840 cm <sup>-1</sup> <sup>58</sup> | Lipids<br>Polystyrene beads<br>Starch Grains | Lipid droplets<br>Myelin sheath <sup>58</sup>            |
| Aliphatic C-H stretching vibration <sup>61</sup>                          | 2870 cm <sup>-1</sup>   | Lipids                                       | Lysosomes, mitochondria,<br>Nucleus envelope,            |
| PO <sub>2</sub> <sup>-</sup> symmetric stretching vibration <sup>61</sup> | 1090 cm <sup>-1</sup>   | DNA  | Chorosomes<br>Weak signal from<br>cytoplasmic organelles |
| Amide I <sup>62</sup>   | 1650 cm <sup>-1</sup>   | proteins                                     |  |
| Symmetric H <sub>2</sub> O stretching vibration <sup>58</sup>             | 3200 cm <sup>-1</sup>   | water  | Water within the axion in<br>spinal tissues              |

**Table 1.5 CARS vibrational modes in biological tissues.**

Living cells have been imaged using CARS microscopy and the following cellular structures were apparent with the laser tuned to the C-H and CH<sub>2</sub> bond vibrations; nucleus membrane, mitochondria (these contain an outer lipid membrane and a folded inner lipid membrane), lysosomes and lipid droplets.<sup>61</sup> In order to confirm that bright rod shaped mitochondria within the images were mitochondria Cheng et al<sup>61</sup> marked these with a fluorescent label and carried out con-focal microscopy on the sample. Tuning to the vibrations within the DNA backbone allowed Cheng et al to image the chromosomes within the cells and observe changes which occur during the cellular processes of mitosis and apoptosis.

CARS is also useful for tissue imaging, where it offers the same advantages as SHG and TPF imaging but also a variety of different contrasts. Some of the tissues investigated to date include skin<sup>63, 64</sup>, spinal tissues<sup>58</sup>, kidney tissue<sup>7</sup> and brain tissue<sup>65</sup>. CARS imaging was found to be able to give high resolution images of mouse skin tissue up to a depth of 120 $\mu\text{m}$ <sup>64</sup>. Structures which contain a high lipid content showed the highest contrast for example the myelin sheath in spinal tissue which is 70% lipid<sup>58</sup> and adipose cells which function as a fat store. The differences between the epi and forwards CARS signals can be advantageous for biological imaging allowing a pair of complementary images to be taken. The Epi detection has very little non-resonant background and allows the visualisation of small scattering objects whereas the forwards CARS contains a large proportion of non-resonant signal. Some structures for example red blood cells have a very high epi CARS signal due to a contribution from two photon enhanced non-resonant CARS. These features of CARS have been used to provide 3D imaging of the red blood cells within the fish gill. With the cells of the gill showing clearly in the epi images and the red-blood cells only visible in the forwards CARS image<sup>66</sup>.

## 1.6 Extracellular Matrix Biology

Biological tissues consist of cells surrounded by an extra cellular matrix, where the cells determine the metabolic properties of the material and the matrix provides structure and determines the physical properties. Non-linear microscopy is a highly valuable tool for investigating the extra-cellular matrix as it enables imaging of individual fibres within the matrix and the differentiation between collagen and elastin fibres<sup>67, 68</sup>. It also allows the cells and some cellular components to be imaged<sup>6</sup>. In this section we discuss the structure of the extra-cellular matrix, its principle fibrillar proteins collagen and elastin and the other major matrix components. A schematic diagram of the extracellular matrix is shown in figure 1-8.

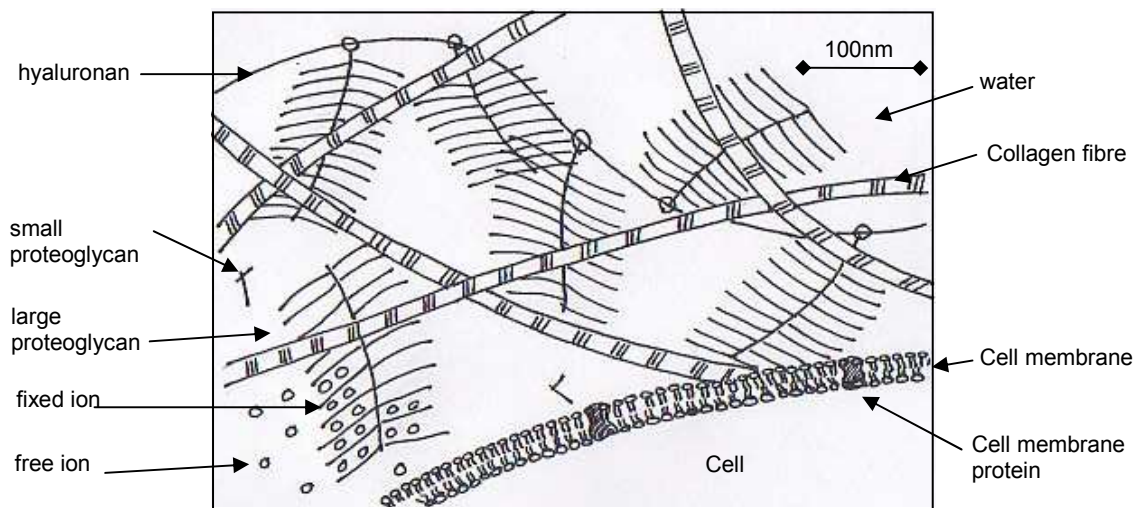


**Figure 1-8** A schematic diagram of the ECM  
( reproduced from a figure by Gribbon et al<sup>69</sup> )

Collagen is the most abundant structural protein in the human body, forming a major component of tendon, bone, skin, ligament, cornea and cartilage. Its physical characteristics are high tensile strength and inextensibility. Collagen fibrils have a hierarchical structure. Each collagen molecule is composed of three polypeptide chains, each approximately 1000 amino acids in length. These chains are referred to as alpha chains, and they have a left-handed helical structure<sup>70</sup>. The three polypeptide chains are coiled together to form a right-handed triple helix<sup>18</sup>, which is about 300nm in length and 1.5nm in diameter<sup>70</sup>. The collagen molecules are then arranged into micro-fibrils consisting of a bundle of 5-6 molecules<sup>18</sup>. The molecules are arranged in a highly regular way so that they overlap by a

quarter of their length. These micro-fibrils are about 4 $\mu\text{m}$  in diameter<sup>70</sup>. The organization of collagen structure from the alpha chains to the microfibrils is described in figure 1-9. The micro-fibrils twist together to form larger bundles called fibrils with diameters between 20 and 500 $\mu\text{m}$ <sup>18</sup>. In some cases, for example in tendon, the fibrils may be organised into structures called fascicles which are bundles of fibrils surrounded by a fascia (sheet of fibrous tissue). These fascicles may be large enough to be seen by the naked eye<sup>18</sup>.

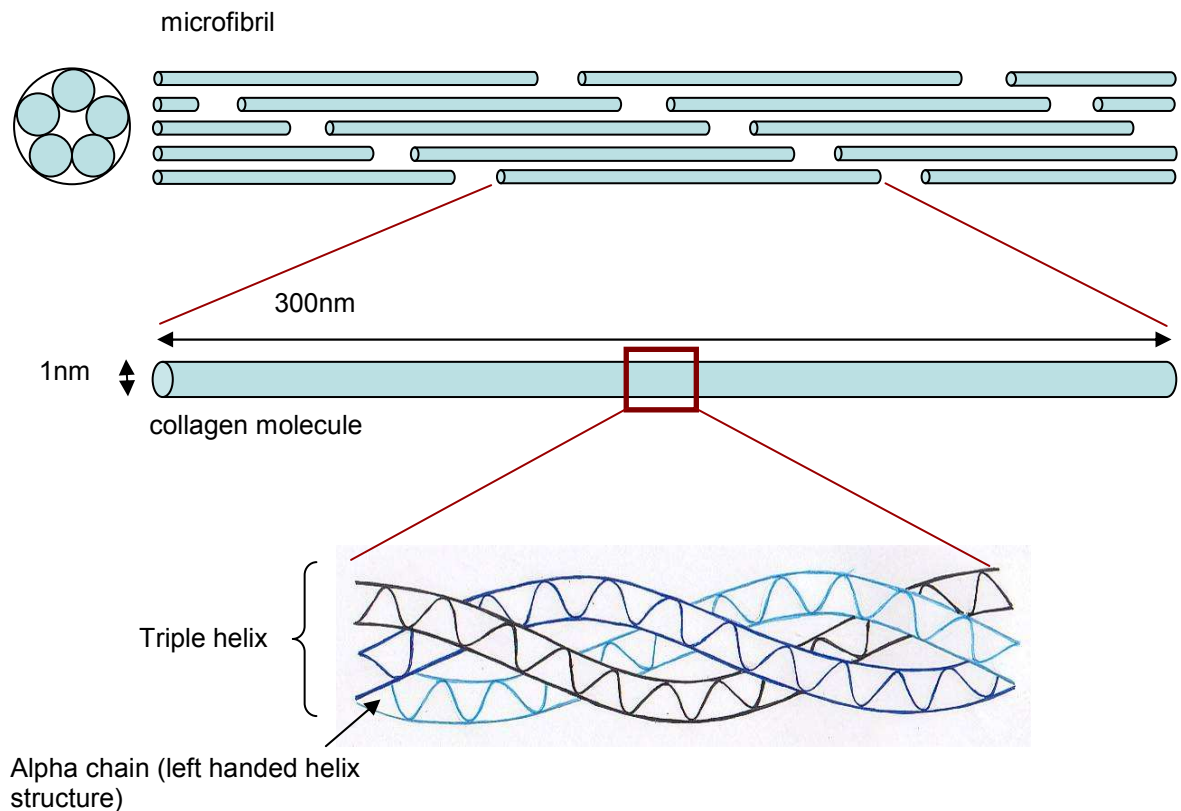


**Figure 1-9 A schematic diagram of collagen structure up to the microfibrillar level.**

There are at least 28 different types of collagen in the vertebrates, and other collagen like proteins<sup>71</sup>. The different types of collagen can be divided into two different groups, fibrillar and non-fibrillar. The fibrillar collagen types form fibrils (type I, II and III collagen) as described above whereas the non fibrillar types form sheets (type IV collagen) or links (type VI and IX collagen)<sup>32</sup>.

The highly ordered structure of collagen also gives it other interesting optical properties as well as a high non-linear susceptibility. Collagen exhibits both birefringence and bi-attenuation. For the type I collagen in tendon the birefringence and bi-attenuation have been measured to be 0.0045<sup>72</sup> and ranging from  $1.2 \times 10^{-4}$  to  $5.3 \times 10^{-4}$  respectively<sup>73</sup>. These

properties become an important consideration when imaging thick tissue samples with high collagen content.

Elastin is an elastic protein found in the extra-cellular matrix and it exhibits 70% extensibility and recoil<sup>74</sup>. It is especially abundant in tissues which have to contract after repeated stretching for example the alveoli, blood vessels, perichondrium and skin<sup>75</sup>. A significant fraction of the amino acids in the elastin polypeptide chains are apolar and these are arranged into hydrophobic domains, whereas the polar amino acids form hydrophilic regions where the chains are cross-linked via the tetra-valent cross links of desmosine and isodesmosine.<sup>74 76</sup> Elastin in tissues is usually in the form of elastic fibres. These consist of a core of elastin surrounded by microfibrils. The microfibrils are thought to form a framework for the growing fibre and the proportion of microfibrils to elastin is found to decrease with the age of the sample<sup>77</sup>.

Proteoglycans are another important constituent of the extra-cellular matrix, these are large macromolecules which are found in all connective tissues<sup>78</sup>. They consist of glycosaminoglycan side chains attached to a protein core<sup>79</sup>. The glycosaminoglycan side chains are un-branched polysaccharide chains consisting of repeating disaccharide units. On these chains there are up to 100 negatively charged sulphate or carboxylate groups. The proteoglycans can have from 2 to 100+ side chains and this leads to a potential of 10,000 negatively charged groups per molecule. The negative charged groups are very important to the properties of the proteoglycans as they are hydrophilic and attract water and positively charged ions into the molecule; this generates a swelling pressure. The swelling pressure caused by proteoglycans is especially important to the physical properties of cartilage (see section 1.6.1). In cartilage the proteoglycans join together to form aggregates with many proteoglycans attached to a hyaluronic acid backbone. These aggregates may be about 1µm diameter. Figure 1-10 shows the structure of a proteoglycans aggregate.

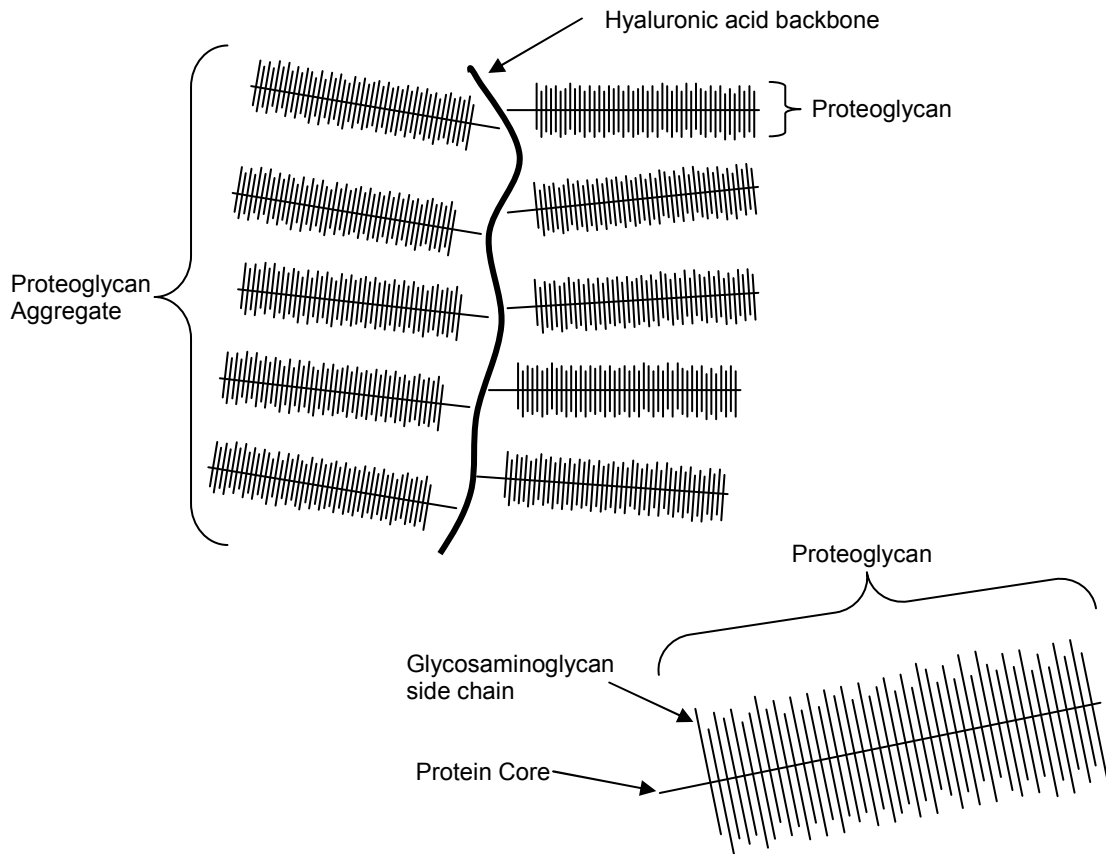


**Figure 1-10** The structure of a proteoglycan aggregate as found in cartilage

In this thesis the cartilage, intervertebral disc, elastic cartilage and tendon are imaged and the structures of these tissues are discussed in the following sections. All these tissues are ideal candidates for imaging using non-linear microscopy as they have a high content of either collagen or collagen and elastin. Both of these structural proteins are well highlighted by our techniques as discussed earlier.

### **1.6.1 Cartilage Biology**

Much of the work in this thesis focuses on imaging articular cartilage. This tissue is highly suitable for imaging with non-linear microscopy as it has a high collagen content (enabling SHG imaging) and also exhibits TPF from the extra cellular matrix<sup>80</sup>. The aim of the research was to interpret the images of healthy articular cartilage and then to make a comparison between healthy and osteoarthritic cartilage tissue.

Articular cartilage is found covering the ends of the bones in the synovial joints<sup>81</sup>. Its purpose is to reduce the friction in the joints and to act as shock absorber in order to protect the joints from jarring<sup>82</sup>. Articular cartilage is composed of 72% water<sup>83</sup>. When the water has been removed collagen makes up approximately 66% of the dry mass and another 18% is composed of proteoglycans. Articular cartilage has a very low cellular content with about 1-10% of the volume of the tissue being occupied by the chondrocytes (cartilage cells).<sup>84</sup> The proteoglycans are held within a mesh of type II collagen fibres. The tension in the collagen fibres acts to balance the swelling pressure generated by the proteoglycans. Collagen fibres also provide the cartilage with mechanical strength, resisting both shear and tensile stresses. The swelling pressure caused by the proteoglycans provides resistance to water flowing through the cartilage. This enables cartilage to support compressive loads<sup>79</sup>.

Type II collagen forms much thinner fibrils (typically 30-200nm) than the fibrils of type I collagen that has been extensively studied using SHG. Under transmission electron microscopy (TEM) the collagen fibres are seen to form a meshwork which appears less ordered than in many other connective tissues, however it is still possible to observe a preferred collagen fibre orientation at both the ultra-structural and macroscopic levels<sup>85</sup> When articular cartilage is viewed between crossed polarizers it is possible to observe four different zones of increasing in depth, which contain different collagen fibril orientations. Here it is only the predominant collagen fibre orientation which is being observed through differences in birefringence as the individual fibres are too fine to be resolved. In the superficial zone of the cartilage fine fibrils of collagen (about 30nm in diameter) are found to be running parallel to the cartilage articular surface, for this reason it is also referred to as the tangential zone. Beneath this is an intermediate or transitional zone containing many

different orientations of collagen fibres. This leads into the deep or radial zone of the cartilage where the preferred fibril orientation is radial from the subchondral bone and orthogonal to the cartilage surfaces. Finally, at the bone cartilage interface there is a zone of calcified collagen (approximately 0.1mm thick), which is separated from the un-calcified cartilage by the tidemark. The collagen fibres in calcified cartilage are also predominately arranged radially from the bone and this region acts to anchor the fibres in the radial zone.<sup>74, 83, 85</sup> The different zones of the articular cartilage are shown in figure 1-11. This structure was first described by Benninghoff in 1925<sup>74</sup>. The thickness of the articular cartilage varies between species and joints. It will also vary over a given joint surface in the equine metacarpophalangeal joint which is used as a sample source in these experiments the thickness ranges from about 700-1400µm. The approximate thickness of the zones are as follows; superficial zone (50µm), transitional zone (100-200µm), radial zone (600-1000µm) and calcified zone (100µm).<sup>12</sup>

In addition to the collagen II fibres, collagens III, VI, IX, X, XI, XII and XVI are also found in articular cartilage. Type XI and XI collagen are predominantly found in the thinner collagen fibres, either in young growing cartilage or in the pericellular matrix. In mature cartilage the content is approximately 1% type IX and 3% type XI. The collagen II, XI and XI are joined together in cross linked polymers.<sup>85</sup> Collagen III fibres are found in small quantities in both normal and osteoarthritic cartilage. In osteoarthritic cartilage the collagen III fibres appear to be mostly synthesised in the superficial and upper middle zones. Type XII and XIV collagen are found in cartilage but are not strongly bound to the matrix. Type X collagen is found in the calcified zone.

The size of the fibril is not uniform throughout the tissue, the superficial zone predominantly contains thin fibres whereas the deeper zones contain a greater variety of fibre diameters. Differences can also be observed between the intracellular matrix and the pericellular matrix, with the fibres becoming increasingly thicker with distance from the chondrocytes.<sup>85</sup> The fibrils forming the fine meshwork of the pericellular matrix are only 5-10nm in diameter. The pericellular matrix is typically 1-3µm wide, with an abrupt transition to the more coarsely fibred extracellular matrix. Beyond the pericellular matrix is the territorial matrix which is a region approximately 50µm in diameter which surrounds a

cell or group of cells. This region of the matrix contains a high concentration of proteoglycans.

The elastic subgroup of cartilages (including cartilage of the ear and the epiglottis) is known to contain elastin fibres, these are most concentrated in the pericellular matrix<sup>86</sup>. Articular cartilage was thought not to contain a significant proportion of elastic fibres. However immunohistological staining carried out by Naumann et al showed a small proportion of the cells staining strongly for elastin in their pericellular matrix<sup>86</sup>, a recent non-linear microscopy study on articular cartilage also reported fluorescent fibres in the superficial zones<sup>80</sup> and an electron microscopy study also found a population of fibres separate to the collagen which were attributed to elastin.<sup>87</sup>

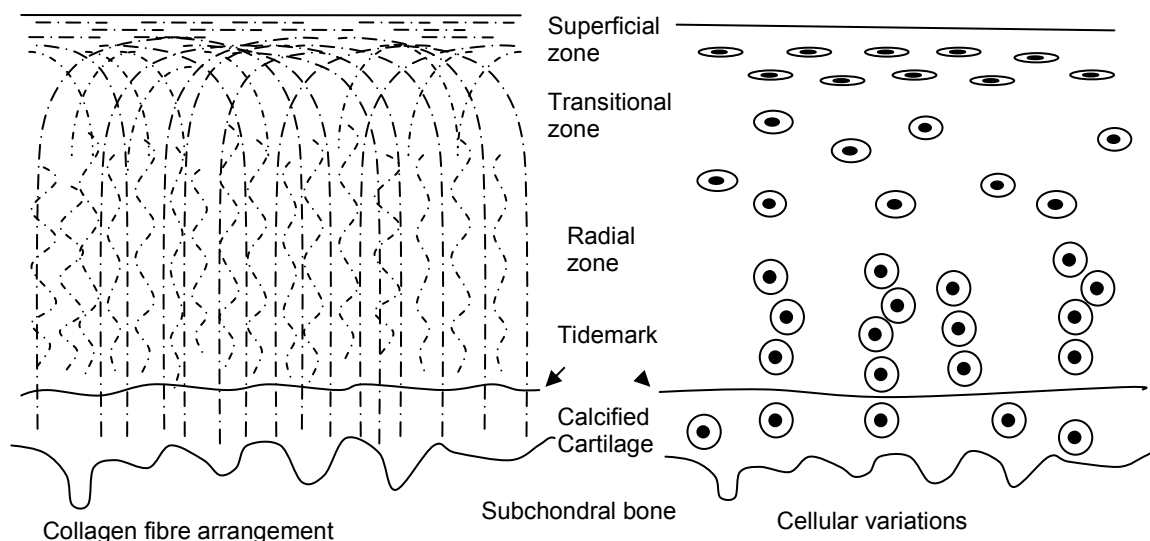


**Figure 1-11** A schematic diagram of the zonal structure of cartilage. Showing the collagen arrangements in the different zones (left) and the changes in the chondrocytes (right)

The distribution of proteoglycans changes throughout the tissue, with the glycosaminoglycan concentration decreasing towards the articular surface. The proportion of the glycosaminoglycan keratan-sulphate relative to the primary component chondroitin sulphate increases with depth into the cartilage and in the deep zones it may form over 50% of the glycosaminoglycans. At the articular surface both chondroitin sulphate and keratan – sulphate have low concentrations. Water content is greatest at the articular surface about 75% of net weight<sup>74</sup>.

The distribution and shape of chondrocytes vary with depth into the cartilage and this is shown in figure 1-11. At the articular surface there is a 2-3 $\mu$ m layer before any cells are observed. The cells in the superficial zone have a flattened shape and are aligned with their flat surfaces parallel to the articular surface. This means that in sections taken perpendicular to the articular surface they appear cigar shaped. They are typically about 14 $\mu$ m in length and 3 $\mu$ m in depth. Chondrocytes are more numerous here than elsewhere in the tissue, and are either found in singularly or in groups of 2-4 cells in sections taken in the plane parallel to the articular surface. In the intermediate zone the chondrocytes are more spherically shaped and have a random orientation. In the deep zone the chondrocytes are mostly aligned orthogonally to the articular surface and underlying bone.<sup>88-92</sup> Also the cells deeper within the cartilage increase in size, with the cells at the bottom of the radial zone being described as hypertrophic.<sup>74</sup>

The articular surface has irregularities on four different scales. On the largest scale are the changes in anatomical contour due to the curvature of the joint. There are also secondary undulations 0.2-0.5mm in pitch. On a smaller scale there are hollows 20-30 $\mu$ m in diameter and 0.5-2 $\mu$ m deep. The smallest variations are ridges 1-4 $\mu$ m wide and 130-275 nm deep.<sup>74</sup>

Cartilage is avascular, aneural and free from lymph vessels and therefore the nutrition for the chondrocytes is supplied by diffusion from the synovial fluid rather than directly from the circulation<sup>93</sup>. The chondrocytes are able to survive in these conditions as they have a low rate of metabolic activity, which is mainly directed to matrix production. When growth is completed the rate of type II collagen production greatly decreases, although it can increase 10 times in the case of an injury. The overall estimated turnover time for human collagen in the femoral head cartilage is 400 years.<sup>85</sup> Therefore even though cartilage has excellent physical properties its slow regeneration rate and limited ability for repair leads to a high incidence of degeneration.

Osteoarthritis is a disease characterised by the degeneration and eventual loss of the articular cartilage from the joint surfaces. In the late stages of the disease the whole joint is affected with the loss or damage to the cartilage causing increased friction, and leaving the

bones unprotected from loading and shear forces. The result is that the joint is extremely painful and has much reduced mobility. Neither the subchondral bone or the articular cartilage contains nerve endings and therefore the painful symptoms do not occur until the later development stages of the disease when the subchondral bone and joint capsule are involved, via an inflammatory response caused by necrotic chondrocytes<sup>94</sup>. The degenerative changes in the articular cartilage are accompanied by changes in the underlying bone such as micro-fractures and subchondral thickening and the development of bony protrusions referred to as osteophytes.

The articular cartilage deteriorates with age even in healthy joints, and the chances of a joint becoming osteoarthritic increase with age, although ageing does not necessarily result in osteoarthritis. This leads to a difficulty in osteoarthritis research in being able to distinguish between early degenerative changes which will progress into a lesion and changes which are the consequence of normal ageing. A range of factors exist which may cause the degeneration of the cartilage to accelerate into osteoarthritis, including excessive stresses, trauma and genetic predisposition. It is thought that osteoarthritic lesions may start at sites of micro-fractures in the underlying subchondral bone. The micro-fractures lead to remodelling of the bone. At the edge of the remodelled area, the cartilage is under increased stresses due to the change in bone properties.<sup>95</sup>

The aetiology and progression of the osteoarthritis is still not fully understood, for several reasons. From histology it is difficult to identify the sequence in which pathological changes occur, as abnormalities are seldom observed on their own and each sample viewed provides only a single snapshot within the progression of the disease. We therefore describe the changes which are commonly observed with normal ageing and then those found in the early and later stages of the disease.

As the cartilage ages the number of chondrocytes decreases, with a marked decrease in the number of cells between juvenile and adult tissues, although the mechanism by which the cells are lost is unclear.<sup>74, 92, 96</sup> Also the zone of calcified cartilage appears to progress into the radial zone with age, with multiple faint tidemarks observed in the calcified zone below the main tidemark which separates the calcified and radial zones.<sup>97</sup> Age also affects the

collagen fibril diameter with mature cartilage containing thicker and more varied fibril diameters than immature tissue. The width of the pericellular matrix at first instance increases with age but then in later life thicker fibrils (150-280nm in diameter) may be found close to degenerate cells.<sup>74</sup>

In the early stages of disease regions of swelling within the tissue may be observed. This is referred to as focal chondromucoid softening and the chondrocytes are observed to be less numerous in the swollen region and more numerous in the tissue surrounding the swollen region<sup>96</sup>. Also there is a decrease in the amount of proteoglycan in the transitional and superficial zones<sup>96</sup> and this is thought to predispose the tissue to fibrillation.<sup>74</sup> Microfractures may be seen at the articular surface, and these have an associated proliferation in the number of chondrocytes, although it is unclear if these have migrated to repair the lesion or are simply taking advantage of the improved nutrient supply from the synovial fluid. Droplets of lipid may be observed in the inter-territorial matrix. The collagen fibre organisation also begins to be lost with the fibres showing looser packing and fragmentation. The swelling of the cartilage may be associated with the fragmentation of the collagen fibre network, as damaged collagen fibres are less able to restrain the osmotic pressure of the proteoglycans.<sup>79</sup> Therefore in the very early stages of osteoarthritis the cartilage thickness may be greater than in healthy tissue.

As osteoarthritis progresses the cartilage is lost from the joint surface by a process of fibrillation. This starts with the formation small microscopic splits parallel to the surface in the superficial layer (sometimes referred to as flaking). In the later stages of the fibrillation process the splits progress into the radial zone, proteoglycans are lost from the tissue and the chondrocytes start to die, with empty lacunae being observed where chondrocytes have been lost. With a decrease in the number of cells the tissue is unable to synthesise more matrix components, increasing the progression of the disease. Eventually the lesions grow so that they are no longer microscopic and can easily be seen with the naked eye. In the later stages of the disease the cartilage becomes thinner compared to healthy cartilage and is eventually lost.

## *Chapter 1 - Introduction*

There is a need for increased understanding of the causes and early stages of the progression of the disease. Non-linear microscopy should be able to make a significant contribution to this, by providing high resolution images of the matrix and information on the collagen fibre alignments, without staining or other tissue processing. Also the 3D scans will be able to provide additional information on structural changes which cannot be gained from traditional histology. These aims are pursued in chapter 4.

### 1.6.2 Intervertebral disc

The intervertebral discs (IVDs) are located between the vertebrae and their role is to transmit compressive loads within the spine and give the spine its flexibility.<sup>98, 99</sup> The tissue of the IVD is similar to that of articular cartilage, as it is largely composed of collagen fibres and proteoglycans, and as in cartilage the swelling pressure from the proteoglycans trapped within a collagen network gives the tissue its resistance to compressive loads. Like articular cartilage the tissue is avascular and the cells are broadly similar to the chondrocytes found in cartilage. The collagen fibres of the disc are mainly type I and type II, with minor components of type III, VI and IX. The majority of the proteoglycan is the large aggregate molecule aggrecan, with the smaller proteoglycans being minor components.

There are three different regions to the disc, the annulus fibrosus, the nucleus pulposus and the cartilaginous endplates, and these are shown in figure 1-12. The nucleus pulposus is contained within the annulus fibrosus and the cartilage endplates are located connecting the vertebral bodies to the disc. The collagen of the disc annulus is arranged into 15-20 lamellae which form approximately concentric rings around the nucleus. In each lamella the fibres (0.1-0.2µm diameter) are arranged parallel bundles, which run obliquely between the vertebral bodies, with an angle from the vertical ranging between 40-70 degrees. At the periphery of the disc these fibres connect with the vertebral body bringing the disc and vertebra together, whereas in the centre they run into the cartilaginous endplates. The angle of the fibres changes alternates between the lamellae to give a woven structure. This arrangement of loosely connected lamellae is thought to enable the disc to bend and extend. The annulus contains the highest proportion of collagen and the lowest proportion of aggrecan within the disc. The collagen of the nucleus pulposus forms a loose mesh of fine fibres (20-50nm diameter) with no known organisation. It contains a large proportion of aggrecan and therefore is highly hydrated, with a hydration of up to 90% water in young discs.<sup>100</sup>

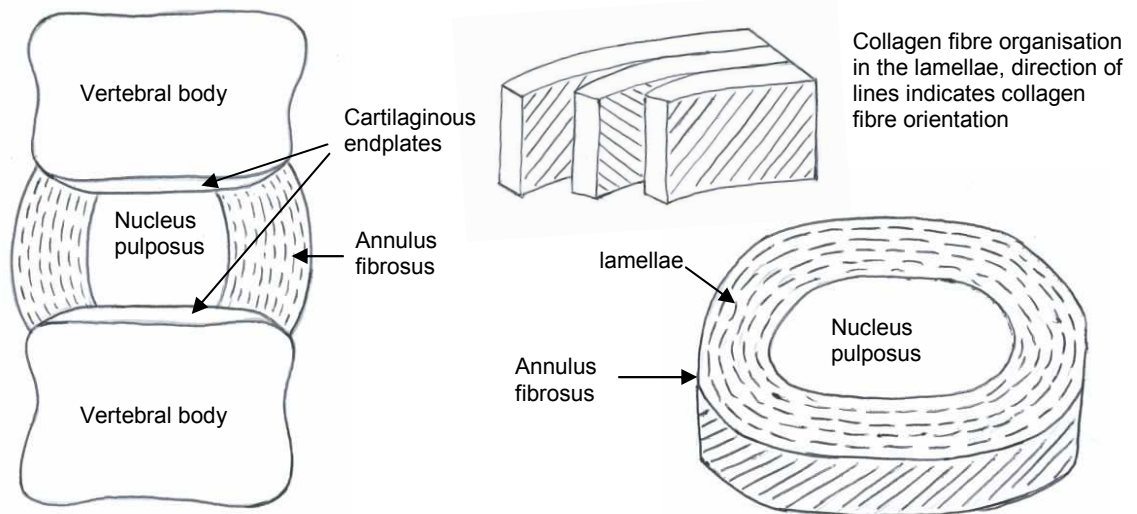
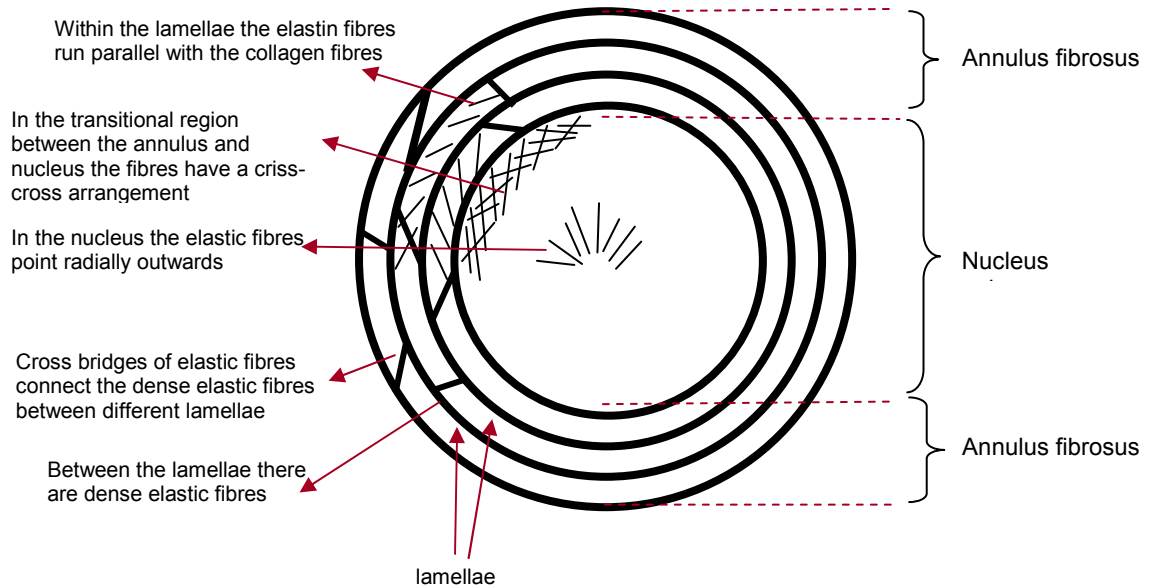


**Figure 1-12 A schematic diagram of the intervertebral disc.**

The disc needs to be able to return to its original size after an extension and therefore contains a network of elastic fibres throughout the disc. The organisation of these fibres has been found to vary between the different areas of the disc. In the disc nucleus parallel aligned fibres have been found both pointing radially out from the centre of the nucleus towards the annulus and vertically between the two cartilaginous endplates (possibility anchoring to them). At the transitional regions between the nucleus and the annulus the elastin fibres are no longer parallel but instead form a crisscross pattern. In the annulus the elastin fibres are densely concentrated between the lamellae, with cross bridges of dense elastic fibres traversing the lamellae to connect the elastic fibres. Elastic fibres are also found running parallel with the collagen fibres within the lamellae. The organisation of the elastic fibres is summarised in figure 1-13.<sup>99</sup>

Transverse section



Longitudinal section

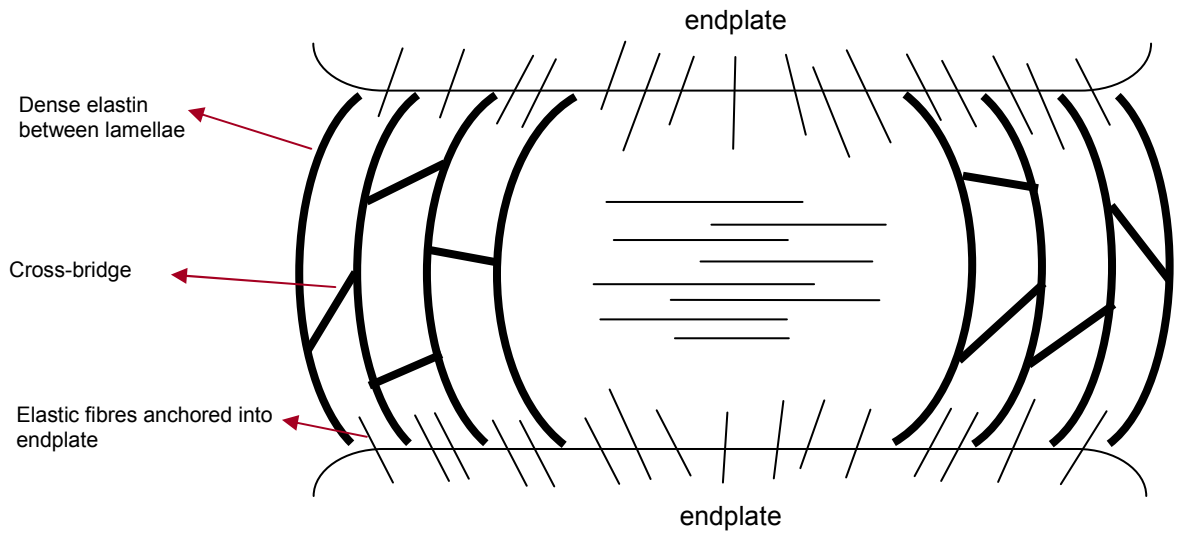


**Figure 1-13 A schematic diagram of the elastin fibres within the intervertebral disc (based on the results published by J Yu et al<sup>99</sup>)**

Although non-linear microscopy is very well suited for imaging the collagen and elastin fibre arrangement within the disc there have been no previous studies using this technique. However the collagen fibre orientations within the disc have been investigated with polarization sensitive SHG<sup>19, 101</sup>. Imaging of the elastin network in unstained disc samples is reported in chapter 5.

Disc degeneration is strongly associated with back pain and resulting disability which is a major clinical problem. Progressive degeneration occurs with aging and starts at an early stage with teenage discs showing the first signs. With degeneration the nucleus becomes more fibrotic and some of the order in the lamellar structure of the annulus may be lost. There is a loss of proteoglycans in the nucleus which causes a decrease in hydration. This results in a decrease in the weight bearing properties of the disc.<sup>102</sup> Fissures may occur in both the nucleus and the annulus and increase the risk of disc herniation.<sup>102, 103</sup>

### **1.6.3 Elastic cartilage**

Elastic cartilage is investigated in chapter 5 of this chapter where the elastin networks are imaged. This type of cartilage is found in the external ear, external auditory canal, eustachian tubes, epiglottis and parts of the larynx. It has increased elasticity due to the presence of an abundant network of elastin fibres. Its appearance is more opaque than hyaline cartilage and is yellow in colour. The chondrocytes are similar to those in hyaline cartilage and appear either singly or in pairs. Staining for elastin reveals an extensive network of branching fibres which are most dense towards the central region. Towards the perichondrium the elastin fibres become finer and less densely packed. Elastin fibres are also found in the surrounding perichondrium.<sup>104, 105</sup>

## 2 Experimental

---

### 2.1 Introduction

Two different non-linear microscope systems were used for the imaging in this thesis, for simplicity I will refer to these as microscope 1 and microscope 2. Microscope 1 was constructed from easily available optical components and custom made pieces from the department mechanical workshop. Microscope 2 was based upon an Olympus FluoView confocal inverted microscope which was modified to allow multi-photon imaging. Microscope 1 allowed TPF and SHG imaging whereas microscope 2 allowed both these modalities and also CARS imaging.

The early work towards this thesis was to construct microscope 1 and carry out imaging and the polarization sensitivity work presented in chapter 6. Later on during the project microscope 2 became available and imaging was transferred from microscope 1 to microscope 2. This was because microscope 2 offered the following advantages. Firstly it allowed CARS imaging to be combined with TPF and SHG imaging. Also it was set-up so that data could be taken simultaneously in both the forwards and backwards directions. The commercial scanning system and software made it easier to use and allowed a wider range of scanning options and also finer movements in the z-direction whilst taking 3D data sets. One advantage of microscope 1 which made it suitable for the polarization sensitivity experiments was its simplicity. Extra optical components could easily be added and the software could be altered to suit the current experiment. The set-up and testing of microscope 1 is described in sections 2.2.1 and 2.2.2 followed by the set-up of microscope 2 in section 2.3.

For the spectroscopy results presented in chapter 3 another microscope was also used. This was coupled to a spectrometer and the scanning system from microscope 1 was used to generate a raster scan for the system. The set-up and work done calibrating the spectrometer is described in section 2.4.

## 2.2 Microscope 1

### 2.2.1 Microscope design

The laser excitation light for this microscope 1 was provided by a Ti:Sapphire laser femto-second pulsed laser (Spectra Physics Tsunami). This laser has a time averaged output of 0.7W, and produced 100fs pulsed at a repetition rate of 82MHz. The wavelength was tuneable between 720 and 900nm although it was most efficient at 800nm. A neutral density filter was used to control the laser power used in imaging. At this component excess power was reflected into a beam dump. Beam samplers were used to reflect 10% of the beam which was used to monitor the spectrum and power of the laser output. When setting up and aligning the microscope a red HeNe laser beam was co-aligned with the Ti:Sapphire laser output. This was used to visualise the light path through the microscope. The optical table set-up is shown in figure 2-1.

In order to establish whether the laser is modelocked the spectrum of the laser output was analysed. The wavelength range and the temporal width of the pulses are related via the uncertainty principle  $\Delta E \Delta t \geq \hbar / 2$ . Substituting  $\Delta E = hc / 2\lambda^2 \Delta\lambda$  the resulting relationship between the temporal width and wave-length range is as follows.

$$\Delta t \approx \frac{\lambda^2}{c\Delta\lambda}$$

Thus, for 800nm emission and 100fs pulses the FWHM of the pulses should be approximately 10nm. The spectrum of the Tsunami output was measured by a spectrometer (ocean optics USB2000+).

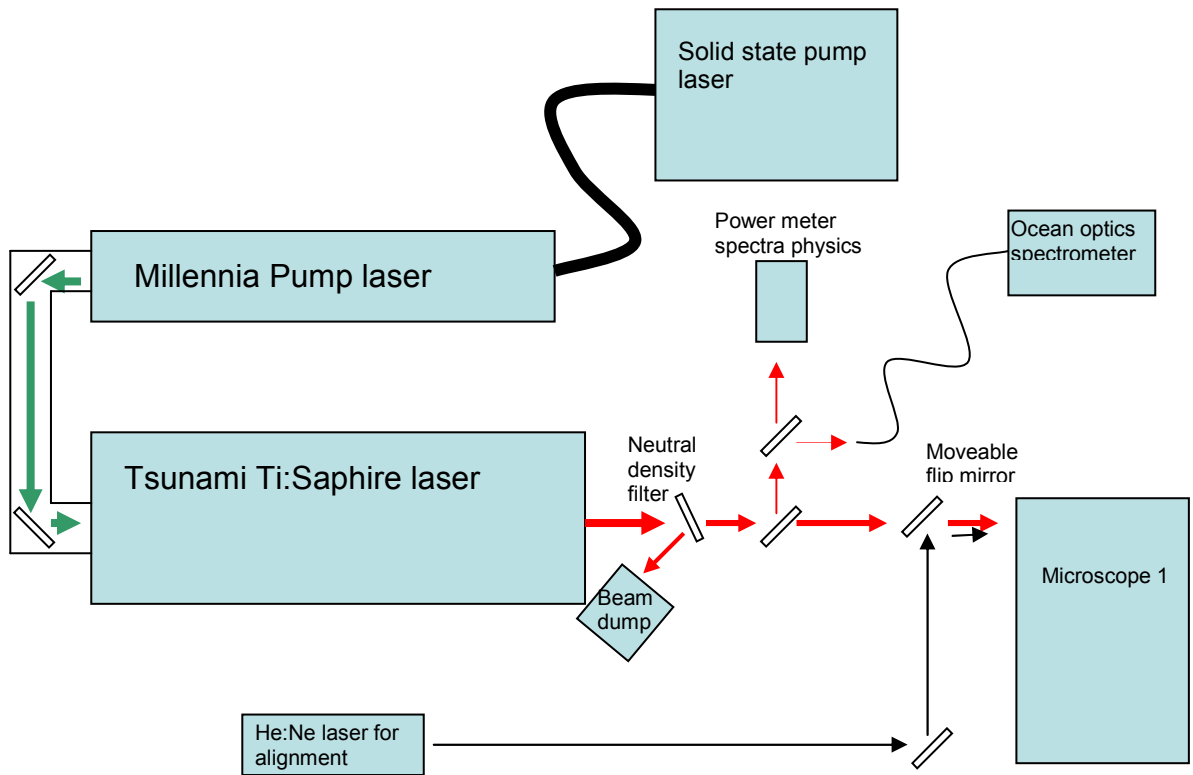


**Figure 2-1** The optical setup for microscope 1.

The microscope set-up is shown in figure 2-2. It was designed to operate in the reflection mode as this was the most practical way of imaging large intact tissue samples, for example cartilage plugs with the bone still attached. The excitation light is directed into the microscope so it arrives centrally at a pair of scanning galvanometer mirrors (Cambridge Technology Incorporated), which are used to create a 2D raster scan pattern. The light then passes through a scan lens and a half wave-plate (at 800nm CVI laser QWPO-800-10-2), and is reflected down towards the objective, at a short pass dichroic beam splitter (CVI laser SWP-45-RS830-TP400-2025-UV). The light is then collimated using a tube lens (Nikon) and passes through another 800nm half-wave plate (meadowlark NH-050-0800-L10) which is placed directly in the back aperture of the objective. The scan lens and the tube lens act as a Keplerian beam expander and expand the beam to fill the back aperture of the microscope objective. The distance between the two lenses needs to be the sum of the focal lengths of the lenses and the ratio of the beam diameters before ( $d_1$ ) and after ( $d_2$ ) the lenses is as follows,  $\frac{d_2}{d_1} = \frac{f_2}{f_1}$ , where  $f_1$  and  $f_2$  are the focal lengths of the scan lens and tube lens respectively. The objective is a Nikon (Fluor  $\times 60$ ) 1.0NA water dipping objective. The

distance between the tube lens and the objective is chosen so that the scan pattern is convergent on the back focal plane of the objective. This means that the laser excitation beams position is largely independent on the scan angle at this point and minimises the vignetting caused by the raster scan pattern entering the objective.

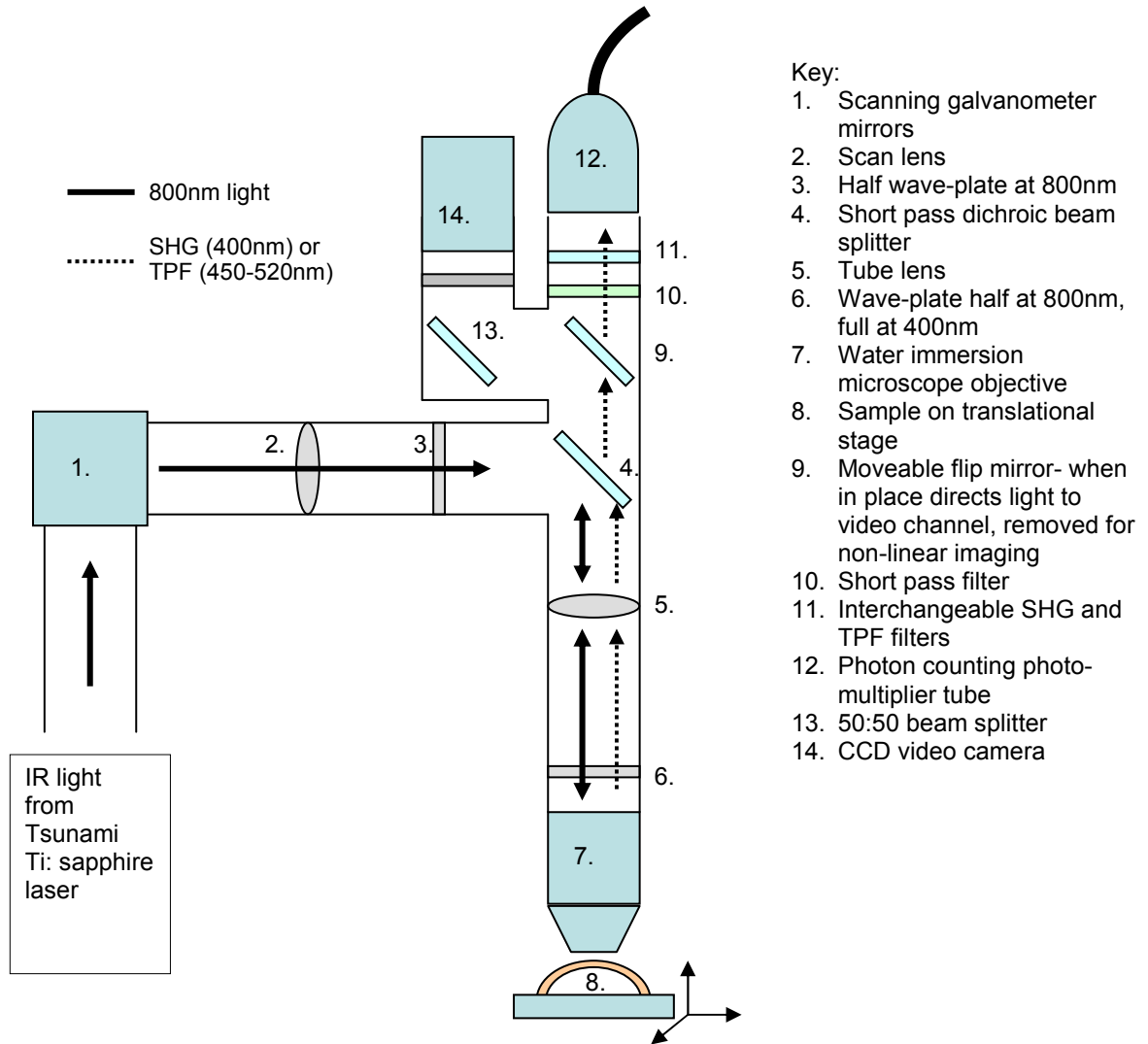


Figure 2-2 A schematic diagram of the optical set-up of our home built microscope

The TPF and SHG light is collected using the same microscope objective and passes back through the wave-plate and the tube lens. The TPF and SHG are separated from the back-scattered laser fundamental at the dichroic beam splitter, with the TPF and SHG being transmitted and the laser fundamental being reflected. Any remaining laser fundamental is removed with a band pass filter (CVI laser CG-BG-39), with the combination of the dichroic and filter giving a combined blocking of 9OD at 800nm. To switch between TPF

and SHG imaging the filter below the photon counting head is changed, with a 450-520nm band pass filter (CVI laser F70-500-3-OCV) for TPF and a 410-390nm band pass filter (CVI laser F10-400-4-326317) for SHG.

The half wave-plates within the system were used in the polarization sensitivity experiments described in Chapter 6. The wave-plate before the dichroic beam splitter was set so to rotate the angle of the laser fundamental so it arrived at this component completely p-polarized. (If the light arrived at the dichroic beam splitter at any polarization between the p and s state the reflected light had a resultant elliptical polarization). The second half wave-plate is used for controlling the polarization of the light incident on the sample, and was rotated for the polarization sensitivity experiments. This wave-plate had to have good transmission at both 800nm and 400nm and therefore has special coatings to reduce any reflection of the 400nm light.

The frame of the microscope is constructed from components in the Thorlabs rigid construction range which include cage rods, cage cubes and cage plates. This is combined with metal base plates and moving parts which were custom built to fit the system in the Physics Department mechanical workshop. The cage system enabled optical components to be easily added or moved around the system in the set-up stage but has a disadvantage that it produces a microscope with less rigidity than a commercial system, causing problems with registering images when filters have been changed.

The light was collected with an integrated photon counting head (Hamamatsu H7360-02), which is sensitive in the wave-length range 300-650nm, with a peak sensitivity at 420nm. The PMT outputs 3V 9ns pulses which are imputed into a photon counting card (Hamamatsu M8784). The card counts the number of pulses received in a time period ranging from 10 $\mu$ s to 10s. For imaging the pixel dwell was chosen to be 10 $\mu$ s so that radiation damage to the tissue would be minimised. There were two different levels of accuracy either 32bit or 16bit, which allowed a maximum of 131072 and 262144 time intervals to be counted in sequence respectively. For this set up the 16bit imaging was chosen as there were insufficient counts detected in the 10 $\mu$ s time interval to require 32bit

counting. This meant that 262144 time intervals could be collected giving a maximum image size of 512×512 pixels but for these experiments 500×500 pixel images were taken.

The microscope was focused on a region of interest by moving the sample in the z-direction using on a motor stage (Physik Instrumente). This stage is controlled by a motor controller card (Physik Instrumente C842) and has a minimum movement of 1µm. The motor stage also allows 3D image stacks to be built up, with the sample being moved upwards by a set distance between each raster scan to take a 2D image. The sample could also be moved in the x and y direction over a range of 50mm using manually controlled micrometer screw translation stages.

The laser scanning system, sample motor stage and data assimilation from the PMT was controlled by a computer program written in C using the “Lab Windows” software (National Instruments CVI). A 2D raster scan was generated with scanning galvanometer mirrors where the scanning pattern was controlled by a signal generator (SONY Tektronix AFG320 arbitrary function generator), which in turn was controlled using the computer software via a GPIB cable. The data collection from the photon-counting head is synchronised with the start of the raster scan via a synchronisation pulse from the signal generator which is fed into the photon counting card.

### **2.2.2 Microscope testing**

Before the microscope could be used to study biological specimens it was important to test whether it was working as designed. In this section tests carried out on the microscope are described.

Firstly the magnification of the microscope was tested so that a scale could be added to any images taken. The maximum angle  $\theta$  moved by the scanning galvanometers was proportional to the amplitude of the voltage provided by the signal generator. As the angular deviations in the back aperture of the objective are small, the small angle approximation can be used and therefore the distance  $d$  the focal point of the laser moves through the sample is also proportional to the amplitude of the voltage wave on the signal

generator, and is also dependent on the focal length of the microscope objective as shown in equation 2.1.

$$d = f \sin \theta \approx f\theta \quad (2.1)$$

The relationship between the voltage and scan distance has been measured for both the scanning galvanometer mirrors, and incorporated into the scanning soft-ware so that the scan size can be entered into the computer and then the correct voltage will be selected. These measurements were taken by viewing the size of the raster scan from the HeNe laser used for aligning focused on a graticule through the microscope video channel. figure 2-3 shows the relationship between the applied voltage from the signal generator and the distance the focal spot moves in the focal plane for each galvanometer mirror. The field of view from the objective was found to have a 180 $\mu\text{m}$  diameter, this allowed the maximum size of square scans to be 130  $\times$  130 $\mu\text{m}$ .

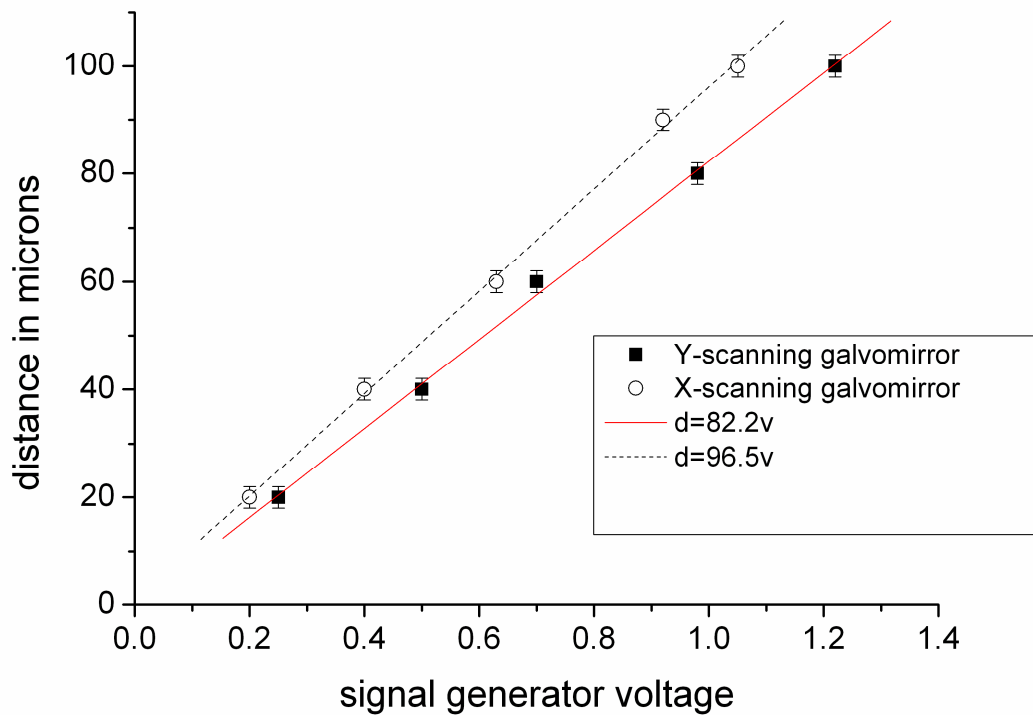


**Figure 2-3** The relationship between the voltage and scan size for microscope 1. The distance each scanning galvanometer mirror moves the focal point is dependent on the applied voltage.

To build up images the counting card output needed to be synchronised with the scanning galvanometers. The time delays were detected by imaging grains of starch which are a strong source of SHG<sup>29, 30</sup>. The grains of starch appeared at a different position on the return scan line in the x direction if the image reconstruction was not correctly synchronised with the signal generator. The amount of time delay was found to be dependent on the signal generator settings. These time delays were measured from the images and correction factors were inputted into the computer program controlling the scanners and the image reconstruction.

We also needed to estimate the power incident on the samples so this could be maintained at a level which would lead to minimum tissue damage. To do this the transmission through the microscope needed to be measured. The laser power was measured before it entered the microscope (at the point after the moveable flip mirror shown in figure 2-1) and then measured exiting the objective using the power meter and an integrating sphere (this was needed due to the high divergence of the light exiting the objective). It was found that a minimum of 17% of the light was transmitted through the microscope. Whilst imaging was carried out the power was monitored by diverting 10% of the beam to the power meter (position shown in figure 2-1), and from this the power at the sample was calculated.

To maximise the sensitivity of the microscope the amount of back-scattered fundamental and noise from the room reaching the detector needed to be minimised and measured. The dark count rate of the PMT photon counting head was measured and found to be about 20 counts per second at room temperature, which was low enough not to effect our results. By placing suitable light shielding around the sample stage the amount of light detected from the room when the laser was switched off could be reduced to less than 1000 counts per second, with the room lights off. The amount of backscattered laser fundamental measured from the system was measured using a sample of intra-lipid (20% solution of purified soya bean oil in water) as a scattering medium. This sample source is not fluorescent or able to produce SHG but is a highly scattering medium, similar to tissue. At low laser powers (10mW) the amount of back-scattered fundamental detected was found to be 600-1200 counts/s but this increased to 13000-16000 counts/s at the maximum laser power (120mW).

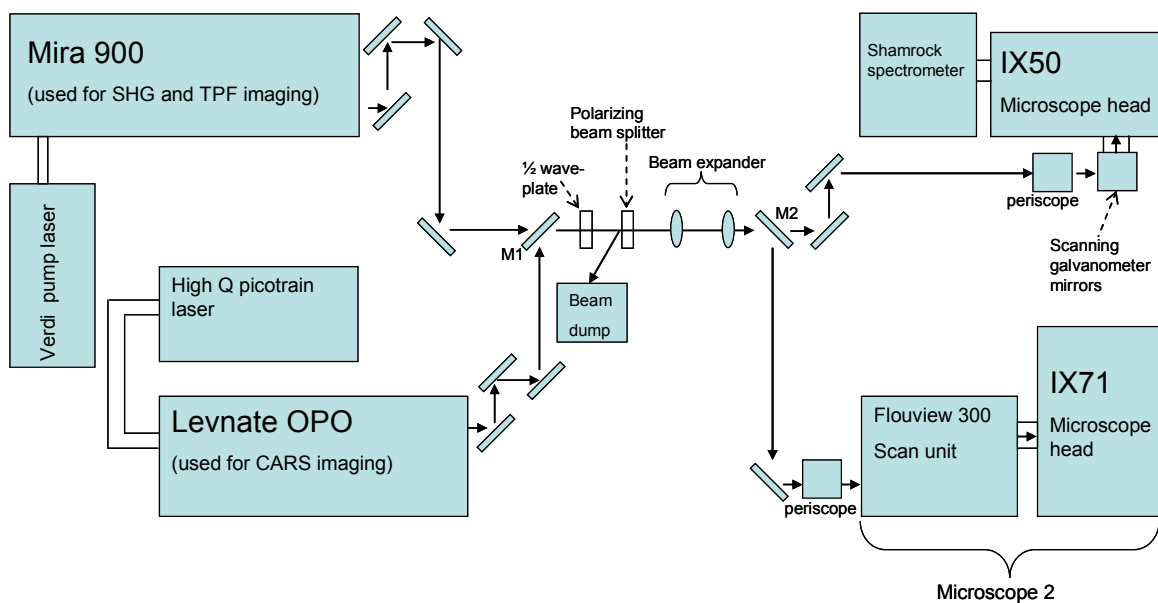
## 2.3 Microscope 2

Microscope 2 is based on an Olympus FluoView microscope which has been converted for multi-photon microscopy. This microscope allows TPF, SHG and CARS imaging in the forwards and back-scattered directions. The scanning system is the Olympus FluoView 300 and the microscope head is the Olympus IX71 inverted microscope and the scanning and image acquisition are controlled via the FluoView version 5 software. This system has been shown to be suitable for conversion into a multi-photon microscope by Nickolenko et al<sup>106</sup> and a similar approach was implemented.

The microscope uses laser excitation light from two different laser systems. For the SHG and TPF imaging the laser excitation light is from a Ti:Sapphire similar to that used for the homebuilt microscope. The laser system is supplied by Coherent and consists of a Mira 900 Ti:sapphire laser pumped by a Verdi (V10) laser (532nm). The maximum power output of the Mira is 1.5W and its wavelength is tuneable between (690nm and 990nm) with a repetition rate of 76MHz and pulse width of 200fs, this is used for both SHG and TPF imaging. The output of this laser is horizontally polarized.

For CARS imaging the laser excitation light is provided by a picosecond pulsed out-put from a Levante OPO. The OPO is pumped by a HighQ Picotrain laser which produces a 6 pico-second pulsed output at 532 nm, with a repetition rate of 76MHz and a maximum power of 10W. In the OPO the 532 nm is converted into two longer wavelength beams in a non-linear crystal. These are called the signal and idler beam. Due to the conservation of energy the sum of the frequencies of the signal and idler beam correspond to the frequency of the pump beam. The signal beam is the higher frequency beam and acts as the pump beam during the CARS process (see figure 1.5 section 1.4.1), the lower frequency beam is called the idler beam and acts as the Stokes beam during the CARS process. The frequency of the signal and idler outputs of the OPO is tuneable allowing different bond vibrations to be probed. The signal beam can be tuned between about 670-980nm and the idler beam between 1450-1130m. The maximum combined power of the signal and idler beam is 2W. The output of both the lasers is monitored using an APE autocorrelator which is able to measure both the wavelength and temporal pulse widths.

The spectrometer described in section 2.4 is also positioned on the same optical table as the Olympus FluoView microscope and also uses the output of the Mira laser. The optical table layout is shown in figure 2-4, showing the components used in the experiments described in this thesis. Flip mirrors are used to change between imaging modes. For TPF and SHG imaging on the FluoView microscope mirror M1 is down and mirror M2 is up, for CARS imaging both mirrors M1 and M2 are up and for taking TPF spectra using the spectrometer both mirrors M1 and M2 are down.



M1 and M2 are moveable flip mirrors

When using microscope 2 mirror M2 is up, M1 is down for SHG and TPF imaging and up for CARS imaging

When taking TPF and SHG spectra using the spectrometer and IX50 microscope both mirrors M1 and M2 are down

**Figure 2-4 A schematic diagram of the optical table layout in the new laser lab.**

In order to avoid the biological samples being damaged by the high laser power the beams are attenuated by using a half wave-plate and a polarizing beam splitter, as the polarization is rotated a different proportion of the beam is split off into a beam dump. This has been set up so light polarized horizontally is transmitted and light polarized vertically is reflected into the beam dump.

The objectives which have been used for imaging with this microscope are an Olympus FN22 10x 0.4NA, and an Olympus UPLSAPO 60x 1.2NA water immersion objective. The

Olympus UPLSAPO lens is been optimised for transmission in the near infra red and is therefore well suited for multi-photon microscopy. Most of the imaging in this thesis has been done with the Olympus UPLSAPO 60x objective which gives a maximum scan size of  $260 \times 260 \mu\text{m}$ . For CARS imaging the field of view is less than the maximum scan size. This is due to optical aberrations caused by the pump and stokes beams being at different wavelengths. The larger the difference in the wavelengths the smaller the field of view<sup>61</sup>.

Modifications have been made to both the FluoView 300 scan unit and the IX71 microscope head to allow the system to be used for multi-photon imaging. The optical components within the system have been coated to allow optimal transmission of excitation light at IR wavelengths. Within the scan unit two of the dichroic beam splitters have been removed and replaced by mirrors. The original scan unit contains two PMTs used for detecting single photon fluorescence in the back-scattered direction. These PMTs are not used for the multi-photon microscopy, as they do not have sufficient sensitivity to detect the low photon counts involved in multi-photon processes. Also these PMTs are placed to work in the descanned mode after the fluorescence has passed back through the scanning galvanometers. The descanned mode is only necessary in confocal microscopy where the fluorescence must pass through a pin-hole to fluorescence from outside the focal spot. In non-linear microscopy this is no longer needed and therefore it is more efficient to place the PMTs closer to the objective before the scanning galvanometer unit. Figure 2-5 shows the changes within the FluoView 300 scan unit. New more sensitive PMTs were added to the system for SHG and TPF imaging (Hamamatsu R3896). The off-set and the gain from the PMTs may be controlled from the FluoView software but the voltage is controlled externally and can be varied between 0-15V.

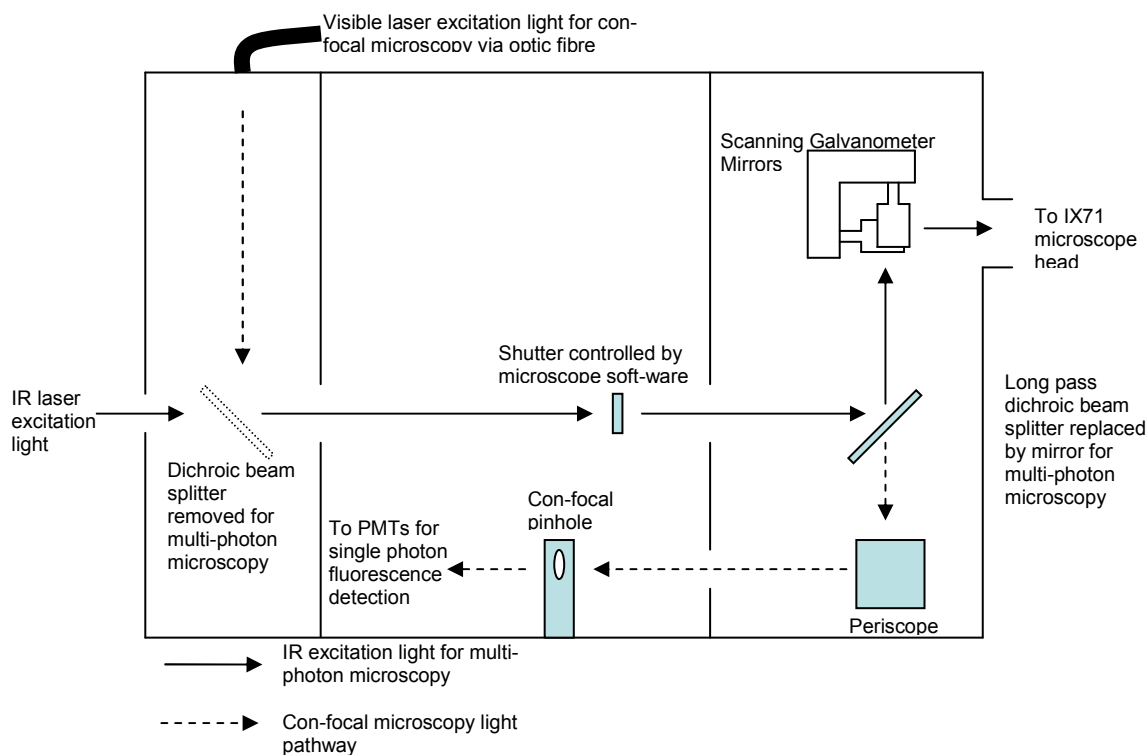


**Figure 2-5 A schematic diagram of the FluoView 300 scan unit. Showing the modifications to allow non-linear microscopy**

The IX71 microscope head has been modified to allow the detection of forward scattered SHG and CARS and back scattered SHG, TPF and CARS. The light paths and modifications to the IX71 microscope head are shown in figure 2-6. IR laser excitation light from the FluoView scan unit enters the microscope and passes through the condensing lens, it is then reflected up towards the objective and passes through an image forming lens. For detection of the epi signal a long pass dichroic beam splitter is placed between the image forming lens and the objective. This transmits the laser fundamental but reflects the epi signal towards a PMT at the back of the microscope. Due to the different excitation wavelengths used for CARS imaging compared to SHG and TPF imaging different dichroics are needed. For CARS imaging a dichroic transmitting  $\lambda > 850\text{nm}$  (z850rdc-xr chroma technologies) is used and for SHG and TPF imaging a dichroic transmitting  $\lambda > 670\text{nm}$  (670dcxr chroma technologies) was used. In front of the PMT there are interchangeable filters for the different imaging modalities. For TPF imaging a band pass filter centred at 500nm with a FWHM of 70nm (F70-500-3-PFU CVI laser) is used, for SHG imaging a band pass filter centred at 400nm with a FWHM of 10nm (F10-400-5-QBL

CVI laser) is used and for CARS imaging a band pass filter centred at 750nm (HQ 750/210 chroma technologies) is used.

The forward generated light is collected using the condenser (NA=0.55) and is reflected towards a dichroic beam splitter (670dcxr chroma technologies) which separates the CARS and the SHG signals. CARS signal ( $\lambda > 670\text{nm}$ ) is transmitted to one PMT and the shorter wavelength SHG and TPF light is reflected to another PMT. In front of the SHG PMT there is a band pass filter centred at 400nm with a FWHM of 10nm is used to exclude any TPF light from being detected. In front of the CARS filter a band pass filter centred at 750nm (HQ 750/210 chroma technologies) is used.

For focusing and orientation purposes the microscope still contains an eye piece. When this is being used the PMTs are switched off and the transmission lamp is switched on. The mirror below the transmission lamp (part 10. in figure 2-6) and the dichroic beam splitter (part 5. in figure 2-6) are removed for the light path and the mirror (part 4. in figure 2-6) is moved into the light path to direct light from the transmission lamp up into the eye piece.

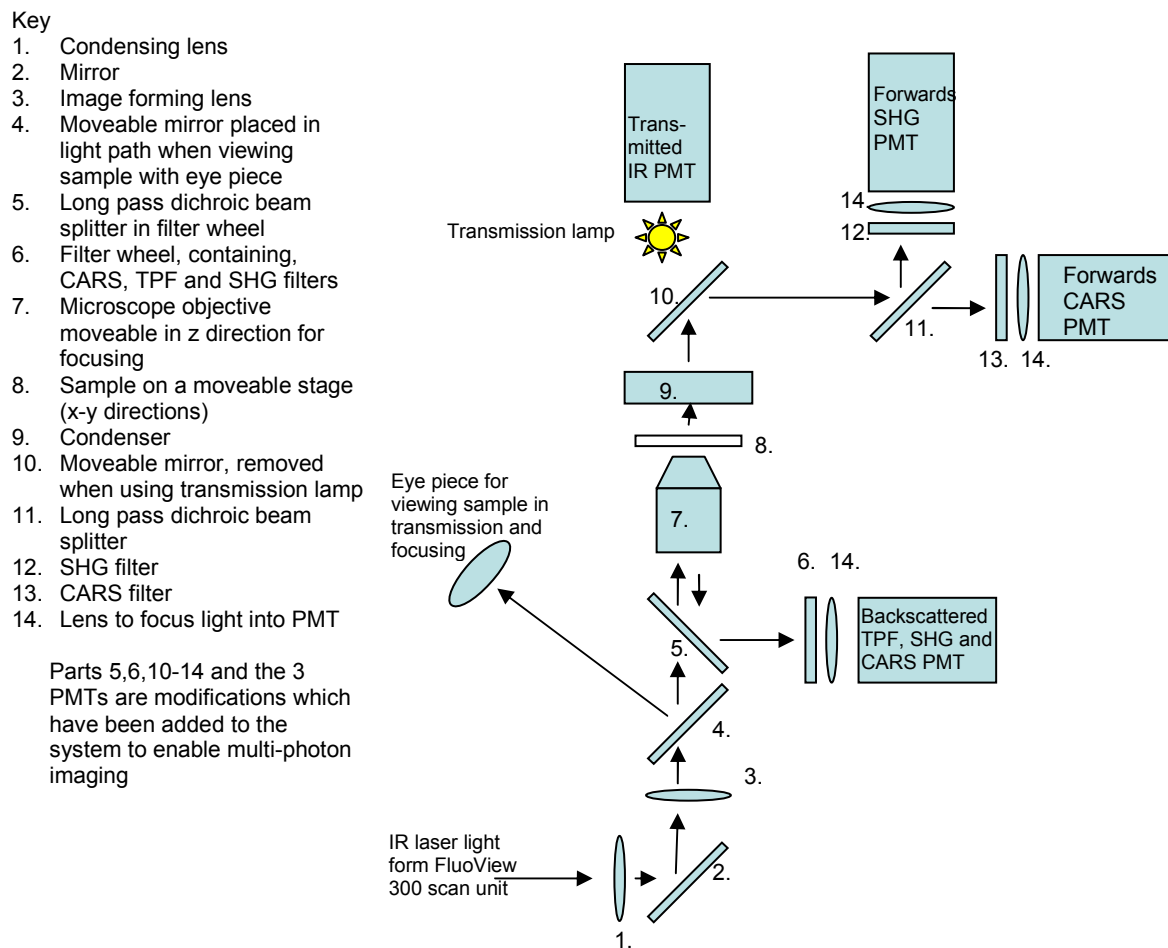


**Figure 2-6 A schematic diagram of the IX71 microscope head. The light path and the modifications for multi-photon microscopy are shown.**

The transmission efficiency of the laser fundamental through the system has been measured for both the CARS excitation light source and the 800nm light source for SHG and TPF imaging. The power was measured before entering the FlouView scan box and then exiting the objective. For the CARS beam (tuned to the  $2845\text{cm}^{-1}$  resonance, signal = 924nm, idler = 1254nm) there was approximately 20% transmission. For the 800nm excitation light from the Mira laser the transmission was measured to be approximately 16%.

## **2.4 Spectrometer Set-up**

For the work carried out in Chapter 3 investigating the source and spectral properties of the SHG and TPF a spectrometer (Andor Technology shamrock sr-303i) was coupled to a microscope (Olympus IX50). The spectra were recorded using a CCD camera (Andor IDUS) which was cooled to  $-65^{\circ}\text{C}$  allowing the system to be sensitive enough to detect the low intensity two-photon autofluorescence. The Olympus IX50 head was modified to allow it to operate as a laser scanning multi-photon microscope. The signal from the sample was collected in the epi direction and could be directed either to a PMT for imaging or the spectrometer. The light path through the spectrometer is shown in figure 2-8 with parts 1-2 and 7-14 being modifications added to allow multi-photon microscopy and spectrometry.

The system was arranged so that the focal point of the laser could be raster scanned through the sample. This was necessary for spectrometry as it reduces photo-bleaching and damage and also allows multi-photon imaging of the regions of interest. When taking spectra of tissue samples it was important to set the integration time over which the spectrum was taken to be an integer number of the time period for one raster scan, otherwise certain areas of the region of interest may contribute more to the scan pattern than others. The raster scan was generated using scanning galvanometer mirrors controlled by a signal generator as described in section 2.2. The beam was expanded to fill the back aperture of the objective after the scanning galvanometer mirrors using a scan lens and a tube lens as described for microscope 1. Although the same scanning galvanometer mirrors and signal generator are used as for microscope 1 the magnification as a function of voltage will be different for this microscope due to the differences in the light path between the scanning galvanometer mirrors and the sample and due to the use of a different microscope objective. The relationship between applied voltage and scan size was measured by imaging a fluorescent slide containing a square array of 169 gold points which was  $30 \times 30 \mu\text{m}$  in size at different voltage settings. The relation between applied voltage and scan size for each scanning galvanometer mirror is shown in figure 2-7. The relationship between the applied voltage and the scan size has been entered into the scanning software.

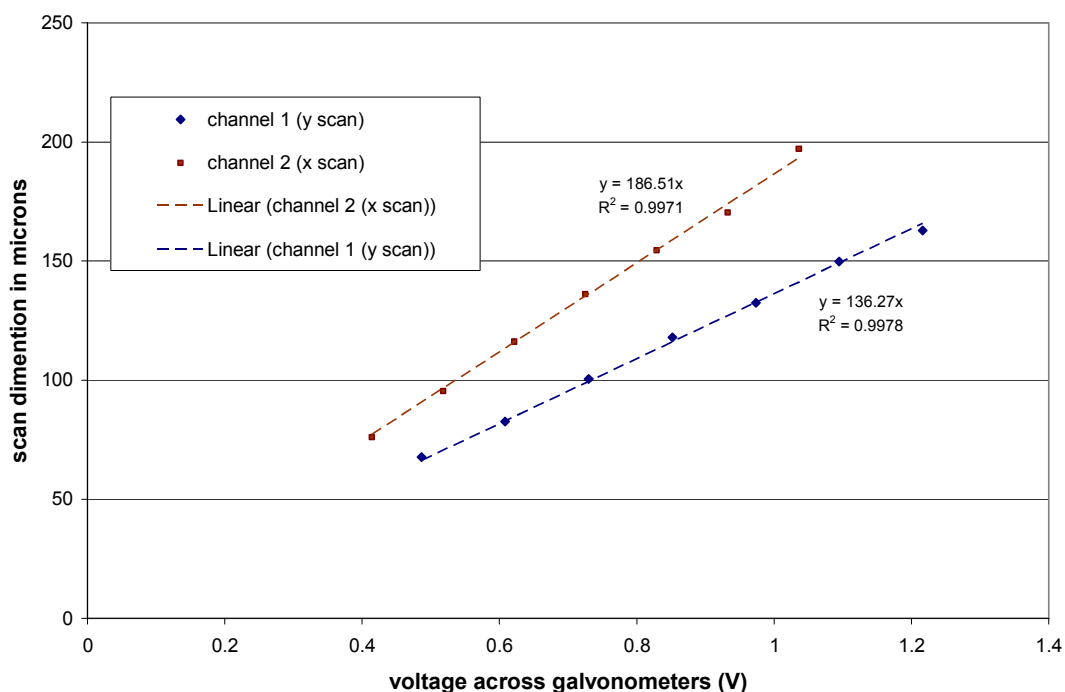


**Figure 2-7** The relationship between the voltage and scan size. The distance each scanning galvanometer mirror moves the focal point is dependent on the applied voltage.

The light was focused onto the sample using an Olympus UAPo/340 40x 1.15NA water emersion objective. To allow focusing on the sample the objective was moveable in the z-direction. When selecting a region of interest the sample could be viewed using transmitted light with the transmitted light being directed to a CCD video camera (see figure 2-8) and displayed on the computer screen. When imaging or taking a spectrum the TPF of SHG signal is separated from the laser fundamental by reflection off a long pass dichroic beam splitter (supplier and part number) which transmits  $\lambda > 670\text{nm}$ .

The spectrometer microscope was also set up to allow multi-photon images to be taken of the samples, with a removable mirror placed in the light path between the microscope and the spectrometer. This allows light to be reflected up to a PMT. We used the integrated photon counting head (Hamamatsu H7360-02) and counting card (M8784) as described in section 2.2 and the set-up for imaging and the program for control and data collection was again the same as described for microscope 1. Filters were also placed between the mirror and the photon counting head and these were the same filters used for the microscope 1.

To allow the maximum signal to be collected by the spectrometer the TPF and SHG light was focused onto the input slit of the spectrometer via an achromatic lens (Thorlabs AC254-060-A1) with a 60mm focal length. The achromatic lens is needed to bring light of different wavelengths to a focus at the same point. (The lens chosen here brings the light in the wavelength range 486-666nm to a focal point within 70 $\mu$ m of each other). If the light is focused to a different point for different wavelengths then the efficiency at which it enters the slit will be a function of wavelength and therefore this will be an additional factor to consider when calibrating the spectrometer. A Schott coloured glass filter (CVI laser CG-BG-39) was placed in front of the spectrometer slit. Together with the dichroic beam splitter this means that only  $8.4 \times 10^{-5}$  % of the laser fundamental at 800nm reaches the spectrometer slit. Without this blocking at 800nm the spectra are distorted by scattered laser fundamental and also the CCD camera may be at risk from damage due to very high count rates.

The laser power was measured before the scanning galvanometer mirrors and then exiting the objective. It was found that 43% of the power was transmitted. This percentage transmission could then be used to estimate the power at the focal point whilst taking spectra.

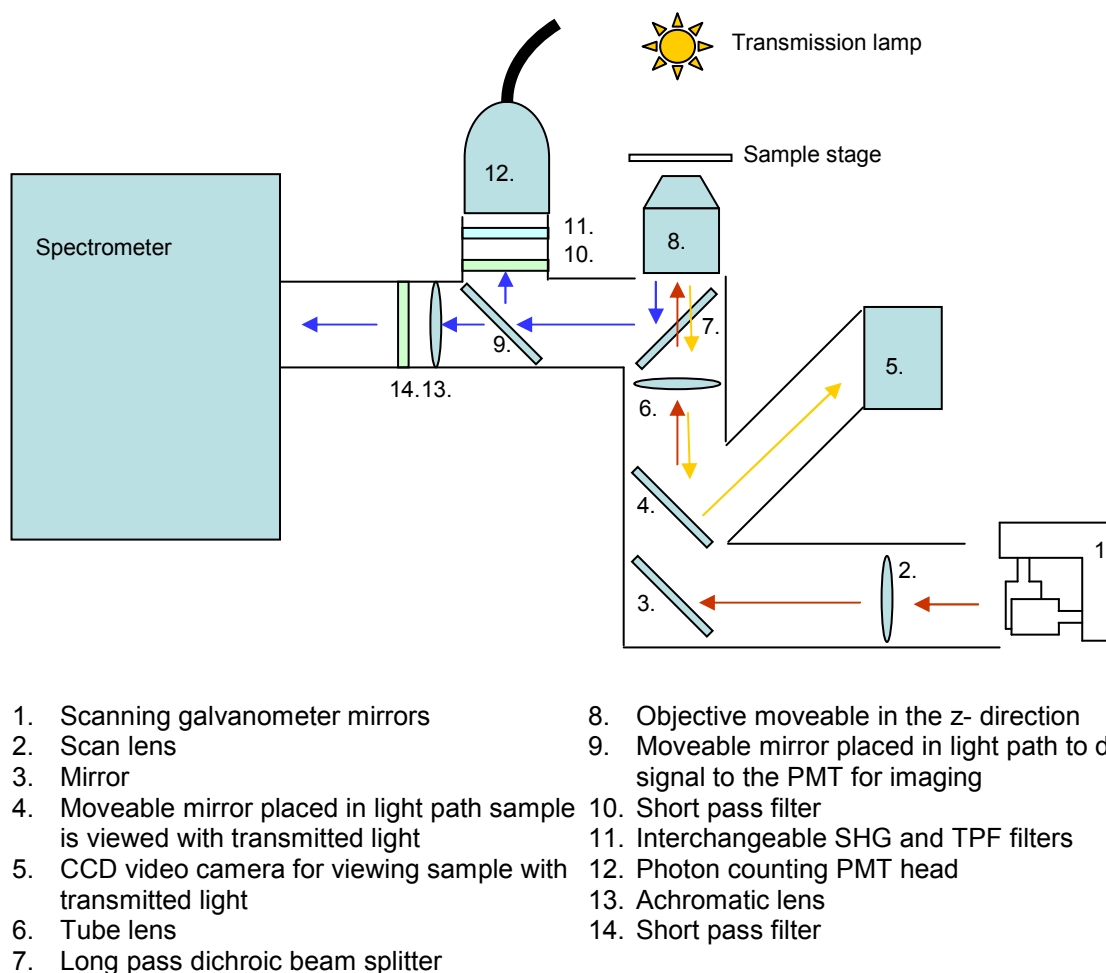


**Figure 2-8 Scanners, microscope head and spectrometer;**  
**A schematic diagram of the light path through the scanners and IX50 microscope head to the spectrometer.**

An ideal spectrometer has an excitation source which produces a constant photon count independent of the excitation wavelength and transmits all possible excitation wavelengths with equal efficiency. Its efficiency is also independent of polarization and all emission wavelengths must be transmitted with equal efficiency. Also the efficiency of the detector should be independent of wavelength. Components should be chosen to have as little wavelength dependence of the transmission over the range for which the spectra are to be taken. In practice it is not possible to construct an ideal spectrometer and therefore results must be calibrated for the efficiency of the system.<sup>49</sup>

To acquire accurate spectra it is important to know the wavelength dependence of light transmitted from the sample stage to the spectrometer and the efficiency of the

spectrometer as a function of wavelength. The optical components in the fluorescent light path are the objective, dichroic beam splitter, focussing lens and colour glass filter. The two components which have the greatest wavelength dependence are the dichroic beam splitter and the coloured glass filter and the combined transmission through these is shown in figure 2-9. Between 341 and 607nm over 50% of the fluorescent signal is transmitted and therefore over this region the corrected spectra should be reasonably accurate. Outside this wavelength range a different choice of dichroic beam splitter or filter may needed.

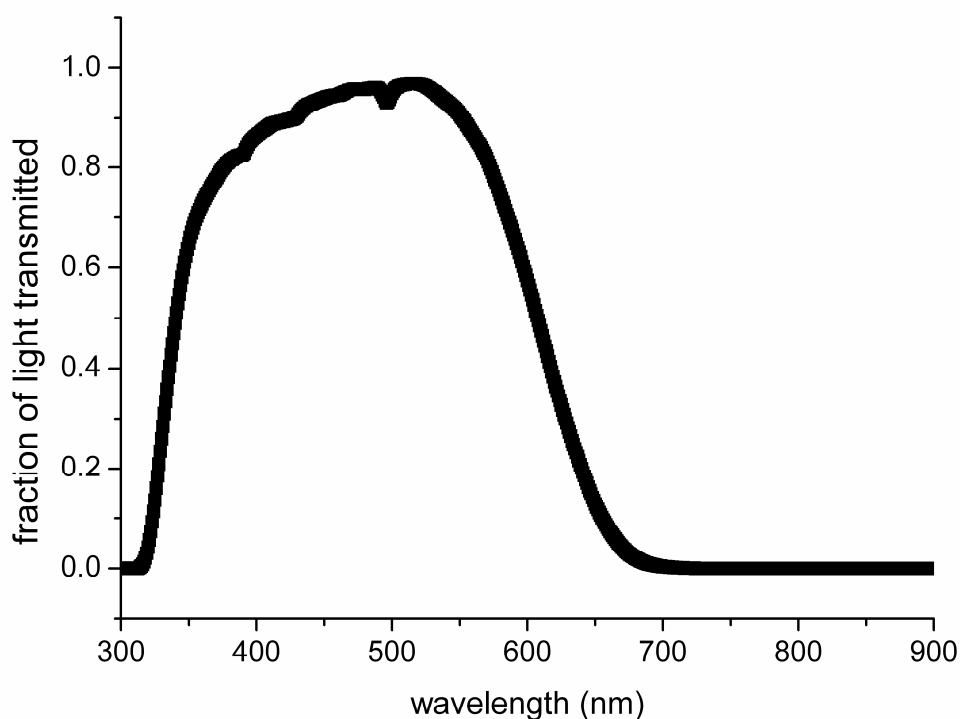
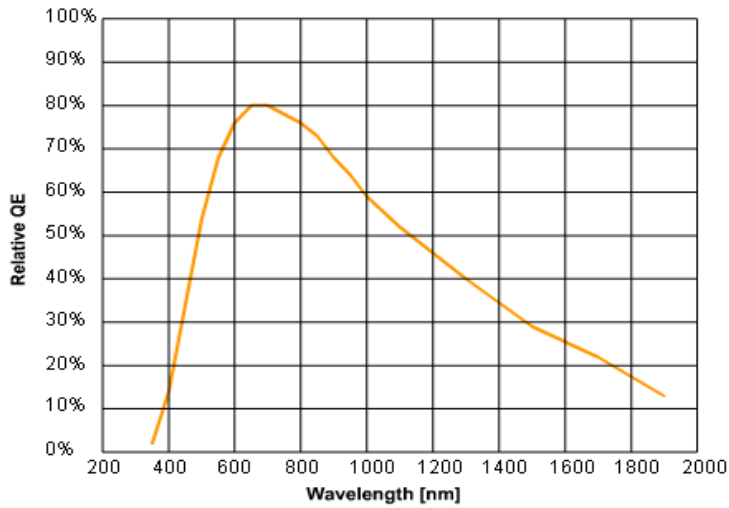
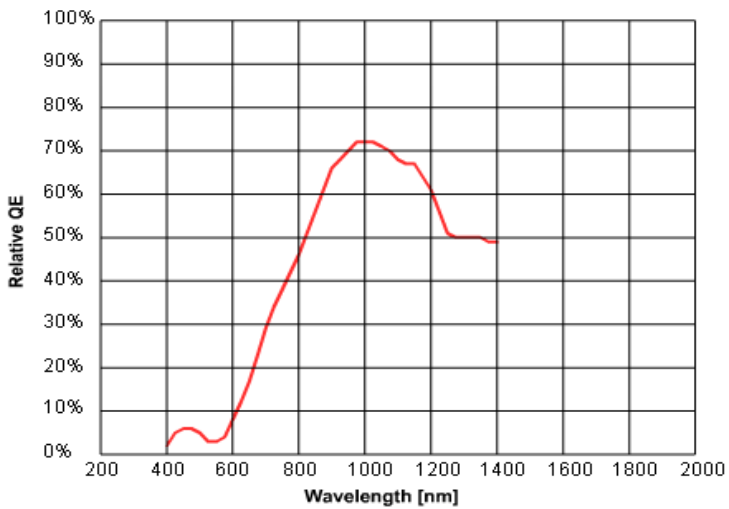


**Figure 2-9 Transmission across the dichroic and coloured glass filter.**  
The combined effect of the dichroic beam splitter and the colour glass filter on the fraction of signal transmitted to the spectrometer. (light is reflected off the dichroic and transmitted through the BG-CG-39 filter)

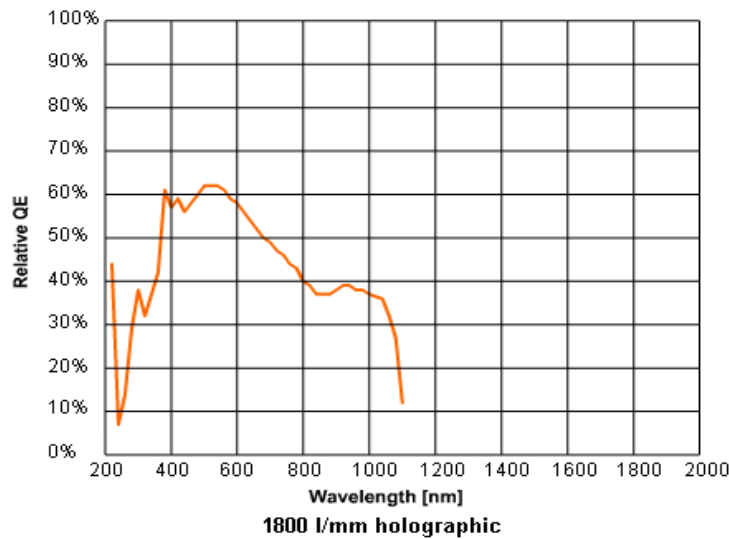
The spectrometer contained a choice of 3 different diffraction gratings which are as follows grating 1 (150 l/mm, 800nm blaze, dispersion 21.4nm/mm), grating 2 (600 l/mm, 1000nm blaze, dispersion 5.2nm/mm) and grating 3 (1800 l/mm, holographic, optimised for 350-900nm). The blaze wavelength is the wavelength at which the diffraction grating is most efficient. The efficiencies of the gratings as a function of wavelength are shown in figure 2-10.



Grating 1:  
150 l/mm  
Blaze 800nm  
Dispersion =21.4nm/mm



Grating 2:  
600 l/mm  
Blaze 1000nm  
Dispersion =5.2nm/mm



Grating 3:  
1800 l/mm holographic  
Optimised for 350-900nm  
Dispersion =1.5nm/mm

Figure 2-10 The efficiency curves for the 3 gratings used in the spectrometer (data taken from the Andor website)

Grating 3 gave the highest and most constant efficiency over the wavelength range of interest (380 – 620 nm) and also has the greatest dispersion and therefore can resolve smaller spectral features. However it was found that grating 1 was best for the tissue samples because it covered the entire spectral range of interest in a single spectrum. For the larger dispersion gratings the wavelength range is less and therefore the spectrum must be built up from a number of small spectra pasted together. This involves the sample being exposed to the laser excitation beam for a longer time period and therefore increased effects of photo-damage and bleaching. The effect of photo-bleaching was found to distort the spectra taken with gratings 2 and 3, resulting in jumps in intensity at the points where 2 different spectra were pasted together as shown in figure 2-11. The loss of spectral resolution as a result of choosing grating 1 will not affect the TPF data reported in this thesis as typical TPF spectra show very broad spectral features which are much greater in size than the resolution limit of grating1.

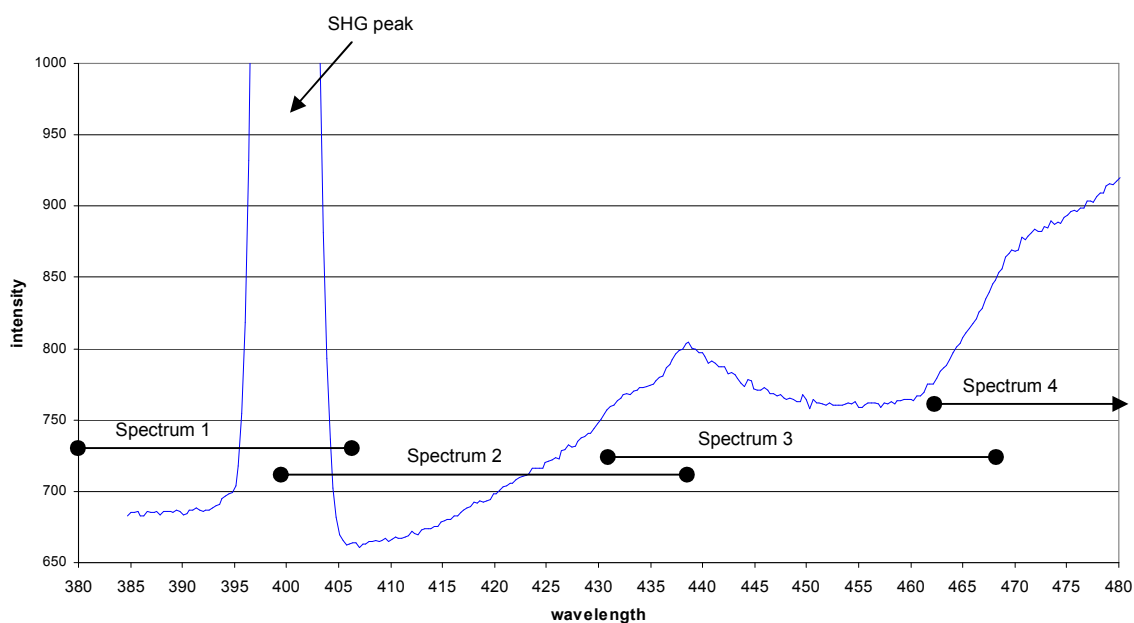


**Figure 2-11 A composite spectrum taken of cartilage using grating 3  
Jumps in the gradient occur where spectra were pasted together.**

As seen from figure 2-10 the efficiency of the spectrometer grating 1 varies significantly over the wavelength range of interest. Therefore to correct for this we generated a correction file by measuring the spectra of standard fluorophores. The standard fluorophores used in this calibration were harmine (in 0.1N H<sub>2</sub>SO<sub>4</sub>), harmane (in 0.1N H<sub>2</sub>SO<sub>4</sub>), quinine sulphate (in 0.1N H<sub>2</sub>SO<sub>4</sub> and in 1N H<sub>2</sub>SO<sub>4</sub>) and fluorescein (in 0.1N NaOH), the standard spectra of these fluorophores are published (Lakowvic<sup>49</sup>) and covered

the wavelength range of 350-650nm. The fluorescent spectra of these fluorophores were taken using both two-photon excitation at 730nm and single photon excitation at 350nm (light source for single photon excitation is a mercury lamp directed through a monochromator (Oriel Cornerstone 130 1/8m monochromator)). For these fluorophores the two-photon and single photon emission spectra were found to be identical and this finding has been previously reported in the literature for fluorescein<sup>48</sup> and quinine sulphate<sup>107</sup>. The measured fluorescent spectra taken with grating 1 and standard fluorescent spectra of the fluorophores are shown in figure 2-12. The position of the peaks for harmine and quinine sulphate have been red-shifted in our measurements with respect to the standard spectra and this is due to the decreasing efficiency of grating 1 at shorter wavelengths.

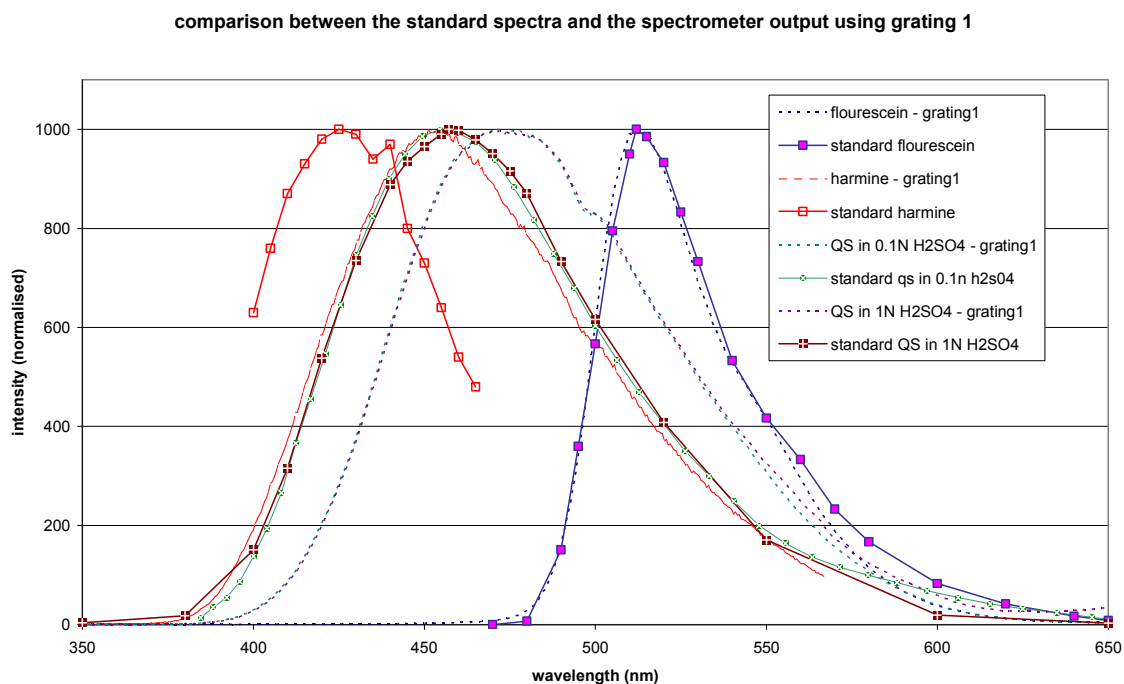


**Figure 2-12 standard and measured spectra of 4 fluorophores used for calibration.**

The correction files were created by dividing the standard spectrum by the measured spectrum for the fluorophores. The results of which are shown in figure 2-13. These have been corrected for the background signal by subtracting the measured counts for the same exposure time when the spectrometer shutter is closed. For correcting the spectra reported in chapter 3 the correction file for quinine sulphate in 0.1N H<sub>2</sub>SO<sub>4</sub> is used. The gradient of this curve was very similar to the gradient for the fluorescein and harmine correction curves over the wavelength range covered by these fluorophores, and also similar to quinine

sulphate in 1N H<sub>2</sub>SO<sub>4</sub> over the wavelength range of 400-550nm. The correction file for quinine sulphate in 1N H<sub>2</sub>SO<sub>4</sub> was found to be inaccurate outside this range due to very low count rates. Multiplying spectra by this factor should correct for any wavelength dependence in the both the spectrometer and the microscope optics. In chapter 3 we report spectra over the wavelength range of 380-620nm as outside this range the signal to noise ratio becomes too high to give a reliable correction.

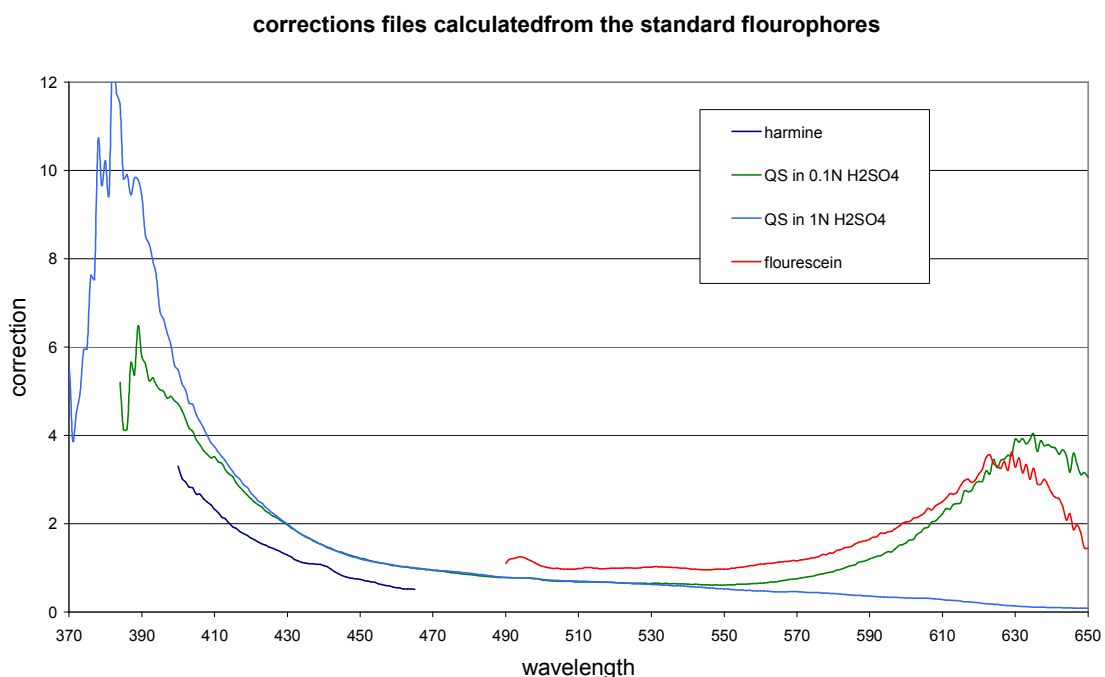


**Figure 2-13 The correction factor for grating 1 calculated from the standard spectra.**

A linear off-set of 8nm towards the blue end of the spectrum was observed for grating 1 when the output of a calibrated monochromator (Oriel Cornerstone 130 1/8m monochromator) was entered into the system. Therefore all the spectra were corrected for this offset.

The measured spectra were also affected by the width of the slit through which the fluorescence entered the spectrometer. Larger slit widths allowed more counts but resulted in broadening of spectral features. For our experiments we found that a slit width of 500 $\mu$ m allowed sufficient counts without causing noticeable broadening of the spectral features.

## **2.5 Sample source and Preparation**

### **2.5.1 Articular Cartilage**

The cartilage samples imaged in this study have been taken from the metacarpophalangeal (fetlock) joint of horses. The forelimbs were obtained from Potter's equine abattoir (Taunton, Somerset) and the age of the horse was obtained from an assessment of the horses teeth by experienced staff. The cartilage was taken from the distal end of the third metacarpal bone.

The metacarpophalangeal joint was chosen as it is a site of frequent lesions and a large proportion of the samples obtained from the abattoir exhibited some kind of degenerate lesion. This allowed both samples of healthy and diseased tissue to be compared. The lesions in equine cartilage are thought to be very similar in aetiology and structure to those seen in human tissue<sup>108</sup>. The high susceptibility of the joint to lesions can be related to the relatively small surface area of the joint bearing the entire weight and impact of the horse and rider during galloping, and also due to the large motion range of the joint<sup>109</sup>.

The location of the cartilage sample within the joint is shown in figure 2-14. There are two notable features in the articular surface, the prominent sagittal ridge running from the front to the back of the joint surface and the cortical ridge which marks the boundary between the areas which articulate with the proximal phalanx and the sesamoid bones. In the dorsal region the joint articulates with the proximal phalanx and in the palma region the joint articulates with the sesamoid bones. During motion the impact is taken on the dorsal region and then the weight is transferred from the proximal phalanx to the sesamoid bones. The radius of curvature is greater in the dorsal region than in the palma region and this is the origin of the cortical ridge. There is also a change in the thickness of the cartilage across the ridge with the cartilage being thicker on the dorsal side of the ridge. These features are summarised in figure 2-15. Samples which had been stored frozen showed no differences in the SHG and TPF images compared to fresh samples so therefore both fresh and frozen samples could be used for these imaging modalities. For the CARS imaging only fresh samples were used as freezing may result in a disruption of the structure of the cell. The

fresh samples used for CARS imaging were kept chilled at 4°C prior to imaging and used within 24hrs of harvesting.

Three different sample preparations were used in this research. The first two preparations were en-face cartilage (imaging plane parallel to articular surface) samples used for imaging the superficial zone of the articular cartilage. When imaging using microscope 1 cartilage plugs were used. Here the cartilage was imaged still attached to the bone, and was immersed in physiological saline throughout the imaging. This sample preparation involves minimal disturbance to the cartilage structure and allows a similar view to that which a future in vivo development of the technique may provide. The sample plugs proved to be impractical for imaging on microscope 2, because it was difficult to position them and keep them immersed in the saline solution whilst imaging on the inverted microscope stage. Also, with the bone still attached they were too thick to allow SHG and CARS imaging in the forwards direction. Therefore for this microscope cartilage slices were used instead. These were prepared by removing the upper-layers of the cartilage with a scalpel blade running parallel with the articular surface. These slices contained all the zones of the cartilage except for the zone of calcified cartilage. They were translucent and therefore thin enough to allow SHG and CARS imaging in the forwards direction. When imaging these were placed between a cover-slip and a glass slide and again kept moist with physiological saline.

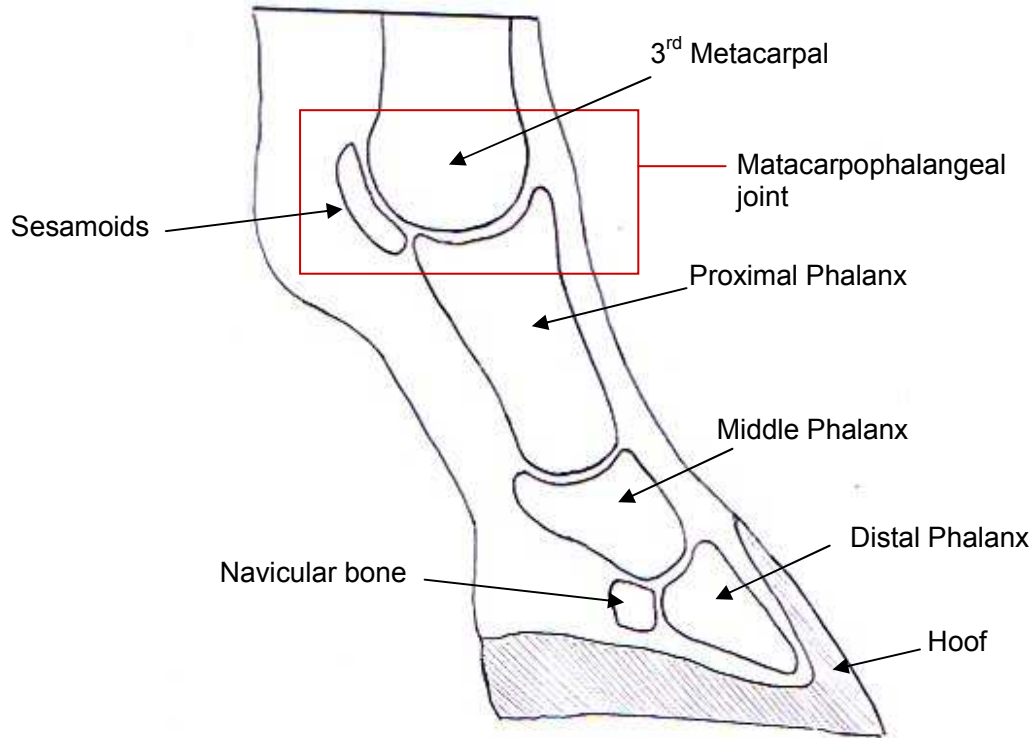


**Figure 2-14** A cross section of the lower end of a equine forelimb  
The metacarpophalangeal joint from which the cartilage samples were taken is marked with a box.

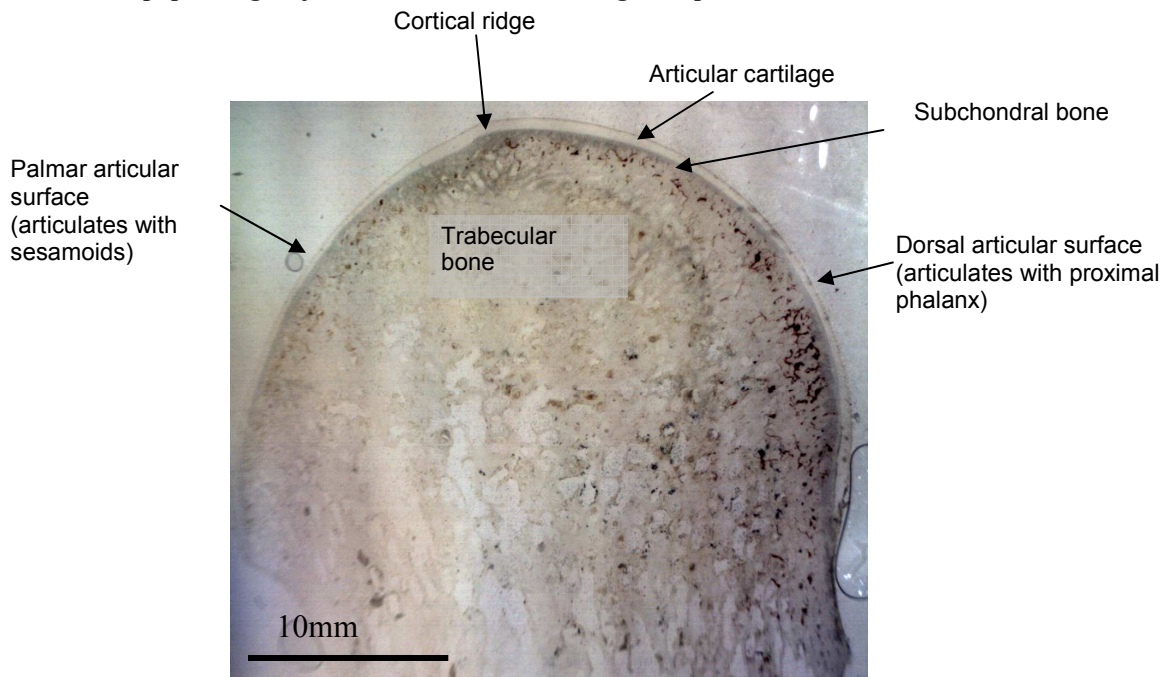


**Figure 2-15** A section of the distal end of the 3<sup>rd</sup> metacarpal showing the cortical ridge.  
This shows that the thickness of the cartilage varies from the palma and dorsal articular surfaces.

The cartilage plugs and slices were used to image the superficial layer of the cartilage but due to the penetration depth of this imaging technique it was not possible to use them to investigate the deeper zones. The maximum depth which we were able to image to was about 150µm with the quality of the images decreasing with depth. For investigating the deeper zones of cartilage transverse sections were produced, 100+ µm thick and consisting of both the cartilage and the underlying bone. These were prepared by cutting sections of the distal end of the 3<sup>rd</sup> metacarpal using the band saw perpendicular to the articular surface, and then lapping to reduce the thickness and produce a smooth surface to the section.

### **2.5.2 Elastic Cartilage**

This is taken from the equine ear. The ear from a 13yr old horse was collected from the abattoir as described above. The ear was skinned using a scalpel to reveal the underlying elastic cartilage structure. Transverse sections were taken using the scalpel to include the inner elastic cartilage and the surrounding perichondrium. Also en-face samples were investigated both with the perichondrium present and after removal of the perichondrium.

### **2.5.3 Intervertebral Disc**

Two different sources of disc (rats tail discs and horse tail discs) have been used in this study. Rats tail discs were thought to be a promising sample to investigate due to their small size. This means that different structures can be observed in a single image and makes the sample preparation easier. The disadvantage of using rats tail discs as a sample source is that there are significant differences both cellular and in chemical composition between the nucleus of rodent tail discs and human discs.<sup>110</sup> The majority of the other work was carried out on horse tail discs. These discs were chosen as they provided a closer model to human discs and we were able to source fresh tails from a local abattoir instead of relying on a frozen stock of rats tails. Two disc preparations were used transverse sections were taken from the discs along with longitudinal sections with a small portion of vertebral bone at each of the disc end-plates

### **2.5.4 Tendon**

Equine flexor tendon from the metacarpalphalangeal joint when the samples were dissected for cartilage harvesting. The samples have been stored frozen and then used for polarization sensitivity experiments. Also rats tail tendon has been used for some SHG experiments as this is the most widely used source of type I collagen for SHG studies.

### **2.5.5 Histology**

After multi-photon imaging many of the samples were investigated using conventional histological techniques. This was important in order to assess whether the samples were histologically normal or contained any pathological lesions. The samples were fixed in 10% formal saline after imaging. 20 $\mu$ m thick histological sections were produced using samples frozen at -20°C in a microtome. The histological slices were then viewed either between crossed polarizers or using bright field microscopy and histological stains.

The cartilage samples were stained for proteoglycans using the following stains Touludine blue (0.13% in distilled water) and Safarin O (0.1% in distilled water).

The elastic cartilage samples were stained with orcein to provide contrast to the elastic fibres. (orcein staining: samples are left 30mins in a solution of 1g orcein in 100ml of 70% ethanol solution with 1ml of 25% HCl. The samples are then removed and washed with both water then ethanol)

## **3 Sources of Multiphoton contrast**

---

### **3.1 Introduction**

All the TPF, SHG and CARS imaging carried out in this thesis has been performed on unstained tissue samples. Therefore it is important to understand and identify the sources of multi-photon contrast in order to be able properly to interpret the images. As discussed in the introduction the source of CARS contrast is derived from intrinsic molecular vibrations within the samples, the SHG sources are from molecules lacking inversion symmetry and the TPF is from fluorophores which have a two-photon excitation spectrum which overlaps with the laser excitation wavelength.

In the tissues investigated in this study collagen was the main source of SHG contrast and the CARS image contrast was primarily derived from the vibrational modes of the CH<sub>2</sub> bonds which are abundant in lipids. In cartilage there is also a CARS signal from the extra-cellular matrix. In section 4.2.1.3 it is discussed whether this signal is resonant signal from the CH<sub>2</sub> bonds or non-resonant background signal. The source of TPF from the samples investigated in this thesis is less clear. A number of two-photon fluorophores which can be excited by the wavelength ranges used in this thesis have been identified already and are discussed in the Introduction (see table 1.4). However during much of our imaging we observed fluorescence originating from tissues not thought to contain significant quantities of these known two-photon fluorophores. The extra-cellular matrix in the samples exhibited autofluorescence and therefore in this chapter we present data on samples of extra-cellular matrix components which have been analysed for their multi-photon properties. This includes measuring the power curves and the spectra of the samples. The spectral data will also be useful for optimising the fluorescence imaging as the filters should be chosen to match the peak fluorescence of the endogenous fluorophores. Later in section 3.4 the spectra of intact tissue samples are reported and these are compared to the spectra of the purified samples.

## 3.2 Experimental Procedure

### 3.2.1 Power curves

In order to test whether a sample produces TPF or SHG the intensity of the signal as a function of illumination power needs to be measured. As discussed in the Introduction both these processes have a quadratic dependence on the excitation power. For a two-photon process the gradient of the  $\log(\text{counts})$  vs.  $\log(\text{power})$  graphs should be 2. When measuring the power curves it is important to stick to the energy range where the response of the PMT is linear. At high photon counts the response of a PMT becomes saturated and the recorded counts will be less than the true counts. For the H7360-02 photon counting head used in the home-built microscope this error is approximately 10% for a count rate of  $6 \times 10^6$  counts/s. Another reason for concentrating on lower powers is that at high powers the power spectra of the TPF may deviate from the quadratic power dependence. This has been reported in previous research<sup>111</sup> and may be explained by either quenching effects or excited state absorption. When taking the power curves photo-bleaching needs to be minimised as this may affect the gradient of the curves, for this reason the system is shuttered between the collection of data for each point.

### 3.2.2 Spectra

Emission spectra were taken of all the samples which exhibited TPF or SHG. These were taken using the spectrometer set-up described in section 2.4. The spectra were taken using a 5s integration time, which was found to be long enough to collect sufficient counts from the relatively weak auto-fluorescent signal but short enough to avoid damage to the samples. The spectra were taken using 800nm excitation light unless otherwise stated. This wavelength was chosen as it was used for all the TPF and SHG imaging reported in the later chapters of this thesis. The spectra were taken using 25mW of excitation power at the sample. The spectra of the biological samples were taken using grating 1 (150 l/mm 800nm blaze). The spectra were corrected for the wavelength dependence of the grating efficiency and microscope transmission using the process described in section 2.4 and reported over the wavelength range of 380-650nm which corresponds to the wavelength range of the

correction file. The spectra are the average of 5 measurements taken at different points within the samples.

### **3.3 Sources of TPF in the extra cellular matrix**

The sources of TPF from the extra cellular matrix require further characterisation. Previous studies have identified elastin and keratin as two-photon fluorophores which can be excited by the wavelength ranges used in our experimental technique,<sup>40, 51</sup> but tissue samples where these proteins are not quantitatively major components, such as cartilage, also exhibit TPF and therefore we test all the major components of the extra-cellular matrix in order to distinguish which ones are fluorescent.

#### **3.3.1 Purified Extra Cellular Matrix Proteins**

Both collagen and elastin exhibit auto-fluorescence, with the fluorescence thought to originate primarily from cross-links between the molecules. In this section we report spectra taken from purified samples of elastin and collagen (type I and type II).

The fluorescent spectra of two different sources of purified elastin were also investigated. The first source was a commercial purified elastin powder (from bovine neck ligament, Sigma Aldrich, prepared by a neutral extraction method) and the second sample was elastin purified from bovine nuchal ligament (this sample was kindly prepared by Mrs Ellen Green by the Lansing procedure which involved heating at 95°C in 0.1M NaOH for 45 mins<sup>112</sup>). Neither sources showed any peak corresponding the SHG at 400nm. This in agreement with the literature which does not identify elastin as a source of SHG. The spectra of the two elastin samples are show in figure 3-1, showing two peaks one at 496nm and another from 506-519nm for the Sigma elastin and a peak at 495nm from the Lansing method purified elastin sample. Previous multi-photon spectral data reports a peak in the elastin fluorescence at 495nm (dermal elastin 764nm excitation)<sup>40</sup> and (coronary elastin 800nm excitation)<sup>113</sup> and therefore our peak at 495-6nm is in good agreement with these results. The extra fluorescence observed at longer wavelengths from the Sigma elastin may be a result of different preparation techniques or contamination. The Sigma elastin was in the form of a powder and the other elastin sample resembled intact tissue.

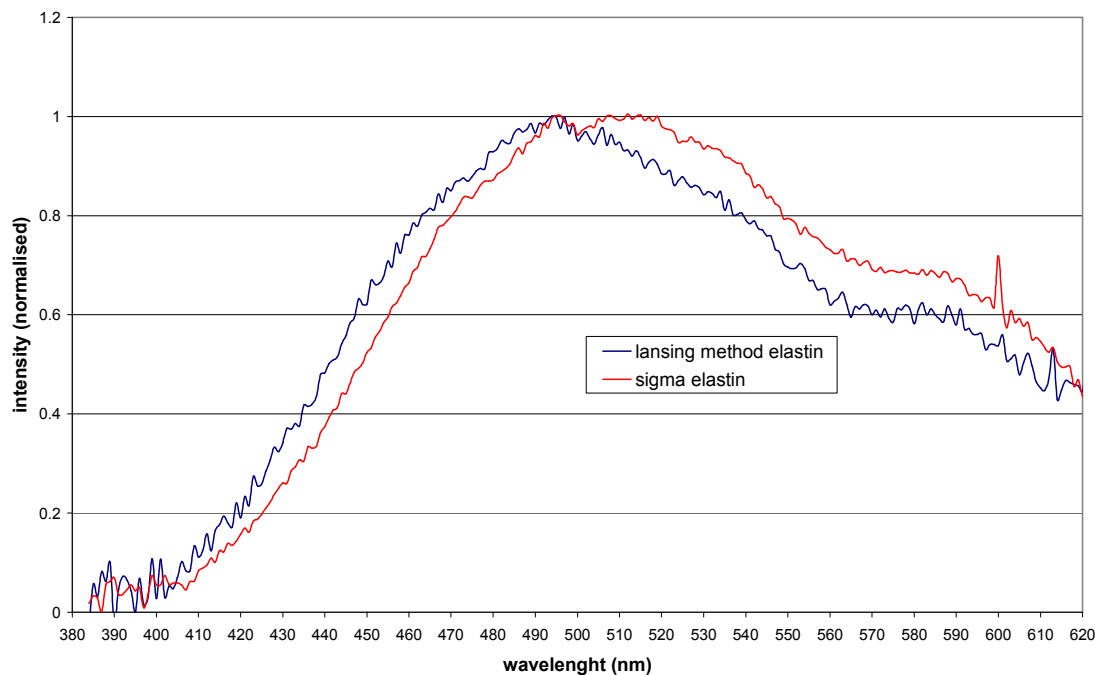


**Figure 3-1 Multiphoton spectra of two purified elastin samples excited at 800nm**

The spectra of type I and type II collagen samples are shown in figure 3-2. Two different sources of type I collagen were used, rats tail tendon collagen and equine flexor tendon. The sample of type II collagen was kindly prepared from equine articular cartilage by Ellen Green (This extraction process involved rinsing in PBS, followed by extraction in a rotator for 24hrs with the enzymes heparinase and hylauronidase, followed by further extraction in a rotator with the enzyme trypsin, followed by rinsing with PBS and enzyme inhibitors (for full recipe see Barnard et al<sup>114</sup>)). All the collagen samples show a strong peak from the SHG at 400nm, the intensity of this peak is approximately 40 times the intensity of the TPF maxima shown on the equine tendon and collagen II spectra and for this reason is truncated to allow the shape of the TPF spectra to be seen. To the side of the SHG peak there is a sharp peak between 410 and 430nm visible for all collagen samples. This peak is unlikely to be fluorescence due to its narrow band width and it was found to move with the SHG peak when the laser was tuned to different wavelengths (data not shown). A very similar peak was observed by Palero et al.<sup>40</sup> Again they thought this peak was unlikely to be fluorescence and suggested that the peak could arise from Raman scattering of the SHG light. However this peak in our spectra is most likely to be an artefact generated by the 400nm SHG light within the spectrometer, as when spectra were taken of rats tail tendon

and starch using both gratings 1 and 3 the 410-430nm peak was only observed when using grating 1 (data not shown).

The rats tail tendon type I collagen sample did not exhibit any TPF when excited at 800nm. However the equine tendon and the type II collagen sample both fluoresced with a peak at 468nm for the type II collagen and a broader peak from 471-494nm for the equine tendon.

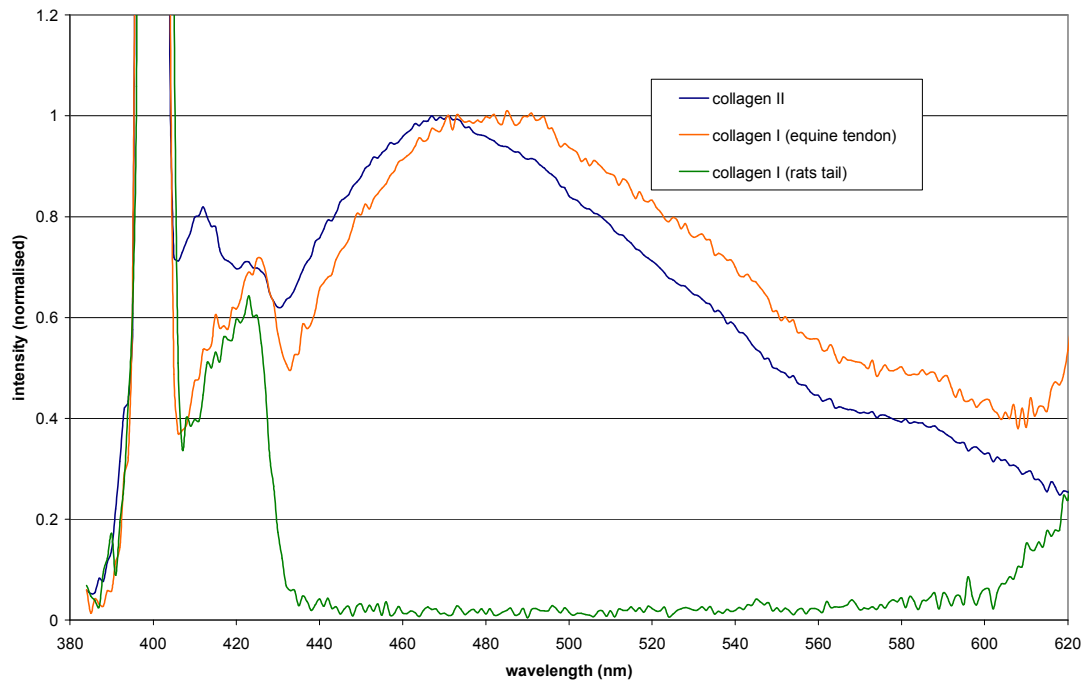


**Figure 3-2 multi-photon spectra taken of collagen samples (collagen II from equine articular cartilage, collagen I from equine flexor tendon and collagen I from rats tail tendon)**

Previous work appears to give contradictory evidence as to whether or not TPF can be excited from collagen using an 800nm laser excitation beam. Zoumi et al<sup>67</sup> were able to detect TPF from a collagen raft (basic polymerized gel of type I collagen from rats tail tendon), with excitation using 730nm and 750nm light, however excitation with 800nm or greater wavelength light gave no TPF signal. The TPF measured from the collagen raft was found to have a peak intensity at 525nm.<sup>41</sup> Palero et al detected very low intensity TPF at about 440nm from Achilles tendon type I collagen excited at 764nm and attributed this to collagenase digestible cross-links<sup>40</sup>. Wu et al were able to detect TPF from a purified collagen sample (type unstated) at wavelengths ranging from 710-810nm albeit with lower signal at the longer wavelengths. They also found that their spectra were red-shifted as the excitation wavelength was red-shifted.<sup>115</sup> A similar effect was found in single photon

studies of collagen fluorescence as a function of wavelength, where the emission peak was found to shift from 415nm with 320nm excitation light to 550nm with 450nm excitation light.<sup>116</sup>

Here the result from rats tail tendon is in agreement with the findings of Zoumi et al<sup>41</sup>. The differences between the spectra from the rats tail tendon and the equine flexor tendon may result from differences in purity. The equine flexor tendon had not been subjected to any purification process and appeared a creamy colour compared to the rats tail tendon which was white in colour. There is no previous literature on TPF from purified type II collagen to compare with the type II collagen spectra. Our collagen spectra have only been taken at 800nm and further work could be carried out to see if the spectra of the 3 samples change with excitation wavelength as suggested in the literature.

Advanced glycation endproduct (AGE) cross-links which increase with the age of the sample are also known to be fluorescent. These occur on all the long lived structural proteins (both collagen and elastin)<sup>117</sup> and increase the stiffness of the tissue.<sup>118</sup> There are a number of different glycation cross-links some of which may have an excitation peak at a long enough wave-length (single photon excitation) to be excited by 800nm light. Two such cross-links are vesperlysine (single photon excitation 370nm emission peak 440nm) and crossline (380nm and 460nm).<sup>116</sup> The peak fluorescence of crossline is close to that of the type II collagen suggesting that this may well be contributing to the fluorescent spectra. If age related cross links are an important component to the collagen spectra then this may explain the differences between the rats tail collagen samples and the collagen samples from equine tendon and cartilage. Rats tails are harvested from young rats less than 6 months which are unlikely to have developed many age related cross links however the equine samples are taken from mature horses.

The emission spectra of AGEs extracted from human articular cartilage by collagenase digestion were taken by Gibson et al using 370nm excitation. There was a peak in the fluorescence at 435nm, but the spectrum also showed a hump at about 500nm. In the study a spectrum of glycated collagen I was also compared to check that the AGE fluorescence was the same. It may be possible that we are exciting similar AGEs with our 800nm, light

but exciting a larger proportion of the fluorophores which fluoresce at 500nm compared to the 435nm fluorescence for which our laser may not have a short enough wavelength to excite efficiently.

### **3.3.2 Elastin and Collagen Crosslinks**

Further to explore the two-photon fluorescence of cross-links we examined four different hydrolysates donated by Professor Allen Bailey, Matrix Biology Research Group in the School of Veterinary Medicine at the University of Bristol. In the hydrolysate the protein has been broken into its constituent amino acids or small polypeptide chains by the hydrolysis of the peptide bonds and partially purified to leave a sample of the protein crosslink.

The samples were as follows:

Sample A: elastin hydrolysate containing large amounts of isodesmosine and desmosine

Sample B: bovine tendon hydrolysate containing aldimine, ketoimine and histidino-hydroxymerodesmosine crosslinks. (this sample contains no mature cross-links)

Sample C and sample D: hydrolysates from human skin C is an unreduced sample and D is a reduced sample these contain hydroxylysl pyridinoline, desmosine, isodesmosine, histidino-hydroxylysinonorleucine and ketoimine with sample D containing a higher proportion of ketoimine than C.

Power curves were measured for all the four crosslinks and these are shown in figure 3-3. The gradients of the graphs are as follows; sample A ( $2.15 \pm 0.07$ ), sample B ( $1.86 \pm 0.07$ ), sample C ( $2.03 \pm 0.08$ ), and sample D ( $2.17 \pm 0.09$ ). All these values are very close to 2 indicating that for each sample there is a quadratic dependence on the laser power and therefore the samples do exhibit TPF. Sample A exhibited a much stronger fluorescent signal than the other 3 samples and therefore to avoid saturation of the PMT the data had to be collected at a lower PMT voltage of 660V compared to 900V used for the other 3 samples.

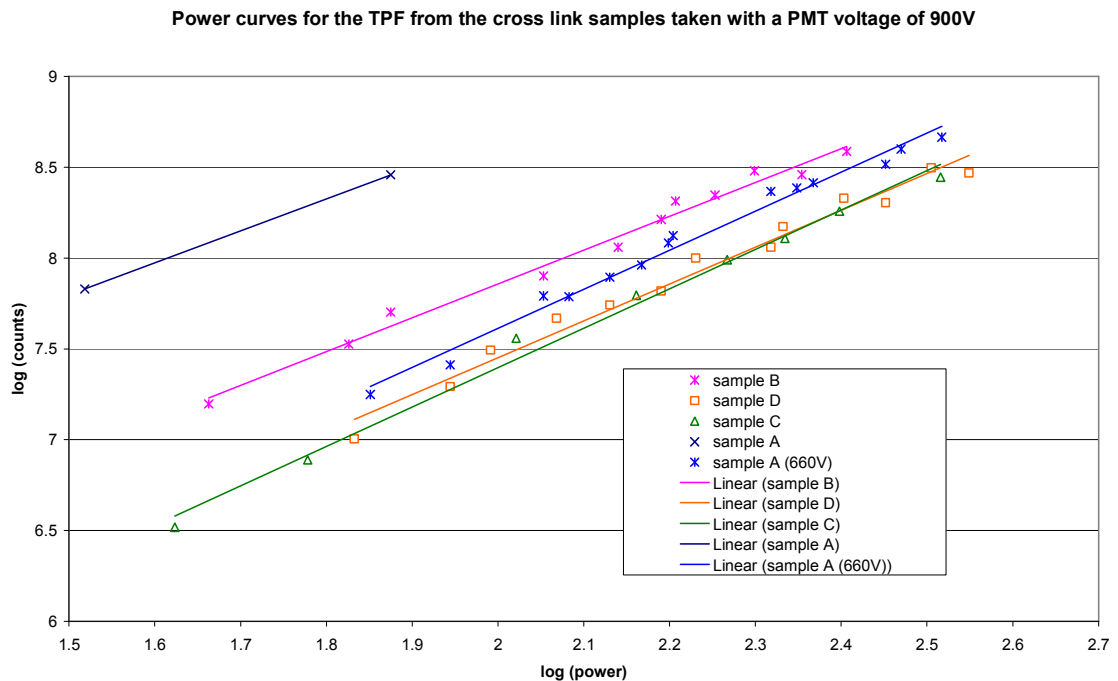


**Figure 3-3 the power curves taken for the 4 extra cellular matrix hydrolysates**

Spectra of the cross link samples are shown in figure 3-4. These spectra show two peaks, one broad peak between 500-540nm and another peak at 583-607nm. I am unsure whether the peak at longer wavelengths is a genuine feature of the spectra or a result of the large correction factor which needed to be applied at long wavelengths. This peak does not appear in the spectra before the correction factor has been applied. The spectra for samples B, C and D were very similar however the spectra for sample A differed and its fluorescence was redder than the other 3 samples. The spectrum for sample B shows a peak at 400nm corresponding to SHG, and this suggests that there may still be some undigested collagen within the sample.

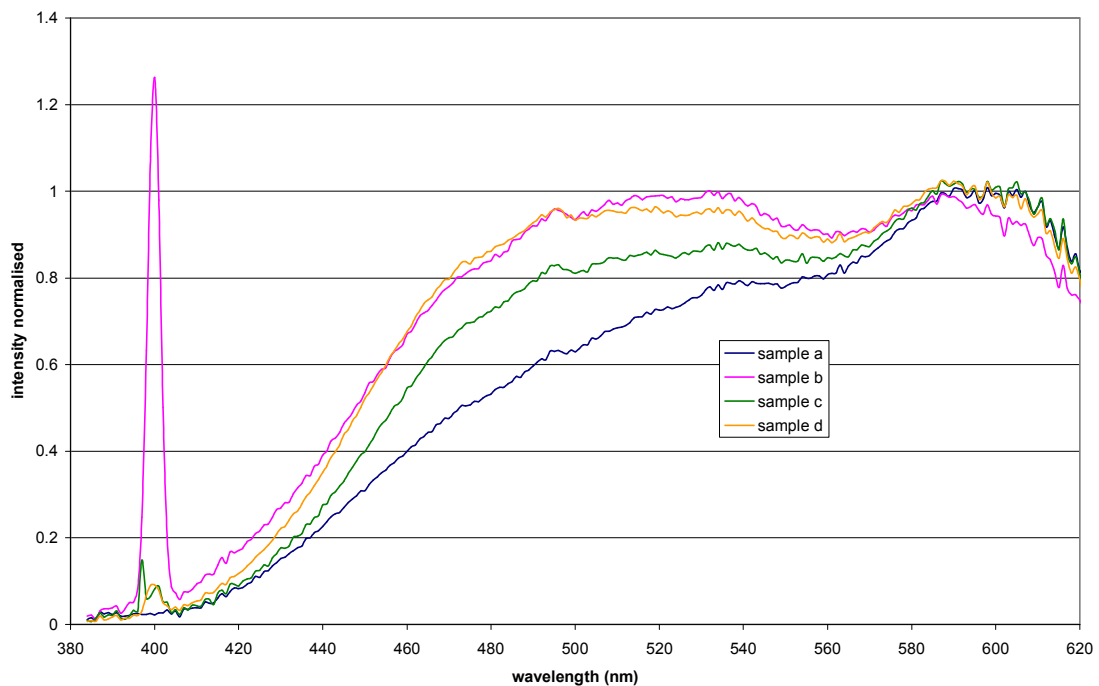


**Figure 3-4 Spectra of the four hydrolysate cross-link samples.**

As sample A is an elastin hydrolysate we have compared the spectra from sample A to the spectra of the purified elastin samples. These are overlaid in figure 3-5. There is little correlation between the two spectra with the elastin fluorescent peaks between 496 and 519nm being absent from the spectra from sample A.

There are two possible explanations for these differences:

1. The pure elastin contains two populations of fluorophores some which emit at around 500nm and other emitting at longer wavelengths. When the sample is hydrolysed then the fluorophores emitting at 500nm are removed leaving a sample with a higher proportion of fluorophores emitting at the red end of the spectrum.
2. The two samples contain the same fluorophores however a change in the chemical environment has shifted the fluorescence to longer wavelengths

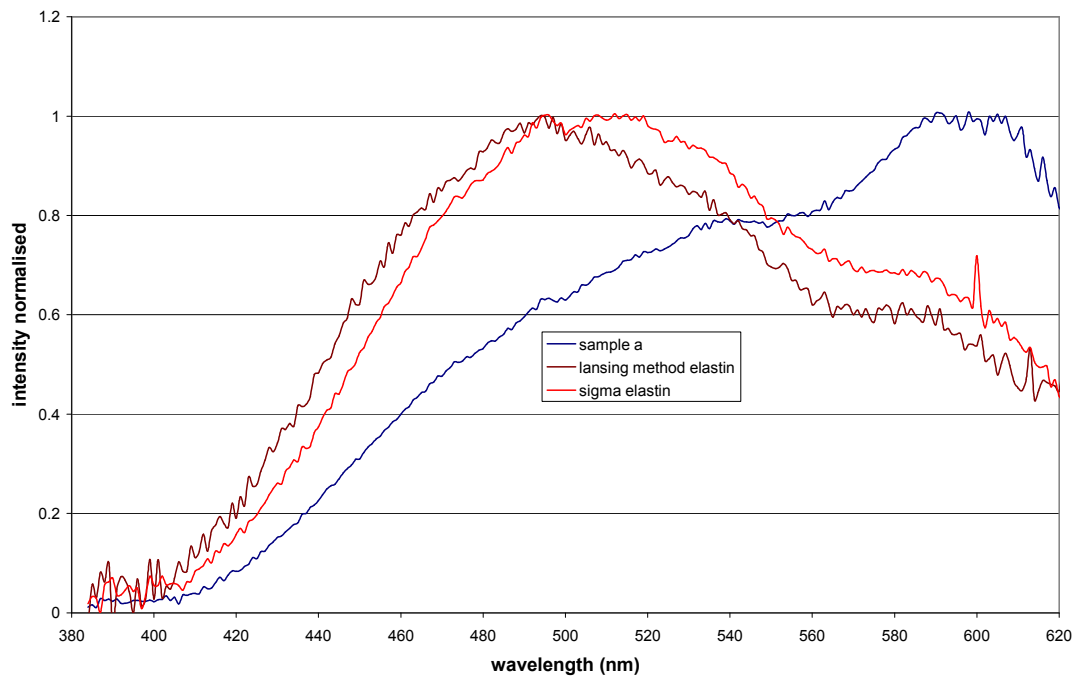


**Figure 3-5 A comparison between spectra from elastin and crosslink sample A (cross link sample A = elastin hydrolysate)**

We also compared the spectra of sample B and the equine tendon spectrum as there is unlikely to be a large difference between the fluorescence from bovine and equine tendon. These spectra are overlaid in figure 3-6. This raises the same questions about the fluorescence as does figure 3-5.

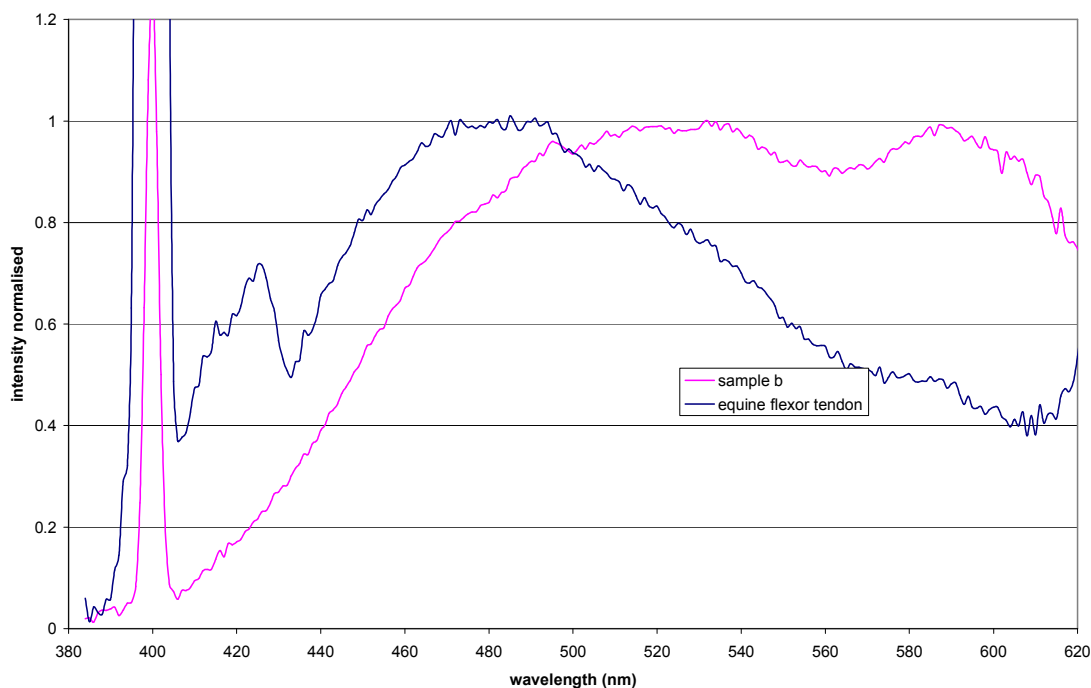


**Figure 3-6 A comparison between equine tendon and cross link sample B spectra. (cross link sample B = bovine tendon hydrolysate)**

Samples C and D contained the cross-link hydroxylysl pyridinoline which has been attributed to the majority of autofluorescence from collagen (along with a very similar cross link lysl pyridinoline) in single photon fluorescence studies. The amount of these cross links has been found to vary between different connective tissues, with rats tail tendon containing no measureable amount of the fluorescent cross-links<sup>119</sup>. However the single photon excitation peak is 325nm with an emission peak at 400nm<sup>116, 119</sup> so it is unlikely that these fluorophores can be excited with the 800nm excitation light used in these experiments.

Desmosine and isodesmosine are two of the main cross-links found in elastin<sup>119</sup> and form a large component of sample A. We were fortunate enough to have purified samples of both these cross-links (kindly prepared by Professor B. Starcher, University of Texas Health Science Centre) which could be tested for TPF. In previous literature there is some disagreement as to which cross-links are the source of fluorescence from elastin, with a paper by Thornhill stating that desmosine and isodesmosine were neither coloured nor fluorescent. However in that study single photon fluorescence was excited using UV light with the peak excitation wavelength being at 350nm and the peak emission at 425nm.<sup>120</sup> In

our two-photon fluorescence experiments we are exciting our fluorescence at a longer wavelength 800nm (equivalent to exciting at >400nm in single photon fluorescence). The desmosine and isodesmosine samples used here were found to be coloured (brownish) and to exhibit two-photon fluorescence. The TPF spectra of desmosine and isodesmosine were measured with 800nm excitation and are shown in figure 3-7. The fluorescence of these two samples is very broad. Like the extra-cellular matrix hydrolysates the spectra contain two peaks, one from 495-535nm and another at 580-595nm. The isodesmosine spectrum is slightly redder than the desmosine spectrum. The spectra of the two cross-links are much broader than the spectra of the pure elastin samples. A possible explanation for this may be environmental effects: the cross link samples used here were in the form of an aqueous gel, however in intact tissue every desmosine or isodesmosine crosslink would be surrounded by four large elastin molecules.<sup>76</sup>

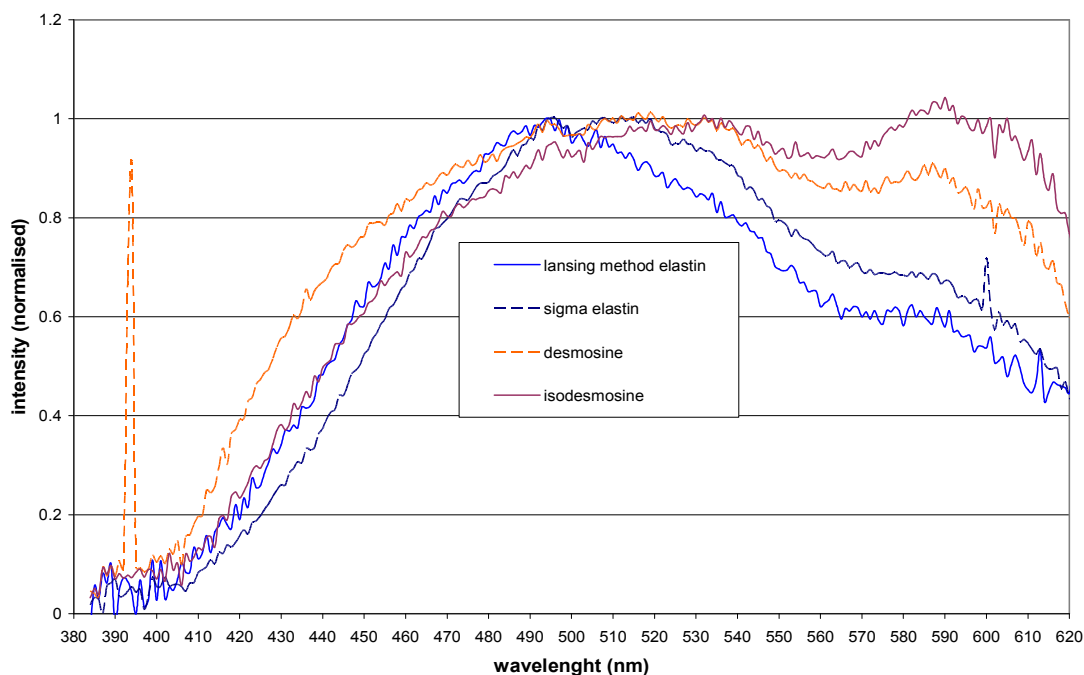


**Figure 3-7 The spectra of desmosine and isodesmosine cross-links the spectra of pure elastin has been added for comparison.**

Single photon studies of elastin fluorescence identified another fluorescent cross-link which is a “trycarboxylic, triaminopyridinium derivative” which has an excitation peak at 320nm and emission peak at 405nm.<sup>116</sup> But again as for hydroxylysyl pyridinoline and lysyl pyridinoline it is unlikely that we would be exciting this fluorophore with 800nm light due

to the very short wavelength single photon excitation peak. Dityrosine is another fluorescent crosslink in elastin<sup>121</sup>, however again its fluorescence is approximately 400nm and is therefore unlikely to be excited in our experiments.<sup>122</sup>

### 3.3.3 Proteoglycans

Proteoglycans make up a large proportion of the extra cellular matrix, especially in articular cartilage and the nucleus of the intervertebral disc. It has been suggested that they may be a possible source of TPF in the articular cartilage by Yeh et al<sup>80</sup>. 5% solutions of pure hyaluronan (cockscomb sigma aldrich), chondroitin sulphate (from bovine trachea Sigma Aldrich) and aggrecan (a gift from Professor Tim Hardingham, Centre for Matrix Biology, Manchester, prepared by guanadinium extraction followed by density gradient ultracentrifugation (Hascall and Sadjera protocol<sup>123</sup>)) were investigated for TPF. These are the most abundant GAGS and proteoglycans within the extra cellular matrix. The concentration of 5% corresponds to the approximate concentration of proteoglycans within articular cartilage. The power curves for these three samples are shown in figure 3-8.

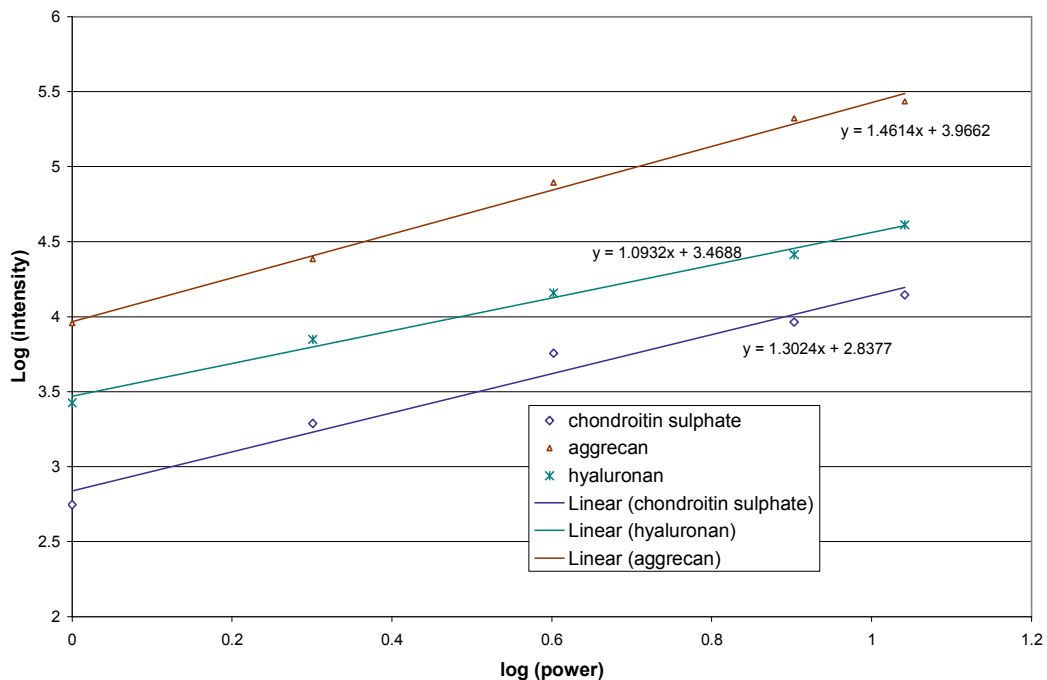


Figure 3-8 The power curves for different extra-cellular matrix proteoglycans.

The gradients for hyaluronan and chondroitin sulphate were close to 1 indicating that the samples were not producing any TPF and any signal detected at the PMT was likely to be back-scattered laser fundamental which had leaked through the blocking filters. The gradient for the aggrecan sample is 1.46 this is slightly larger so it may not be possible to rule out that there may be some TPF from this sample. Although chondroitin sulphate and hyaluronan are the major components of aggrecan the aggrecan molecule also contains core proteins and linkage complexes where the proteoglycan side chains join the hyaluronan molecule. The amount of signal from this sample was still low compared to the TPF from cartilage tissue so from these results it appears unlikely that proteoglycans are an important source of fluorescence within the matrix of cartilage or disc. We attempted to take a spectrum of 10% aggrecan gel however the count rate from this sample was found to be too low to take a spectrum.

### 3.3.4 Hydroxylapatite

The amount of auto-fluorescence was seen to increase from the radial cartilage into the zone of calcified cartilage (see Chapter 4) One major difference between these two regions is the presence of hydroxylapatite in the zone of calcified cartilage. To see whether this was the source hydroxylapatite ( $\text{Ca}_5\text{HO}_{13}\text{P}_3$ ) (reagent grade powder Sigma Aldrich) was tested for TPF. The power curve taken of this sample is shown in figure 3-9, here the gradient is one indicating that the sample does not exhibit TPF or SHG. An alternative explanation of the behaviour of tissue is that the increased TPF may arise from the debris left by apoptic cells at the tidemark and should be explored in future work.

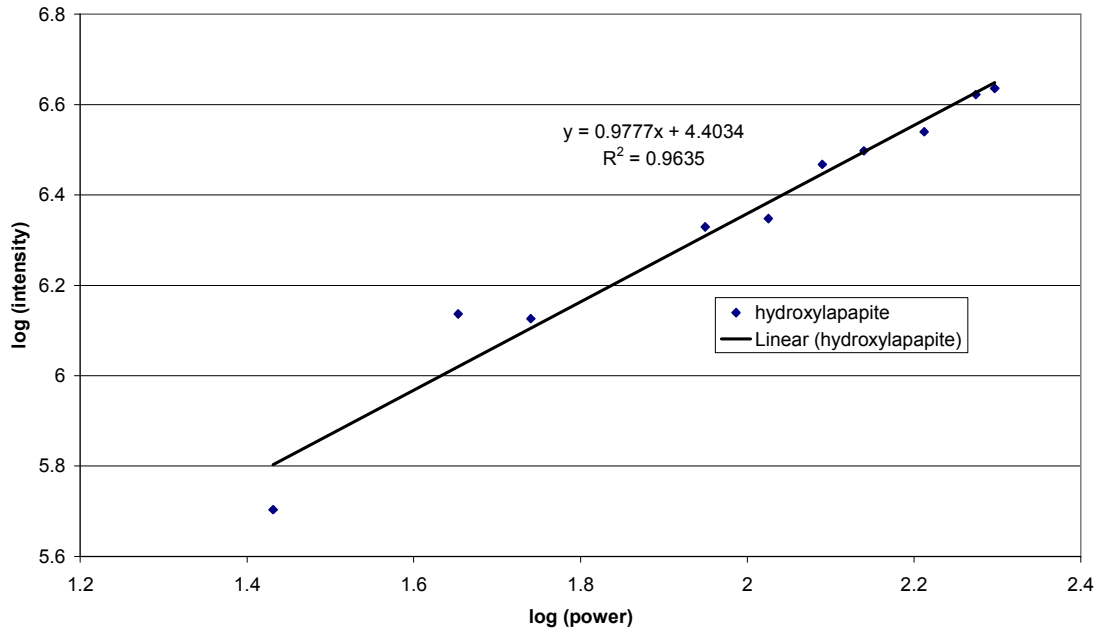
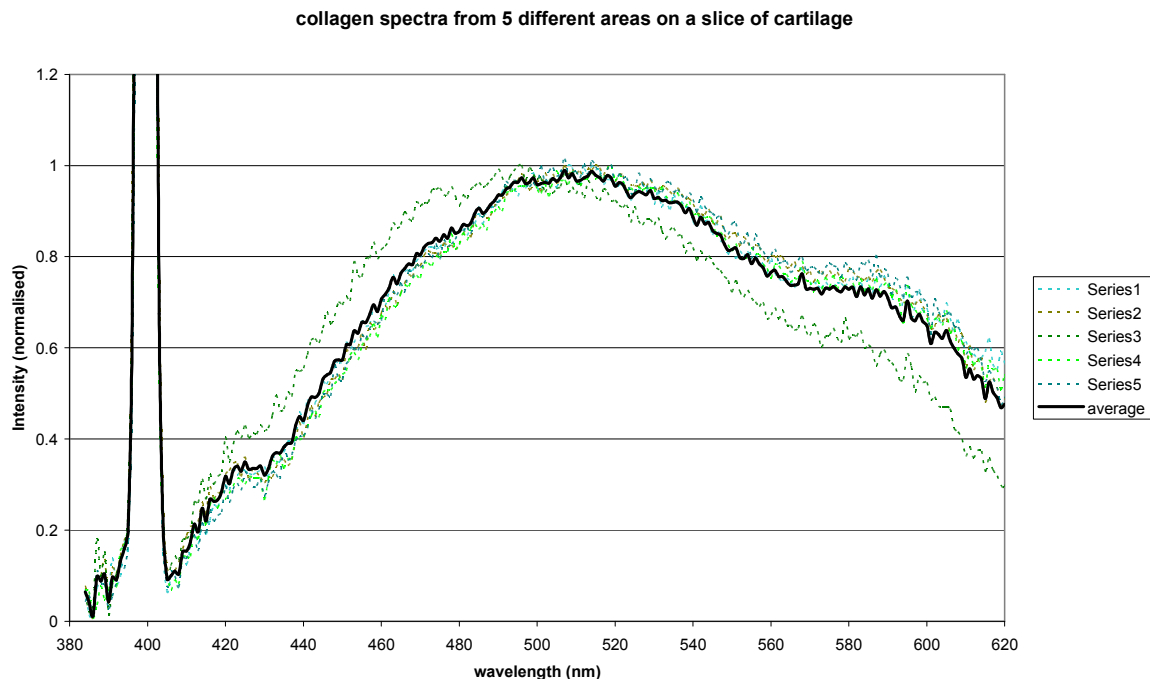


Figure 3-9 The power curve for hydroxylapatite

### **3.4 Intact tissue samples**

The spectra from these samples were taken using unfixed tissue as fixation is known to increase the autofluorescence of the tissue and to change the spectrum due to the increased cross-linking generated by some fixation processes.<sup>124</sup>

When investigating the multi-photon spectra of cartilage both slices of superficial cartilage cut parallel to the articular surface and histological sections were investigated. In tissue samples there was a possibility that the spectra may depend on the area of the sample imaged. Therefore spectra were taken at 5 different areas within the sample. A comparison of the spectra from different areas and the average spectra is shown in figure 3-10. This shows some variation between the areas and one of the areas investigated produced a bluer spectrum than the other four. This shows that it is important to take multiple spectra from a sample and to calculate the average spectrum in order to compare the overall fluorescence in different samples. There are several possible reasons why the spectra may vary with region. The spectra are taken from a relatively large area of tissue (95 x 85 microns) and therefore within this area along with extra cellular matrix components there will also be cells contributing to the fluorescence (the cellular fluorophores will have different spectra), differences in the number of cells between the scan areas may result in changes in the spectrum. Also the area with a different spectrum may have pathological changes, as pathology has been found to affect the fluorescence of cartilage in single photon studies<sup>125, 126</sup>, although the areas investigated in this experiment showed no obvious signs of disease. Further work on a larger number of spectra from different imaging areas would be needed to investigate whether the changes in spectra were associated with characteristics of the images, for example the number of cells.



**Figure 3-10 Spectra of articular cartilage at different areas within a given sample.**

Variations in the spectra were observed between cartilage samples, and in figure 3-11, average spectra from 3 different samples are shown. The age of these cartilage samples was unknown. In the whole group of samples, the peaks were in the range of 495-515nm and were all broad and the spectra had a similar shape to that of elastin. Yeh et al also recorded a multi-photon spectrum of bovine articular cartilage excited at 800nm.<sup>80</sup> In their spectrum the TPF peak was very broad with a maximum between 450-500nm. This is bluer than our peak for TPF from cartilage, although it is difficult to be sure whether this is due to sample variation or differences in experimental set-up, as calibration procedures for their spectrometer were not mentioned in the paper. If some of the fluorescence arises from age related cross-links then the spectra are likely to be dependent on the age of the sample. Investigations into the differences in cartilage auto-fluorescence with age would be an interesting extension of these results.

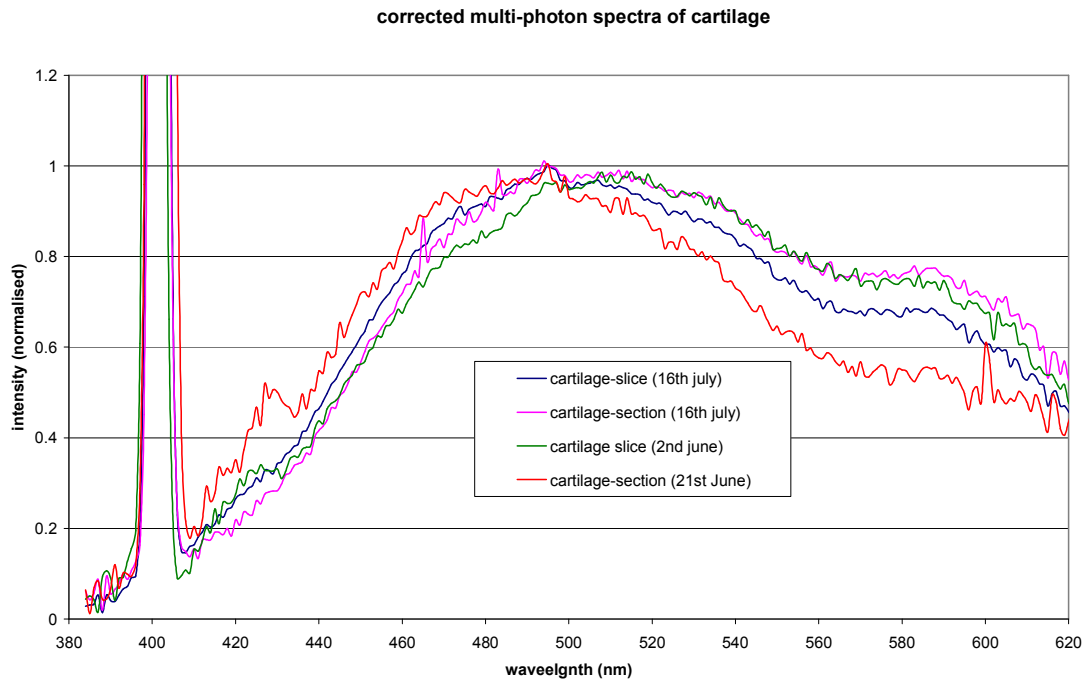


**Figure 3-11** The sample variance in the fluorescent spectra of articular cartilage  
All spectra were taken in the superficial zone.

When investigating cartilage sections the superficial layer the zone of calcified cartilage and the subchondral bone were investigated separately, and these are shown in figure 3-12. From this we see that there is no difference between the spectra taken in the calcified cartilage compared to the spectra from the superficial cartilage, with a broad peak from 471-511nm for both zones. Together with the previous result that the hydroxylapatite is not fluorescent, this suggests that there is not a change in the fluorophores between the different zones. The spectrum from the underlying bone is slightly bluer than that of the cartilage, with a spectral peak from 469nm-495nm.

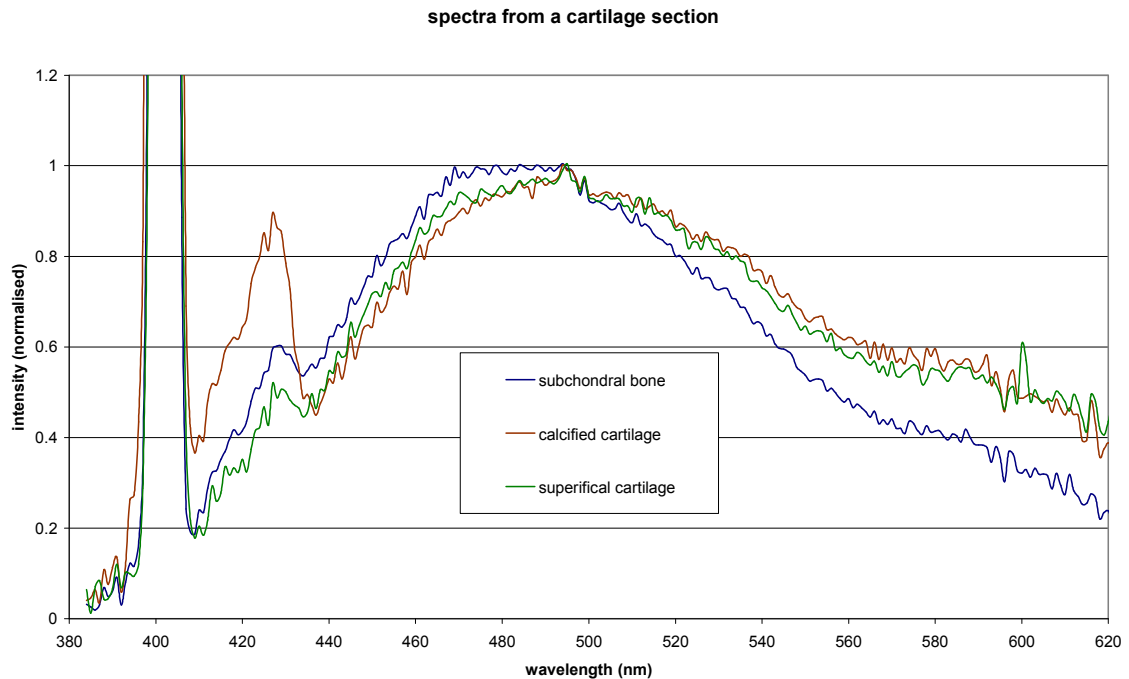


**Figure 3-12** The spectra of different regions of section of articular cartilage.

In order to establish whether the cartilage fluorescence is due mainly to the collagen II, the fluorescence plots were overlaid for the two samples as shown in figure 3-13. The spectra were normalized with respect to the SHG peak, instead of the fluorescence peak, and the relative intensities of the fluorescence were compared. This was reasonable because the two samples should contain the same concentration of collagen II, and the sample of collagen II showed the same degree of order when imaged with SHG as the intact collagen samples, with the lacunae where the cells would have been still clearly visible in the images. The purified collagen II sample maintained the form of the slice of superficial cartilage from which it was derived and therefore the spectrum was compared with cartilage from the superficial zone. The TPF from the collagen II is much less intense than the signal from the cartilage, indicating that a large amount of the fluorophores are removed from the cartilage when a sample of collagen II is prepared. The spectra of the collagen II and the intact articular cartilage are also very different with the fluorescence from the collagen II being at bluer wavelengths, showing that it is fluorophores which fluoresce at longer wavelengths which have been removed from the sample. From this we conclude that there must still be some unidentified fluorophores.

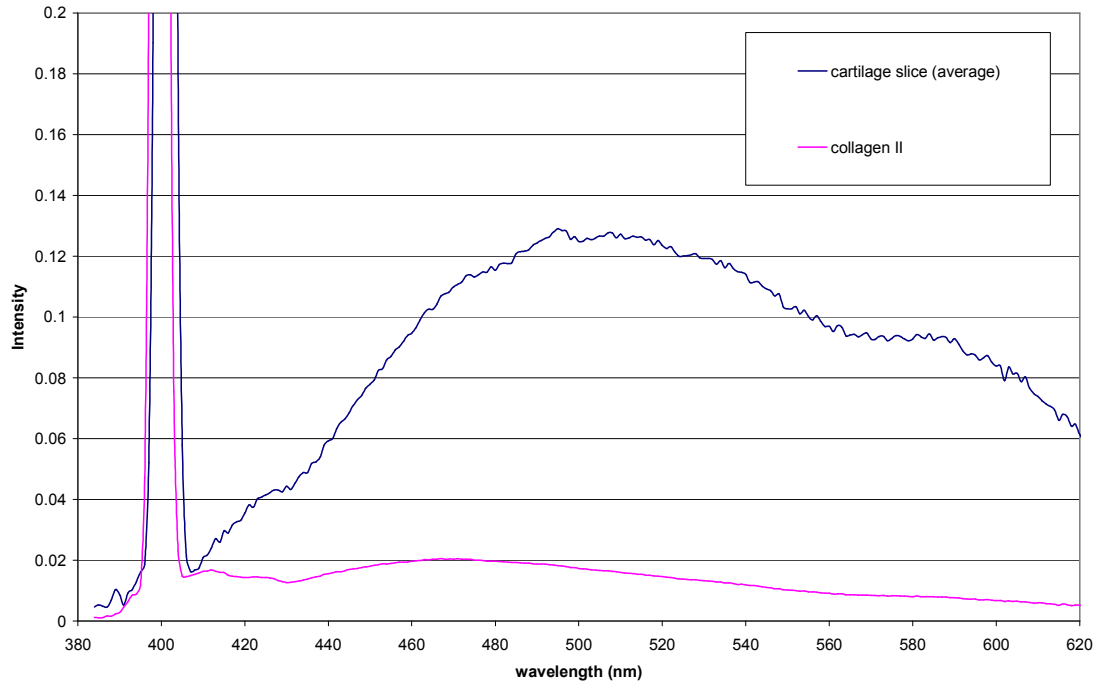
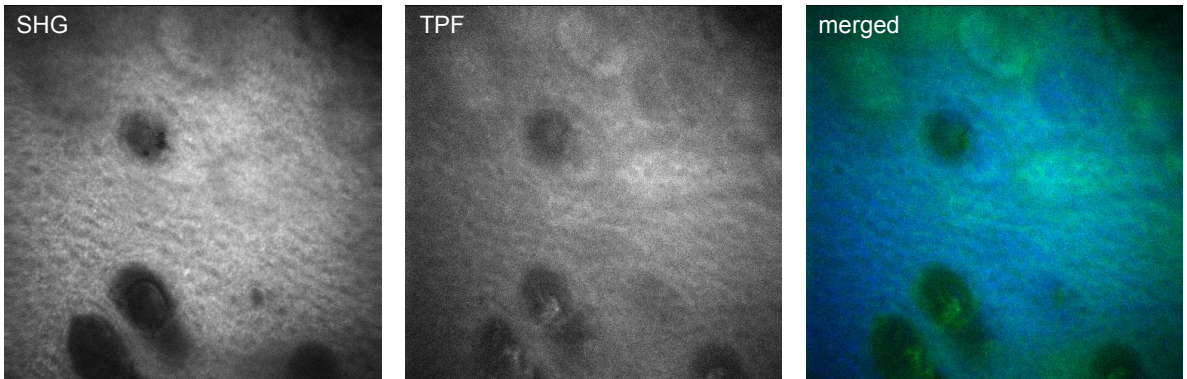


Figure 3-13. A comparison of the spectra of type collagen II and cartilage (normalized to the SHG peak =1)

Purified type II collagen from equine articular cartilage



Intact equine articular cartilage

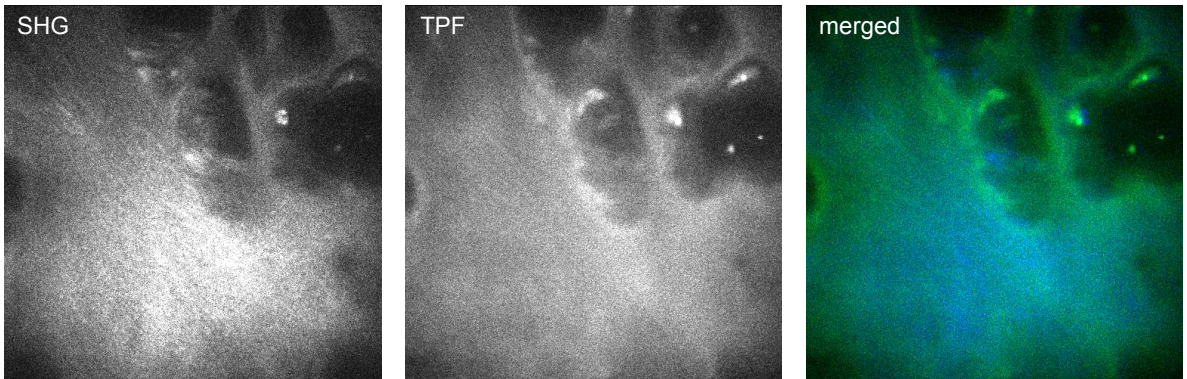
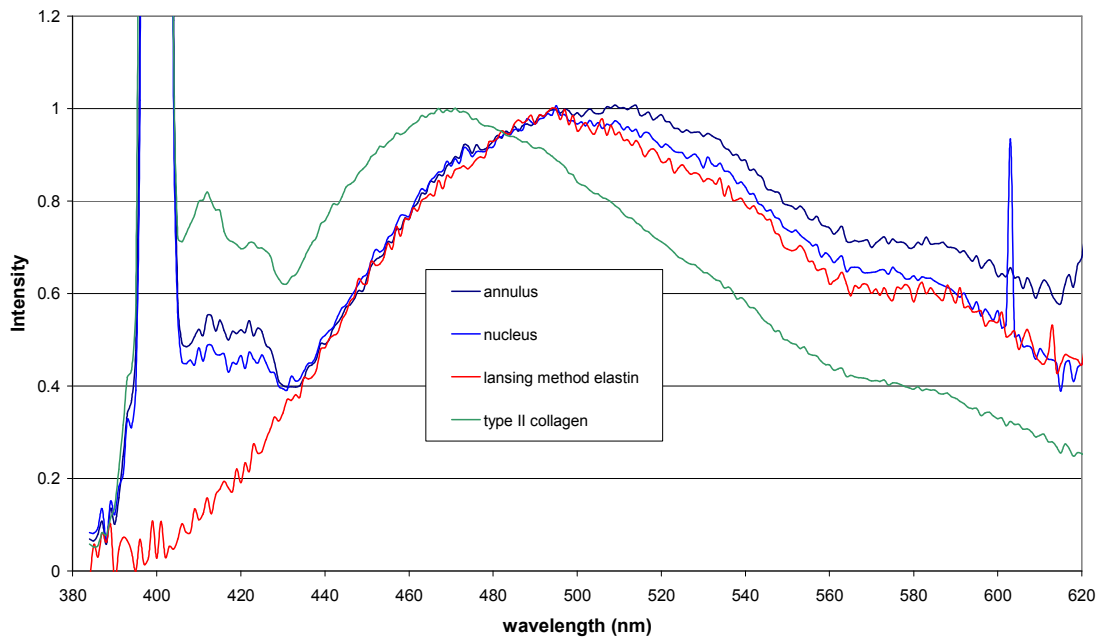


Figure 3-14 Images of the purified type II collagen, compared to intact cartilage.

The spectra have also been measured from the annulus and the nucleus of equine intervertebral disc samples and these are shown in figure 3-15. There was little difference between the spectra of the disc annulus and the disc nucleus, although these two parts of the disc have different compositions with the annulus containing a greater proportion of type I collagen and the nucleus containing less collagen and a larger proportion of proteoglycans. The spectra are compared to the spectra for elastin and collagen II (as collagen is a major component of the disc matrix and elastin is a minor component), and are found to be very close to the elastin spectrum.



**Figure 3-15 Spectra of the intervertebral disc annulus and nucleus**  
The spectra of type II collagen and elastin are added for comparison

### **3.5 Discussion**

The results of this chapter are summarised in table 3.1. We have identified TPF from elastin and the collagen type II and collagen type I from equine flexor tendon. The source of the fluorescence in these proteins is thought to be mainly the cross-links between the proteins. Cross-link samples were found to exhibit TPF and their spectra have been measured, however the spectra for the cross-link samples peak at longer wavelengths than the tissue samples and the whole protein samples. This suggests that there are additional fluorophores within the intact tissue samples and the protein samples which fluoresce at shorter wavelengths. This additional fluorescence may result from advanced glycation end-products, (AGE) these are fluorescent cross-links which form on the collagen molecules as a result of glycation, and the number of these increase with the age.

For future work it would be interesting if possible to obtain samples of the age related cross links and test these for TPF and measure their spectra under 800nm excitation light in order to be able to conclude whether or not these are a major source of the TPF from our samples as we hypothesize.

| Sample                                  |                     | SHG    | TPF | TPF peak             |
|---|---------------------|--------|-----|----------------------|
| <i>Extra-cellular matrix proteins</i>   |                     |        |     |                      |
| Elastin                                 | (ellens)            | ✗      | ✓   | 496nm                |
|   | (sigma)             | ✗      | ✓   | 495nm and 506-519nm  |
| Collagen I                              | Rats tail tendon    | ✓      | ✗   | N/A                  |
|   | Equine tendon       | ✓      | ✓   | 471-494nm            |
| Collagen II                             | Equine cartilage    | ✓      | ✓   | 468nm                |
| <i>Collagen and elastin cross links</i> |                     |        |     |                      |
| Elastin hydrolysate (sample A)          |                     | ✗      | ✓   | 540nm, 583-607nm     |
| Tendon hydrolysate (sample B)           |                     | Maybe* | ✓   | 500-540nm, 583-607nm |
| Skin hydrolysate (samples C and D)      |                     | ✗      | ✓   | 500-540nm, 583-607nm |
| Desmosine                               |                     | Maybe* | ✓   | 495-535nm, 580-595nm |
| Isodesmosine                            |                     | ✗      | ✓   | 495-535nm, 580-595nm |
| <i>Other matrix components</i>          |                     |        |     |                      |
| Proteoglycans                           |                     | ✗      | ✗   | N/A                  |
| Hydroxylapatite                         |                     | ✗      | ✗   | N/A                  |
| <i>In tact tissue samples</i>           |                     |        |     |                      |
| Cartilage                               | Superficial zone    | ✓      | ✓   | 495-515nm            |
|   | Calcified cartilage | ✓      | ✓   | 471-511nm            |
| Subchondral bone                        |                     | ✓      | ✓   | 469-495nm            |
| Disc                                    | nucleus             | ✓      | ✓   | 495-520nm            |
|   | annulus             | ✓      | ✓   | 495-520nm            |

**Table 3.1** A summary of the TPF and SHG from the samples investigated in this chapter

\*The results for tendon hydrolysate and desmosine cross-link showed a small amount of SHG, however it is inconclusive whether this results from impurities in the sample.

In this study we have been able to identify fluorescent components within our samples and eliminate other molecules which are not fluorescent. The spectra of the fluorescent molecules have been taken and compared to those from the intact tissue samples. A useful extension of this work would be to collect quantitative data on the efficiency of the TPF from the various fluorophores, and from this assess the likely contribution that they are

likely to make to the overall tissue fluorescence. In order to do this we would need to know the concentration of all our samples and the approximate concentration of these components within the tissue samples and the purified protein samples. Unfortunately for all the cross-link samples no information was available as to their concentrations. Another factor which would need to be considered is the power at the focal point of the sample as a function of the power measured at a given point on the optical table. This will be dependent on the depth of the focal point within the tissue (which can be controlled) and also on the scattering properties of the sample, with the power decreasing faster with depth in the highly scattering samples. There will be a large variation in the scattering properties of our samples, many of them are highly scattering, these include the intact tissue samples (disc, cartilage and tendon), the hydroxyapatite sample and the protein samples (collagen and elastin) other samples were not highly scattering and formed clear gels these include the proteoglycans and the cross-link samples. In order to minimise the effects due to the differences in scattering between the samples data should be taken as close to the sample surface as possible. Another effect of the scattering in the sample may be that a larger proportion of the TPF generated may be detected in the highly scattering samples as a proportion of the forward generated signal may be scattered back to the epi detector. If these factors have been calibrated for then the intercept on the power curves for the samples will allow a comparison of the relative intensities.

The area from which the spectra were taken was  $95 \times 85 \text{nm}$  and images of these areas showed regional variations in the tissue samples. For example in cartilage, the images contain bright spots within the cells, increased intensity from the pericellular matrix, possibly elastin fibres and then the back-ground fluorescence from the interterritorial matrix (For details see figure 4.1 in chapter 4). An extension of this work would be to develop spectrally resolved multi-photon imaging similar to that carried out by Palero et al on mouse skin.<sup>40</sup> The chemical composition of the pericellular matrix differs from the interterritorial matrix. The collagen is type VI with only small amounts of type II at the interface between the interterritorial matrix.<sup>127, 128</sup> There are also differences in the proteoglycan types and the proportion on glycoproteins.<sup>127</sup> It is therefore possible that there may be different fluorophores in this region and spectrally resolved imaging would help to investigate this. Also if used on samples with osteoarthritis it may be possible to link

changes in spectra with structural changes which are occurring with the disease. This would be an interesting study as changes in the intensity of the fluorescence from cartilage have been associated with pathological structures in a single photon study on the auto-fluorescence of osteoarthritic articular cartilage.<sup>126</sup>

The fluorescence from human articular cartilage has been found to increase with age due to both enzymatic cross-linking and glycation cross-links. These are found to also result in a change in the physical properties of the tissue<sup>129</sup>. Changes in fluorescence intensity have also been linked to disease<sup>125</sup> and therefore it is important to fully characterise the TPF from cartilage and individual fluorophores responsible for this in order to relate TPF changes to potential pathological and age related changes.

When taking the present spectra there was significant variation between the samples and this highlights the need for a larger sample size. Future work could also be carried out to test for correlations between the TPF spectra and TPF intensities and the age of the sample. In single photon studies a positive correlation has been found between the AGE cross-link pentosidine and the age of the sample<sup>130</sup> however this has its fluorescent peak at 385nm and therefore will not be excited in our studies so we need to characterise these changes for the fluorophores emitting at longer wavelengths.

As seen in Chapter 2 the response of our spectrometer set up was not flat over the spectral range of interest with a large decrease in the efficiency of the system at both ends of the spectral range. This meant that at the ends of the spectra a large correction factor had to be applied, which leads to decreased accuracy in these regions and a higher level of noise. If the work in this thesis was to be extended then it would be worthwhile to use a grating which has been optimised for this range. (the current grating was purchased for multiplex CARS imaging and has been optimised for 800nm). This would increase the accuracy and also the intensity of the spectra. This would be essential as the exposure times for each spectra would have to be greatly reduced for spectral imaging. If longer wavelengths needed to be investigated then a different choice of dichroic beam splitter and filter to block the laser fundamental would be needed. Alternatively if the data was collected in the forwards direction the dichroic could be eliminated altogether.

A fluorophore is characterised by both an excitation and an emission spectrum and future work should include a study to measure both of these. This is technically more difficult than taking an emission spectrum. The laser output is tuneable between 720 and 900 nm, allowing a reasonable spectral range to be investigated. However when the laser is tuned to different wavelengths the efficiency of the mode locking varies and therefore the temporal width of the pulses changes. This affects the instantaneous power at the sample and therefore the pulse width must be measured and corrected for. Also when tuning over a large wavelength range the mirrors at the ends of the cavity need to be adjusted and this alters the beam path on the optical table, therefore the alignment of the microscope must be adjusted, and this leads to increased errors. The efficiency of transmission of the laser fundamental through the system as a function of wavelength must be measured and corrected for and this must be distinguished from changes in alignment caused by the laser cavity adjustment. An additional factor when measuring the SHG excitation spectra is that the wavelength of the SHG changes with the laser fundamental and therefore the wavelength dependence of the collection optics must also be minimised and characterised.

Additional knowledge of the effect of the excitation wavelength on the TPF would help in the task of identifying fluorophores. It would also help to investigate changes which may occur in the fluorescent spectra as the excitation wavelength changes. For example the collagen spectrum has been found in previous literature to change with the excitation wavelength.

Knowledge of the excitation spectra of various fluorophores within the tissue may be useful when choosing the excitation wavelength for imaging to give the maximum TPF intensity. For studies where the SHG signal is most important, for example polarization sensitivity experiments, it is useful to know which wavelengths do not correspond to a TPF excitation peak within the sample. If the laser can be tuned to longer wavelengths away from the TPF excitation peaks then the photo-damage to the sample can be minimised whilst carrying out TPF imaging. This is also true for CARS imaging as tuning the pump laser away from the excitation peak for the TPF in the sample then the two-photon enhanced non-resonant background will be reduced.

## 4 Imaging cartilage

---

### 4.1 Introduction

The structure of articular cartilage has been discussed in section 1.6.2. In this section we present SHG and TPF images of articular cartilage and discuss what structures we are able to identify. So far only one previous study has been carried out on multi-photon microscopy of articular cartilage<sup>80</sup> and one on nasal septal cartilage<sup>131</sup>. The previous studies were used as a starting point for developing a more detailed investigation, with the initial step being a comparison between our images and their findings. As multi-photon microscopy is a new technique in this field we also used well established histological techniques for distinguishing between normal and diseased tissue.

Firstly the images taken on healthy articular cartilage are shown and discussed. After this images from lesion sites are presented showing the differences between the normal and diseased states. Imaging of the lesion tissue is carried out in the hope that the technique may contribute to an increased understanding of the aetiology of osteoarthritis and that we may be able to identify changes that could be early markers of the disease. This chapter contains imaging carried out on both microscope 1 and microscope 2. Initially data on both healthy and diseased tissue were taken using the microscope 1. When the microscope 2 became available the imaging of healthy tissue was repeated with CARS imaging combined with the SHG and TPF imaging to provide additional information on the chondrocytes. In this chapter an overview of the different structures in cartilage are discussed. Two areas of special interest, elastin networks and a polarization analysis of the collagen fibre organisation are presented in later chapters.

## 4.2 Healthy Cartilage

Healthy cartilage was defined as tissue from a young animal (2-6yrs), which exhibited no macroscopic signs of osteoarthritis and appeared normal when classical histology was carried out on it after imaging. The characteristics reported here from the young healthy tissue were also found in older joints in the regions which appeared macroscopically normal and were located away from any areas of osteoarthritic damage. In this section we carry out imaging on enface samples in which the articular surface and the superficial zone are imaged followed by imaging on cartilage sections where all the cartilage zones are investigated.

### 4.2.1 Enface cartilage samples

It is important to characterise the features of healthy tissue in the superficial regions as this is one of the areas where the first signs of osteoarthritis may occur, it is believed though excessive stresses or loading.

#### 4.2.1.1 TPF images

In figure 4-1 a TPF image of the articular cartilage is shown. This image shows clearly the fluorescence from the extracellular matrix (which is discussed in chapter 3) and an increase in fluorescence surrounding the cells corresponding to the pericellular matrix. The chondrocytes show less fluorescence than the matrix except for small spots within them which exhibit intense fluorescence which is most likely to be due to the fluorophores NAD(P)H and flavoprotein which are associated with cell metabolism. The cells appear to be approximately 15 $\mu$ m in diameter. The image shows a few fluorescent fibres within the matrix, these have been identified as elastin fibres and are discussed in more detail in chapter 5. The appearance of the image is in good agreement with the TPF images of cartilage reported by Yeh et al<sup>80</sup>. Also the increased fluorescence from the pericellular matrix is also reported in a single photon study of the auto-fluorescence of articular cartilage by Gibson et al.<sup>126</sup>

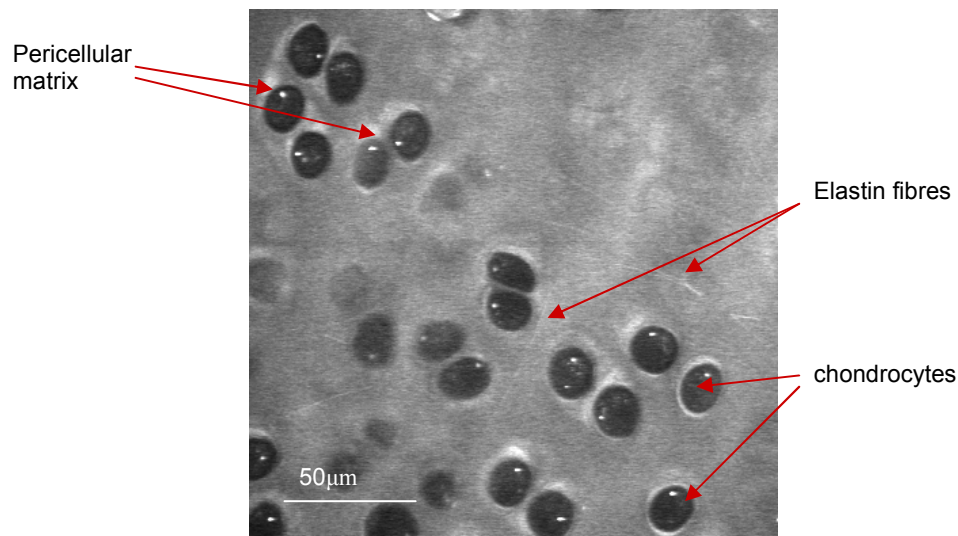


**Figure 4-1** A TPF image of articular cartilage.  
The image is taken from the superficial zone at a depth of 13 μm from the articular surface

#### 4.2.1.2 SHG images

An SHG image of the same area of cartilage is shown in figure 4-2. The SHG image shows collagen matrix and the locations of the cells appear as dark voids where there is no collagen. These images are also in agreement with the SHG images of cartilage reported by Yeh et al.<sup>80</sup> The extra-cellular matrix in the images appears textured however the collagen fibres are too fine for individual fibres to be resolved. However the predominant organisation of the collagen fibres can be found by utilising the fact that the SHG is sensitive to the polarization of the laser excitation beam and this feature of SHG imaging is discussed further in chapter 6.

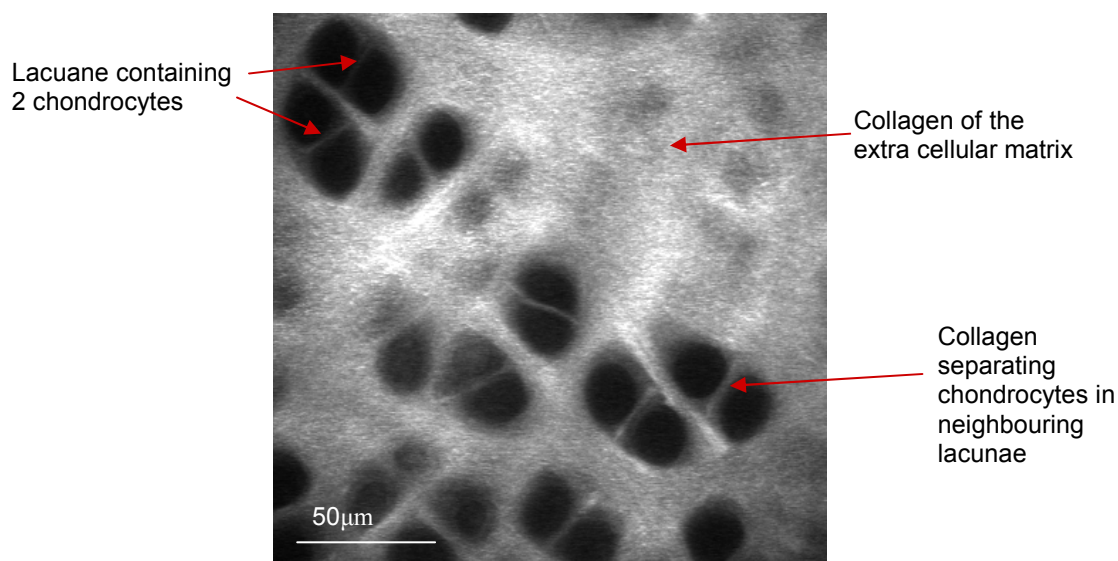


**Figure 4-2 An SHG image of cartilage.**  
 This image was taken from the same area of articular cartilage as in figure 0-1

#### 4.2.1.3 CARS images

The CARS imaging in this chapter has been taken at  $(\omega_p - \omega_s) = 2845 \text{ cm}^{-1}$  which corresponds to the  $\text{CH}_2$  symmetric stretching bond vibration. In the images both the cells and the matrix are visible with the cells having a slightly higher intensity than the background. Bright spots are seen within the cells and these are thought to correspond to vesicles or lipid droplets. The extra-cellular matrix is not thought to contain significant amounts of lipids and therefore it is important to identify whether the CARS signal from the matrix arises from resonances in  $\text{CH}_2$  bonds in other molecules (proteoglycans or proteins) or is non-resonant background.

In order to be able to distinguish between the resonant signal from the  $\text{CH}_2$  bonds and the non-resonant back-ground images need to be taken at different values of  $(\omega_p - \omega_s)$ . Forwards CARS images have been taken of the same area of cartilage at  $(\omega_p - \omega_s) = 2845 \text{ cm}^{-1}$ ,  $(\omega_p - \omega_s) = 2972 \text{ cm}^{-1}$  and  $(\omega_p - \omega_s) = 3150 \text{ cm}^{-1}$ . The first value shows the resonant image combined with any non-resonant background and is shown in figure 4-3a. The second value corresponds to the wavelength at which there is negative contrast between the  $\text{CH}_2$  bond vibrations and the non-resonant background<sup>7</sup> and this is shown in figure 4-3b. In this image there are back spots of negative contrast, co-localised with the bright spots

within the resonant image. This confirms that these spots within the cells are due to CH<sub>2</sub> bond resonances and supports the conclusion that these are either lipid droplets or vesicles. The extra-cellular matrix still shows up brightly in this image showing that there is a non-resonant signal from this region. In figure 4-3c,  $(\omega_p - \omega_s)$  is tuned far away from and bond resonances and the image is entirely due to the non-resonant background. In this image the lipid droplets/vesicles are no-longer visible however there is still signal from the extra-cellular matrix. Image c was subtracted from image d to provide an image which only contained resonant CARS signal and this is shown in d. In this image only the lipid droplets within the cells appear with high contrast indicating that the rest of the image is non-resonant CARS signal. The images in figure 4-3 have been corrected for any changes in power caused by tuning the OPO to different resonances. Both the OPO signal and idler power were recorded for each image and the value of  $I_p^2 I_s$  was calculated for the images and then the brightness of each image was adjusted accordingly. (All the images were taken using the same PMT settings)

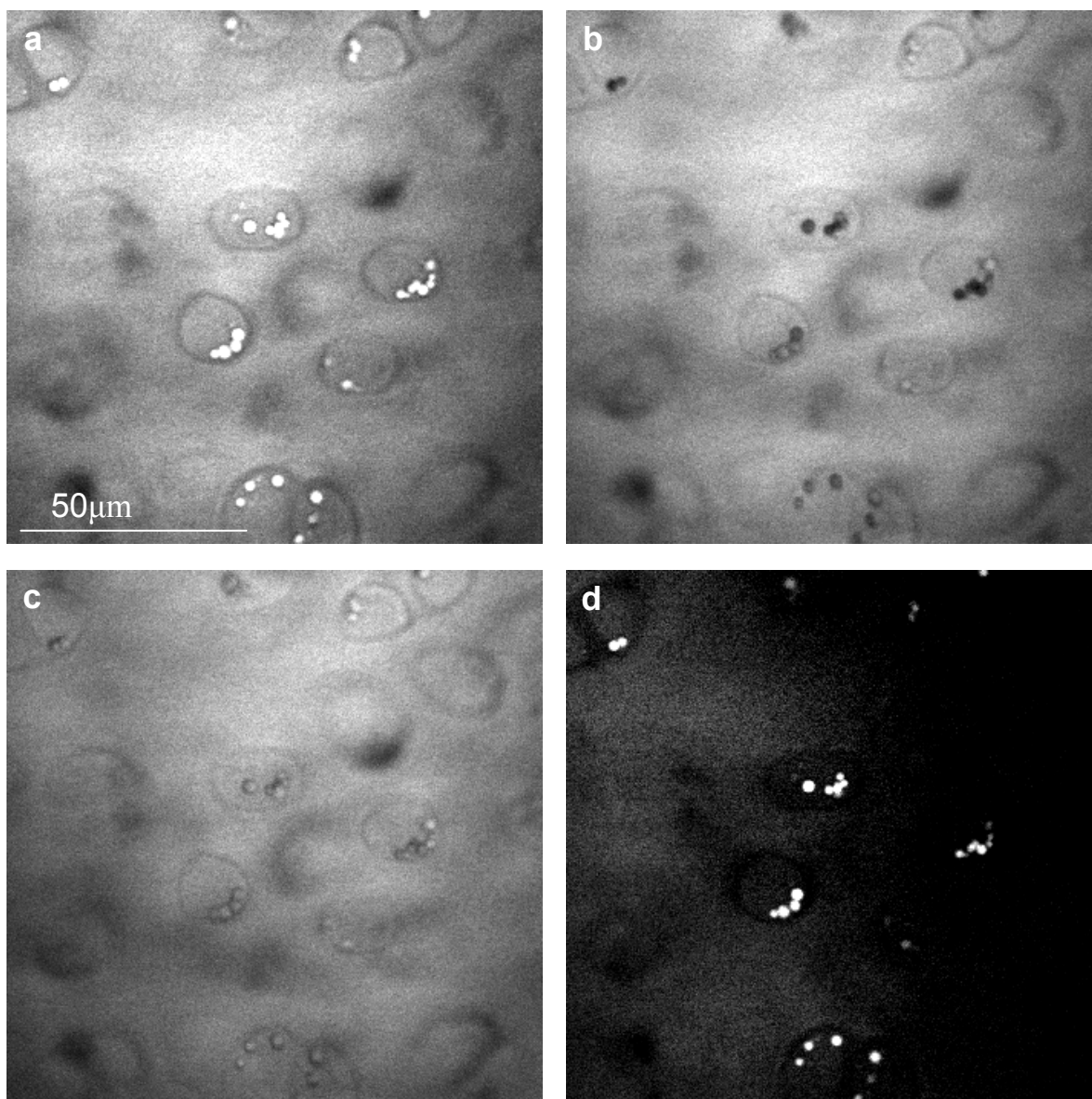


**Figure 4-3** Forwards CARS images taken of chondrocytes in the superficial zone. (a) shows the image taken with  $(\omega_p - \omega_s)$  tuned to  $2845\text{ cm}^{-1}$  which represents the  $\text{CH}_2$  symmetric stretching bond vibration, (b) show the image of the same area with  $(\omega_p - \omega_s)$  tuned to  $2972\text{ cm}^{-1}$  which corresponds to destructive interference from the CARS signal from the C-H bond and (c) shows the image taken when  $(\omega_p - \omega_s)$  is tuned to  $3150\text{ cm}^{-1}$  which corresponds to no Raman peaks and therefore shows only the non-resonant back-ground. (d) is the result of subtraction image c from image a and therefore now only shows resonant CARS signal.

From these results we see that the CARS signal from the extra-cellular matrix is mostly non-resonant background. The extra cellular matrix exhibits TPF when excited at 800nm and therefore it may be useful to investigate whether the 924nm pump laser used for CARS imaging is close enough to the TPF excitation maxima to allow two-photon enhanced non-resonant CARS. This process has previously been observed for red blood cells<sup>66</sup>. Although

the non-resonant background does not provide chemically specific data it can still provide useful structural information<sup>66</sup> and in the CARS images of cartilage it shows the locations of the chondrocytes and therefore provides a context for the strong resonant signal from the lipid droplets.

Some features like “shadows” of cells outside the focal plane appear in the CARS images which we need to be able to explain and illustrate these features. In the forward CARS images cells that lie above the focal plane are still visible, these cells do not appear in the epi-CARS images (see image set **a** in figure 4-4) this is true for about 10 microns in the z-direction beneath the cell. When lipid droplets occur within the cells there is a high CARS signal in both the epi and the forwards CARS (see image set **c** in figure 4-4). When the focal plane is just above the lipid droplet, a dark spot appears within the forwards CARS image which is not present in the epi CARS (see image set **d** in figure 4-4). When the focal plane is in the matrix above the cells the cells are also still effecting the CARS images in this case both the epi and forwards CARS (although effect is more pronounced in the forwards CARS) (image set **e** in figure 4-4). Also in some of the images the cells appear to be surrounded by a dark ring in both the forwards and epi CARS (see image set **b** in figure 4-4). This is thought also be an effect due to interference as from the relative density of lipids the cell edge would be expected to show up brightly due the lipids in the cell membrane.

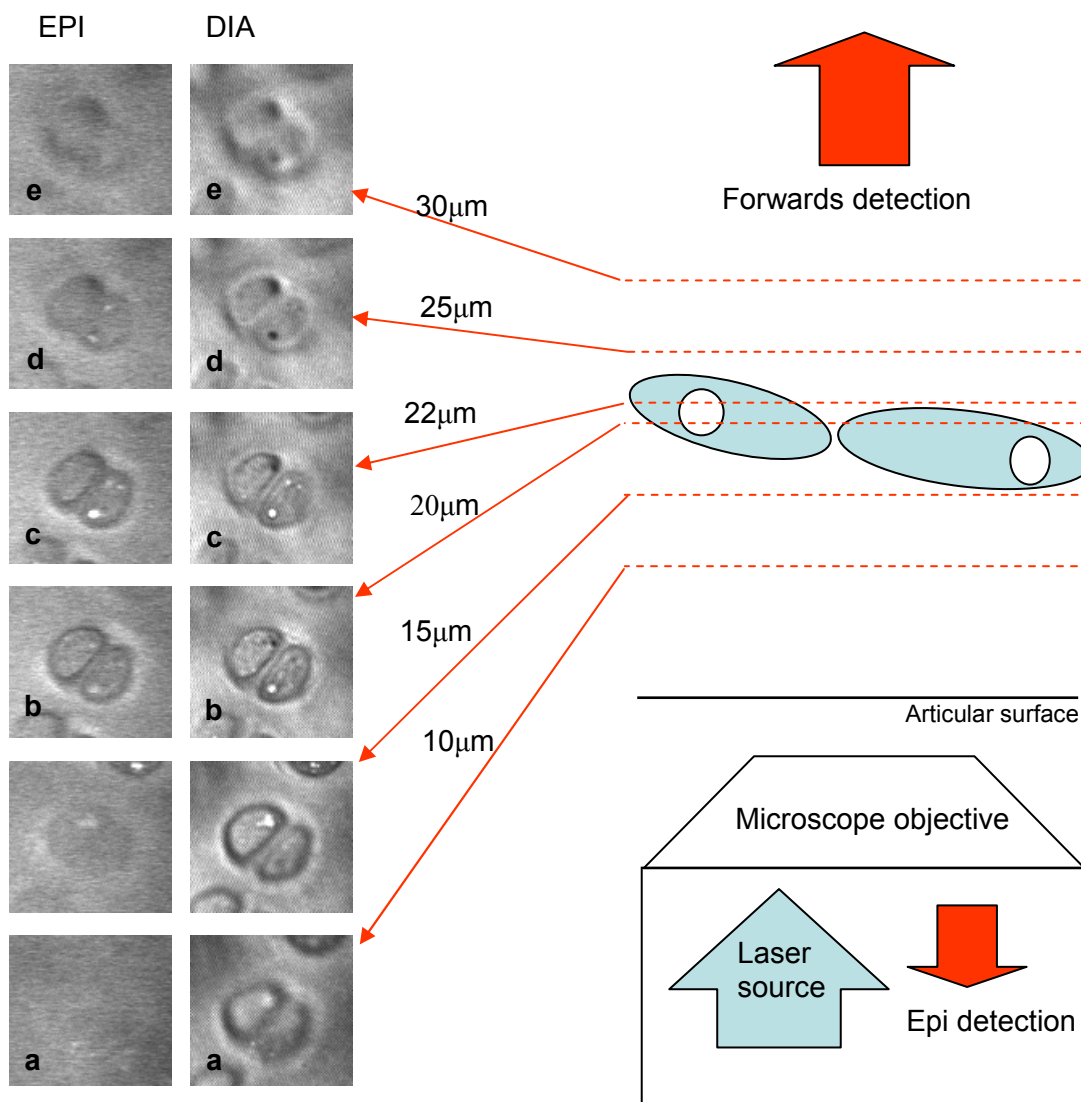


**Figure 4-4 “Shadows” of cells in the CARS images.**  
 The effects of the coherent nature of CARS on the imaging of a pair of cells within the cartilage matrix. Imaging in both the epi and forwards (dia) directions. CARS wavelengths tuned to the  $2845\text{ cm}^{-1}$  which corresponds to the  $\text{CH}_2$  bond vibrations.

Similar dark spots have been observed in the forwards CARS images of cells in a study by Cheng et al 2002<sup>61</sup> where bright spots were observed simultaneously in the epi CARS image. Cheng et al offered the explanation that the dark spots in the forwards CARS images were due to a distortion of the focal point of the laser excitation beam due to the changes in refractive index between the lipid droplet and the surrounding cytoplasm. However in the epi direction the signal is enhanced at the interface between the scatter and the surrounding medium and hence the droplet will appear bright within the epi CARS image. A distortion of the laser focal point at the interface between media of different refractive indices could

also explain the observation of a decrease in CARS signal at interface between the cells and the pericellular matrix.<sup>61</sup>

#### **4.2.1.4 Combined imaging**

Typical images of an area of healthy cartilage from a 2yr old horse are shown in figure 4-4. These have been taken using the following imaging modalities SHG, TPF and forwards and epi CARS. The images are registered and therefore can be merged, here blue represents SHG, green represents TPF and red represents CARS. Bright spots have been seen within the cells in both the TPF and CARS images. The merged image shows that these features are not co-localised and therefore must represent different cell structures.

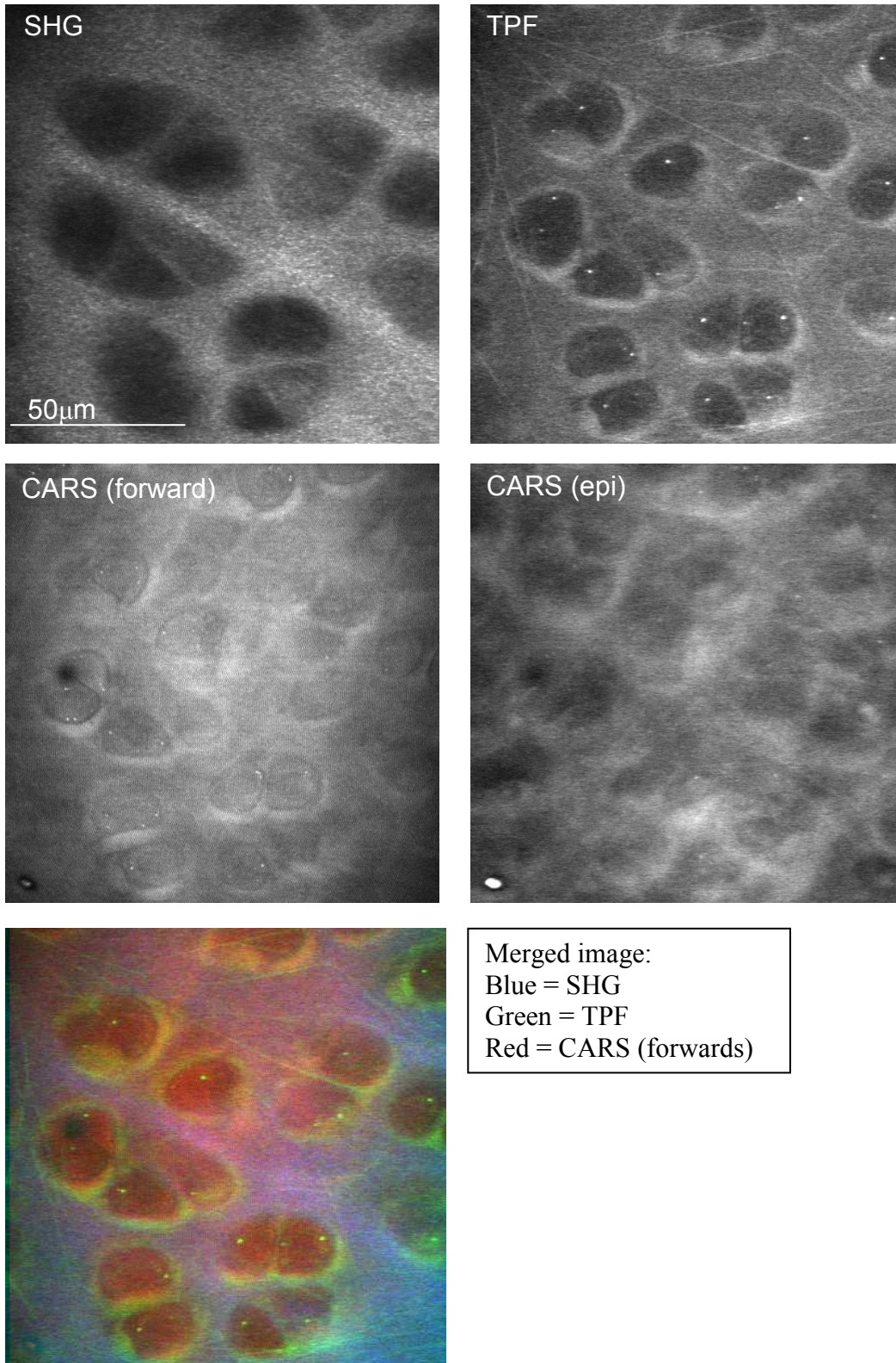


**Figure 4-5 SHG, TPF and CARS images from the superficial zone**  
Images taken at a depth of 7µm below the articular surface in a sample of healthy tissue (from a 2yr old horse)

Multi-photon intensity profiles across a pair of cells

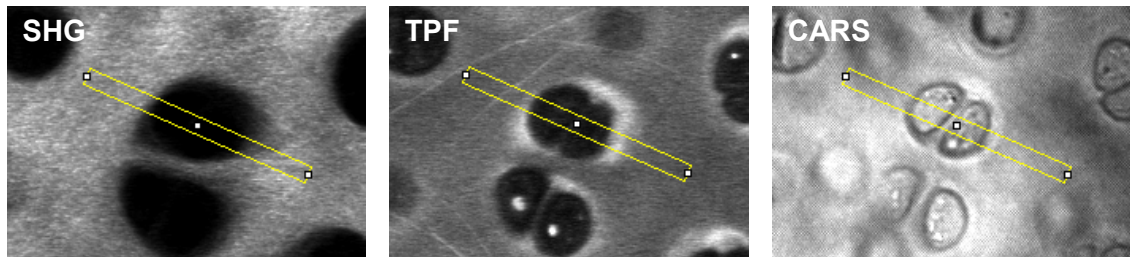
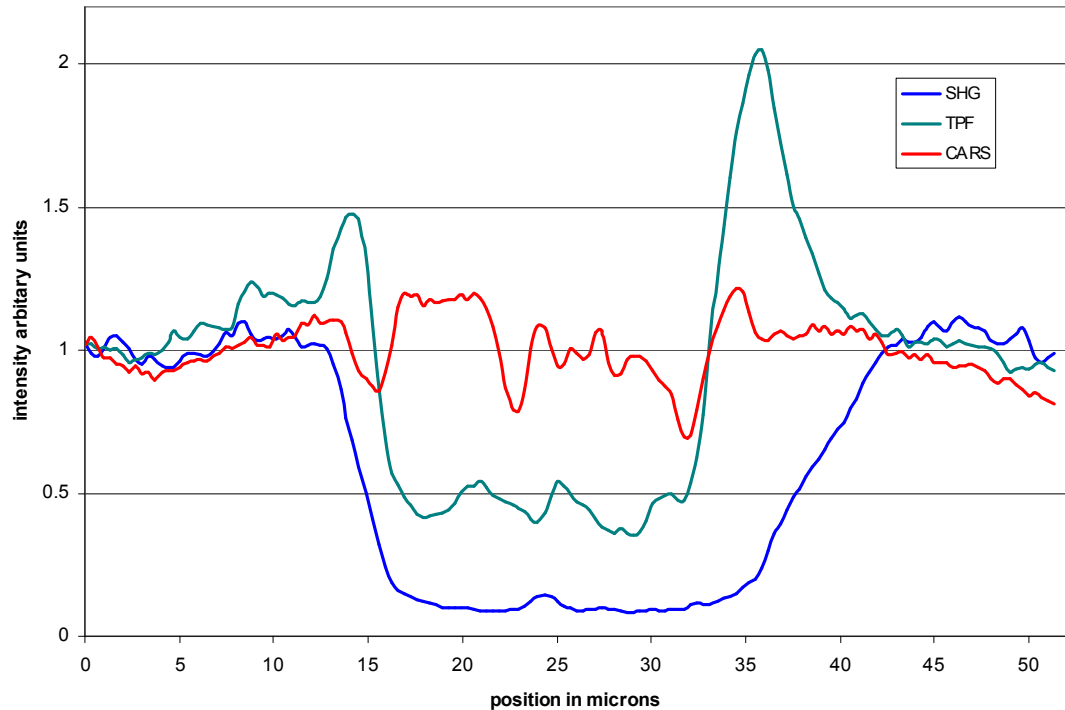


**Figure 4-6** The SHG, TPF and CARS intensity profiles across a pair of cells.

The insets show the images in each modality of the cells. The intensity is plotted in arbitrary units as it is not possible to compare the actual intensities of the different signals due to possible differences in the collection efficiency.

Figure 4-6 shows the SHG, TPF and CARS intensity profiles across a pair of cells. From this it is clear that the intensity of the SHG drops on approach to the cell at the same time as the intensity of the TPF increases associated with the pericellular matrix. A decrease in the SHG intensity in the pericellular matrix may be expected as the literature has previously reported that the collagen fibres there are finer and less ordered<sup>127, 132</sup>. The CARS intensity profile shows a dip in intensity at the edges of the cells and this coincides with the point at which the TPF intensity drops at the interface between the cell and the pericellular matrix. From this we see that the TPF and the CARS images provide more accurate information on the size of the cells, and if the SHG image was used it would provide a large overestimate

of cells size. Also the CARS image shows clearly that this lacunae contains two chondrocytes, which is not clear from the SHG and TPF images.

Stacks of multiphoton images can be used to investigate the distribution of cells in the cartilage and look at the variations in cell shapes. Figure 4-7 shows a reconstruction of the most superficial 100 $\mu\text{m}$  of tissue, constructed from stacks of SHG and TPF images taken at 1 $\mu\text{m}$  steps. The reconstruction shows a high cell density near the articular surface. The cells at the articular surface also appear flattened disc shaped, with increasing depth the cells become less flattened.

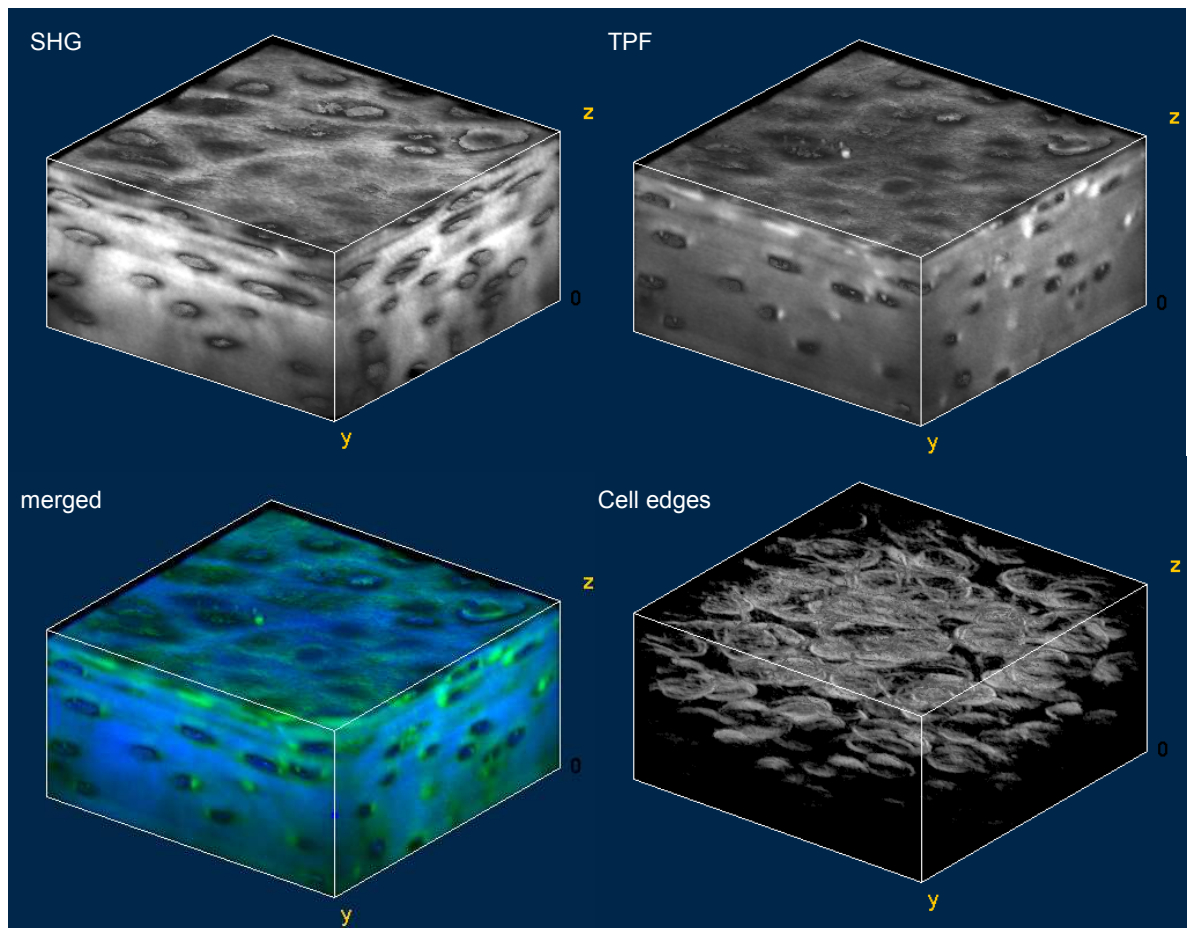
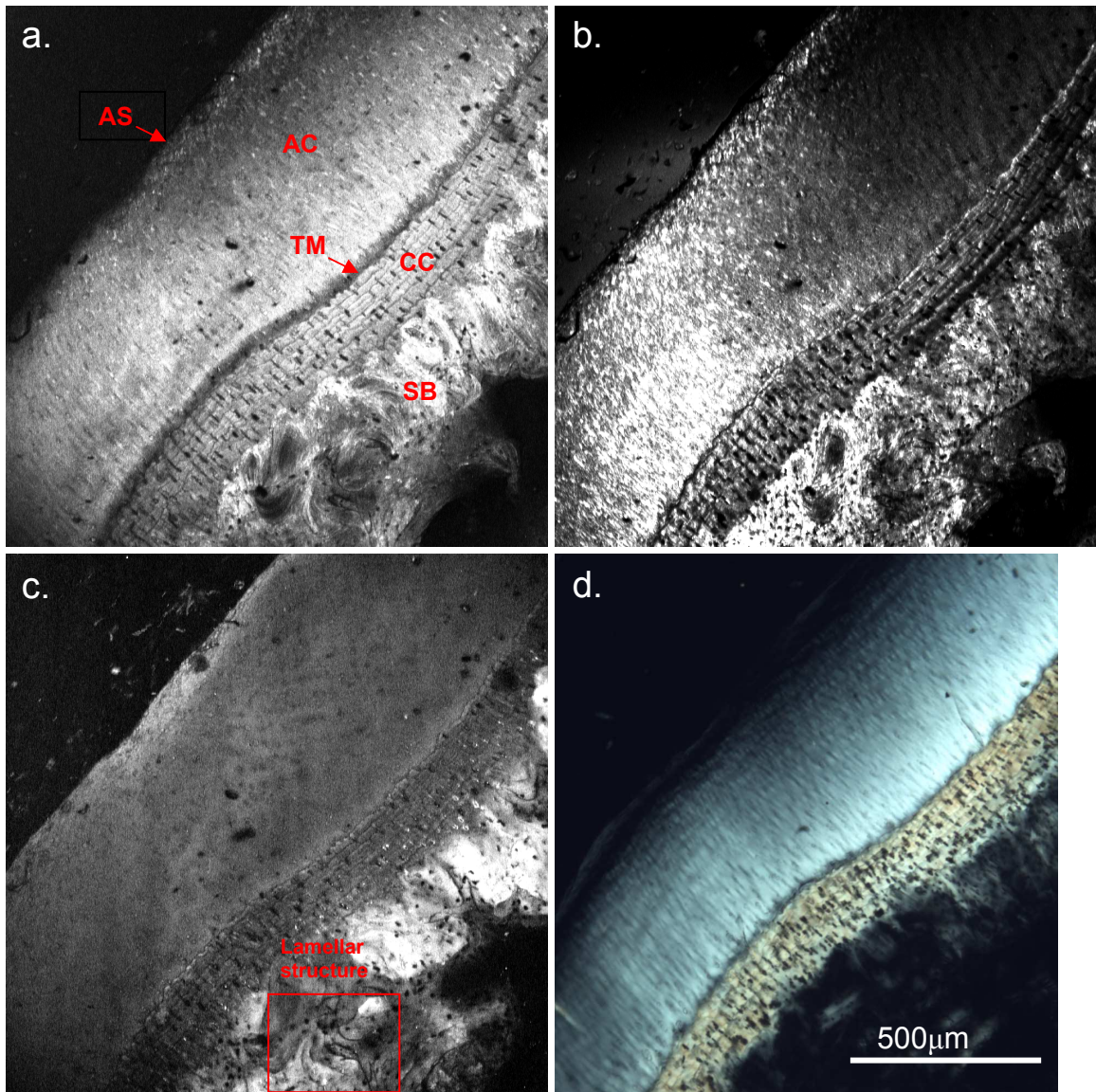


**Figure 4-7** A reconstruction of the surface of the articular cartilage. The size of cartilage portion reconstructed is 100 $\times$ 200 $\times$ 200 $\mu\text{m}$ . Data taken from the palma region of a 4yr old horse.

### 4.2.2 Cartilage Sections

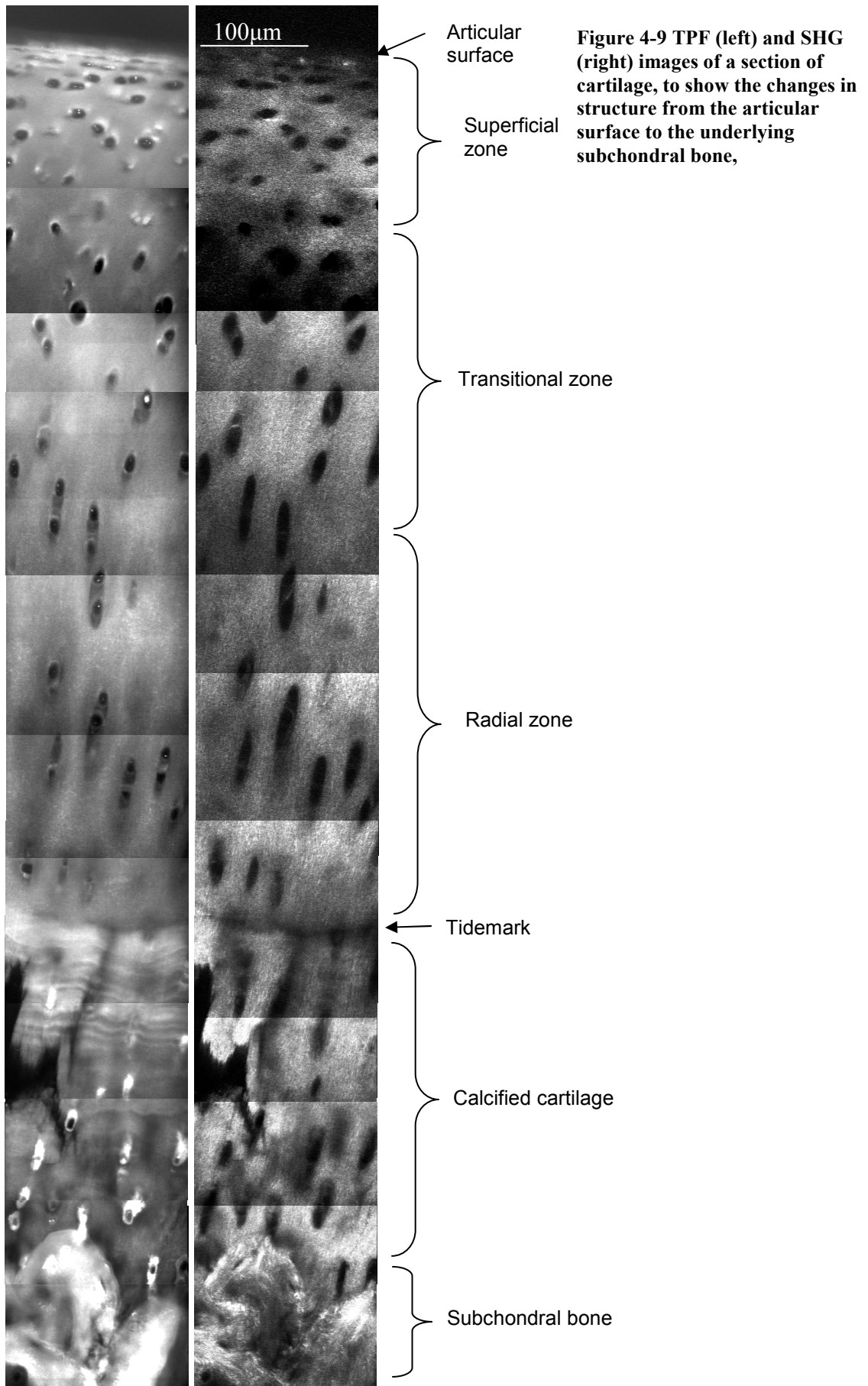
Imaging en-face cartilage only enabled us to image to a depth of 100-150 $\mu$ m. This is because imaging depth, is limited by the scattering and absorption of the IR excitation light in the tissue. The intensity of the excitation light drops off as an exponential function with depth into the tissue. Also effects in the tissue cause pulse broadening due to scattering and variations in the refractive indices within the tissue, the 100fs laser pulse can easily be broadened to 500fs after travelling through the microscope optics and the tissue sample and hence this reduces the instantaneous power at the focal point.<sup>4</sup> It is inconclusive as yet whether or not the scattering of the light increases the point spread function of the focal point in the tissue, if this is the case then it would act to decrease both the intensity and the resolution of the images taken.<sup>5</sup> As the structure of cartilage changes significantly with depth (see section 1.6.1) it was necessary to take transverse sections of the cartilage in order to investigate the deeper zones of articular cartilage.

Figure 4-8 shows a sections of articular cartilage and underlying subchondral bone viewed using SHG, TPF and conventional transmission light microscopy with crossed polarisers, to reveal collagen fibre orientation. These multi-photon images have been taken using a 10x objective and allow a direct comparison with the histology. In these images the articular surface (AS) is to the top left and the underlying bone (SB) is in the bottom right. In the SHG and TPF images the bone shows up clearly and the osteocytes appear as dark specs against the bright signal from the bone matrix. The TPF and SHG images show some structural features of the bone, the SHG images revealing areas with different collagen orientations and the TPF images showing a lamellar structure around some of the vessels. The tidemark (TM) is visible on all 4 images showing a distinct boundary between the calcified cartilage (CC) and the articular cartilage (AC). The tidemark region is discussed in more detail in section 4.2.3.3. In the SHG images the arcade like structure first described by Benninghoff is apparent.



**Figure 4-8** A full depth section of articular cartilage. Images taken at the cortical ridge of the 3<sup>rd</sup> metacarpal imaged using epi and forwards SHG (a and b respectively), TPF (c) and transmission light between crossed polarizers (d). Images a-c were taken on the microscope 2 using a 10x 0.4NA objective and a laser excitation power of 14mW. Image d was taken using a 5x objective on a transmission microscope.

Further, more detailed imaging of the sections was carried out using the 60× water immersion objective as used on the cartilage slices. This allowed the changes in cells and pericellular matrix with depth to be investigated, along with more detailed investigations of the bone and tidemark structure. A series of adjacent TPF and SHG images have been aligned in figure 4-9 to produce an image of the cartilage from the articular surface to the subchondral bone.



#### **4.2.2.1 Superficial and Transitional Zones**

The SHG and TPF images of the sections clearly show variations in the cell shape and distribution with these being most evident in the TPF images. The variations shown in these images are consistent with previous histology<sup>89, 91, 92, 133</sup>. In the superficial zone the cells appear flattened in the radial direction and are more numerous than in the other zones. In the transitional zone the cells become more rounded and appear singly or in pairs. In the superficial and transitional zones the pericellular matrix surrounding the cells appears brighter than the rest of the matrix and this agrees with the results reported on the enface samples.

In the SHG images the intensity increases with depth into the tissue. This is likely to be due to variations in the collagen fibre orientations: the collagen fibres in the surface of the tissue may be orientated end on to the imaging plane resulting in a very low SHG intensity from the sample. The sections used in this chapter have been cut parallel with the joint articulation, and therefore they need to be repeated with the sections cut perpendicular to the joint articulation.

#### **4.2.2.2 The radial zone**

Figure 4-9 shows that the cells in the radial zone are organized into groups of 2-4 cells aligned in a row radially from the subchondral bone. This is in agreement with the previous literature<sup>89, 91, 92, 133</sup>. The pericellular matrix in this zone differs from that in the superficial and transitional zones. Instead of an increase in the TPF from this region there is a decrease in TPF compared to the interterritorial matrix. In figure 4-10 gives a higher resolution image of the radial zone. In the SHG image the fibre orientation can be clearly resolved, and shows the fibres pointing radially from the subchondral bone. This conforms with the well established description of collagen fibre orientations in cartilage.

In the en-face imaging reported at the articular surface we were unable to resolve the direction of the collagen fibres. There are two possible explanations of this, possibly the collagen fibres in the radial zone are thicker and more ordered than those in the superficial layer, however previous studies using x-ray diffraction have not reported any differences in the collagen spacing.<sup>12</sup> Alternatively this may be due to the different imaging arrangements

used; the SHG image in figure 4-10 was taken in the forwards direction however for the en-face imaging the forwards images contained a very low count rate due to the thick sample size used and therefore the epi-SHG images were recorded instead. The epi and forwards SHG images of collagen have been found to differ with the forwards images showing a more fibrous structure.<sup>44</sup> Consequently more work may need to be done on epi and forwards SHG images from different thickness cartilage samples to investigate whether this determines our ability to resolve the collagen fibre directions.

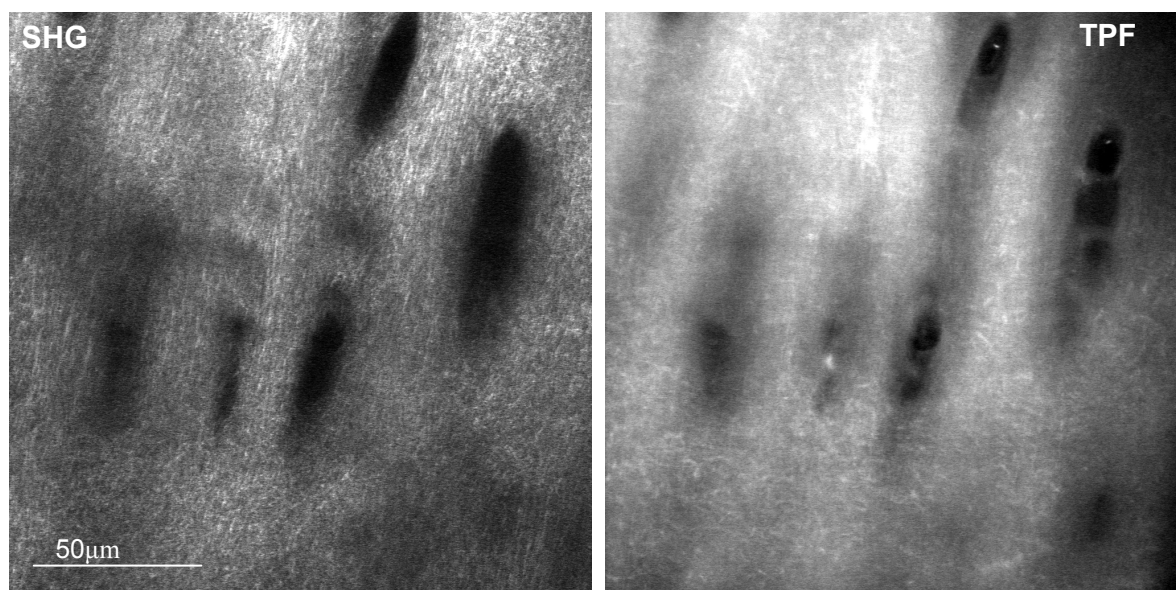


Figure 4-10 SHG and TPF images of the radial zone.

#### 4.2.2.3 The tidemark

Cartilage is not a static system, although in healthy tissue the relative thickness of the zones is approximately maintained. The tissue is in dynamic equilibrium and studying the tidemark, calcified cartilage and subchondral bone may be important for understanding this. The underlying bone is continuously remodelling in response to the applied forces, with vessels from the subchondral plate converting the calcified cartilage to bone. However the thickness of the zone of calcified cartilage remains constant as the tidemark progresses into the radial zone. The thickness of the upper layers of cartilage must be maintained by the matrix components generated by the chondrocytes.<sup>134</sup> The zone of calcified cartilage also provides a route for nutrition to reach the chondrocytes from the vascular supply to the

subchondral bone<sup>135, 136</sup>. Therefore it is also important to study this region as a disruption of the equilibrium may cause degeneration and a change to the nutrition of the cells.

The tidemark shows up clearly in both the SHG and TPF images and is shown in both figure 4-8 and figure 4-9. Beneath the tidemark multiple undulating tidemark like lines and these are most clear in figure 4-8. It has been postulated that these may represent the location of previous tidemarks<sup>134, 137, 138</sup>. The intensity of the TPF signal is greater in the zone of calcified cartilage compared to the un-calcified cartilage. This corresponds with previous work involving single photon fluorescence<sup>93</sup>. At the centre of the tidemark the TPF intensity is decreased with comparison to both the calcified and un-calcified cartilage. In the SHG images the tidemark appears as a dark band across the images.

These features are shown in figure 4-11 where a profile of the intensity of the SHG and TPF across the tidemark is shown. There are two possible ways of interpreting this finding, possibly that there is less collagen at the tidemark or that the collagen at the tidemark is less aligned than elsewhere in the tissue. An electron microscopy study by Redler et al<sup>139</sup> identified variations in the collagen fibre orientation at the tidemark and suggested that the collagen fibres are not all radially aligned across the tidemark and that some branch and lie along the tidemark. Alternatively at the tidemark there may be increased attenuation of the light. This explanation is plausible as the tidemark appears dark when sections are viewed with transmitted light microscopy, and it would simultaneously explain the dip in TPF intensity centred on the tidemark. The thickness of the tidemark is about 2-5 $\mu\text{m}$ <sup>139</sup>, however in our images the decrease in intensity across the tidemark is a broad feature from 10-30 $\mu\text{m}$  in diameter.

The source of increased fluorescence from the zone of calcified cartilage still remains unknown. In chapter 3 pure hydroxylapatite was tested for TPF but was found not to be fluorescent. Spectra from the zone of calcified cartilage were found to be similar to those from the un-calcified cartilage. There are three possible explanations for the increased fluorescence in the calcified cartilage; (1) there is an additional fluorophore in the calcified cartilage not present in the uncalcified cartilage, (2) there are the same fluorophores in both the calcified and un-calcified cartilage but the concentration is greater in the calcified

cartilage or (3) there are the same fluorophores and concentrations in both zones however the fluorescence in the calcified cartilage is more efficient due to a different chemical environment.

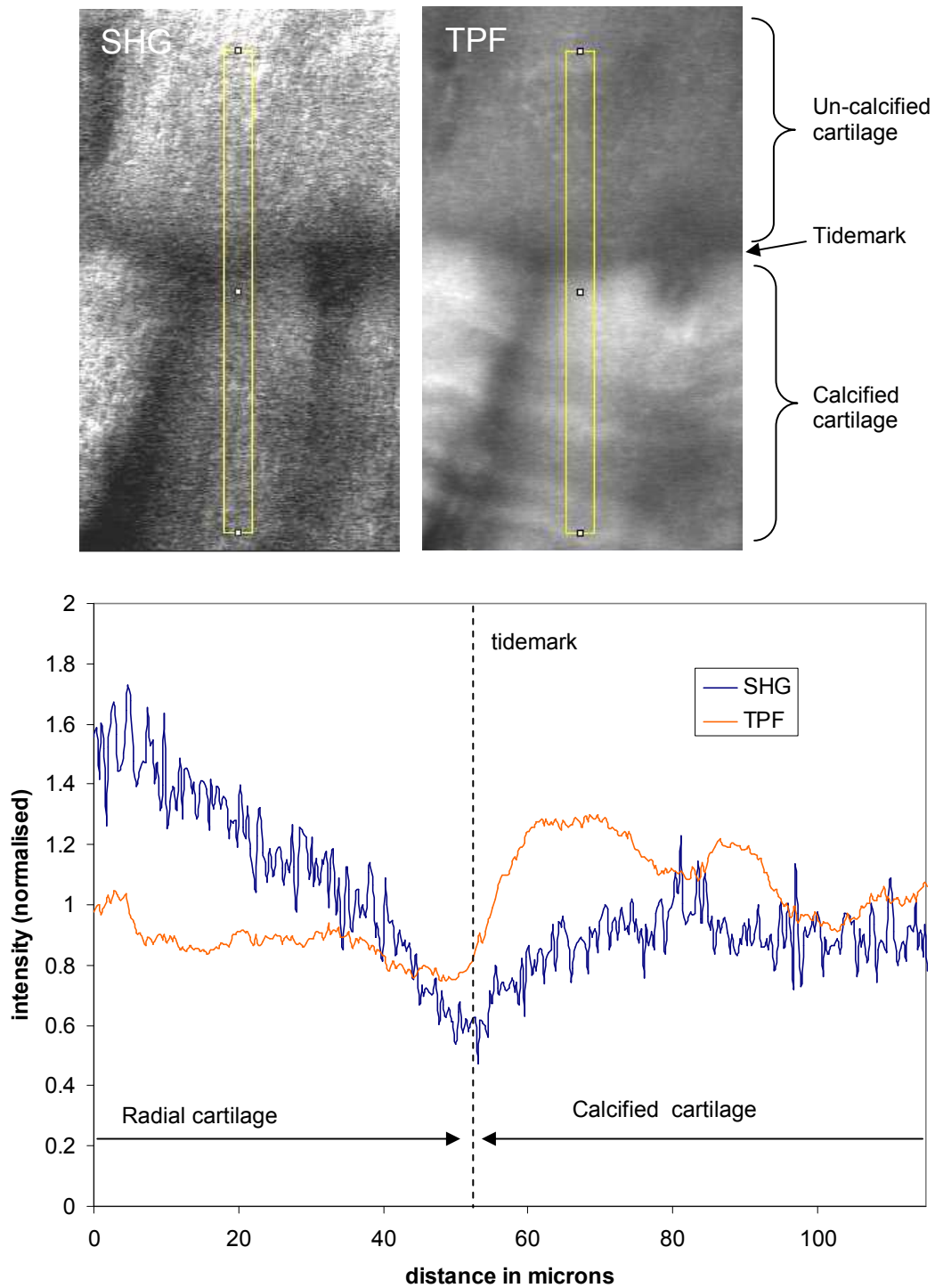


**Figure 4-11 TPF and SHG intensity profiles taken across the tidemark.** The two insets at the top of the figure show the area over which the profile was taken. This figure shows that after the tidemark an increase in TPF intensity is seen and that at the location of the tidemark the SHG signal is at a minimum.

#### **4.2.2.4 Calcified cartilage and subchondral bone**

The intensity of the fluorescence surrounding the cells in the calcified cartilage is greatly increased, and this is clearly shown in figure 4-9. It would be interesting to investigate this further with combined CARS imaging as the chondrocytes in the calcified cartilage are thought to die via apoptosis or a similar process, and in doing this they generate matrix vesicles which contribute to the calcification of the tissue.<sup>140, 141</sup> In the TPF image the articular cartilage appears faint in comparison to the underlying bone which exhibits a higher level of auto-fluorescence. Further work is still needed to identify the reason for this increased fluorescence. Vessels in the subchondral bone are visible along with their surrounding Haversian systems and these are shown at the interface between the bone and the calcified cartilage in figure 4-12. Increased fluorescence is seen at the cement line between the bone and the cartilage. Earlier studies have stated that the collagen fibres do not cross the cement line from the calcified cartilage to the subchondral bone<sup>138</sup> and the images here support this consensus.

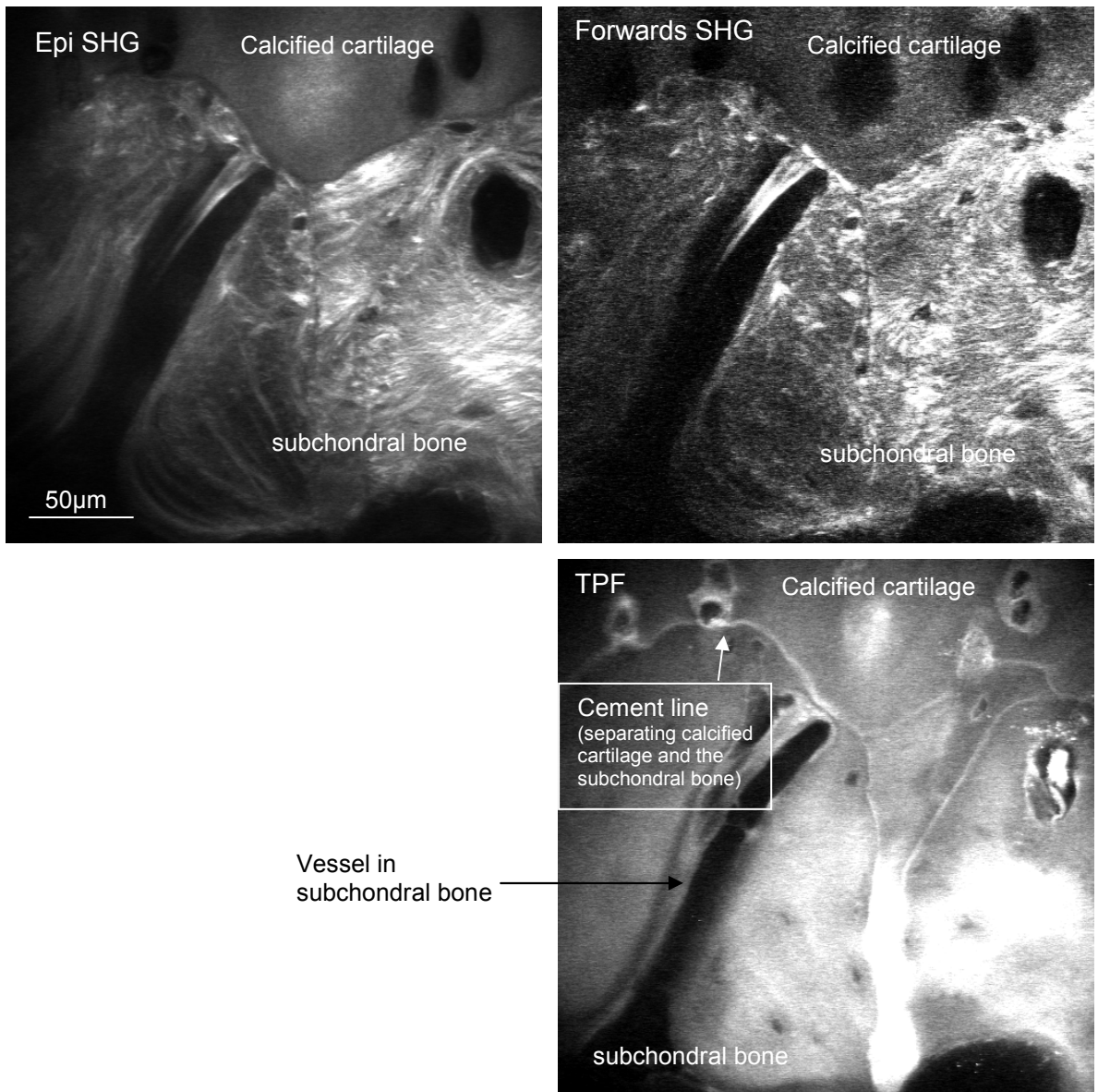


Figure 4-12 The interface between bone and calcified cartilage

### **4.3 Lesions**

Previous studies of the metacarpophalangeal joint have identified a variety of different lesion types, ranging from small microlesions on the surface to extensive lesions where the cartilage has been lost and exposed the bone at the lesion site.<sup>93</sup> There also exist on some joints grooves which run with the direction of articulation which are referred to as wear lines.<sup>109</sup> Faced with this large range of lesion morphologies and locations it was beyond the scope of this project to do a systematic study of all lesion types, therefore in this study we have concentrated on the “butterfly” lesions, which occur on the cortical ridge<sup>142</sup> (see Figure 4-13). These lesions appear to be the most common type of lesion of this joint, appearing on all samples which showed signs of degeneration. The lesions chosen for investigation were large enough to be visible with the naked eye but not so extensive that the underlying bone would be exposed. In this section we present data showing marked changes in the non-linear images of cartilage over an area extending from the core of the lesion into the macroscopically normal tissue surrounding it. These images are then compared to histological sections of the lesion viewed between crossed polarizers to reveal collagen organisation. Sections across the lesions were also fixed and stained for proteoglycans using the following stains Touludine blue (0.13% in distilled water) and Safarin O (0.1% in distilled water). We also report abnormalities in sections away from lesion sites which may represent early degeneration (section 4.3.2) and also images taken from a highly degenerate joint (section 4.3.3).

### 4.3.1 Butterfly lesions

When imaging the enface samples stacks of images were taken at points along a line (13mm long) which crossed a “butterfly” lesion on the cortical ridge. Figure 4-13 shows the location of the line of imaging points on the articular surface.

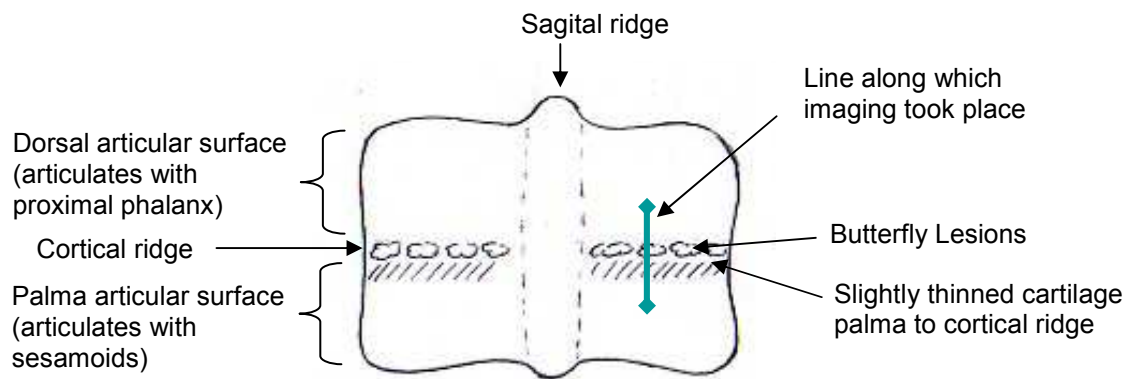


**Figure 4-13** A schematic diagram of the distal end of the 3<sup>rd</sup> metacarpal. The location of the lesion is marked along with the line along which the sample has been imaged.

Four different butterfly lesions were imaged. Features which have been observed in different regions approaching the lesion are summarised in figure 4-14. These images were taken from a 15yr old horse which contained a butterfly lesion but no other degenerate sites. The sample was sectioned after imaging and viewed between crossed polarizers and this is shown in figure 4-14d this clearly shows the progression from the normal histology to the diseased state approaching the lesion at the cortical ridge. Staining with Toluidine blue revealed that the proteoglycans had been lost from the core of the lesion (region c) however the other areas showed an uptake of stain which was comparable to healthy tissue.

Large amounts of fibrillation (splitting of the cartilage) at the centre of all lesions investigated, with voids free of collagen being observed within the imaging area to fully map the fibrillation a larger field of view would be required. The changes shown in figure 4-14c are very pronounced, especially at the central lesion site. In the region shown in figure 4-14c there is rippling of the extracellular matrix which is most pronounced in the SHG images, this effect has also been seen in bovine tissue with osteoarthritis by Yeh et al<sup>80</sup>. The diseased area shown in part c is largely acellular with only one lacunae visible. In the region close to the lesion (region b) intense SHG signal was seen adjacent to the chondrocytes. In the TPF images the intensity surrounding these chondrocytes is no greater

than the TPF from the pericellular matrix in healthy tissue. It is possible that these images may be showing increased collagen production by the chondrocytes.

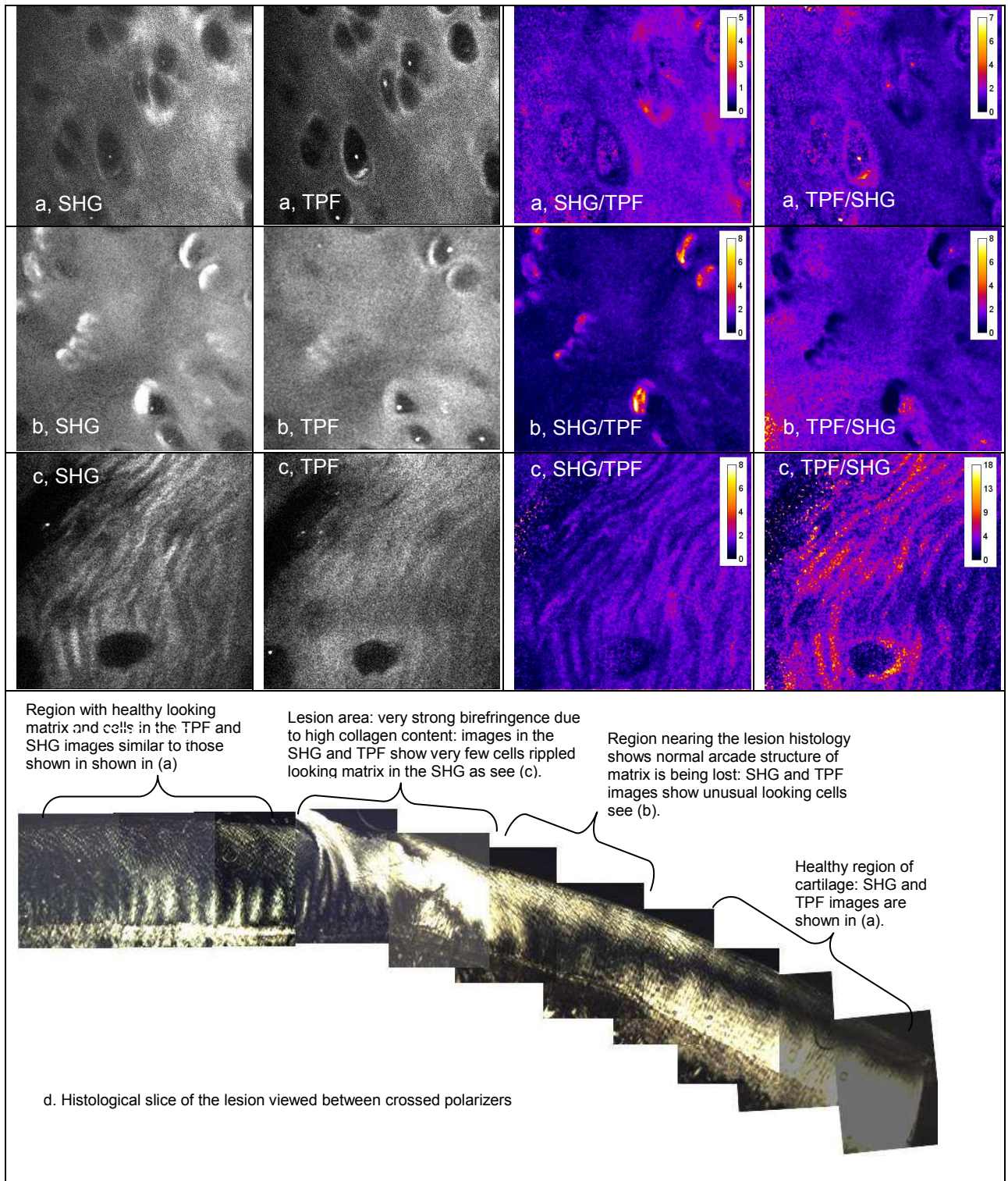


**Figure 4-14 Multi-photon imaging on a sample containing a butterfly lesion. The images marked SHG/TPF show the result of dividing the SHG image by the TPF image and the images marked TPF/SHG show the converse. These results are displayed using a false colour LUT with the scale in the right hand corner. The lesion was imaged enface and then sectioned after imaging (d) shows the section viewed between crossed polarisers.**

### 4.3.2 Early superficial lesions

Many regions of cartilage which appeared macroscopically normal demonstrate disruption to the surface of the cartilage. In this section images and stacks taken of these features are presented. Figure 4-15 shows a 3D reconstruction of a superficial lesion found on the dorsal region of the joint, this is reconstructed from a stack images of 80 separated by  $0.5\mu\text{m}$  steps and the dimensions are  $227 \times 160 \times 40 \mu\text{m}$ . This lesion is approximately  $15\mu\text{m}$  in depth and runs parallel with the direction of articulation in the joint. This lesion was found on a  $5 \frac{1}{2}$  year old horse which also demonstrated some early osteoarthritic “butterfly” lesions on the cortical ridge. The tissue surrounding the lesion still contains elastin fibres but no fibres travel across the lesion.

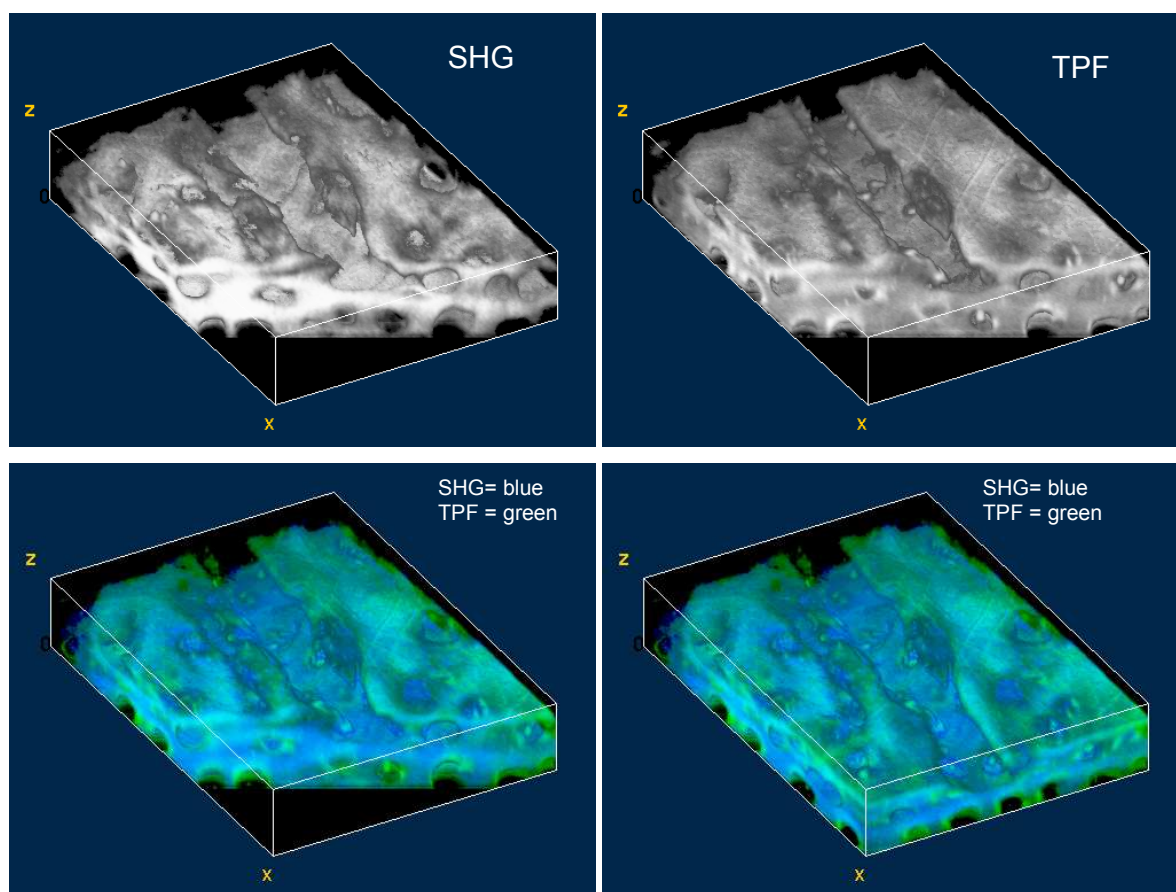


**Figure 4-15: A 3D reconstruction of a microlesion.** This has been generated from SHG and TPF stacks from the dorsal region of a  $5 \frac{1}{2}$  yr old sample exhibiting early OA. The size of the slab of tissue in this reconstruction is  $227 \times 160 \times 40 \mu\text{m}$ .

When histology was carried out on this tissue sample after imaging we were unable to locate the microlesion. The histological sections showed “normal” tissue structure, with the sample taking up the stain for proteoglycans and no disruption to the articular surface.

These are shown in figure 4-16. This supports the hypothesis that this lesion represents some of the earliest degenerative changes as no other degeneration is noted on the histology.

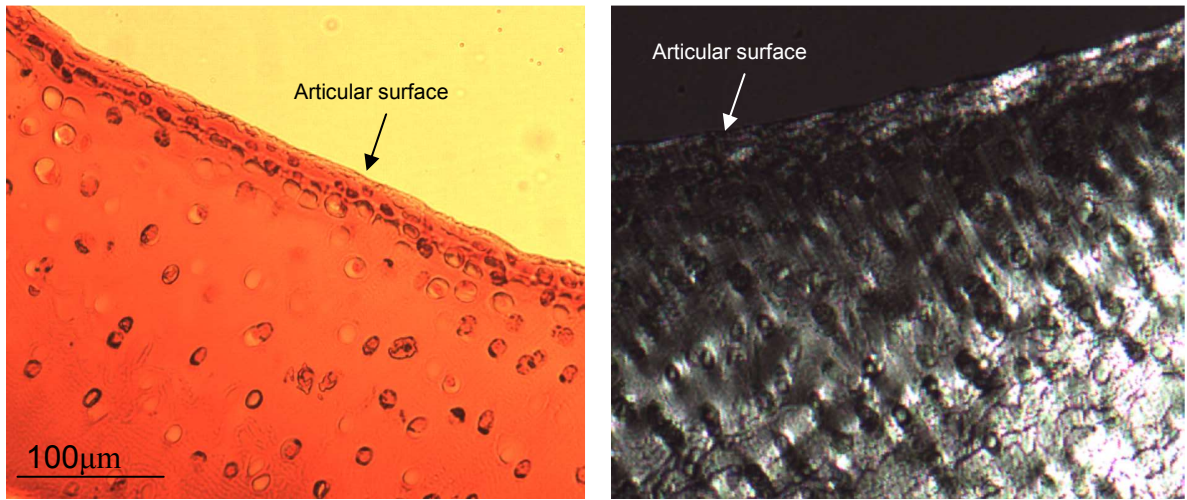


**Figure 4-16** histological sections of the sample imaged for figure 4-15.

**A section has been stained for proteoglycans with safranin O (right) and viewed between crossed polarizers (left). These images show an apparently healthy structure containing proteoglycans and no disruption to the articular surface.**

Another feature has been observed which may represent early osteoarthritic changes is splits seen in the SHG images of the extra-cellular matrix. These splits are only visible in the SHG images and not in the TPF images indicating that they are a feature of the collagen in the extra-cellular matrix. These split features have been observed in the sagittal ridge of 2 samples. TPF and SHG images of a region with the split like features are shown in figure 4-17. Histology on this region showed an undisrupted structure at the articular surface with no signs of fibrillation at the surface. The sample stained strongly with safranin O indicating a normal proteoglycan content.

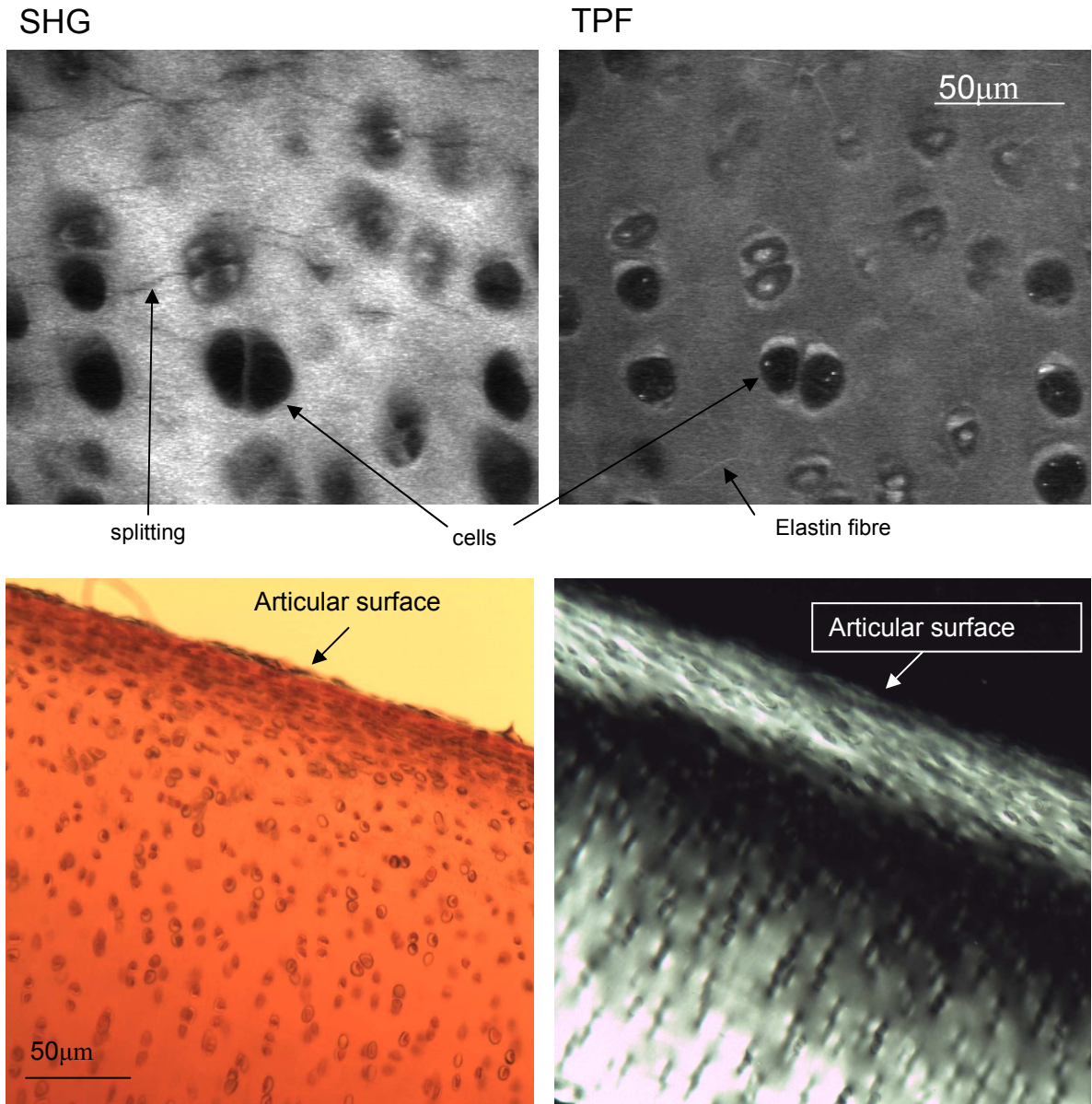


**Figure 4-17** A SHG and TPF images showing splitting of the collagen matrix. These images were taken at a depth of 15µm from the articular surface, on a cartilage slice taken from the sagittal ridge of a 5.5yr old sample demonstrating early OA. Histological sections were taken of the sample after multi-photon imaging, and stained for proteoglycans with safranin O (bottom left) and viewed between crossed polarizers (bottom right). These images show an apparently healthy structure containing proteoglycans and no disruption to the articular surface.

Another sign of early degeneration is fibrillation at the articular surface. This was observed at the surface of a 15yr old horse demonstrating early disease. Figure 4-18 shows a region where the collagen at the articular surface has broken up into a highly fibrillated arrangement at the top 15µm of the articular surface. Beneath the fibrillated tissue at the surface the multi-photon images showed the same features as reported in healthy tissue. The reconstruction of the fibrillated structure is generated from a stack of 20 SHG images

taken from the surface to a depth of 20 $\mu$ m. The fibrillated tissue at the surface did not exhibit much TPF suggesting it had a different composition to healthy matrix. histology taken from this region showed a disrupted articular surface with the tissue beneath appearing histologically normal.

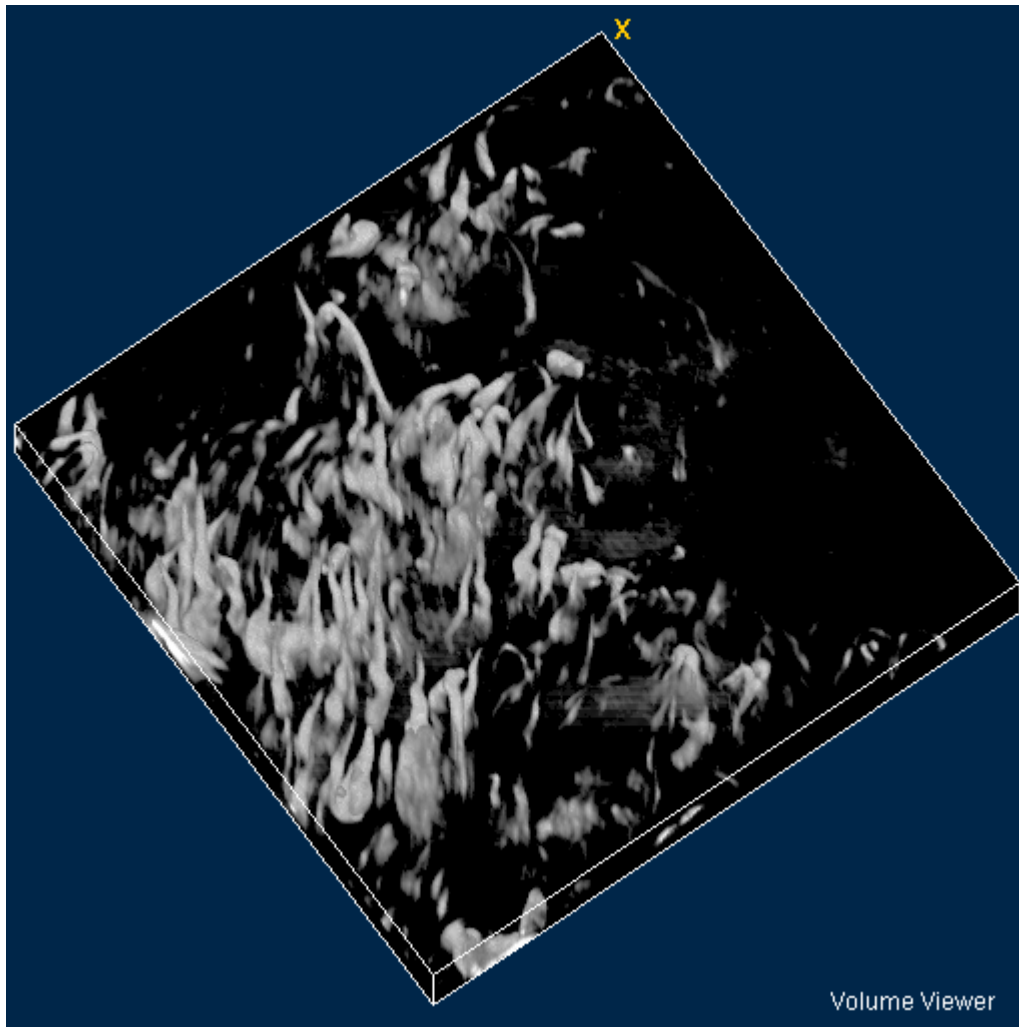


**Figure 4-18** A reconstruction of fibrillated collagen at the articular surface. The size of the reconstruction is 170 x 170 x 15  $\mu$ m and is generated from a stack of SHG images taken at the surface.

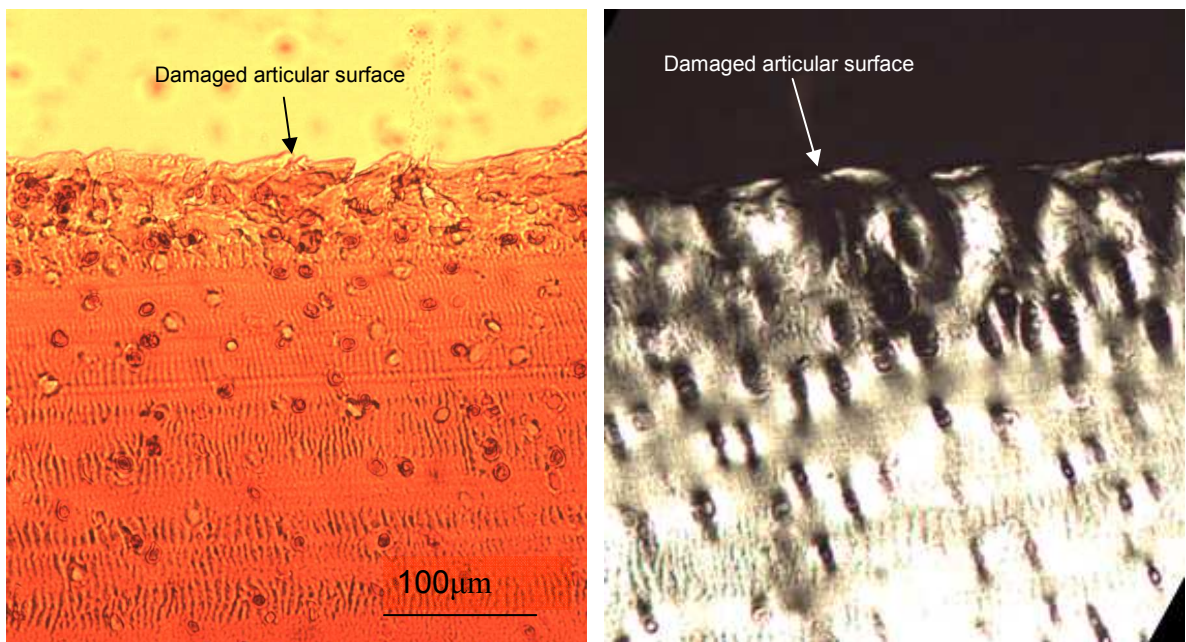


**Figure 4-19** Histology of the region shown in figure 4-18.

### 4.3.3 Highly degenerate tissue

In this section we report data taken from a 4yr old horse with very advanced degeneration, with large areas where the cartilage was eroded so that the underlying bone was exposed. Many regions of this joint showed cartilage which was completely acellular, and highly fibrous in nature, this cartilage is likely to consist of type I collagen rather than type II collagen. The TPF signal from these regions was very low indicating that the sample was composed mainly of collagen. A pair of TPF and SHG images of this region are shown in figure 4-20, accompanied by histological sections carried out on this sample after imaging. The histology reveals that underneath the acellular tissue at the surface there are clusters of cells.

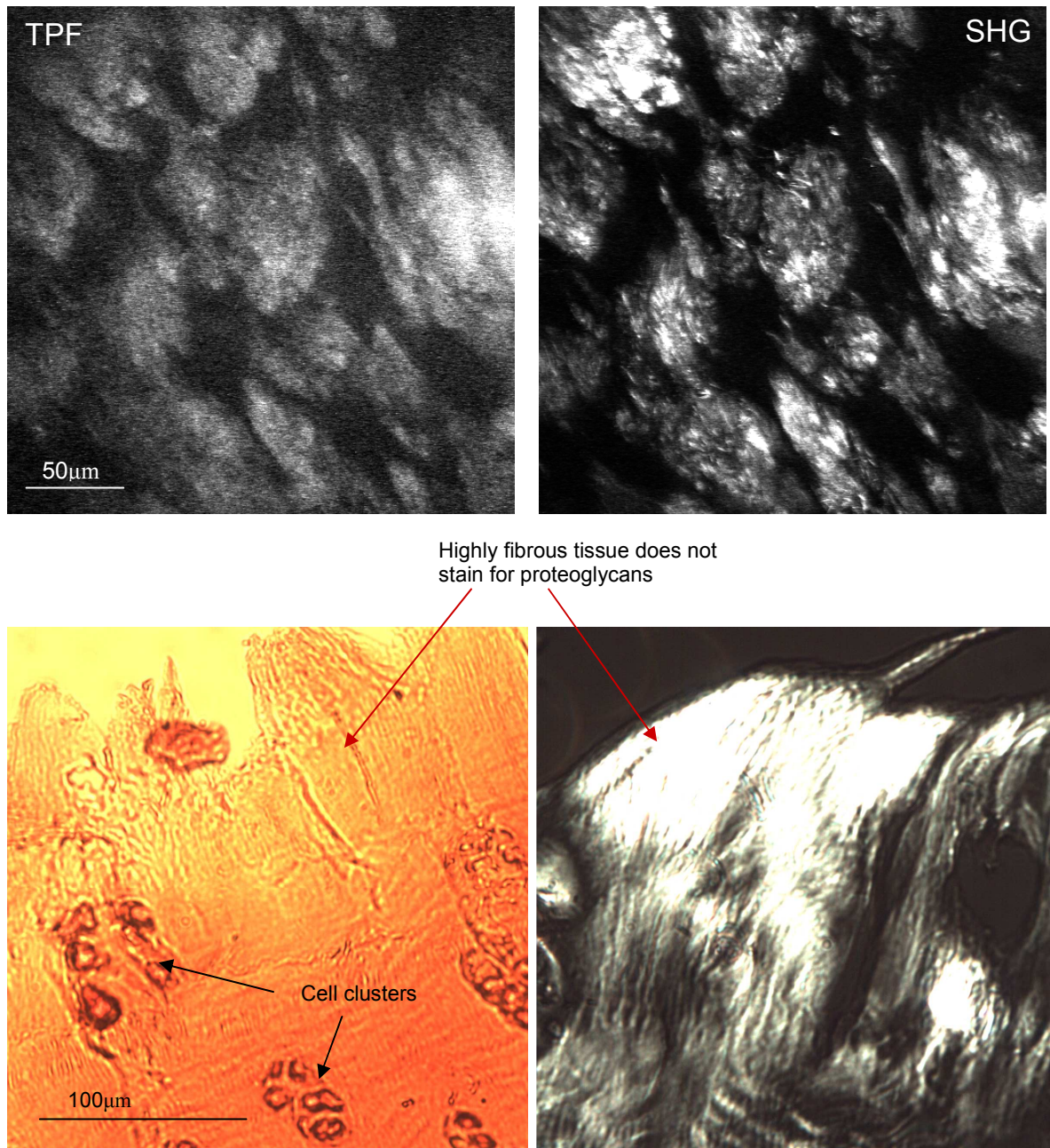


**Figure 4-20 Highly degenerated tissue showing a very fibrous structure. TPF and SHG images taken of a region of highly diseased tissue showing a highly fibrous structure and the absence of any chondrocytes. This sample was taken from the region dorsal of the 3<sup>rd</sup> metacarpal. Histology taken after multi-photon imaging revealed clusters of cells below the acellular fibrous tissue.**

The area of the joint which showed least degeneration was the sagittal ridge. In this area no macroscopic lesions were visible. However when viewed using multi-photon microscopy there were abnormalities in the organisation of the cells in the superficial layer, with the cells appearing to be small and arranged into tight clusters of about 4-6 cells. TPF and SHG images of some of these clusters are shown in figure 4-21, along with the histology of this region. The clusters of cells were evident on the histological section and there were also

signs of some damage to the articular surface. Bellow the articular surface in the transitional zone the histology revealed that the structure of the tissue resembled that of healthy tissue.

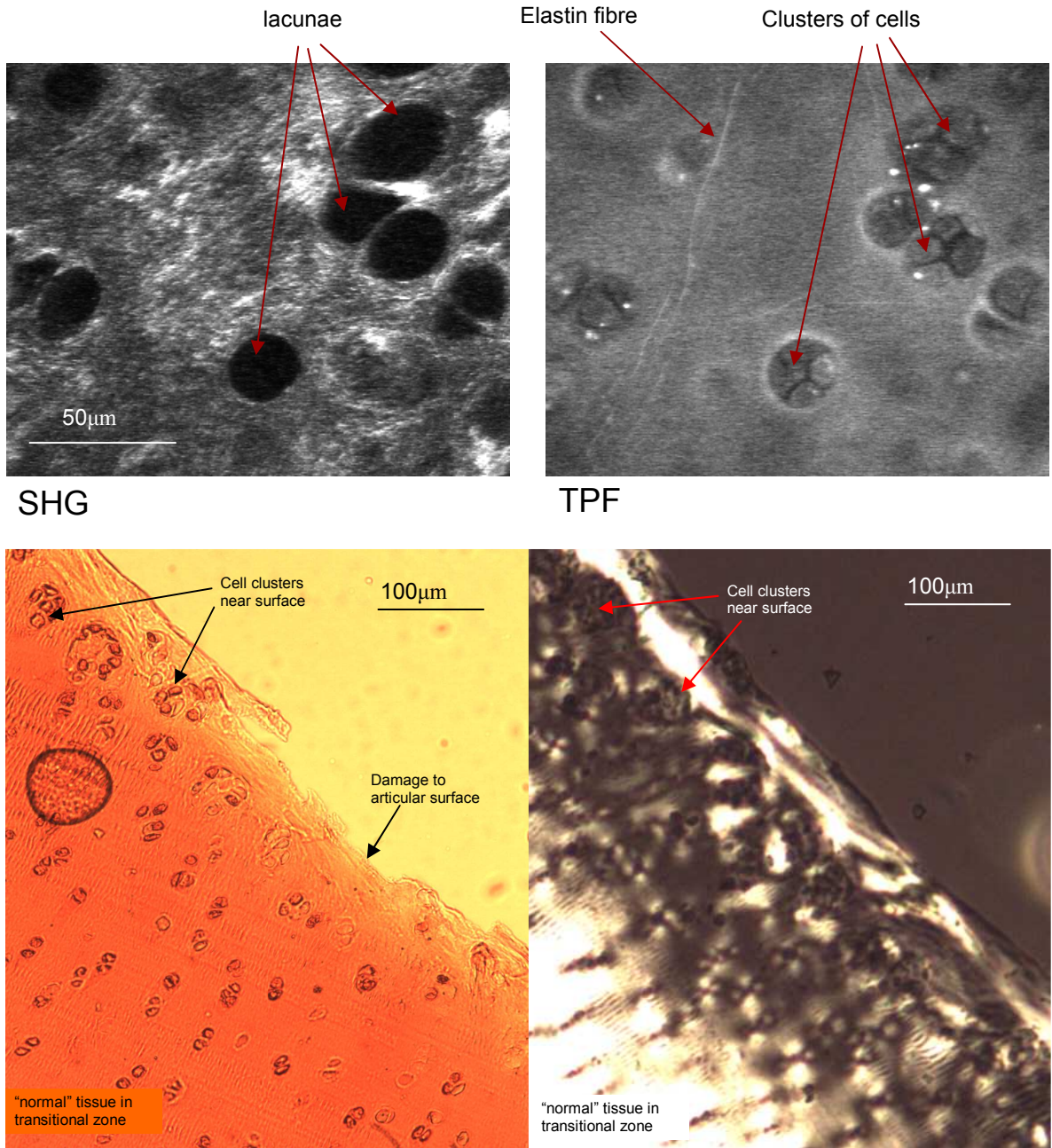


**Figure 4-21 Cell clusters seen on the sagittal ridge of a sample with advanced OA. The SHG and TPF Images were taken at a depth of about 13µm from the articular surface. The Histology also revealed cell clusters and damage to the articular surface, however the deeper zones appeared “normal”.**

In some regions of the tissue the cells formed larger clusters, up to 70µm in diameter and containing 10 or more cells. Some of these clusters appear to be surrounded by a fibrous capsule of collagen fibres this is demonstrated in the 3D reconstruction of the SHG image

of the region surrounding one of the clusters of cells shown in figure 4-22. The appearance of the cell clusters was also observed on histological sections taken of the sample after imaging.

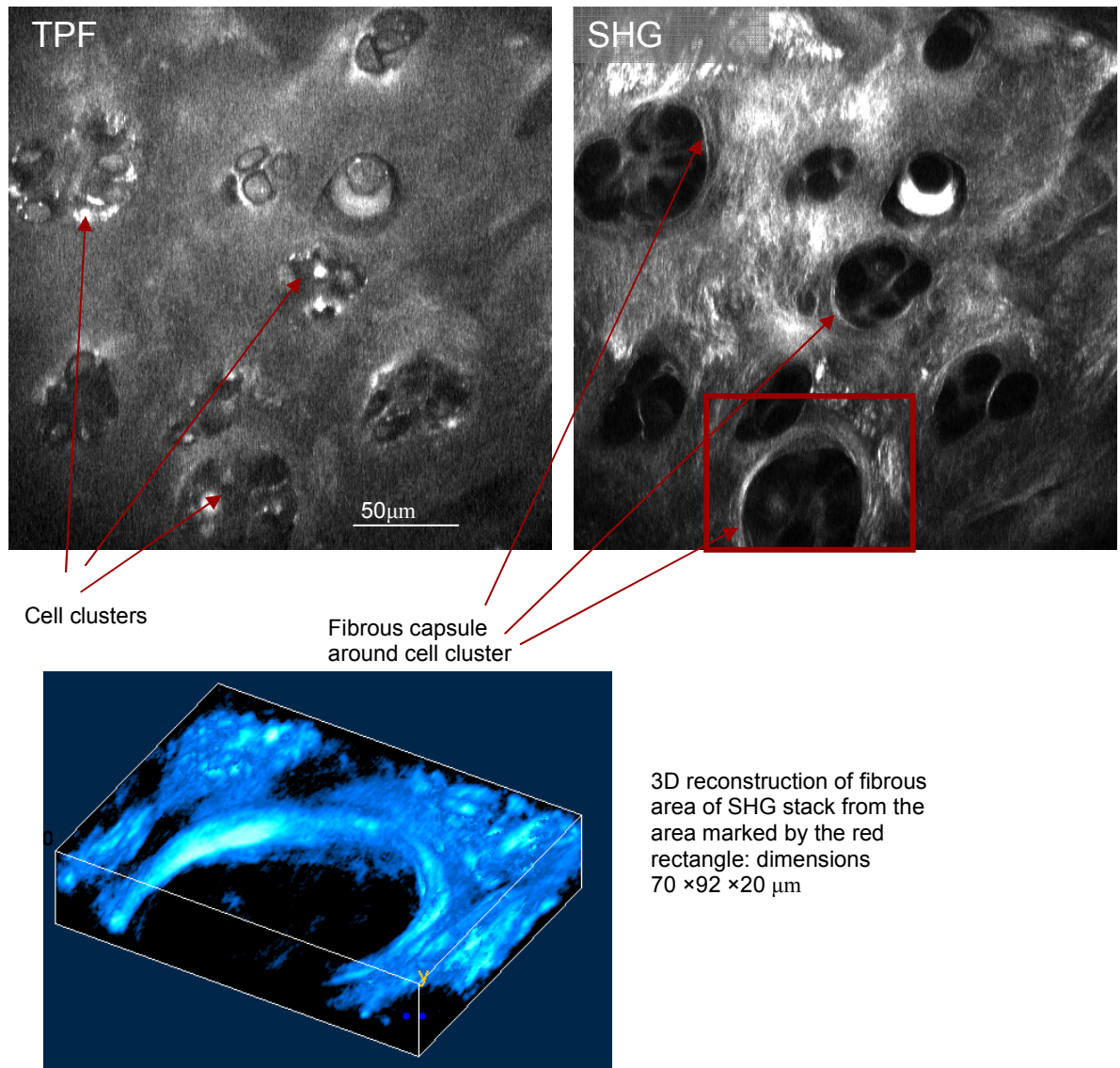


**Figure 4-22 Cell clusters at the with a surrounding fibrous capsule. Images taken from a stack on the cotical ridge of articular cartilage in a highly degenerate joint, showing large clusters of cells surrounded by fibrous capsules.**

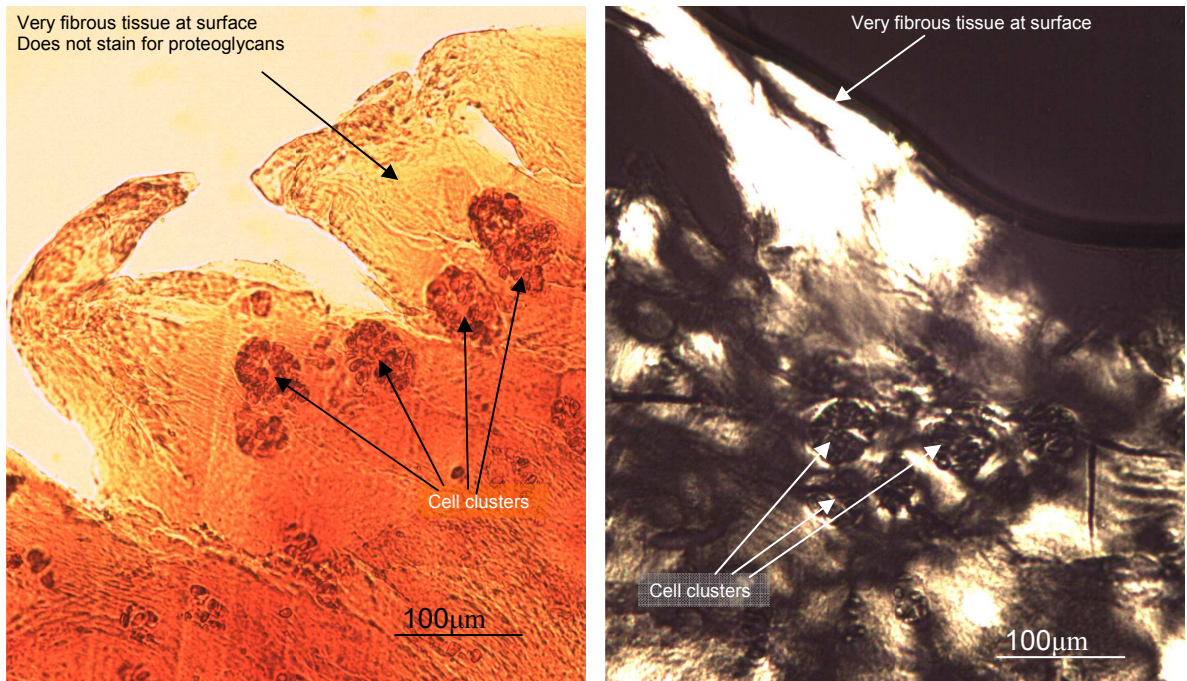


**Figure 4-23** histology carried out on the cortical ridge sample from figure 4-22. The histology shows that the sample contains many large clusters of cells like those observed with the multiphoton microscopy. It also reveals that there is a very fibrous layer at the surface where the tissue does not stain for proteoglycans.

## 4.4 Discussion

We have characterised the healthy tissue in all of the zones of articular cartilage, with the images showing clearly the chondrocytes within the extra cellular matrix. The pericellular matrix in the superficial and transitional zones was characterised by an increase in the fluorescence and a decrease in the SHG intensity. The chondrocytes were found to contain bright spots in both the CARS and the TPF images. These were not colocalised indicating that they were from different structures. A 3D reconstruction generated from a stack of images taken at the articular surface showed the flattened shape of the chondrocytes. En-face imaging only allowed the superficial tissue to be imaged and therefore to investigate the deeper zones cartilage sections were used which included the zone of calcified cartilage and the underlying subchondral bone. Multi-photon images of these sections showed clearly the changes in cell shape and distribution with depth which corresponded well with previous descriptions. The tidemark showed up clearly on the images and there was an increase in the TPF from the calcified tissue compared to the non-calcified tissue. The tidemark was characterised in the SHG images by a decrease in intensity and further work will be needed to investigate whether this relates to a change in collagen fibre organisation.

When carrying out the CARS imaging of the cartilage the OPO was tuned to the resonant frequency of the CH<sub>2</sub> symmetric stretching bond vibration. This provides good contrast for the lipids within the tissue which for which each molecule contains many CH<sub>2</sub> bonds. The CARS imaging could be extended to imaging other molecules by tuning the laser to the frequency of another bond vibration for example the O-P-O bond vibration for DNA<sup>61</sup> or the amide bond for proteins<sup>62</sup>. Tuning to image the DNA would provide additional information on the nuclei of the chondrocytes and imaging the amide bond in protein may provide good contrast for both the cells and the extra-cellular matrix. TPF images showed bright spots within the cells which were not co-localised with the bright spots within the CARS images when imaging with the CH<sub>2</sub> bond vibration. Experiments to see if they were co-localised with any alternative CARS bond vibrations should help to discover the identity of the bright fluorescent spots. Another possibility is to investigate bond vibrations from the proteoglycans, if a suitable vibration could be identified in the Raman spectra for proteoglycans then this could be used to map their distribution in the cartilage.

When imaging osteoarthritic tissue using SHG and TPF we were able to see changes which occurred in both the inter-territorial matrix and the pericellular matrix. This investigation needs to be extended by combining the SHG and TPF imaging with CARS imaging. As shown in section 4.3 CARS imaging of the CH<sub>2</sub> bond provides information on the chondrocytes within the tissue. The cell morphology has been observed via con-focal microscopy to change in degenerate tissue<sup>133</sup> and CARS imaging could provide information on the health of the cells in our samples. It may possibly be able to provide a method for identify cells which are undergoing apoptosis and combined with TPF and SHG imaging would enable one to clearly identify empty lacunae left as a result of cell death. This would be a useful tool in osteoarthritis research as the significance of cell death by apoptosis into the progression of osteoarthritis is an area of debate<sup>140, 141, 143-146</sup>.

There is scope to extend the work on imaging lesions carried out in this chapter. As mentioned previously there is a large variety of the different types of lesion which occur even within a single joint. It is difficult to determine whether different lesion types are different stages of the disease process or represent different degenerative pathways within the tissue. In order to characterise the changes which occur with osteoarthritis a much larger sample size would be needed to account for the large amounts of variation. There may too be more subtle changes occurring near the lesion such as changes in the number and size of the chondrocytes. These are difficult to distinguish from the normal variants of the healthy state, and therefore would require larger sample sizes to study them. The most promising advantage of the present techniques is the imaging of the micro-lesions seen in the samples which appear macroscopically normal, especially since the early stages of the disease progression are the least well understood. For larger lesions the overall structure of the lesion is not apparent from the multi-photon images as it is much larger than the field of view of the microscope. The investigation into osteoarthritic tissue has focused on the surface and superficial cartilage. Future work should be carried out to investigate any changes which occur with disease deeper within the tissue and at the tidemark and zone of calcified cartilage. In the osteoarthritic tissue changes occur in the collagen fibre organisation, this can be investigated using polarization sensitive non-linear microscopy as discussed in chapter 6.

## 5 Imaging Elastin Networks

---

### 5.1 Introduction

Multi-photon microscopy has been useful for revealing the elastic fibre networks in other tissues which contain a network of both collagen and elastin fibres for example in the dermis<sup>40, 147</sup> blood vessels<sup>67, 148</sup> and heart valves<sup>68, 149</sup>. In this chapter we use a combination of SHG and TPF imaging to reveal the network of elastin fibres within the collagen matrix of cartilaginous tissues.

The imaging of articular cartilage presented in Chapter 4 revealed a significant network of fibres in the TPF images, which were presumed to be elastin fibres due to the well known fluorescent properties of this protein. These fibres are evident in the TPF images but not the SHG images and therefore cannot be collagen fibres. Although this network of fibres had previously been observed by Yeh et al<sup>80</sup> no detailed study into their distribution and organisation had been carried out. Previous to multi-photon research into cartilage it was believed that articular cartilage contained no elastin fibres and there were only two other papers reporting the possibility of these fibres<sup>86, 87</sup>. In this chapter we confirm that these fibres are indeed elastin via the technique of immuno-staining and investigate the organisation of the fibres within the cartilage. The elastin fibres within the articular cartilage may contribute to the physical properties of the tissue. In order to provide a basis for future research into the possible mechanical function of these fibres we carry out imaging to find the orientation of the elastin fibres with respect to the articular surface and variations with depth and between different joint regions which are subjected to different stresses. The relationship between the number of fibres and the age of the sample is also investigated.

Elastin is known to occur in other cartilaginous tissues. In this chapter multi-photon imaging results from intervertebral disc and elastic cartilage are also presented. The elastin network in all three tissues are investigated and compared.

The sample sources and preparation of all three tissues is described in Chapter 2. We examine elastin fibres in both en-face samples and transverse sections using microscope 2.

## **5.2 Elastin in articular cartilage**

### **5.2.1 Confirmation of the identity of elastin fibres using immuno-staining**

As there has been no previous work which definitively proved the presence of elastin fibres within articular cartilage immuno-staining was used to identify the fluorescent structures revealed by TPF. Multi-photon images were taken of the slices of cartilage directly after dissection and the fibres within the samples were visualised. The samples were then taken by Dr Jing Yu (Department of Physiology, Anatomy and Genetics, University of Oxford) who carried out immuno-staining and sectioning. For the immuno-staining fresh tissue slices (as described in section 2.5.1) were firstly blocked with normal donkey serum for 5 hrs at 40 °C, then incubated with elastin antibody (Biogenesis, UK) overnight at 4°C. A secondary antibody conjugated with the fluorescent dye Cy3 was then added, to allow the fibres to be visualized. 20 micron sagittal sections were cut from frozen and mounted using a DAPI-containing medium on poly-lysine coated slides.

Figure 5-1 shows an en-face multi-photon image taken from the sagittal ridge of an 8yr old horse and alongside it an image of an immuno-stained section taken from the same sample viewed using transmission fluorescence microscopy with a polarized filter combination. The immuno-staining confirmed the presence of a network of elastin fibres in the superficial zone of the articular cartilage, with the majority of fibres within the first 50µm below the articular surface but with some fibres seen at depths up to 175µm towards the end of the section. The TPF fibres were observed within the same region of the cartilage and therefore we conclude that the fibres within the TPF images are indeed elastin. The pericellular matrix exhibited TPF, and there was also fluorescence associated with the cells in the immuno-stained images this suggested that some of the fluorescence from the pericellular matrix may be from elastin, however there may be additional fluorophores contributing to this fluorescence and no individual fibres have been resolved in this region.

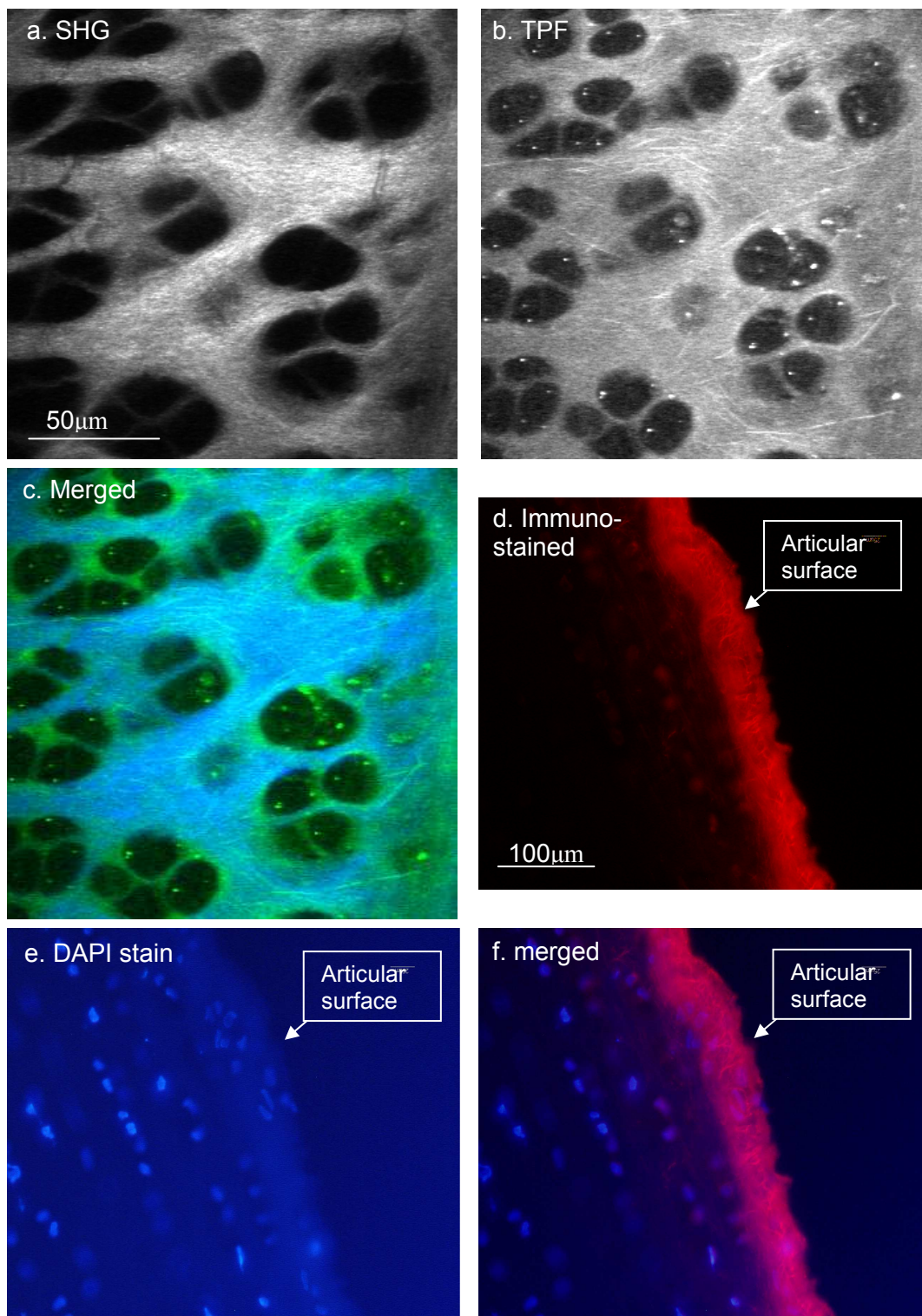


**Figure 5-1 Multi-photon imaging and immuo-staining of elastin fibres.** Elastic fibres from the sagittal ridge of 8yr old horse (sample with no OA). Parts a-c show multi-photon images taken of the sample directly after dissection (in the merged image green = TPF and blue = SHG) enface imaging at a depth of 5µm below the articular surface. Elastin fibres are clearly visible within the TPF images. Parts d-e show stained histological sections taken from the same sample, these demonstrate the distribution with depth. (d) shows the sample immuno-stained for elastin using a fluorescent dye, (e) shows DAPI staining for the nuclei within the sample and (f) shows the merged immuno-stained and DAPI stained sample. Images (d-f) courtesy of Dr Jing Yu.

### 5.2.2 Transverse Sections

As the immuno-stained sections showed elastin to a depth of approximately 50 $\mu$ m, transverse sections were also investigated with multi-photon imaging. Figure 5-2 shows TPF and SHG images of the superficial and transitional regions in a transverse section taken at the cortical ridge. Before the section was prepared enface TPF imaging was carried out on the cortical ridge and this revealed a network of elastin fibres (these are also shown in figure 5-2). The TPF images show bright spots within the matrix, however they do not show a network of long fibres. This may be because many of the fibres are perpendicular to the imaging plane. The brightest spots are about 1 $\mu$ m in diameter and approximately 50% brighter than the surrounding matrix.

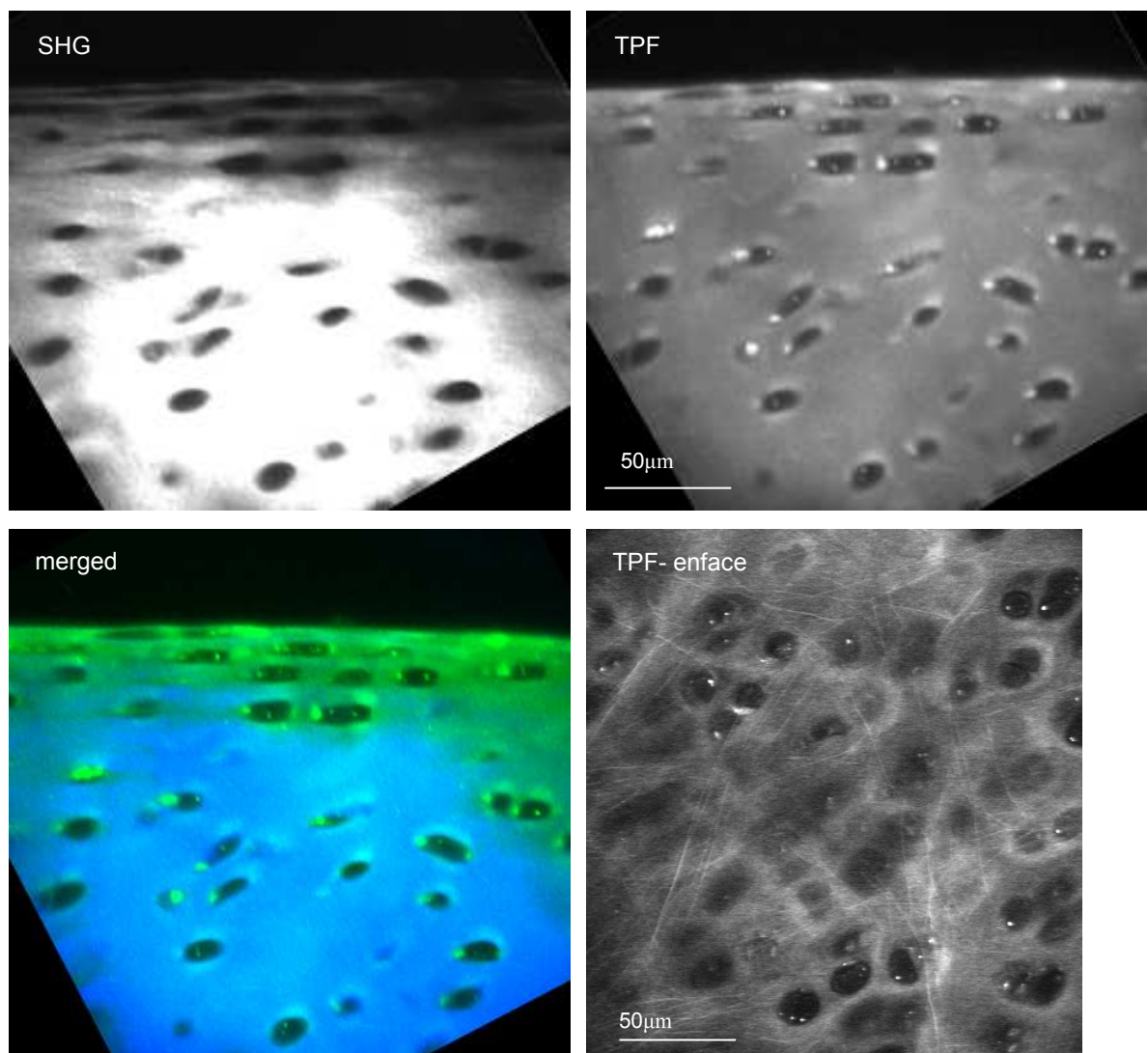


**Figure 5-2** TPF and SHG imaging on a transverse section. The section has been taken from the cortical ridge region, enface imaging of this region revealed elastin fibres in the superficial layer.

### 5.3 Distribution of elastin fibres across the joint surface

The forces on the cartilage vary hugely between different regions in the metacarpophalangeal joint and therefore we investigated the distribution of elastin fibres at different regions on the joint surface. The different regions investigated are shown in figure 5-3. The dorsal region of the 3<sup>rd</sup> metacarpal articulates with the proximal phalanx, and therefore areas 5,6 and 8 experience high shear forces due to the extensive rotation of the joint<sup>150</sup>. The sesamoids bear the weight of the standing horse and during galloping therefore this region is subjected to large compressive forces. The cortical ridge marks a change in curvature between the palma and dorsal regions, this area is subjected to the largest shear stress and is the most common site of lesions.<sup>151, 152</sup> At each region 2 stacks of both SHG and TPF images were taken to a depth of 30 microns. This experiment was repeated on 3 horse samples with the ages 5 ½, 6 and 8 yrs.

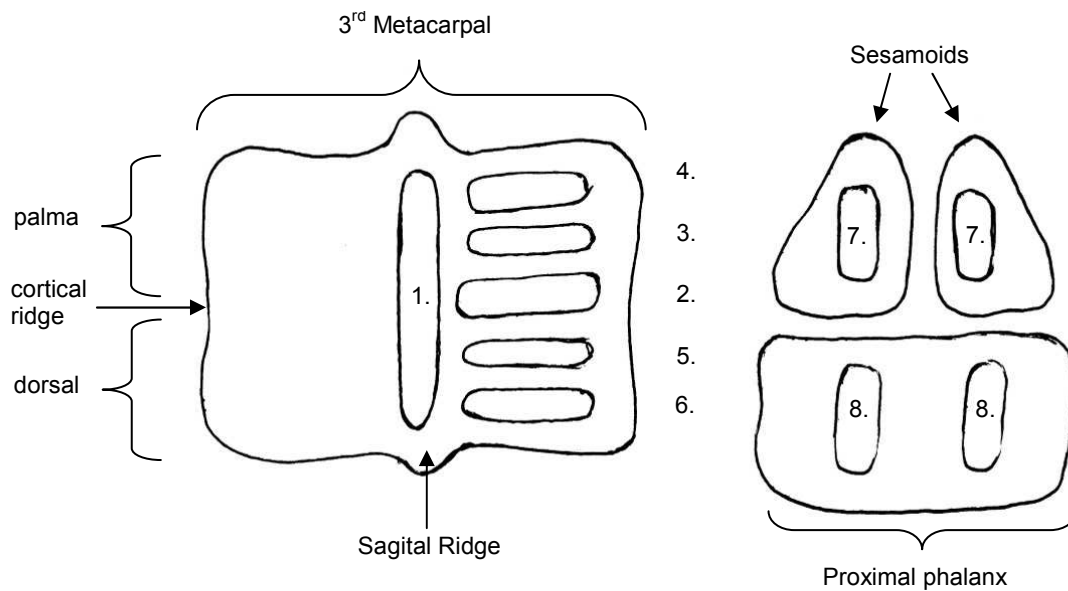


**Figure 5-3** Areas imaged for elastin fibres within the metacarpophalangeal joint.

All the regions investigated contained elastin fibres in the superficial zone. However variations in the organisation and density of the fibres were observed as summarised in figure 5-4. In the cortical ridge and sagittal ridge areas the fibres were generally parallel (see figure 5-4 a) and lying across the joint perpendicular to the joint articulation. Whereas in the dorsal and palma regions there was a network of crossed fibres (see figure 5-4b). In the sesamoid region there was a sparser fibre network no apparent organization (see figure 5-4c). Figure 5-5 illustrates features of the fibres distribution that were common to all three

joints examined. In some regions (dorsal, palma and proximal phalanx) there is variation between horses and a larger study will be required to fully characterise patterns and variability.

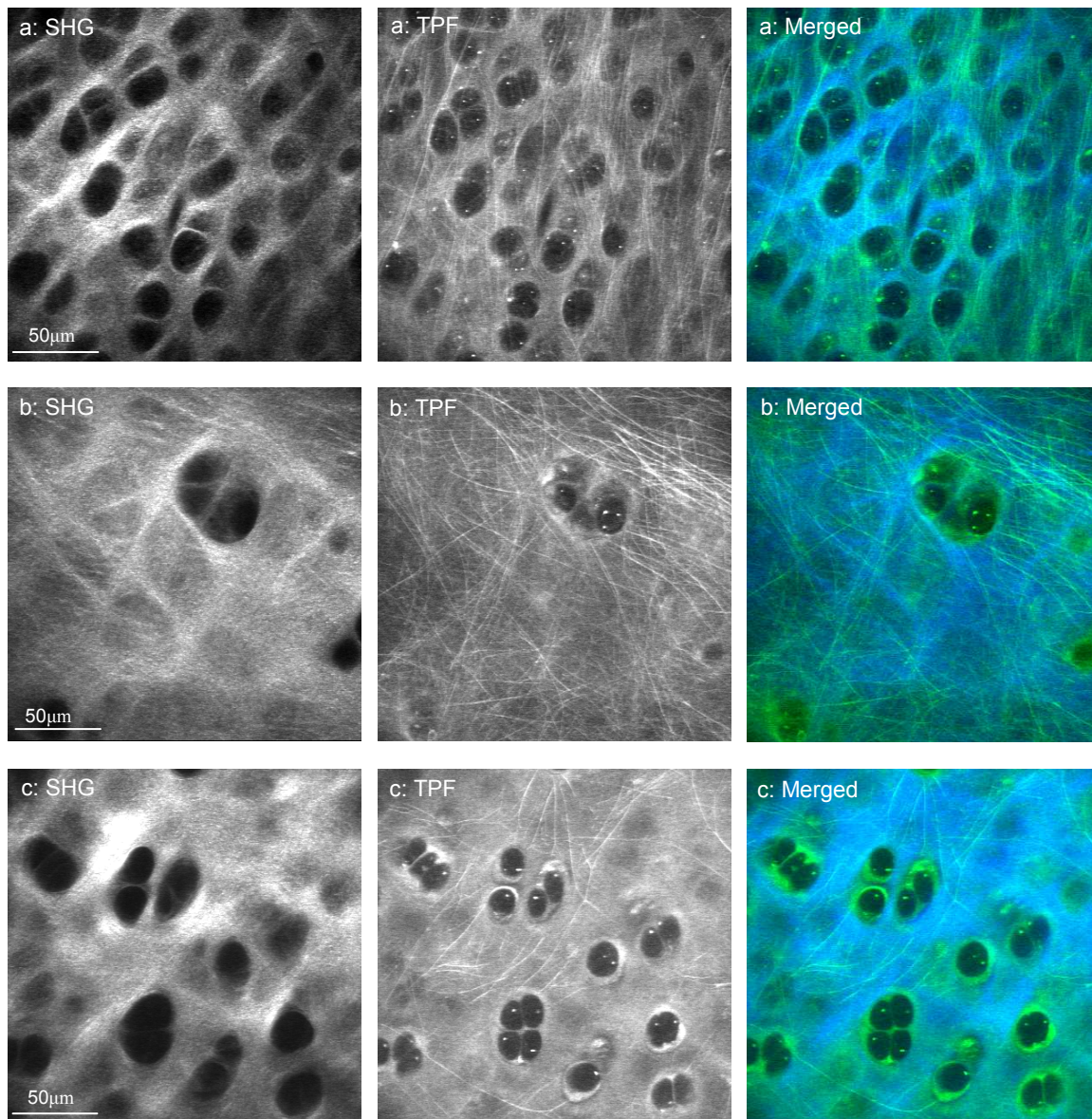


**Figure 5-4 Elastin fibre arrangements from different regions.**

Multiphoton images taken at different areas on the articular surface (all at a depth of 3 microns from the articular surface) The SHG images show the collagen matrix and the TPF images show the elastin fibres and back-ground fluorescence from the extra-cellular matrix. In the merged images blue= SHG and green = TPF. Parallel elastin fibres were found in the cortical ridge area (a) this pattern of fibres was also repeated on the sagital ridge (image not shown). A dense network of crossed fibres were seen in the palma 1 region (b) similar arrangements were also seen in the dorsal area. Some areas for example the sessamoids showed a sparser network of elastin fibres with no apparent preferred orientation (c).

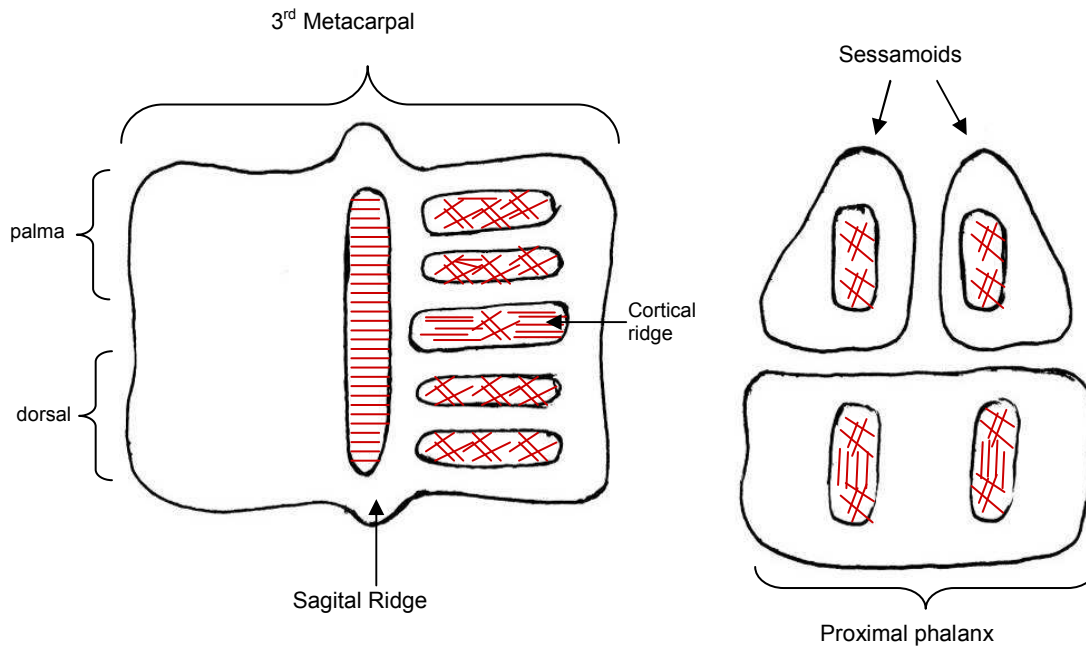


**Figure 5-5** A schematic diagram of elastin fibre orientations in different regions. The red lines represent the predominant fibre orientation. The data shows the most commonly observed fibre orientations summarised from the 3 samples.

To investigate the variations in fibre density with depth in different areas the number of fibres was counted in each frame within stacks of images taken from the most superficial 30µm of tissue at the articular surface. The results are shown in figure 5-6. From these results the distribution of elastin fibres as a function of depth did appear to vary for the different regions; however a larger sample size would be needed to investigate this further.

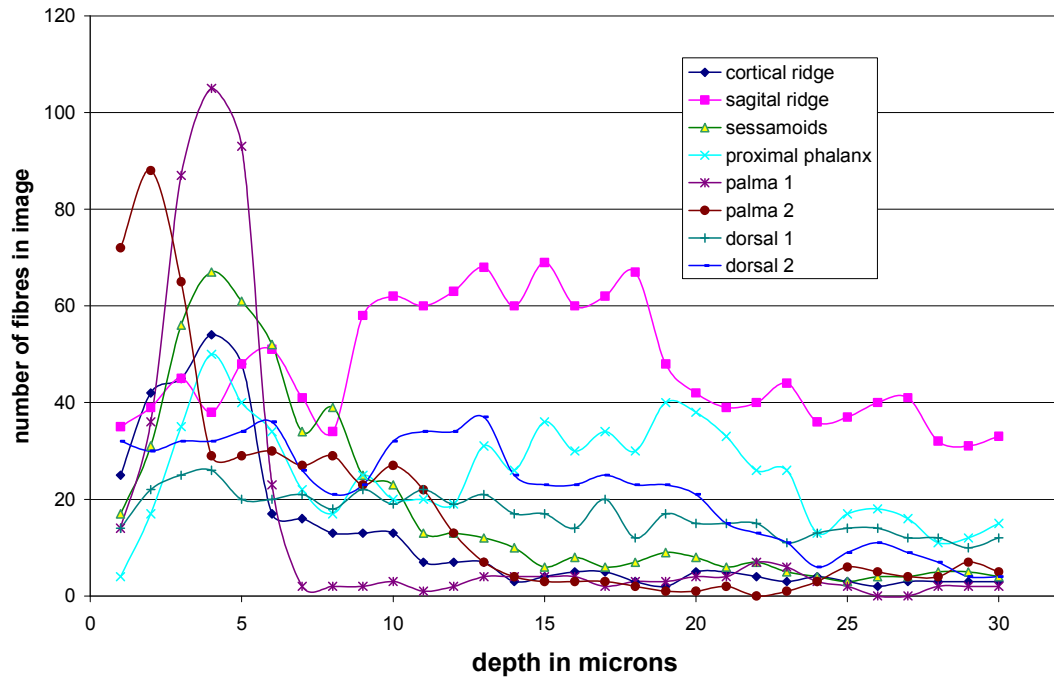


**Figure 5-6** The number of elastin fibres as a function of depth. Data has been taken for 8 the different areas investigated on the joint surface (the data was collected from an 8yr old sample showing no OA)

### 5.3.1 Fibre properties

The majority of the fibres within the articular cartilage appear to be long and straight suggesting that they may be under tension. In some areas curve fibres have been observed like those seen in the sesamoids (figure 5-4c). The stacks of images have been analysed to find branching elastin fibres and examples of these are shown in figure 5-7. These images are taken from regions where the elastin network is sparse in order to avoid confusion between sites where two elastin fibres may cross within the same field of view. The elastin fibres showed a wide range of branching angles from 8 – 85degrees, also some fibres split into multiple branches.

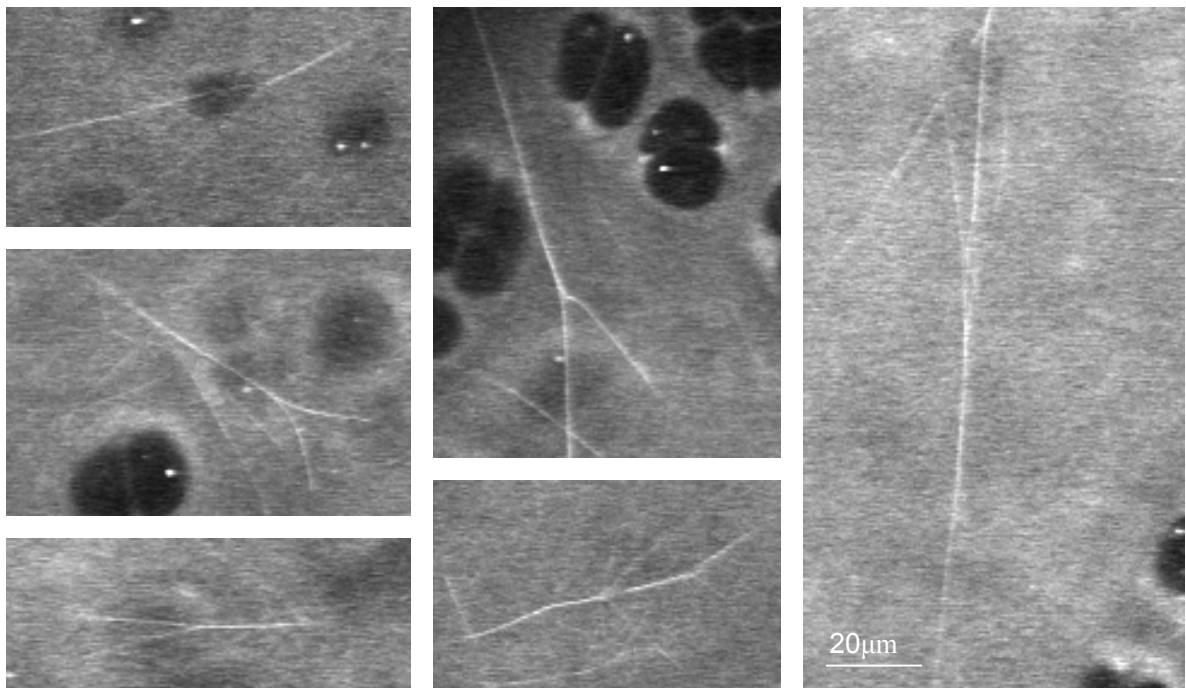


**Figure 5-7 Montage of TPF images showing branching elastin fibres.**

Variations in the thickness of the elastin fibres were also observed. In a given image there are differences in the fibre thicknesses and also variations between imaging areas. The larger elastin fibres are brighter with respect to the back-ground fluorescence of the matrix and appear thicker on the images. The thickest fibres are often visible in more than 1 frame in the stack of images, at  $1\mu\text{m}$  separation as for example the thick fibre shown in figure 5-8 is visible in 3 frames. However this does not mean that the fibre is greater than  $1\mu\text{m}$  in diameter as the focal spot dimensions are greater than  $1\mu\text{m}$  in the z-axis so a fibre with submicron diameter may still appear in 3 images separated by  $1\mu\text{m}$ . The finest fibres visible on the image (for example the fibre in figure 5-9) are only 1 pixel in width and are approximately 25% brighter than the background matrix. Finding fine elastin fibres within the matrix is made more difficult by the fact that the background intensity of the matrix is not uniform but fluctuates between the pixels by between 5 and 10%. It is possible that the cartilage contains more elastin fibres than those visible in the TPF images, as below a certain size the fibres probably will not be visible against the back-ground fluorescence of the extra-cellular matrix. From this we conclude that all the elastin fibres in articular cartilage have a diameter  $\leq 1\mu\text{m}$ . We are unable to give a value for the minimum fibre diameter due to the resolution limitations and the difficulties of detecting very fine fibres against the background fluorescence.

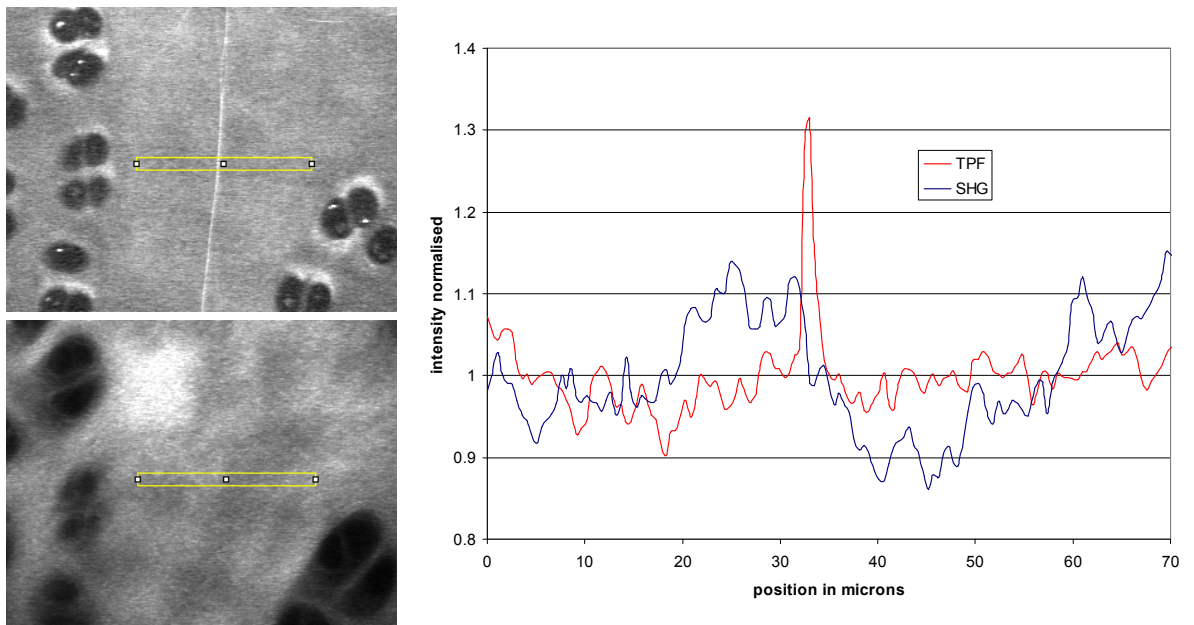


**Figure 5-8 Profile across a thick elastin fibre.**  
This fibre is from the sessamoid region and appears in 3 different frames within the stack

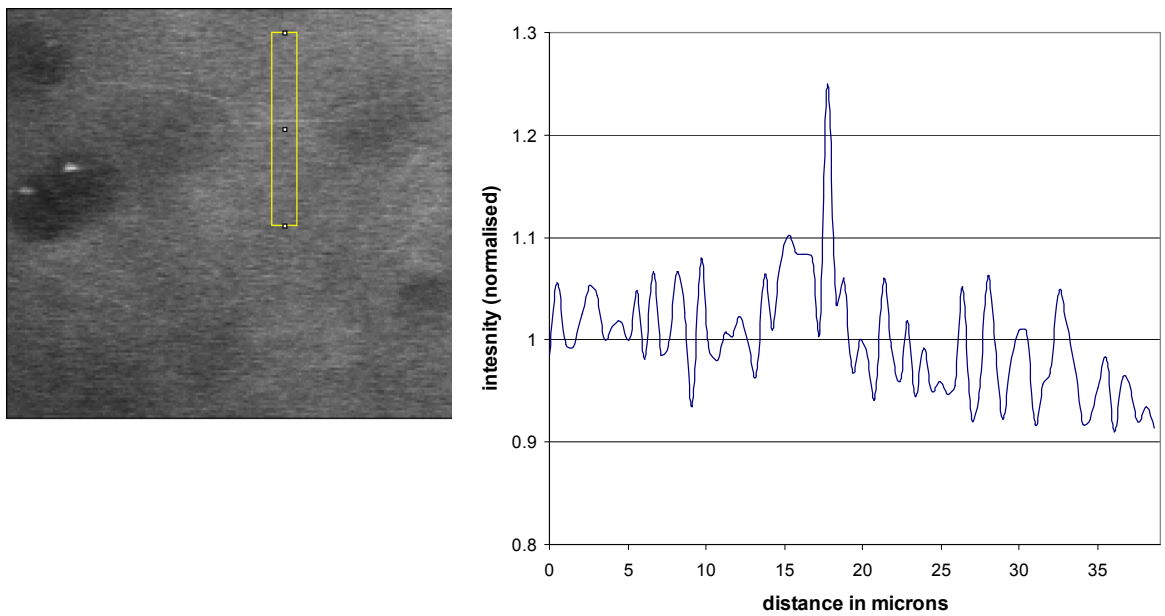


**Figure 5-9 Profile across a thin elastin fibre.**  
This fibre is from the dorsal regions.

### 5.3.2 Elastin fibre variations with age

The ability of cells to produce elastin is lost at maturity and therefore the amount of elastin in tissues may be age dependent. To investigate this we imaged the cortical ridge region of samples of different ages and counted the number of elastin fibres within the images. As the fibres were found to be most abundant in the superficial layer we counted the fibres within the first 30 microns below the articular surface. The number of fibres in each image of the 30 image stack was counted and then averaged over the entire stack and corrected to give the mean number of fibres within a  $100 \times 100$  micron area at the articular surface. 11 samples were imaged with an age range of 2-20yrs and all the samples used had no or only very early signs of osteoarthritic damage. In samples demonstrating very early lesions the imaging site was chosen to be far away from the lesion area. Samples containing advanced lesions were rejected as in these samples there is likely to be a loss of elastin fibres due to a pathological process rather than the normal aging process.

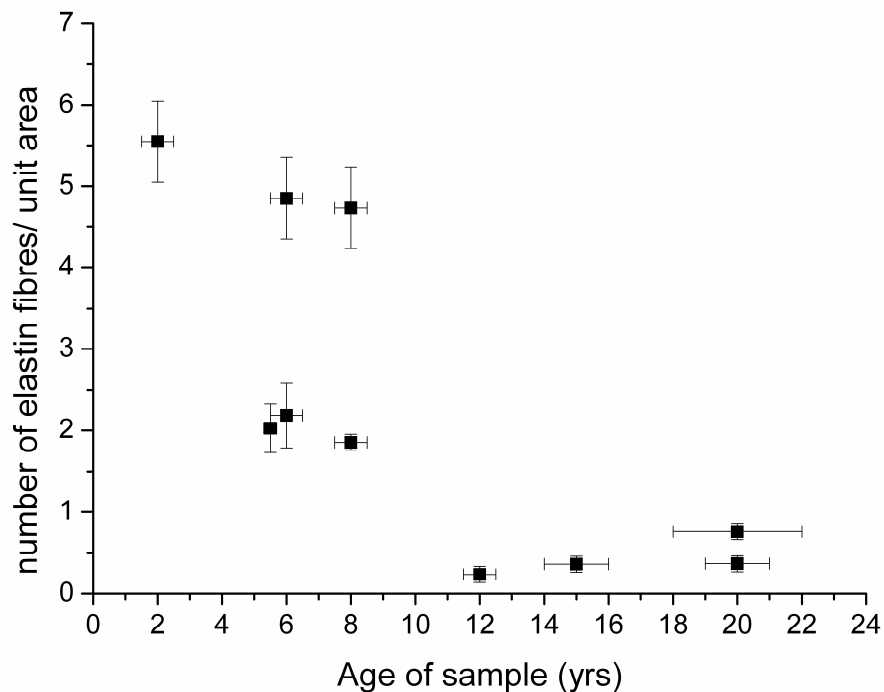


**Figure 5-10** Age dependence of elastin fibre density. The number of fibres per unit area in the superficial cartilage of the cortical ridge area of cartilage is plotted against the age of the horse.

The correlation coefficient for this data was calculated and found to be -0.78 indicating a negative correlation between the age of the sample and the number of elastin fibres. A

significance test was carried out on the correlation coefficient and from this it was found that the null hypothesis that the number of elastin fibres within the sample was independent of age could be rejected with 99.5% certainty. This raises the question of how the elastin fibres are lost. Are the elastin fibres removed locally by enzymatic digestion or by mechanical wear at the articular surface? Figure 5-11 shows broken elastin fibres near a small split at the articular surface. The large number of broken elastin fibres in this image suggests that they were damaged by a mechanical process.

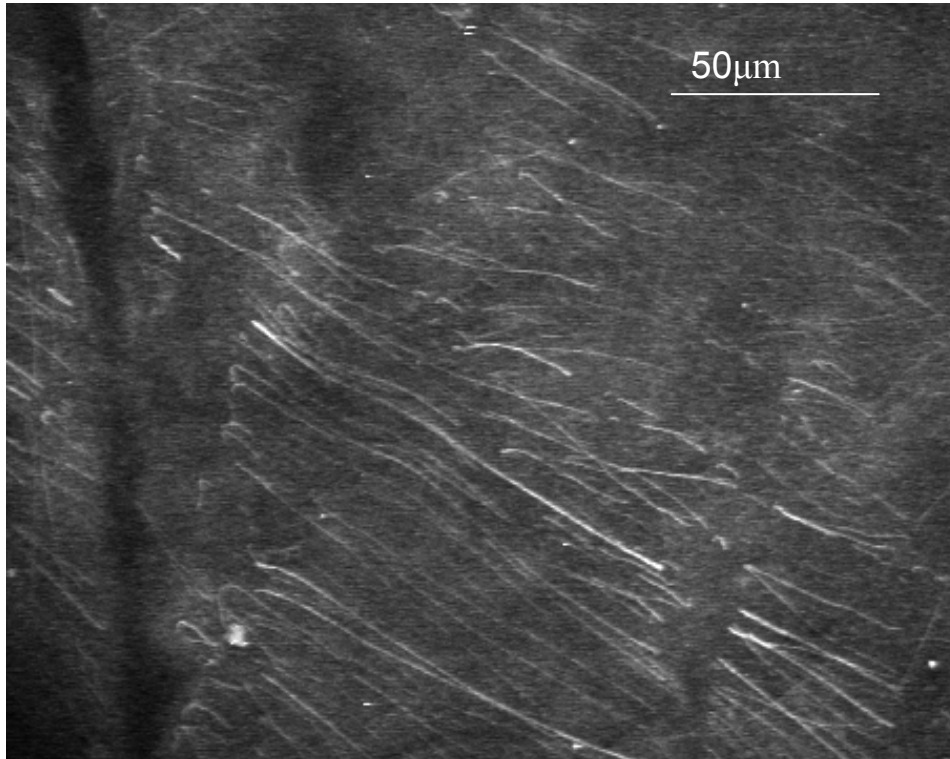


**Figure 5-11 TPF image showing broken elastin fibres at the articular surface**

There are two other factors which it would be interesting to correlate the elastin fibre density against, these are level of disease in the sample (both local and global) and joint work-load although the later is very difficult to quantify.

## **5.4 Elastin in the intervertebral disc**

Elastin has been found in the disc annulus and the nucleus as reported by Yu et al using single photon fluorescence immuno-staining<sup>99, 153</sup>. In the annulus from the horse tail disc the elastin fibres could be seen with TPF to be running parallel with the collagen fibres and this is shown in figure 5-12. In the study by Yu et al similar fibres were seen in bovine and human tissue.<sup>99</sup> In the SHG images of the disc annulus the fibrous structure of the collagen can be clearly resolved (unlike in the articular cartilage). This is because the annulus collagen is mainly thicker type I collagen fibres<sup>100</sup> compared to the fine type II collagen fibres within the articular cartilage.

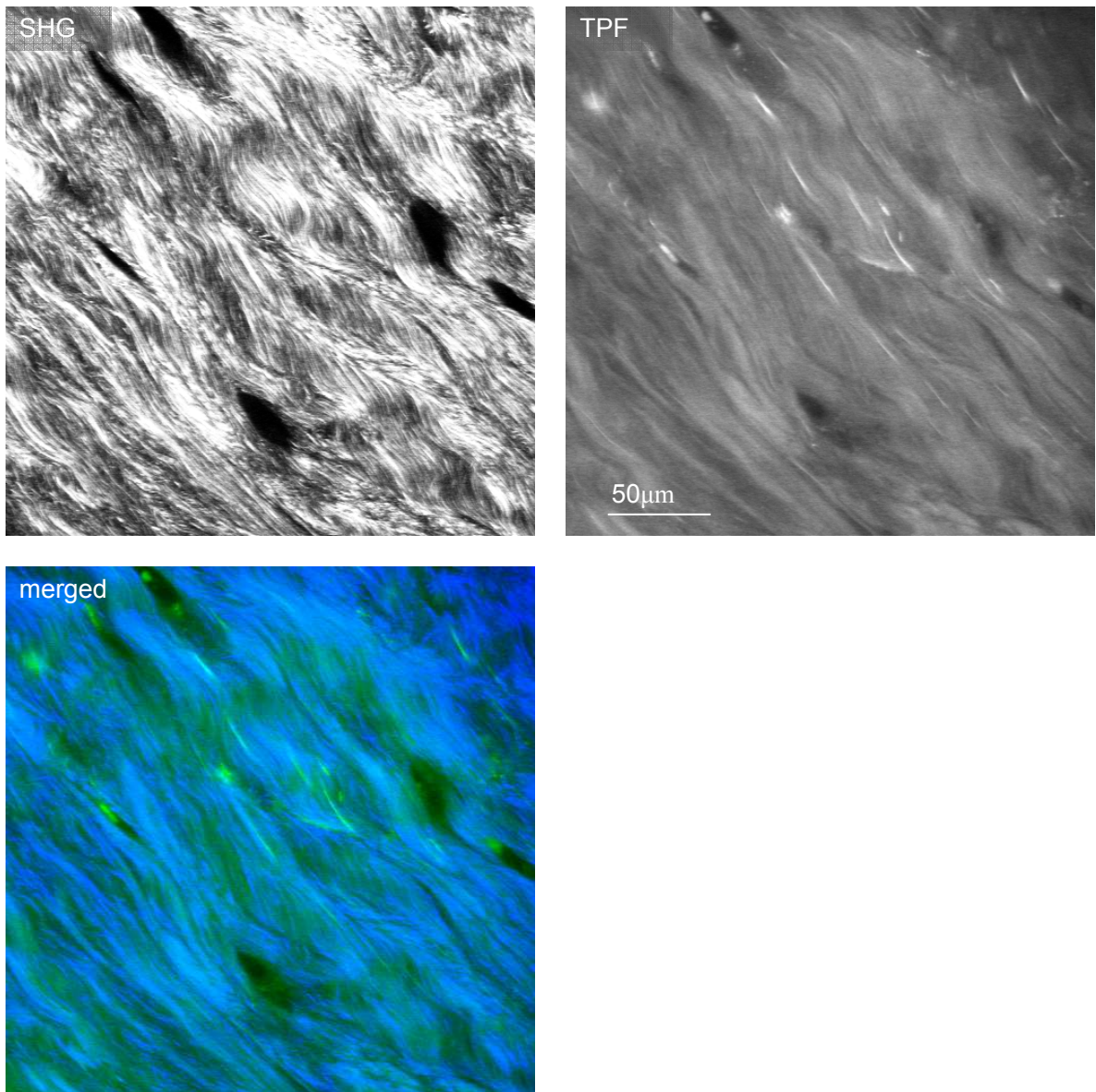


**Figure 5-12 Multi-photon microscopy of the intervertebral disc annulus.** Images from an equine tail disc (transverse section). Elastin fibres can be seen to run parallel with the collagen fibres within the disc.

A three dimensional reconstruction has been created from a stack of 44 images (separated by 1 μm steps) taken of this region and this is shown in figure 5-13.

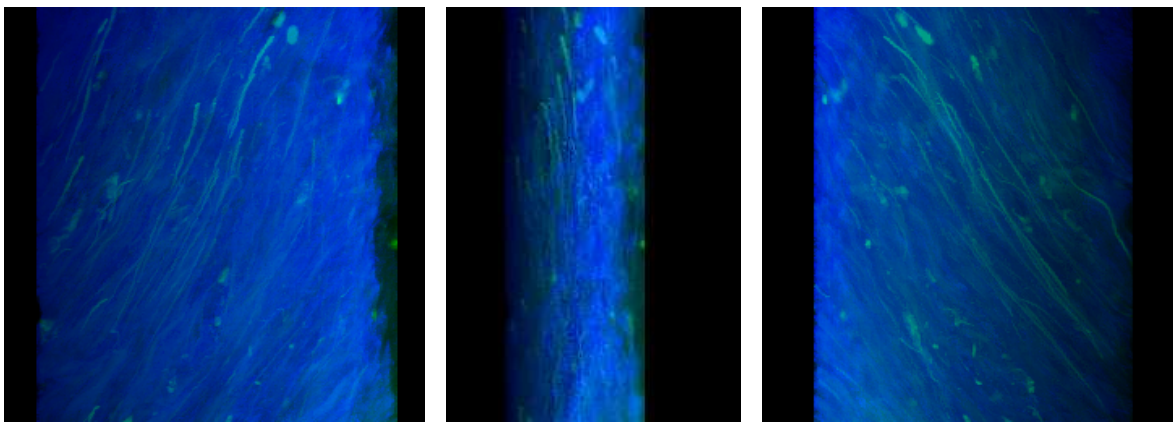


**Figure 5-13** 3 frames from a 3D reconstruction of the disc annulus. Generated from a stack of 44 images (size  $260 \times 260 \mu\text{m}$ ) taken from a transverse section of the disc annulus.

The thickness of the lamellae in the intervertebral disc depends on the species. In the discs dissected from rats tails several lamellae could be seen within a single field of view. This allowed the interlamellar space to be investigated. Yu et al had reported a much denser elastin structure in this region.<sup>99</sup> The images taken from the annulus of the rats tail disc are shown in figure 5-14. In these images increased fluorescence is seen between the lamellae, indicative of increased elastin in this region. However within the individual lamellae no elastin fibres can be resolved running parallel with the collagen fibres. This poses the following questions: Are there none of these fibres within the rats disc? Or are the fibres within the rats disc too fine to be resolved? Or are the fibres running in a different direction? To answer these questions further work would need to be carried out combining multi-photon imaging with immuno-staining. Figure 5-14 clearly shows the change in collagen fibre alignment between the lamellae. Alternate lamellae show a weaker SHG signal. This effect is due to the polarization sensitivity of the SHG from collagen, and in the faint lamellae the collagen fibres are orientated approximately perpendicular to the laser polarization, which is marked on the image.

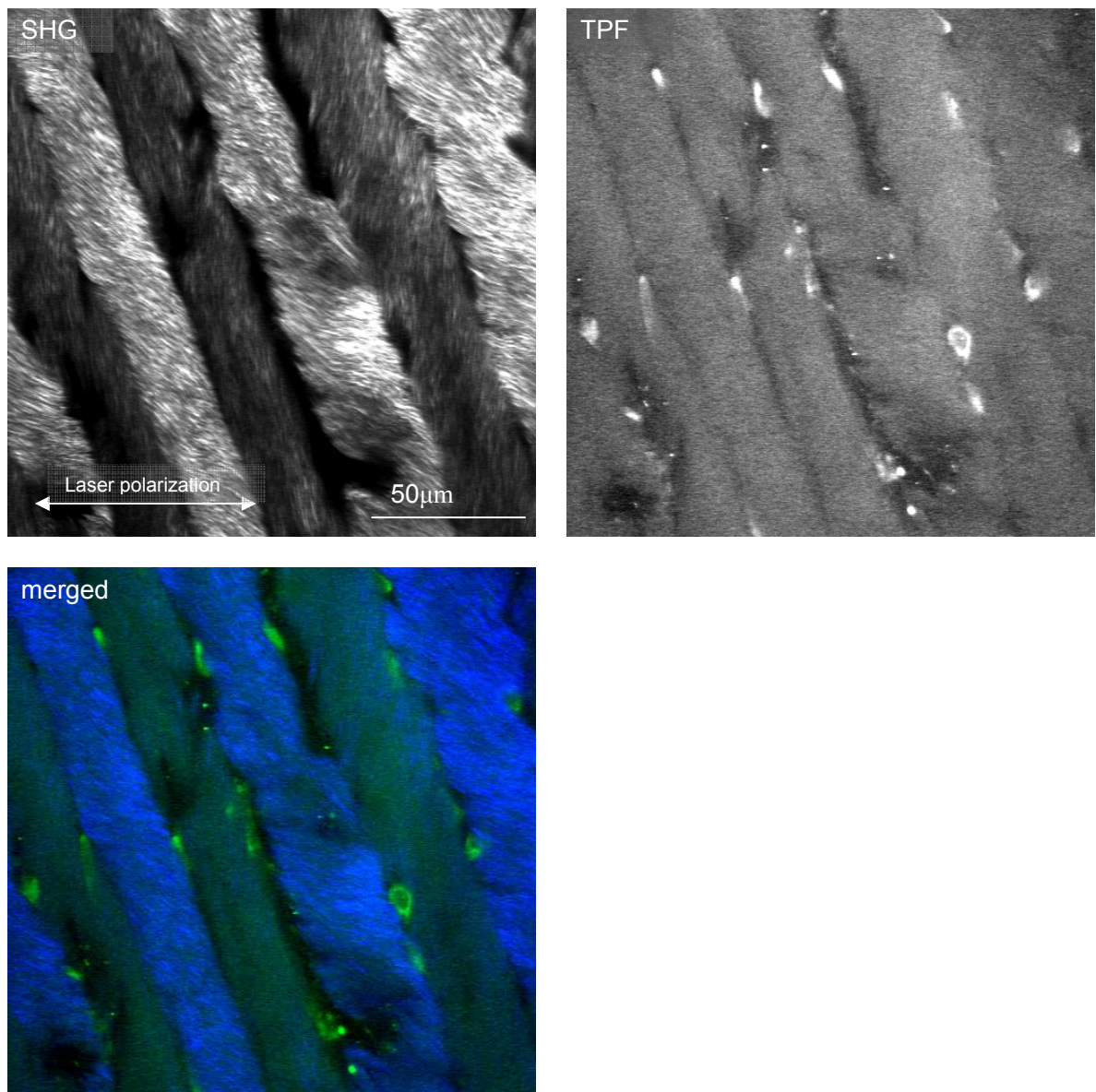


**Figure 5-14 Multi-photon images of the rat's tail annulus.**  
 The image shows increased fluorescence between the lamellae and the different collagen fibre orientations within the alternate lamellae.

Yu et al<sup>99</sup> reported fibres in the nucleus running radially towards the disc annulus and also fibres running longitudinally in the nucleus towards the cartilaginous endplates. The multi-photon pictures taken of the nucleus of an equine disc are shown in figure 5-15. There are a few elastin fibres within the matrix in the TPF images, and these appear short and this is because they are not lying parallel with the imaging plane. The SHG images from the nucleus show a less organised collagen structure in comparison with the annulus and this is in agreement with the previous literature.<sup>100</sup>

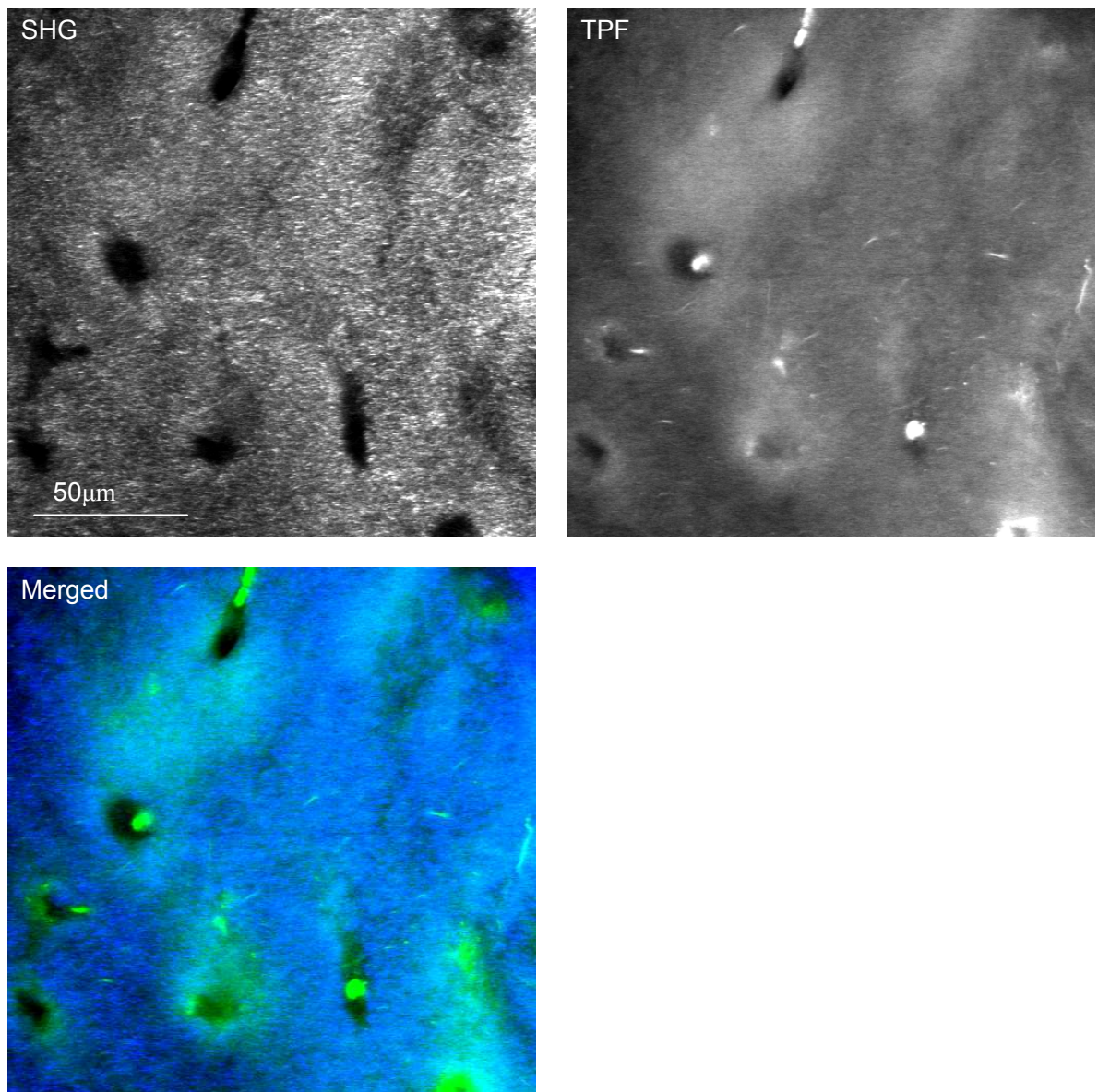


**Figure 5-15** Multi-photon images from the nucleus of the equine disc. The SHG image reveals the collagen matrix along with cell lacunae and the TPF image shows some elastin fibres. No fibre arrangement is apparent from this image and the elastin fibres appear short although this is most likely to be due to the fibres not lying parallel with the imaging plane. (transverse section).

## 5.5 Elastic Cartilage

The elastic cartilage from the ear contains two zones, an outer perichondrium and an inner layer. Both regions have been imaged, both as en-face tissue samples and transverse sections. In the inner zone we observed a mesh-work of thick elastin fibres as shown in figure 5-16 and figure 5-17. These were much larger in diameter (up to 5 $\mu$ m) than the fibres observed in either the articular cartilage or the intervertebral disc. In the SHG images the chondrocytes showed up as dark voids, as in articular cartilage. However, there were also smaller dark voids within the collagen matrix where the thickest elastin fibres were located. In the top right TPF image in figure 5-16 the matrix surrounding the elastin fibres appears black, however adjusting the contrast reveals the fluorescence from the rest of the extracellular matrix (see bottom right image in figure 5-16). Unlike in articular cartilage there is no increase in fluorescence in the pericellular matrix.

A 3D reconstruction has been generated from a stack taken in the inner region of the elastic cartilage (figure 5-17) and this clearly reveals the structure of the network of elastin fibres. Unlike in the articular cartilage and the disc, the fibres in elastic cartilage are not long and straight. Instead the fibres branch or join at approximately 10-40 $\mu$ m intervals, with a change of direction at the point of branching. There appears to be a wide range of branching angles and often more than 2 elastin fibres splitting off at a branching point. This is in agreement with previous descriptions of the elastin network in elastic cartilage as a branching honeycomb like or trabecular structure of thick fibres<sup>77</sup>.

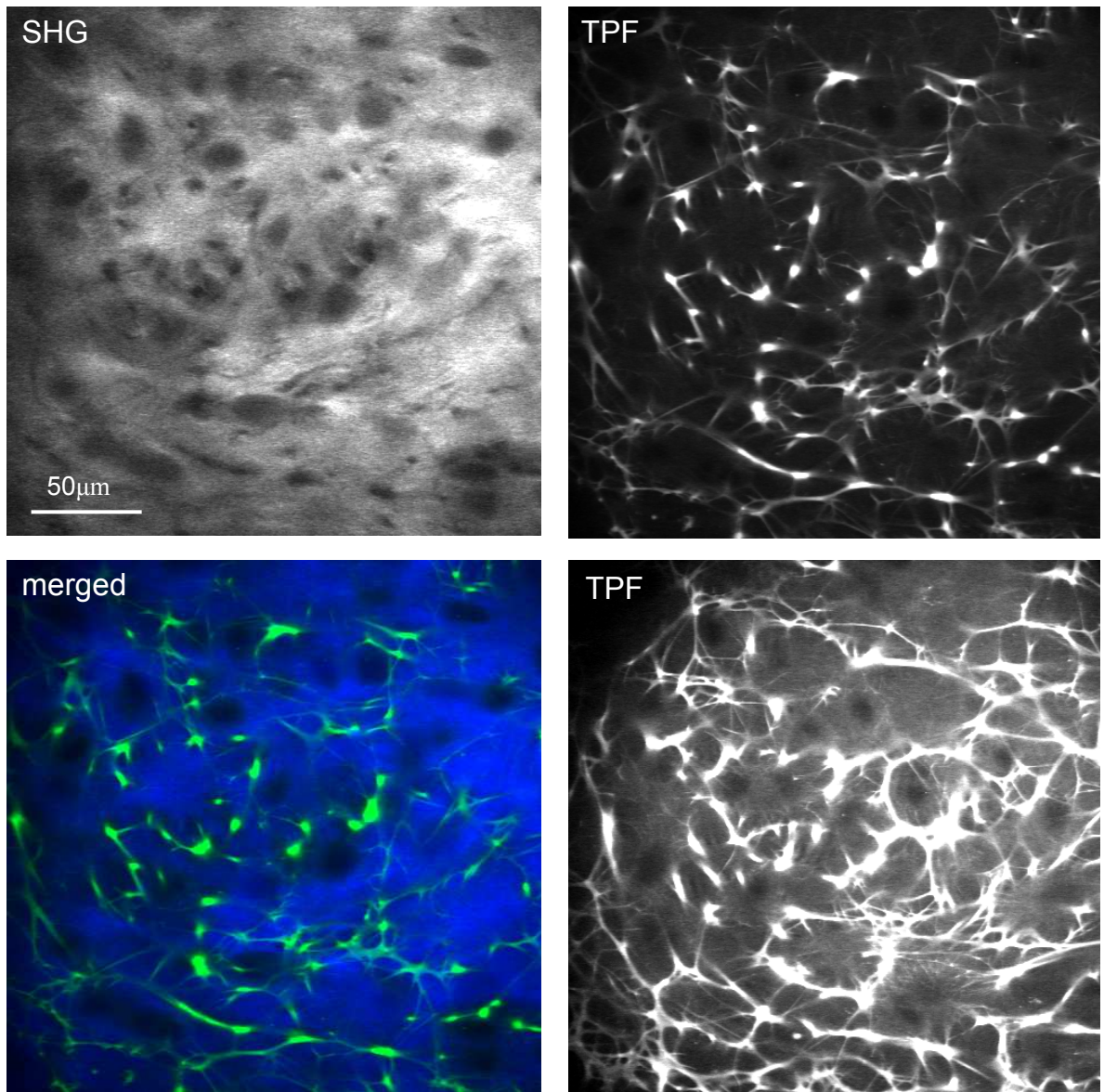
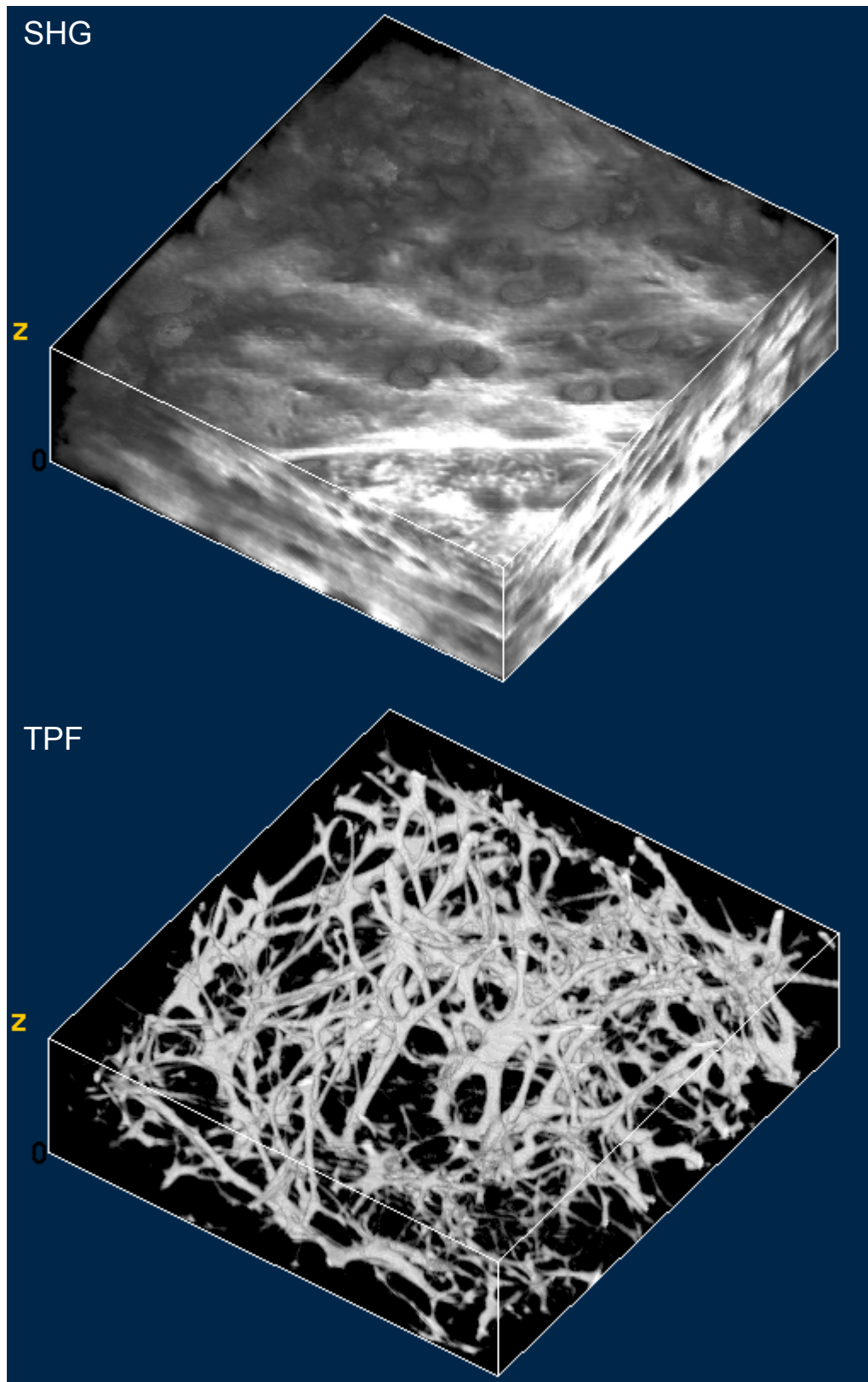
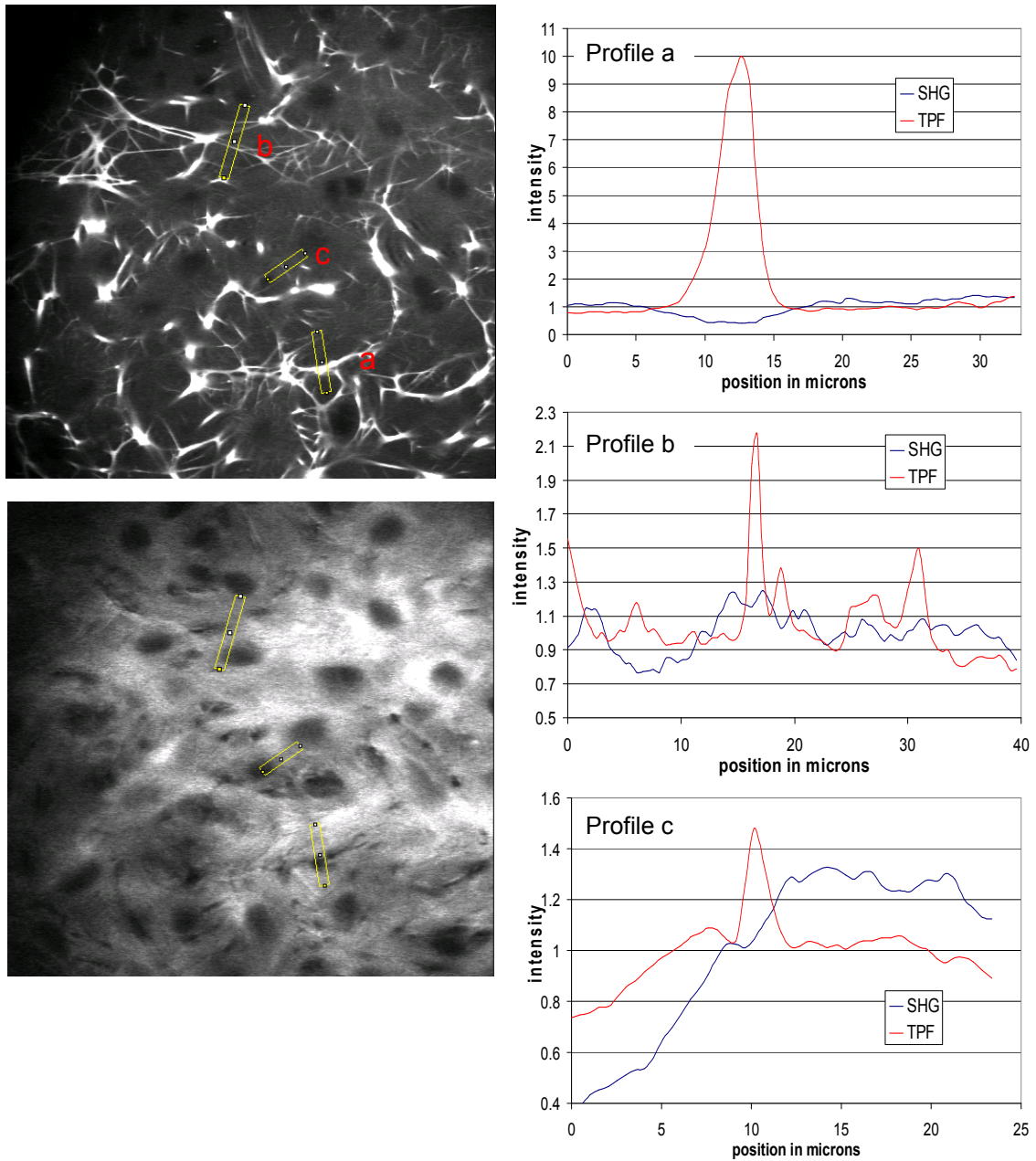


Figure 5-16 enface imaging of the inner portion of the elastic cartilage of the ear.



**Figure 5-17** 3D reconstruction of the inner portion of the elastic cartilage. This was generated from the SHG and TPF data taken in a stack of 62 images separated by 1 $\mu$ m. The dimensions of the reconstruction are 220x230x62 $\mu$ m.



**Figure 5-18 Profiles across elastin in elastic cartilage.** Profiles have been taken across elastin fibre structures of different sizes, thick fibres (profile a), intermediate sized fibres (profile b) and fine fibres (profile c). The intensity is normalised to the intensity in the region with no elastin fibres.

The elastin fluorescence is very bright in comparison to that seen from the elastin network in articular cartilage or intervertebral disc. TPF and SHG profiles taken across different sizes of elastin fibre structures within the elastic cartilage are shown in figure 5-18. The thick fibres shown in profile a shows the TPF intensity from the fibre is 10× the background intensity of the matrix surrounding the fibre. Intermediate fibres shown in profile b have a TPF intensity about 2× the background intensity and the fine fibre shown

in profile **c** have a TPF intensity about  $1.45\times$  the background intensity. Even the fine fibres show a higher intensity relative to the background intensity than the bright fibres within the articular cartilage. This suggests that these fibres are thicker than the fibres within the articular cartilage. The very thick fibres show a decrease in SHG intensity of over 50% corresponding to the position of the peak intensity of the elastin fibres. However for the smaller fibres there is no correlation between the SHG profiles and the TPF profiles.

Enface imaging of the perichondrium (figure 5-19) showed a woven structure of collagen fibres and a meshwork of elastin fibres between the collagen. The elastin fibres in this region are finer and straighter than the fibres within the inner region. The fibres appear most numerous in regions where there is a gap in the collagen matrix and in some areas appear to be running across linking different regions in the collagen matrix with different fibre orientations.

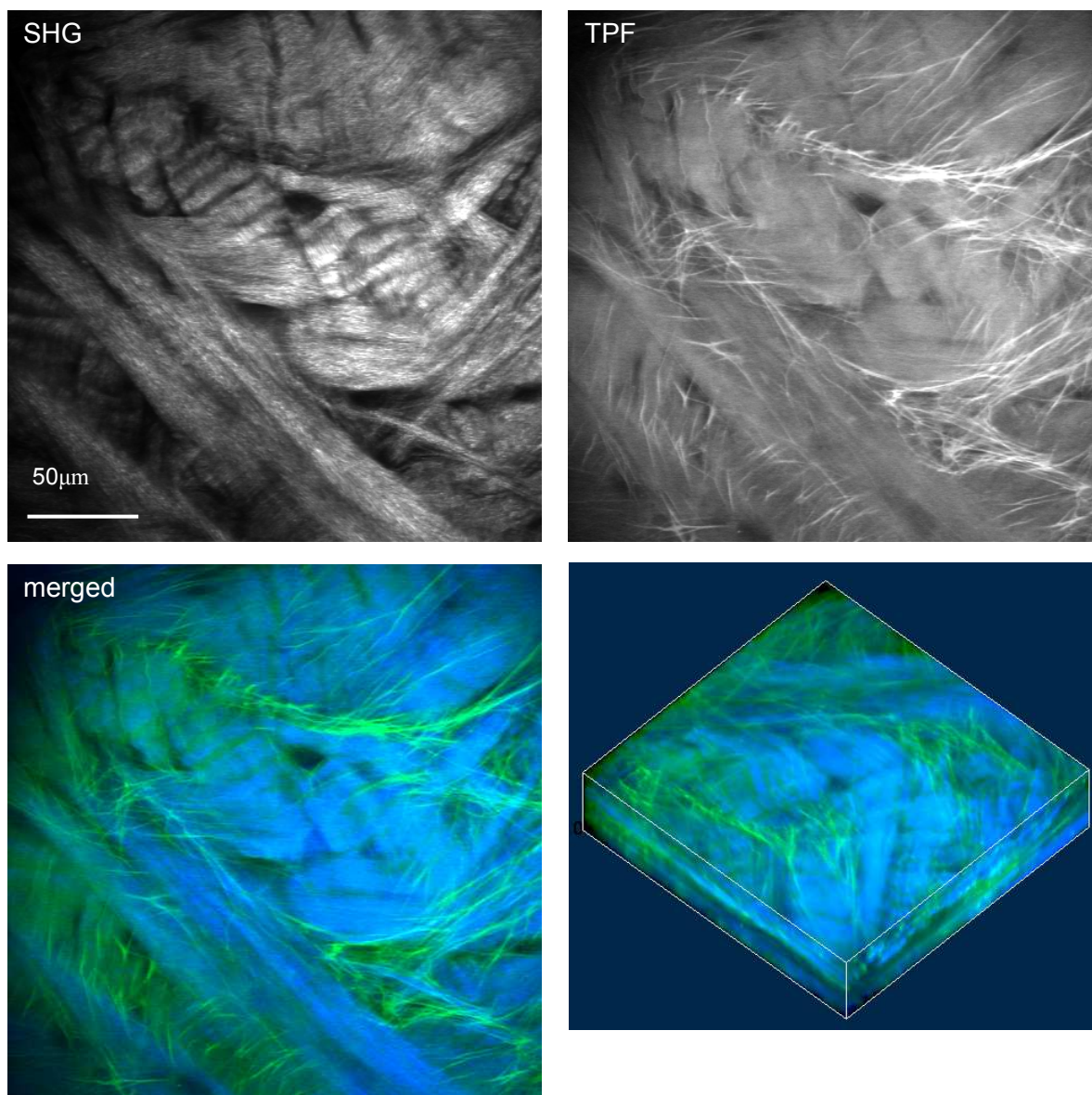


**Figure 5-19** The perichondrium layer of elastic cartilage viewed enface. The SHG image shows a structure of woven collagen and the TPF image shows a network of elastin fibres. A 3D reconstruction is generated from the stack of merged TPF and SHG images, the size of the reconstruction is  $204 \times 198 \times 50\mu\text{m}$

A cross-section of the elastic cartilage was imaged and the region containing the transition between the outer perichondrium and the inner cartilage is shown in figure 5-20. In this view of the perichondrium layer the elastin fibres appeared long and straight. These fibres were found to be lying parallel with the collagen fibres in this region. The collagen fibres of the perichondrium region were thicker than those seen in articular cartilage and more closely resembled the structure of the disc annulus. The change in elastin fibres between the two regions is not completely abrupt, with an intermediate zone with a meshwork of fibres

which are finer than those in the inner zone and some straight long fibres. This transition can also be observed through histological staining<sup>104</sup> and is shown in figure 5-21.

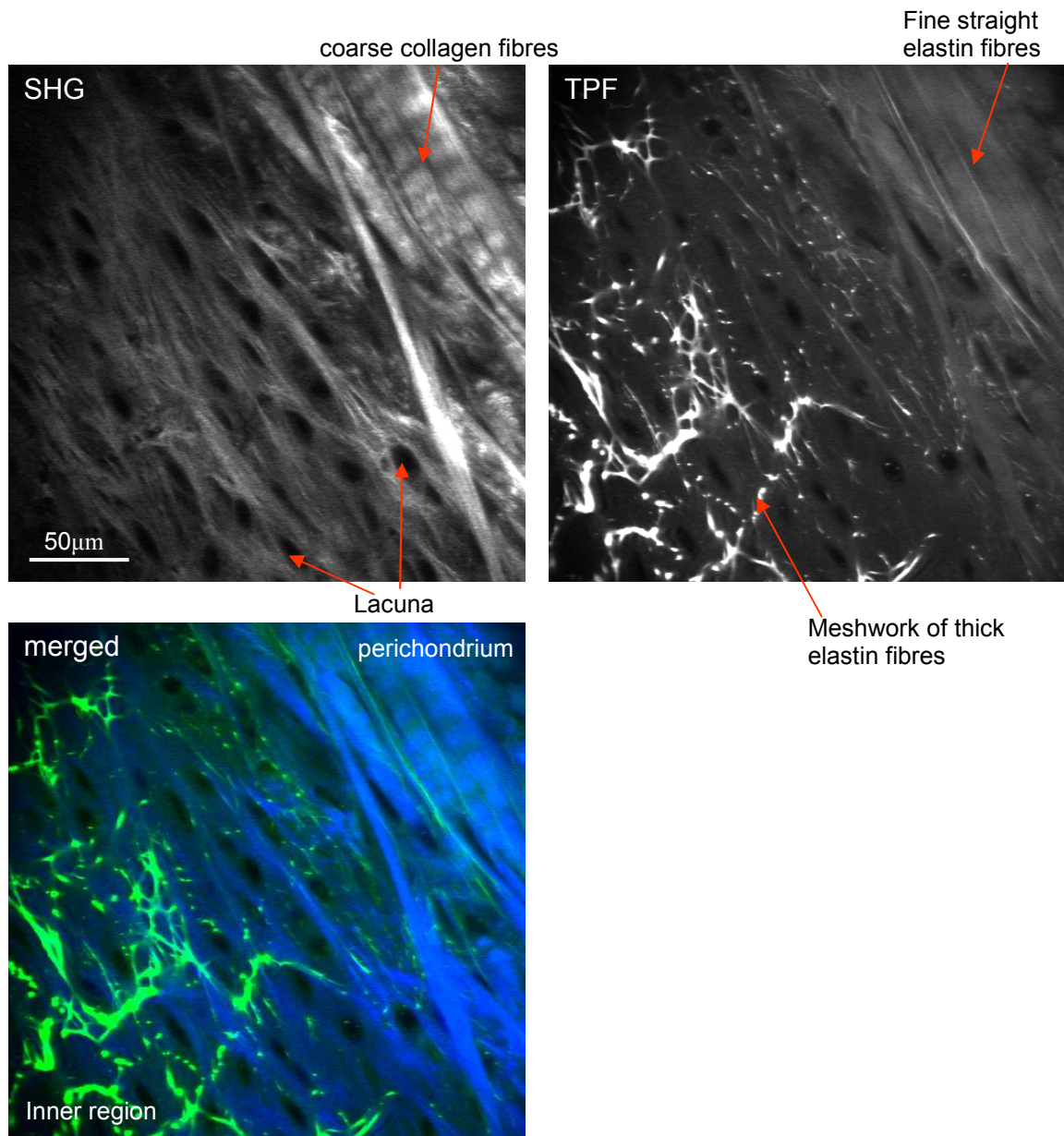


**Figure 5-20 SHG and TPF images from a transverse section of elastic cartilage. The region imaged shows both the outer perichondrium and the inner cartilage region.**

Multiphoton imaging of elastic cartilage has been carried out in a previous study by Yu et al<sup>154</sup> this study used both TPF and third harmonic generation (THG) with a 1230nm excitation laser source. Their TPF imaging at this wavelength gave a very low contrast against the back-ground noise. With the 800nm excitation the elastin used in our images the elastin fibres showed up with a high contrast against the background fluorescence. This

implies that the 800nm excitation light is more efficient at exciting elastin fluorescence than 1230nm light.

Histological sections were taken from the elastic cartilage of the ear and stained with orcein to reveal the elastin. The staining showed the same thick network of fibres within the centre of the elastic cartilage, with finer fibres seen towards the perichondrium layer as shown in figure 5-21.

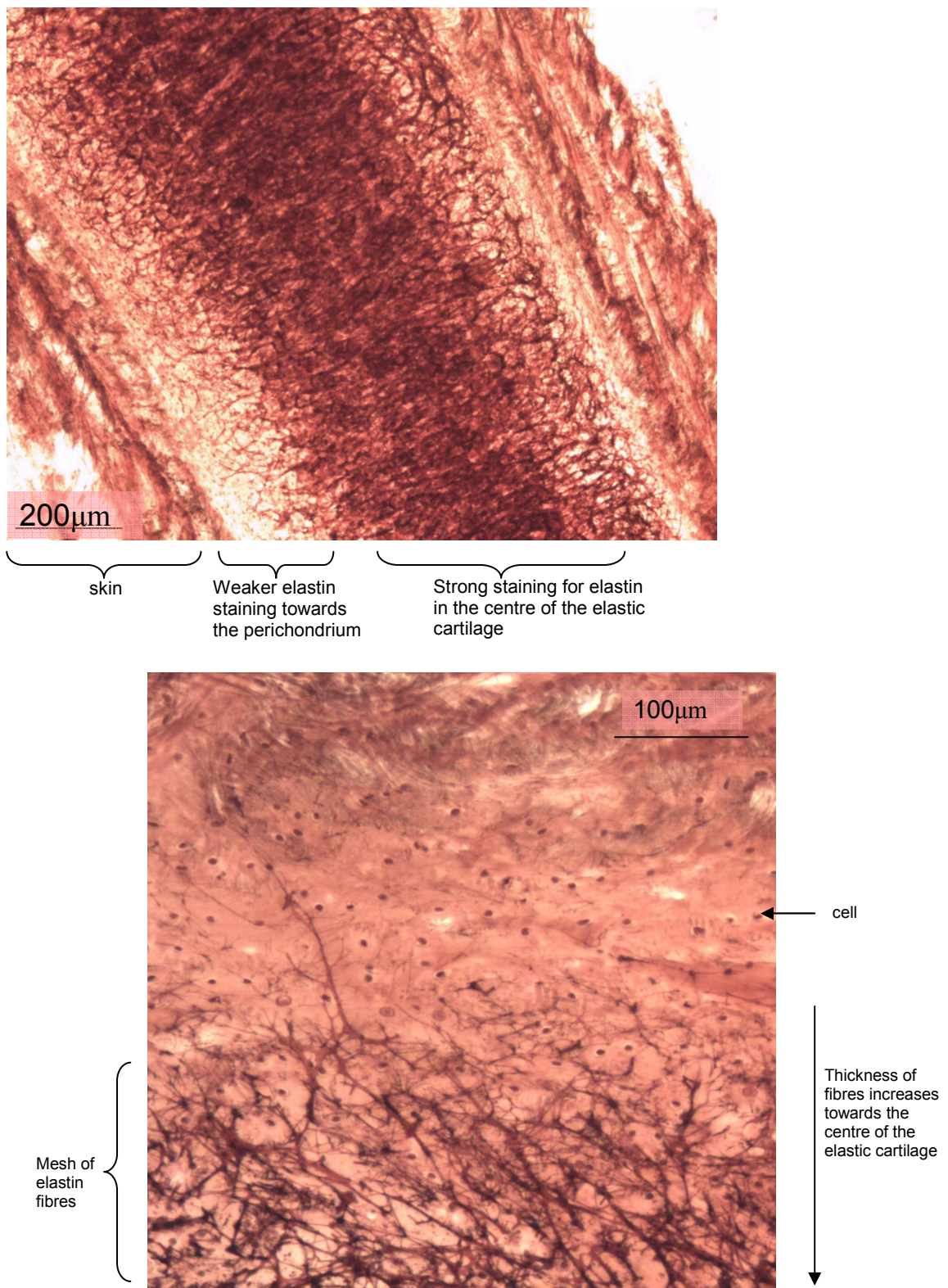


**Figure 5-21 Elastic cartilage stained with orcein**  
This provides contrast to the elastin fibres (elastin fibres are dark against the pink background)

## **5.6 Discussion**

The fluorescent fibres identified in the TPF images of articular cartilage are a significant finding for cartilage research. Previously it was thought that collagen was the only fibrous protein to be found in the articular cartilage extracellular matrix, with only one paper reporting the existence of elastin like fibres<sup>87</sup>. The identity of the elastin fibres in the superficial zone of articular cartilage has been conclusively proven by immuno-staining.

The fibres were found to be most abundant in the most superficial tissue (top 50µm) and to lie in the plane parallel to the articular surface. The majority of fibres are long and straight indicating that they may be under tension and they also often have a preferred orientation. It is therefore likely that they provide a biomechanical function. One possibility is that they are required to maintain the alignment of the collagen fibres, providing a restoring force when the fibres are not held in swelling equilibrium by the proteoglycans. Future work could be undertaken to relate the organisation of these fibres to the collagen fibre orientations. The organisation of the fibre network is not constant over the joint surface. Some areas show parallel aligned fibres whereas others show either a criss-cross fibre arrangement or a sparse network of fibres. A larger volume of samples would be needed to characterize these variations more fully but it may then be possible to relate them to the different forces in the different areas of the cartilage.

The amount of elastin within the superficial zone was found to be significantly less in samples taken from older horses. This indicates that elastin fibres are lost from this region in an age related process. It would be interesting to investigate whether the amount of elastin in the articular cartilage is related to the level of wear and disease in the joint. However for this study a much larger sample size would be needed to eliminate compounding factors such as age.

The elastin fibres have also been imaged in the intervertebral disc and the elastic cartilage from the ear. The elastic fibres of the disc, articular cartilage and perichondrium of the elastic cartilage are long and straight. The elastin within the inner portion of the elastic

cartilage was not in this form and instead formed a large branching honeycomb structure. The elastin fibres from the elastic cartilage were also much thicker than those found in the disc and articular cartilage, and therefore appeared brighter within the images.

It is unknown whether the elastin fibre identified in the cartilage and the disc differs in composition from the elastin which forms large lamellar structures in the blood vessels. The majority of biochemical and structural analysis has been carried out on the elastin from blood vessels. There is some evidence that the amino acid composition of the material isolated from the disc and elastic cartilage is different, however it is inconclusive whether this is due to difficulties in removing contaminating proteins.<sup>155, 156</sup> Other elastin-like materials for example lamprin also exhibit a strong TPF signal. Further work would be needed to identify whether it is the same fluorophore responsible for the TPF in the elastin from different tissue sources and elastin-like proteins.

## **6 Polarization sensitive non-linear microscopy**

---

### **6.1 Introduction**

As discussed in the introduction section 1.3.3.2 the production of SHG light from collagen is dependent on the polarization of the laser excitation beam, with respect to the long axis of the collagen fibres. In this chapter we report measurements of the polarization sensitivity of SHG and TPF in two different collagen-based tissues, tendon and cartilage. The polarization sensitivity results are used to find the collagen fibre orientations within the superficial layers of the tissues. We also investigate the polarization sensitivity at different depths into the tissue and how this is affected by the optical properties of the overlying tissue. Finally in the end of the chapter we demonstrate that polarization sensitivity measurements can be used to observe structural changes which occur between the healthy and the diseased state (osteoarthritis) in articular cartilage.

### **6.2 Polarization Sensitive Measurements**

All measurements were taken on microscope 1 which is described in section 2.2. In polarization sensitivity experiments the polarization of the light incident on the sample was rotated in 10 degree steps using the half-wave-plate behind the microscope objective. The total intensity from the area scan was measured and the intensities for each angle were combined to create the polarization sensitivity curve. This process was repeated at depth steps into the tissue of 10  $\mu\text{m}$  in tendon and healthy cartilage and 15  $\mu\text{m}$  in cartilage lesions. The depth steps were chosen as a compromise between collecting a very detailed data set and minimising the total scan time.

For investigating the change in the polarization sensitivity with depth a power of 30mW was used for acquisition of surface images, but power was increased with scanning depth so that at 200  $\mu\text{m}$  depth the power exiting the objective was 140mW.

### 6.2.1 Validation of Polarization Sensitive Microscope Set-up

Preliminary tests were made to check that there was no intrinsic polarization sensitivity within the microscope. A fluorescein solution was used as a sample for these experiments as it should have no polarization sensitivity due to the homogeneous isotropic distribution of the fluorescein molecules. Figure 6-1 shows the results of rotating the polarization angle of the laser excitation signal through 360 degrees. The intensity of the fluorescence from the sample remained constant ( $\pm 1.6\%$ ), indicating that the microscope was not preferentially transmitting any polarizations.

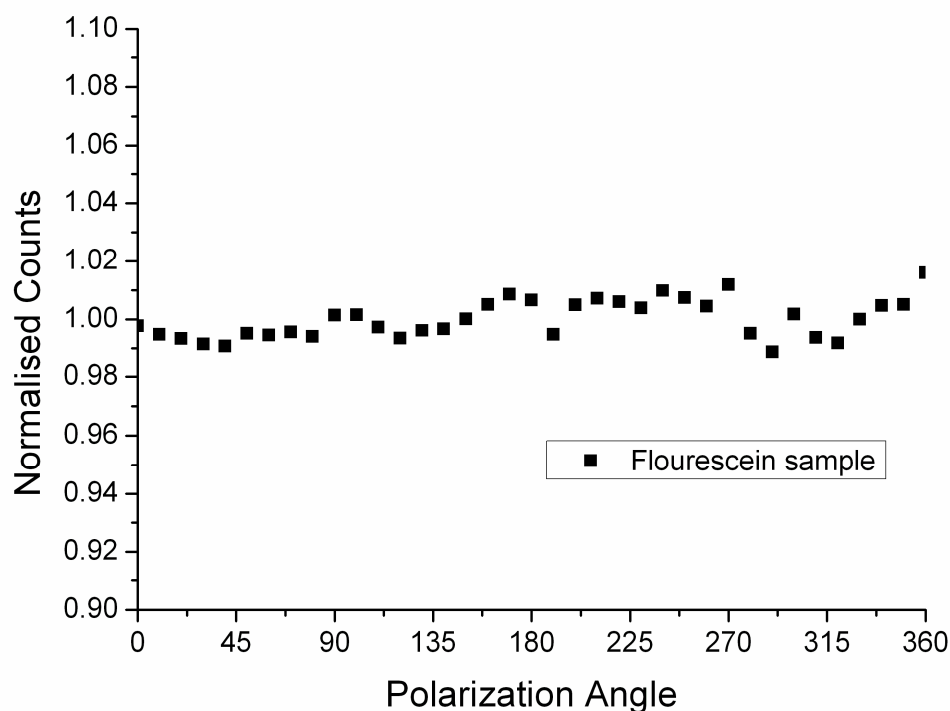


**Figure 6-1 The polarization sensitivity of TPF from fluorescein.**  
The intensity of TPF from fluorescein as a function of polarization angle, the variations are small less than  $\pm 1.6\%$ , therefore demonstrating that our experimental set-up has no intrinsic polarization sensitivity

The normalised intensity values used in this graph represent the sum of the counts from all the 250000 pixels in the microscope image, divided by the mean intensity for polarization angles.

Previously, polarization sensitivity measurement have been used to find the orientation of the collagen fibres within tissue samples<sup>35</sup>. To validate that we were able to do this with our experimental set up we compared the fibre orientations found using polarization sensitivity measurements in tendon samples to the orientations found from the SHG image taken of the same area. This was repeated 3 times and the maximum difference between the angles found with the two techniques was 5°. A representative polarization sensitivity plot and image of tendon is shown in figure 6-2.

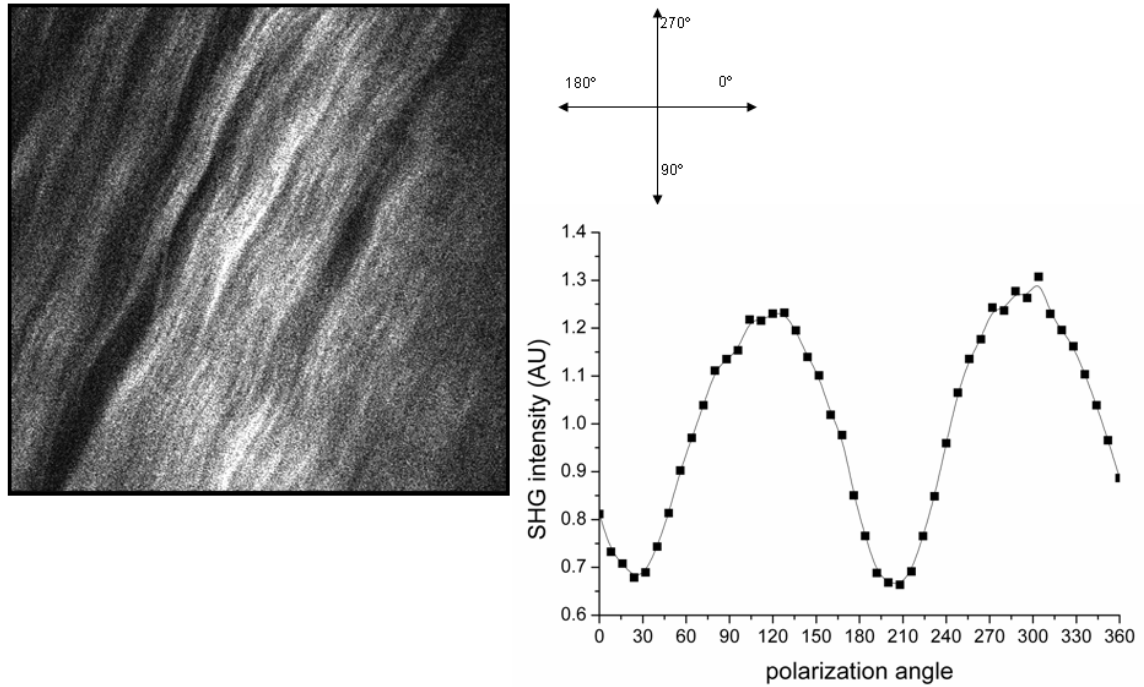


**Figure 6-2** Fibre orientations found from imaging and polarization sensitivity.

The image shows the collagen fibres within the tendon (with the fibre angle marked in red) and this is compared to the polarization sensitivity of the SHG signal plotted for the same area of the tendon. In the polarization sensitivity graph 0° corresponds to the light being polarized horizontally across the image. For this sample the collagen fibre angles were measured to be 118°±1.5 from the image and 116°±3 from the polarization sensitivity plot.

## 6.2.2 Polarization Sensitivity Curves in the Superficial Layers of Cartilage and Tendon

The polarization sensitivity of the generation of both SHG and TPF has been measured in the surface of two different tissues; tendon and cartilage. The results for cartilage and tendon at a depth of 10 $\mu$ m from the surface are shown here in figure 6-3.

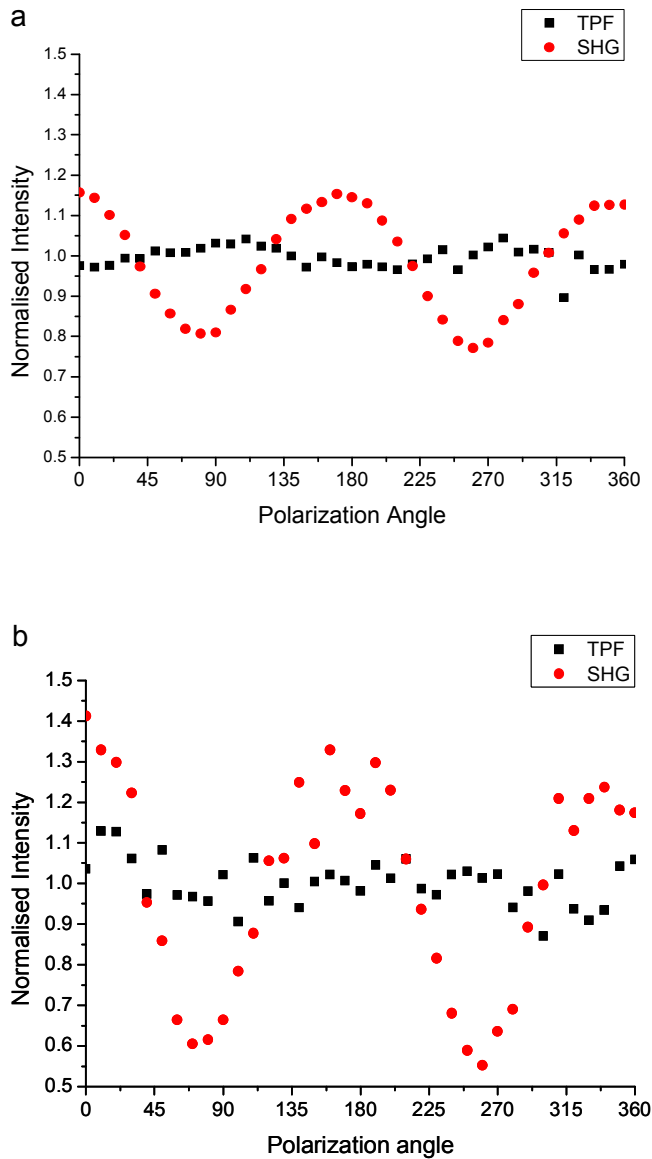


**Figure 6-3 TPF and SHG polarization sensitivity in cartilage and tendon.** Representative polarization sensitivity curves are shown for both TPF and SHG data taken at the surface in cartilage (a) and tendon tissue (b), with the x axis showing the polarization of the laser fundamental. The intensities have been normalized by dividing through by the mean intensity for each curve. The data was taken at a depth of 10 microns into the tissue

As expected from the previous literature the SHG from tendon exhibited a strong polarization sensitivity. The SHG from cartilage also displayed polarization sensitivity. This result differs from that previously reported<sup>80</sup>, but is consistent with well established histological evidence<sup>74, 85</sup>. In both tendon and cartilage the polarization sensitivity of the TPF only showed very small variations with angle and therefore we concluded that the TPF has no significant intrinsic polarization sensitivity or that the two-photon fluorophores are randomly distributed for both tissues.

The visibility  $((I_{\text{peak}} - I_{\text{trough}})/(I_{\text{peak}} + I_{\text{trough}}))$  the SHG polarization sensitivity curves gives a comparative measure of the degree of order within the tissue sample. The visibilities of the three tissue types investigated here are shown in table 6.1. The visibility for cartilage is noticeably less than that for tendon and pericardium. This is likely to be due to the fact that the collagen in cartilage is predominantly type II, whereas the collagen in tendon is predominantly type I. The type I collagen fibrils of tendon are thicker in diameter than type II collagen fibrils. In cartilage there is also a variety of collagen fibre alignments with some zones containing parallel aligned fibres and others where the collagen is arranged to form a mesh to trap proteoglycan molecules within the tissue.

| tissue    |     | Number of samples | Mean visibility | Standard deviation |
|-----------|-----|-------------------|-----------------|--------------------|
| cartilage | SHG | 6                 | 0.11            | 0.05               |
|           | TPF | 5                 | 0.04            | 0.02               |
| tendon    | SHG | 6                 | 0.29            | 0.04               |
|           | TPF | 5                 | 0.045           | 0.005              |

**Table 6.1**The visibility of the polarization sensitivity of SHG and TPF.

The polarization sensitivity properties of tendon have been used previously to characterise the second-order non-linear susceptibility tensor for collagen<sup>18, 19, 23, 25, 33, 34</sup>. Using a similar approach, we fitted the Freund model<sup>25</sup> (discussed in section 1.3.3.2) to our polarization sensitivity curves for tendon, using the Microcal Origin curve-fitting tool based on the Levenberg-Marquardt algorithm. Two equations have been fitted the first is the equation used by Freund et al (equation 6.1a) and the second contains an additional constant which allows an offset in the data (equation 6.1b).

$$I_{SHG} = A \left[ \left( \rho \cos^2(\theta + \alpha) + \sin^2(\theta + \alpha) \right)^2 + \left( \sin(2(\theta + \alpha)) \right)^2 \right] \quad (6.1a)$$

$$I_{SHG} = A \left[ \left( \rho \cos^2(\theta + \alpha) + \sin^2(\theta + \alpha) \right)^2 + \left( \sin(2(\theta + \alpha)) \right)^2 + B \right] \quad (6.1b)$$

The parameters A, B,  $\rho$  and  $\alpha$  were all variable parameters in the curve fit.

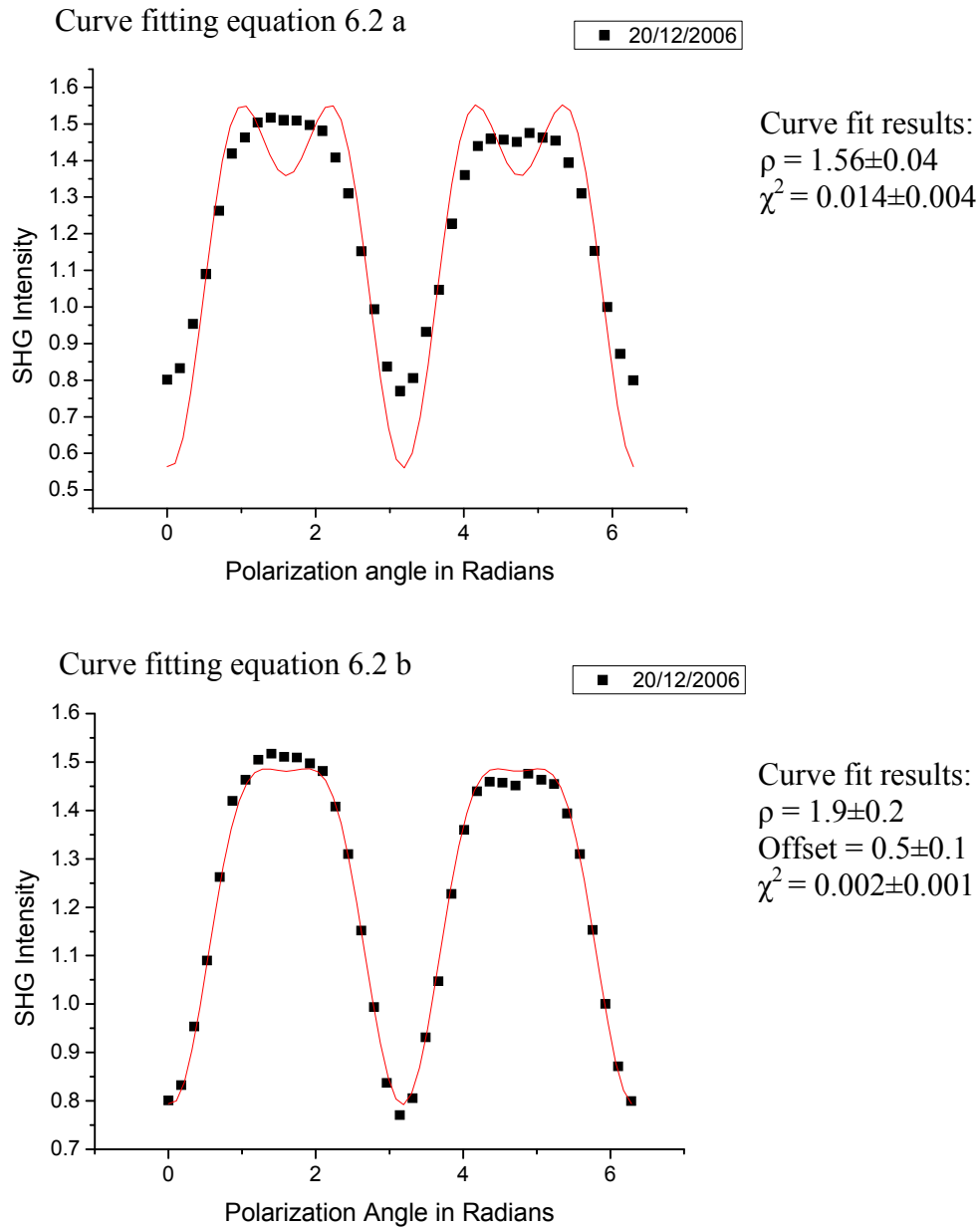


**Figure 6-4 Polarization sensitivity curve fitting.**

**A representative polarization sensitivity curve of SHG from tendon and the curve fits of equations 6.2a and 6.2b**

The curve fitting was carried out on polarization sensitivity curves taken from 5 different samples of tendon. The fitting of equation 6.1a to the data gives an average value of  $\rho = 1.55 \pm 0.04$  with a reduced  $\chi^2$  for the fitting of  $0.016 \pm 0.003$ . When equation 6.1b is fitted to the data the average value of  $\rho = 2.05 \pm 0.24$  and the offset  $A \times B = 0.46 \pm 0.1$ ,

with a reduced  $\chi^2$  for the fitting of  $0.001 \pm 0.001$ . Fitting equation 6.2a gives a lower value for the parameter  $\rho$  than expected and a poorer fit than equation 6.2b (the average value of  $\chi^2$  was 1 order of magnitude larger), this may be for two possible reasons, heterogeneities in the tissue or effects of the objective lens. Figure 6-4 shows the equations fitted to a representative polarization sensitivity curve for tendon.

Previous works found that the choice of imaging area affects the measured value of  $\rho$ , in young rat tail tendons where the fibres are crimped. This is due to the presence of multiple fibre orientations within the imaging area (i.e the fibres were not all aligned with the fibre axis), when a small area containing only one fibre orientation then the values of  $\rho$  as high as 2.6 have been observed.<sup>23</sup> When Stoller et al, modelled the polarization sensitivity in tendon allowed for a Gaussian distribution of collagen fibres about the tendon axis with an angular distribution of  $15^\circ$ . This was found to have only as small effect on the polarization sensitivity patterns with a maximum effect of approximately 12.5% on the overall amplitude of the intensity variations.<sup>18</sup> The tendon samples used in our experiment were from the equine flexor tendon, which does not exhibit the crimping observed in rats tail tendon, and the images show almost uniform collagen fibre alignment. Therefore multiple collagen fibre orientations appear unlikely to be the sole explanation of the poor fit of the Freund equation to our experimental data.

The focusing of the light through objective will have an effect on the polarization of the light at the focal point. The effects will be greater the higher the numerical aperture used and therefore the measured polarization sensitivity will be less. At the focal point a proportion of the linearly polarized excitation light becomes elliptically polarized. The angle between the plane of the ellipse and the original linear polarization and the degree of eccentricity of the polarization vary throughout the focal plane. Figure 6-5 summarizes how the polarization of different rays is changed by the microscope objective, for linearly polarized light in the x-direction. The p and s-polarized rays are shown on figure 6-5 these rays remain linearly polarized as they travel through the objective, although at the focal point the p-polarized ray will now clearly have a component of its polarization in the z-directions as well as in the x-direction. Rays which travel through the shaded areas on

figure 6-5 become elliptically polarized, the pattern of the cross of linearly and elliptically polarized light is referred to as the airy cross.<sup>157, 158</sup>

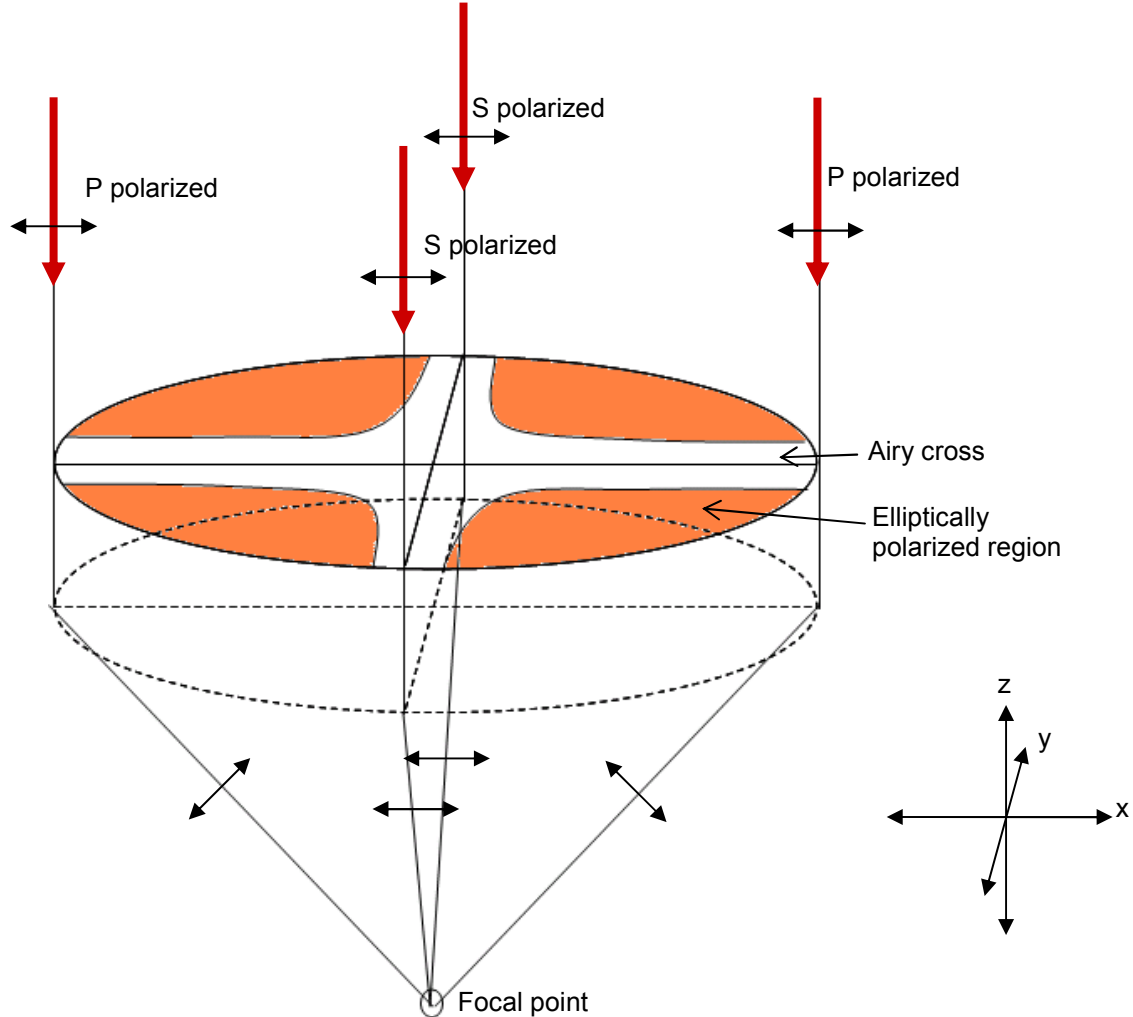


**Figure 6-5 The effect of the objective on polarization.**  
 A diagram to summarize the effect focusing through the microscope objective has on the polarization of the different rays within a linearly polarized beam. Adapted from Paul Keatlys thesis.<sup>157</sup>

Rays on the focal axis are the only ones to remain completely linearly polarized in the same direction as the original laser polarization.<sup>159</sup> The loss of linear polarization may go some way to explain the lower polarization sensitivity visibilities we have measured, compared to the other research groups which carried out their experiments using lower NA objectives (for example Stoller et al<sup>18</sup> used a 0.42NA objective, Williams et al<sup>23</sup> used a 0.75NA objective compared to the 1NA objective used in our experiments). Therefore we could interpret the constant B included in the curve fitting as a contribution to the overall SHG intensity from SHG which has been excited by the proportion of laser fundamental which is no longer linearly polarized at the focal point.

### 6.2.3 Polarization Sensitivity relative to Split Lines

The orientation of the collagen fibres within articular cartilage has traditionally been estimated by means of a split line experiment. This experiment involves the surface of the tissue being picked with the end of a round pin and the direction of the split line this causes being observed. These split lines are said to correlate with the orientation of the collagen fibres within the cartilage and are repeatable on a given joint surface<sup>84, 160, 161</sup>. In order to highlight the direction of the split line Indian ink is applied to the surface of the tissue, where it is washed away from all areas except the split lines. In table 6.2 the angle of the collagen fibres as estimated from polarization sensitivity measurements are compared to those estimated from split line experiments following the protocol of Bullough et al<sup>162</sup> carried out on the same point in the cartilage after the optical measurements. This data was taken at the apex of the 3<sup>rd</sup> metacarpal of a joint from a young horse (5years) which displayed no signs of osteoarthritis. Figure 6-6 shows a photograph taken of the split lines.

| Site on tissue | Split line angle ( $\pm 10^\circ$ ) | Angle of fibres from polarization sensitivity experiments at 3 different depths. ( $\pm 10^\circ$ ) |            |            |         |
|----------------|-------------------------------------|---|------------|------------|---------|
|                |                                     | 20 $\mu$ m  | 30 $\mu$ m | 50 $\mu$ m | Average |
| 1              | 40                                  | 30  | 30         | 30         | 30      |
| 2              | 45                                  | 0   | 5          | 10         | 5       |
| 3              | 55                                  | 0   | 0          | No pattern | 0       |
| 4              | 95                                  | 40  | 30         | 35         | 35      |
| 5              | 65                                  | 20  | 25         | 25         | 23.3    |
| 6              | 40                                  | 35  | 30         | 35         | 33.3    |

**Table 6.2 A comparison of split line and polarization sensitivity results. The fibre orientations have been calculated on 6 sites on the apex of the joint, using the split line experiment and polarization sensitivity data at depths of 20,30 and 50 microns.**

The results shown in table 6.2 show no correlation between the collagen fibre orientations calculated from the polarization sensitivity data and the split line experiments. This may be because the splits caused by the pinprick progress much deeper into the tissue than the depth at which the measurements of polarization sensitivity were taken. Research by Jefferey et al<sup>161</sup> suggests that the direction of the split lines in cartilage depends on patterns in the collagen fibre organisation to a depth of up to 600 $\mu$ m. Therefore the two techniques

are likely to be providing information on different levels of collagen fibre organisation with the SHG polarization sensitivity data giving describing the fibre orientations on a small scale in the superficial zone and the split line data describing the a larger scale organisation in the fibres which progresses to a greater depth into the tissue.

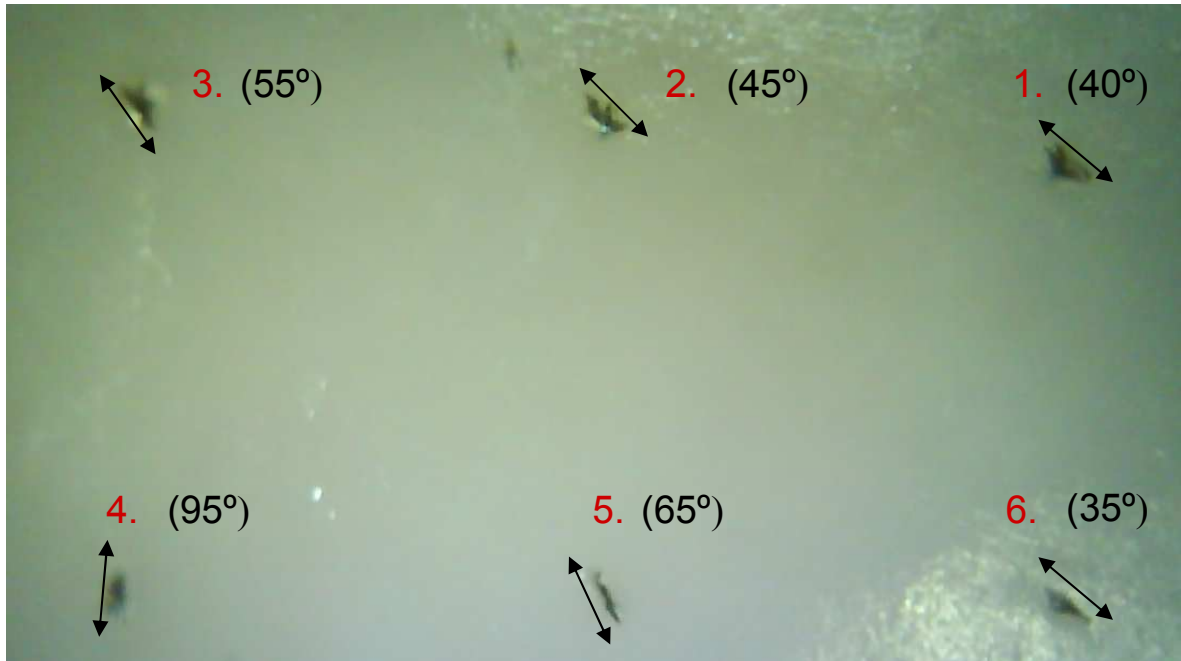


**Figure 6-6 Split lines in articular cartilage.**

The split line were generated with a round pin on the cartilage sample at 6 points after the collagen fibre orientation had been measured from the polarization sensitivity curves.

### 6.2.4 Ratio Images of Polarization Sensitive Measurements

The polarization sensitivity curves are not measured for a single collagen fibril but for a  $100 \times 100$  micron scan area. This area is large enough to contain a variety of different fibre orientations. To investigate the effects this may have, we have used ratio images to display variations in polarization sensitivity within our imaging area. The ratio images are produced by dividing the image taken with the laser polarization rotated to give the maximum intensity image by the image taken with the laser polarization perpendicular to this. These have been generated for cartilage images from the superficial zone. The main interest for investigating the ratio image for cartilage was to see if the fibre orientations were constant in the imaging area or whether there were variations surrounding the cells. We expected variations in the pericellular matrix surrounding the cells because previous studies with electron microscopy have found that in the pericellular matrix the collagen fibrils are finer and form a basket like structure around the cell<sup>74, 85, 88</sup>. The results for cartilage are shown in figure 6-7. This shows that the orientation of the fibrils is not constant across the area. The dark region on the ratio image represents an area where intensity in the overall minimum intensity image (b) is in fact brighter than the overall maximum intensity image (a) and therefore in this region the orientation of the collagen fibrils is different from the surrounding area.

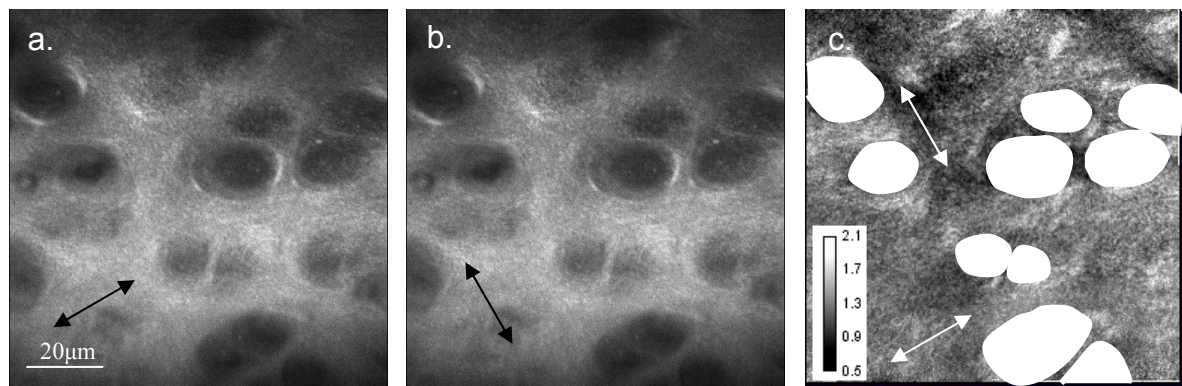


**Figure 6-7** Ratio images taken in cartilage.

SHG images acquired with the polarizer at the position of maximum intensity (a) and rotated through  $90^\circ$  (b), with the arrows indicating the polarization direction. Panel (c) shows the ratio of the two images (a/b). The dark regions in (a) and (b) represent the locations of the chondrocytes. In the ratio image these areas are circled and filled with white. The dark region in the top left quarter of the image represents an area where the polarization sensitivity varies from that found in the rest of the scan area. In this area the ratio is less than 1 indicating that the collagen in this region is predominantly orientated perpendicular to the rest of the image.

## 6.3 Variations in Polarization Sensitivity with Depth

The structure of many tissues is not constant with depth, and therefore it would be useful to be able to take depth resolved polarization sensitivity measurements. At increased depths into a tissue the polarization sensitivity pattern will no longer solely depend on the organisation and nonlinear susceptibility properties of the SHG sources within the tissue but will also depend on the birefringence and biattenuance (a term introduced by Kemp et al<sup>73</sup> to describe differential absorption and scattering of the excitation light and/or emitted light for different polarizations) properties of the overlying tissue. In order to use the polarization sensitivity patterns at increased depth to extrapolate information on the fibril organisation it is important to characterise these effects.

### 6.3.1 Tendon

Polarization sensitivity variations with depth were first investigated in tendon as this tissue provided the simplest collagen organisation. In tendon the fibre organisation remains constant with depth as do the birefringence and biattenuance properties which have been measured<sup>72, 73</sup>.

Polarization sensitivity of both the TPF and SHG signal from tendon was measured in tissue at depths up to 200 $\mu$ m, (data was not taken from any deeper due to low signal intensities caused by the attenuation in the tissue). Typical plots of the polarization sensitivity with depth are displayed in figure 6-8a-d. These patterns have been reproduced on 3 repeat experiments and figure 6-8e displays the ratio of  $I_{max}/I_{min}$  for the TPF in all 3 repeat experiments. The collagen fibres in these tendon samples were orientated at 90° to the original laser polarization (0°).

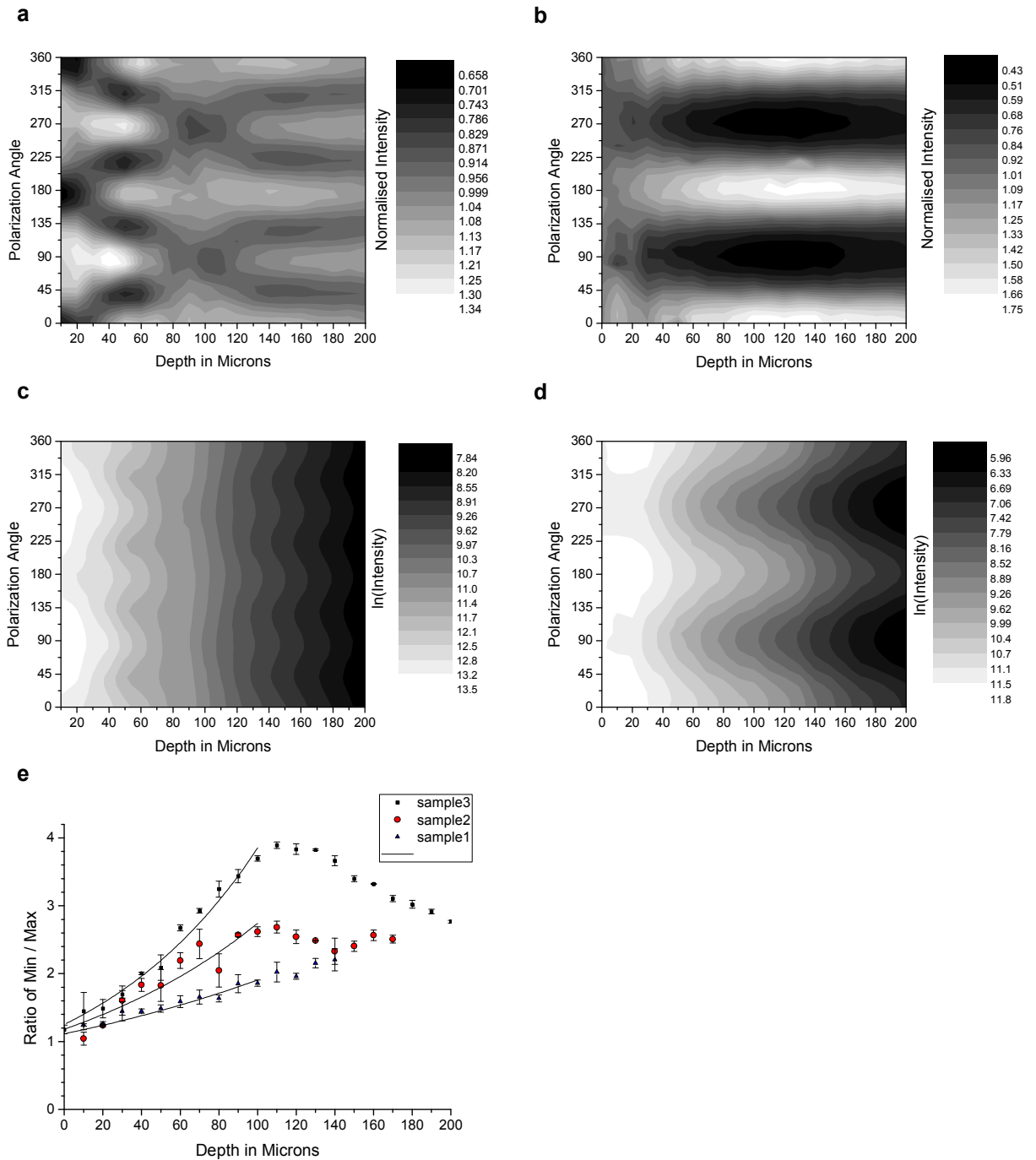


**Figure 6-8 Polarization dependence with depth in tendon.**

SHG and TPF polarization sensitivity data is taken at different depths on a sample which has the collagen fibres orientated at  $90^\circ$ . (a) and (b) show the polarization sensitivity of SHG and TPF with depth into tendon, with the intensities normalised by dividing through by the mean intensity at each depth. (c) and (d), show the natural log of the un-normalised polarization sensitivity for SHG and TPF. (e), shows the ratio of maximum intensity of the TPF/ the minimum intensity of the TPF at each depth into the tissue from 3 tendon samples, sample 3 is the same sample used for the polarization sensitivity plots shown in parts a –d

The TPF polarization sensitivity increased dramatically with depth into the tissue, and as the results displayed in section 6.2.2 showed that the TPF had no intrinsic polarization sensitivity we can conclude that this effect arises from biattenuance, with the light polarized perpendicular to the collagen fibres being preferentially transmitted. An upper bound for the amount of biattenuation in the tissue can be estimated from fitting an exponential to the data shown in figure 6-8e, based on the following assumptions. Firstly we assume that the tissue contains a well defined transmission axis such that the field strengths of light linearly polarized parallel and perpendicular to it are subjected to a differential attenuation coefficient given by  $2\pi\Delta\chi/\lambda_0$  where  $\Delta\chi$  is the biattenuance of the medium. Also one must assume that the transmission axes are co-incident with the fast and slow axes of the birefringence as this allows the optical properties of the tissue to be described by the following Jones' matrix. Where  $\Delta\chi$  is the biattenuance,  $\Delta n$  is the birefringence  $\lambda$  is the wavelength and  $\Delta z$  is the depth into the tissue.

$$\bar{J} = \begin{bmatrix} \exp((\Delta\chi + i\Delta n)\pi\Delta z/\lambda_0) & 0 \\ 0 & \exp((-\Delta\chi - i\Delta n)\pi\Delta z/\lambda_0) \end{bmatrix} \quad (6.2)$$

Incident linearly polarized light which is aligned with either of these axes will remain polarized along these directions with increasing depth and therefore the differential attenuation between these directions will have a maximum value. Linearly polarized light at other angles will be converted into elliptically polarized light by the birefringence of the tissue and therefore will experience an intermediate amount of attenuation. This is a reasonable assumption in tendon, as collagen is know to be birefringent with the fast axis aligned parallel with the collagen fibre axis<sup>19</sup> and the attenuation has been found to be greatest for linearly polarized light parallel to the collagen fibres. Previous tests (shown in section 6.2.1) showed that the detection system was polarization insensitive and therefore if the emitted TPF was un-polarized then the emitted light would propagate to the detector with equal efficiency independent of the polarization state of the excitation light.

The analysis described by Kemp et al<sup>73</sup> shows that the ratio of the field strengths along the axes is given by the equation,

$$\frac{E_{\max}}{E_{\min}} = \exp\left(\frac{2\pi\Delta\chi}{\lambda_0} \Delta z\right) \quad (6.3)$$

where  $\Delta z$  is the depth into the tissue and  $\lambda_0$  is the wavelength of the excitation light. The intensity of the TPF depends on the fourth power of the field and therefore the ratio of the TPF fluxes should have an exponential increase described by the following equation.

$$\frac{I_{\max}}{I_{\min}} = \exp\left(\frac{8\pi\Delta\chi}{\lambda_0} \Delta z\right) \quad (6.4)$$

Therefore for a tissue with biattenuance a plot of  $\ln(I_{\max}/I_{\min})$  versus  $\Delta z$  would have a slope of  $8\pi\Delta\chi / \lambda_0$ , where  $\Delta\chi$  unambiguously represents the biattenuance at the excitation wavelength (800 nm).

Figure 6-8e shows that, it is possible to fit an exponential form to the data for the first 100-140 $\mu\text{m}$  but at greater depths the ratio becomes constant or begins to fall. Two possible explanations for this are that at increased depths the excitation light becomes depolarized due to scattering<sup>163</sup> or that the collagen fibres have become less well aligned. Therefore we estimated the biattenuance from an analysis restricted to the most superficial 100 $\mu\text{m}$ .

Equation 6.4 was modified to  $\frac{I_{\max}}{I_{\min}} = \exp\left(\frac{8\pi\Delta\chi}{\lambda_0}(z - z_0)\right)$  and was fitted using Microcal

Origin where  $z$  is the depth into the tissue. The  $z_0$  is a factor was introduced to allow for any uncertainty in identifying the surface of the tendon,  $\lambda_0$  is the wavelength of the incident light and  $\Delta\chi$  is the biattenuance. This gave a biattenuance of  $2.65 \times 10^{-4}$  (range  $1.7\text{-}3.6 \times 10^{-4}$ ,  $R^2 > 0.85$  for all fits) which is comparable with values measured for different types of tendon using polarization sensitive OCT (rats tail tendon  $5.3 \times 10^{-4}$ , rat Achilles tendon  $1.3 \times 10^{-4}$ , chicken patellofemoral tendon  $2.1 \times 10^{-4}$ ).<sup>73</sup>

From these measurements we were only able to estimate an upper bound for the biattenuance of tendon as even for an isotropic distribution of fluorophores the TPF may be partially polarized. As discussed in section 1.4.1 fluorescent dipoles which are aligned parallel with the incident laser excitation polarization will be excited most efficiently and this results in the TPF being partially polarized in the direction of the laser excitation polarization (unless the fluorescent dipoles are rotating on a time scale comparable to the fluorescent life-time, which will be unlikely for collagen)<sup>49</sup>. This means that the emitted light will be transmitted to the detector with different efficiencies for the two orthogonal polarization states, and therefore the intensity ratio  $I_{\max}/I_{\min}$  will depend on the value of  $\Delta\chi$

at both the excitation and emission wavelengths. The precise relationship between our value of  $\Delta\chi$  and the true values at 800 and 450nm will depend on the degree of fluorescence anisotropy. This highlights the need for further research into identifying and characterising the properties of endogenous fluorophores.

For the SHG the pattern of polarization with depth in tendon represents the combined effects of the biattenuance, birefringence and the intrinsic polarization sensitivity of the collagen SHG. The birefringence of tendon is significant with ( $\Delta n$ ) for equine flexor tendon being approximately  $0.0045^{72}$ , indicating that a 180  $\mu\text{m}$  thickness of tendon would act as a whole wave-plate at 800nm. The SHG generated in the sample is also polarized with its polarization depending on the fibre orientations and the incident laser polarization (as shown in equation 13 Section 1.3.3.2). Therefore when analysing the SHG polarization sensitivity with depth patterns we also need to consider the polarization effects the overlying tissue will have on the emitted light as it travels back to the detector. For the 400nm SHG light the values for biattenuance and birefringence will be different and need to be characterised. If we are to accurately assess the effects of the birefringence and bi-attenuation on the SHG signal we would need to know what proportion of the signal detected was generated propagating in the backward direction, and how much was light generated in the forward propagating direction and back-scattered towards the detector in the bulk of the tissue. Polarization effects may be different for the back-scattered light as this may have become partially depolarized due to multiple scatterings. This problem is non-trivial as the proportion of light generated in the forward and backward scattering directions depends on the distribution of SHG sources within the focal volume.<sup>22, 23</sup>

It may be possible to reproduce our polarization sensitivity with depth patterns for tendon using either a Jones matrix or a Muller matrix (if depolarization due to scattering is found to be a significant effect) to describe the effects of the overlying tissue and the Freund<sup>25</sup> model to describe the collagen polarization sensitivity. However there are added complications due to beam geometry such as varying interaction lengths and ray-to-fibre inclination angles across the beam profile. These are likely to be significant due to the high numerical aperture lens used in these experiments.

### **6.3.2 Cartilage**

The structure of articular cartilage is not constant with depth but instead four zones can be observed on polarized light microscopy at different depths with changes occurring in collagen fibre arrangement between the zones (described in section 1.6.1). The collagen fibre arrangement within articular cartilage contributes to the tissues biomechanical properties and therefore methods of measuring the collagen fibre arrangement within an intact tissue sample will be of use to cartilage research.

The same polarization sensitivity with depth experiments carried out on tendon were repeated on 3 samples of normal cartilage. The data was taken to a depth of 200 $\mu\text{m}$ , this corresponds to the superficial and transitional zones of the cartilage. Like in tendon the data was reproducible in each sample and a representative data set is shown in figure 6-9.

In contrast to tendon the TPF does not show a strong polarization sensitivity even at depths of 200 microns and this indicates that biattenuance is not as significant an effect in cartilage as it is in tendon. Even though the data collection time was minimised it was still sufficiently great for the results to be affected by photo-bleaching, making the results more difficult to interpret. From figure 6-9b it is possible to see that at a depth of 150-200 $\mu\text{m}$  the polarization sensitivity pattern did become clear and showed 4 peaks in intensity. The visibility of these peaks is very small compared to that in tendon with the visibility is tendon and cartilage at 200 $\mu\text{m}$  being 0.6 and 0.05 respectively.

The SHG polarization sensitivity with depth in cartilage showed a clear repeatable pattern in all the healthy samples. At the tissue surface there were two intensity peaks but as the depth into the tissue increased additional peaks occurred between the original peaks. There was also an increase in the visibility of the peaks with depth into the tissue. The depth at which the additional peaks appeared varied slightly between the samples from about 60-90 $\mu\text{m}$ .

Relating the polarization sensitivity with depth to the fibre orientations is a relatively complex problem. The polarized excitation light will be influenced by the birefringence and biattenuance properties of the overlying tissue and unlike tendon these will change with the

zone structure of the cartilage. Also the fibre orientations are more complex than in tendon. The fibre axis in the transitional zone is no longer in the imaging plane and this increases the difficulty in interpretation. The polarization sensitivity for collagen fibres at an angle to the imaging plane is discussed in the appendix.

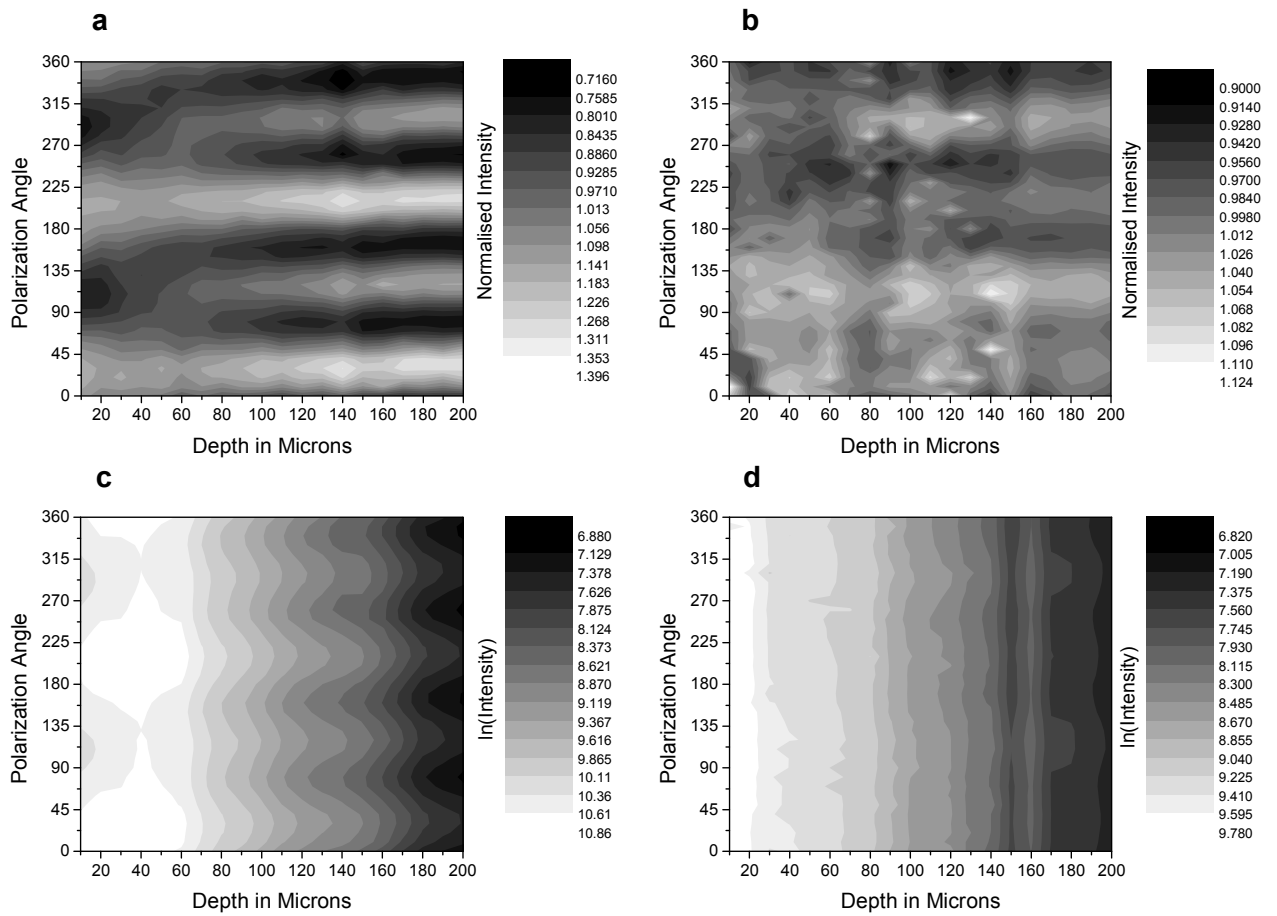
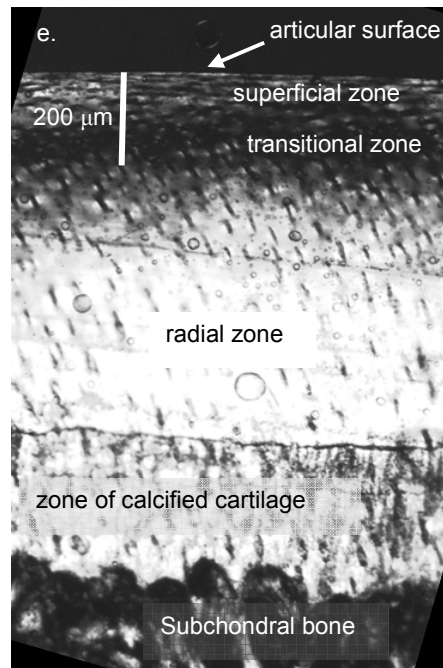


**Figure 6-9 Polarization sensitivity with depth in cartilage.**

SHG and TPF polarization sensitivity plots taken from a healthy equine sample 5 years old with no signs of osteoarthritis. (a) and (b) show the polarization sensitivity of SHG and TPF with depth into cartilage, with the intensities normalised by dividing through by the mean intensity at each depth. (c) and (d), show the natural log of the un-normalised polarization sensitivity for SHG and TPF. (e), shows a histological slice taken from the sample after the polarization sensitive measurements, and viewed between crossed polarizers.



### **6.3.3 Polarization Sensitivity in Degenerate Lesions**

As discussed in the introduction there are changes in the organization of the collagen fibres in osteoarthritic lesions. A previous study on non-linear microscopy of cartilage detected SHG polarization sensitivity in osteoarthritic tissue but not in healthy tissue<sup>80</sup>, and this provided motivation for investigating the changes in the polarization sensitivity properties which occur at lesion sites. In this section the changes observed in the polarization sensitivity with depth patterns are investigated in two spontaneous “butterfly” lesions which occurred on the apex of the third metacarpal bone (see section 4.3.1). These lesions occur spontaneously and have been investigated in detail elsewhere<sup>93</sup>. The data were taken in conjunction with non-linear imaging of the tissue in SHG and TPF. Histological sections were taken of the samples after imaging and viewed between crossed polarizers, which allowed the larger scale changes associated with the lesions to be investigated.

The patterns of TPF and SHG polarization sensitivity was measured at three points on a lesion. The approximate location of these points is shown on figure 6-10 which depicts a histological section of the lesion viewed between crossed polarizers. (Site 1 is 2mm anterior to the lesion centre, site 2 is central to the lesion and site 3 is 2mm posterior to the lesion centre). The polarization sensitivity with depth profiles from these sites are shown in figure 6-11. As in the healthy tissue the TPF polarization sensitivity was only a weak effect, with sites 1 and 3 at the periphery of the lesion showing some TPF polarization sensitivity but with site 2 central to the lesion showing none.

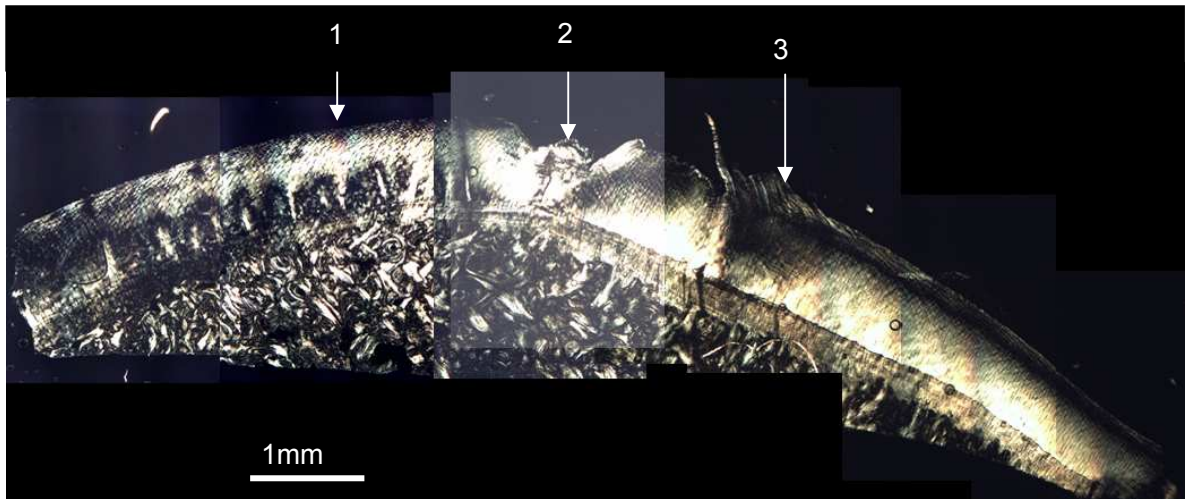


**Figure 6-10** Histology of the lesion investigated for figure 6-11. The section is viewed between crossed polarizers the approximate sites at which data was taken are indicated by the white arrows.

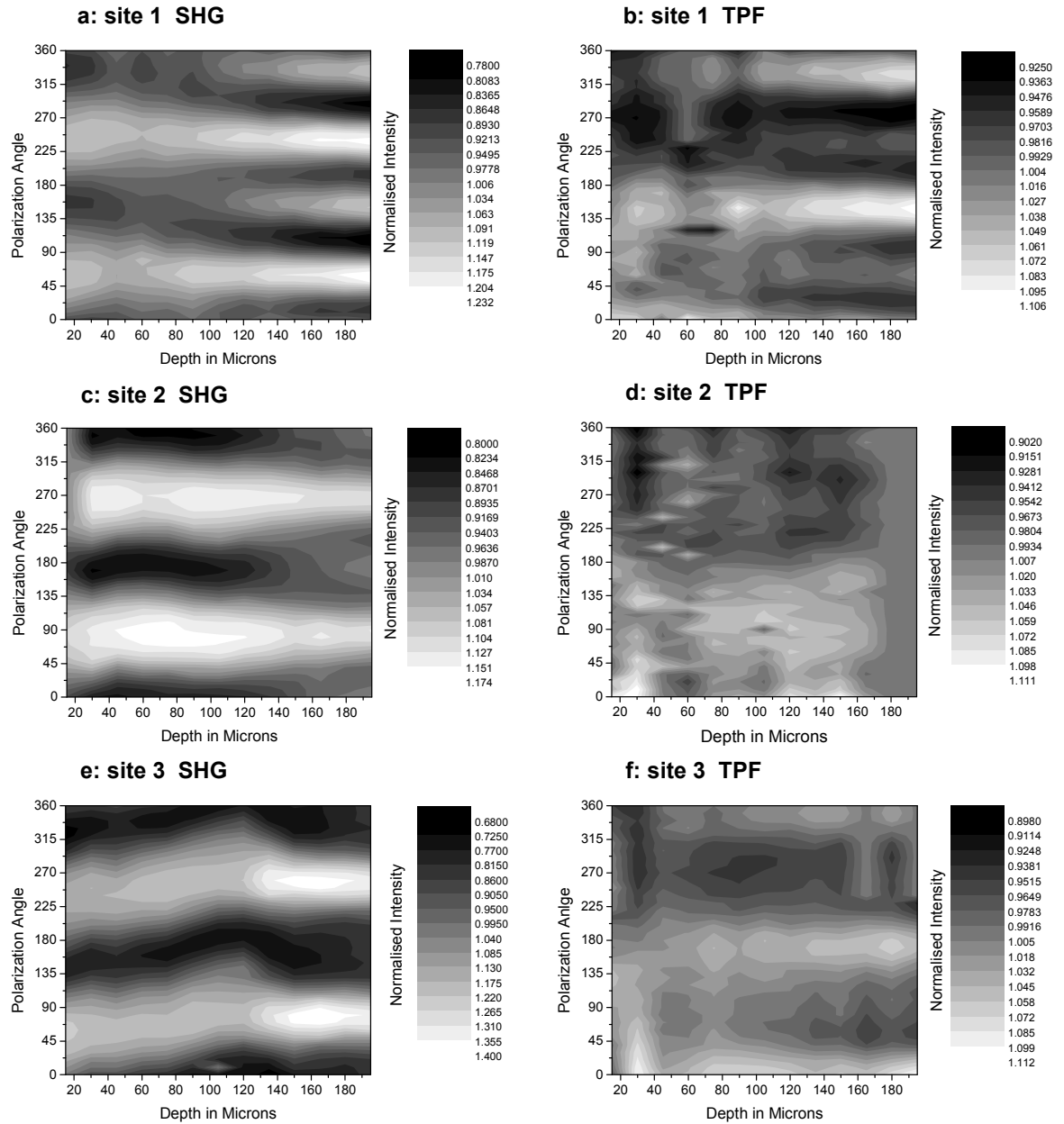


**Figure 6-11** The polarization dependence of TPF and SHG at a lesion.

The sites at which the data were taken are indicated in figure 6-10. Site 1 was macroscopically normal looking tissue close to the lesion, site 2 was approximately central to the lesion and site 3 was tissue in the periphery the lesion.

The changes observed in the SHG polarization sensitivity pattern are much more pronounced than the changes in TPF polarization sensitivity and therefore a more detailed study was carried out of the former and the results are displayed in figure 6-13. This figure displays the data taken from 9 sites along a line which crosses the lesion from the anterior to posterior edge. The histological section of the lesion viewed between crossed polarizers

is shown in figure 6-12. The 9 sites from which data was collected were separated by 1mm steps and the approximate locations of these sites have been marked on the figure. In the first four sites anterior to the lesion the SHG polarization sensitivity pattern is similar to that found in the healthy tissue, with two peaks in intensity at the surface progressing to four intensity peaks at a depth of about 80 $\mu$ m. The histology showed the normal structure of 4 zones for sites 1-3 but for site 4 the different zone were no longer clear. At the lesion site (site 5) and posterior to the lesion (sites 7-9) there are only two peaks in intensity with angle at all depths into the tissue. No data is available for site 6 as at this location the tissue was so disrupted it was not possible to take any polarization sensitivity data. The angle at which these peaks occur is not constant with depth at sites 5-8 and this effect is most pronounced at site 8, where it looks like there is a distinct change in fibre direction. The magnitude of the polarization sensitivity variations was greatest at site 5 which may be in agreement with the findings of Yeh et al that the polarization sensitivity was greater at the site of a lesion to that in healthy tissue<sup>80</sup>. The histology of the tissue showed that the structure was hugely disrupted at sites 5 and 6 and at sites 7-9 the surface of the tissue appeared damaged.

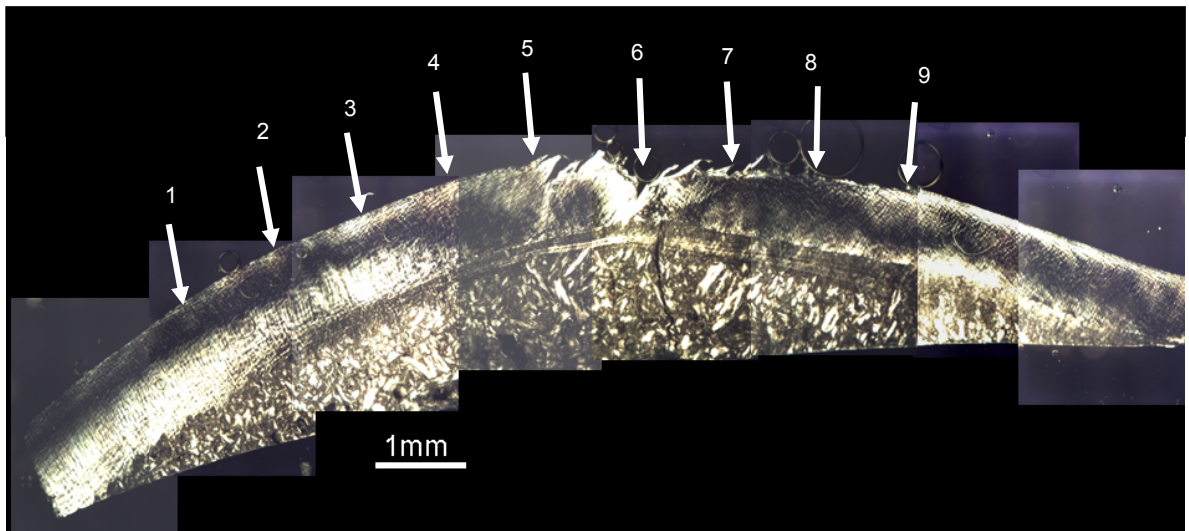


**Figure 6-12 Histology of the lesion investigated for figure 6-13. The section is viewed between crossed polarizers the approximate sites at which data was taken are indicated by the white arrows.**

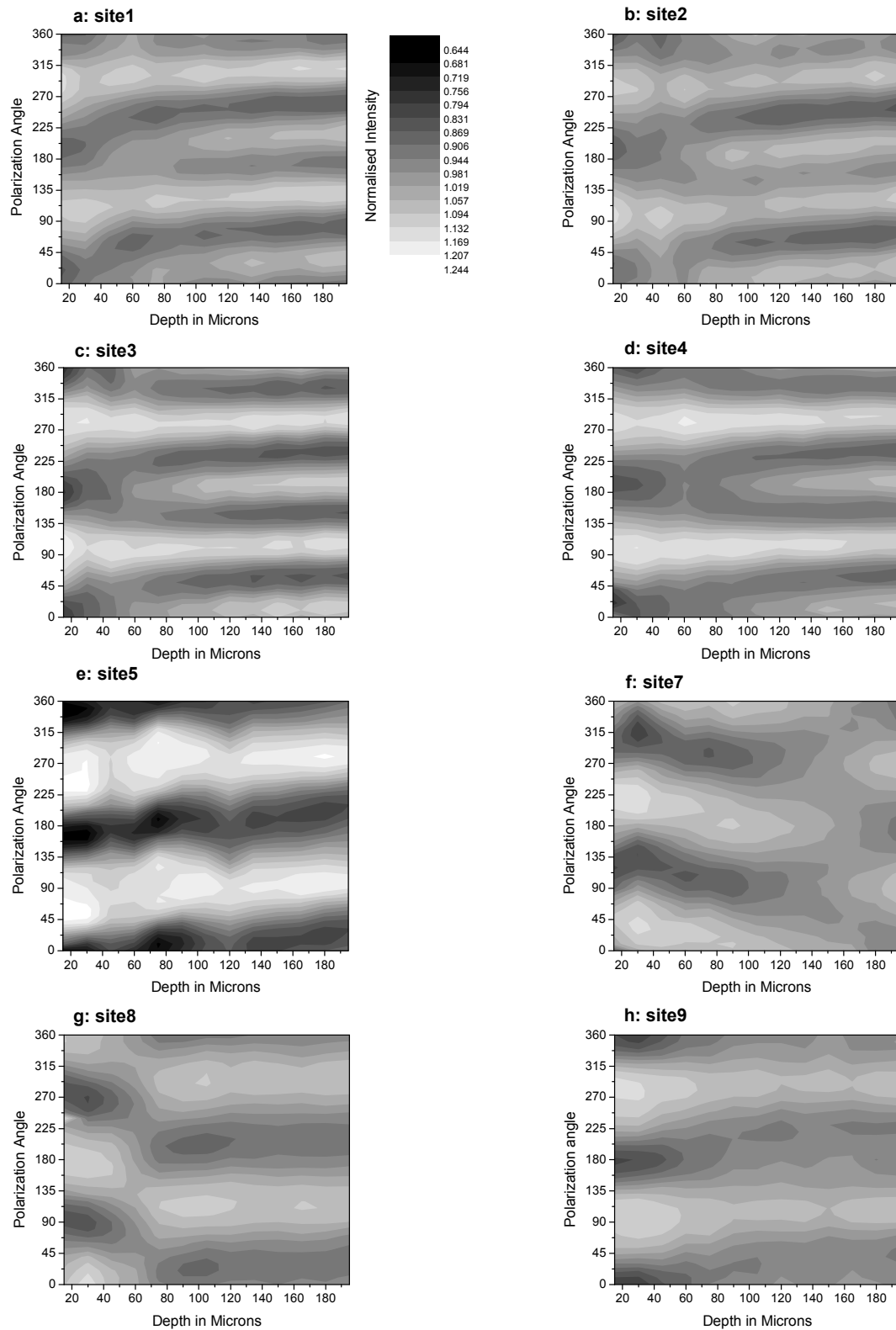


**Figure 6-13 Polarization dependence of SHG with depth at a lesion.**  
**The data is from the 9 sites shown in Figure 6-12. At position 6, at the centre of the lesion, the structure was too broken to detect any pattern of polarization sensitivity with depth. (All scales as in (a)).**

## **6.4 Discussion**

In this chapter it has been shown that microscope 1 described in section 2.2 is able to be used to take polarization sensitivity measurements, and we have reported the results of polarization sensitivity measurements taken on the SHG and TPF signal from tendon, cartilage and pericardium. As the polarization sensitivity of tendon had previously been investigated in detail, this tissue was used for characterising the performance of our experimental set-up. The SHG polarization sensitivity curves from tendon have been used to fit the Freund model of polarization sensitivity of SHG from collagen fibres and to estimate the parameter  $\rho$ . It was found that to get a good curve fit an offset parameter was needed. This difference between the results and the model is thought to be due to the high NA objective used for imaging during our experiments, leading to the light at the focal point no longer being entirely linearly polarized. In order to investigate this point further future work should be carried out to measure the polarization sensitivity curves using a range of different NA objectives and comparing the values of  $\rho$  found from the curve fits.

The curve fitting of the Freund model was not extended to the tissues other than tendon. This is for two reasons, firstly that there is a large degree of uncertainty in our estimate of the parameter  $\rho$  as the calculated value appears to be affected by the experimental procedures, and secondly in many different tissues the organisation of the collagen fibres becomes more complex. For more complex tissues the assumption that the collagen fibres are lying parallel in the imaging plane is no longer appropriate and therefore  $\rho$  can no longer be estimated. In cartilage tissue the collagen fibres are finer and can be not easily seen in the images, previous literature reports that they are aligned parallel with the surface in the superficial zones of the tissue but they intertwine to form a meshwork, this means that for this tissue the exact distribution of collagen fibres remains unknown.

We were only able to measure the polarization sensitivity of the SHG and TPF from the sample and not the polarization of the SHG and TPF signal in these experiments. This was due to the fact that the microscope was operating in the epi mode. The collected light had to pass back through the wave-plate before reaching the detector, but for the 400nm SHG light and the 450-500nm TPF light the wave-plate was no longer acting as a half wave plate but was converting the polarization of any signal into an elliptical polarization state. This

problem could be overcome in future by modifying microscope 2 to allow polarization measurements on the SHG in the forwards direction.

Photo-bleaching problems were experienced whilst taking the TPF polarization sensitivity data. These were minimised by the use of a manual shutter, although the effects could be further limited if there was an automatic shutter which would only allow light on the sample when imaging was taking place.

Although we discovered the above limitations to the experimental set-up, SHG polarization sensitivity curves were still able to accurately measure the orientation of the collagen fibres in tendon. Therefore the main aim of the research was to extend this to measuring the polarization sensitivity properties of cartilage and relate this to the collagen fibre organisation within the tissue. The research was concentrated on the superficial zone of the articular cartilage where we found that it was possible to find the predominant fibre orientations at the articular surface. The collagen fibres in the superficial zone are too fine to be visualised directly using light microscopy and therefore in other cartilage research the following methods have been used to investigate the collagen fibre organisation; x-ray diffraction<sup>12</sup>, polarization sensitive OCT<sup>72</sup>, polarized light microscopy and electron microscopy. In this chapter a direct comparison was carried out between the split line method of finding collagen fibre orientations in cartilage and our polarization sensitivity measurements. There was found to be no correlation between the results from the two methods and this was concluded to be because the two techniques were measuring the collagen fibre organisation on different scales.

The visibility of the polarization sensitivity curves is related to the degree of the collagen fibre organisation. Therefore this work could be extended to use the visibility of the polarization sensitivity to investigate whether changes in organisation could be detected through changes in visibility if a collagen based tissue was subjected to mechanical forces for example stretching. Smaller variations in the collagen fibre organisation can be found from ratio images taken by dividing the image taken at the polarization angle which gives maximum intensity and the polarization angle perpendicular to that. In cartilage we found

there were areas with different collagen fibre orientations within the  $100\times 100\mu\text{m}$  imaging area used in these experiments.

The later half of this chapter describes the measurements taken of polarization sensitivity at increasing depths into the tissue. These measurements were found to be strongly affected by the optical properties of the overlying tissue. This makes measuring the collagen fibre orientations from the polarization sensitivity curves a more complicated process and dependent on characterising the birefringence and biattenuation of the overlying tissue. Tendon was used as a test subject for the polarization sensitivity with depth measurements. Here the collagen fibre organisation was known to be constant with depth and we were able to estimate the amount of biattenuation from the polarization sensitivity with depth of the SHG results. To more fully understand the TPF polarization sensitivity with depth results the polarization anisotropy of the fluorophores within the tendon and cartilage needs to be measured. These experiments would need to be carried out on forwards transmitted light from thin samples. To do this microscope 2 would need to be modified to allow measurements of the polarization of both TPF and SHG light in the forwards direction.

For the polarization sensitivity with depth in cartilage the interpretation was more complicated and a computer model will be needed to relate the patterns to the fibre orientations. Also further measurements would be needed to characterise how the birefringence and biattenuance of the cartilage changes with depth. The collagen fibres in the transitional zone of the cartilage are orientated at an angle with respect to the imaging plane, with our experimental set-up we are unable to measure this angle. Yoshiki et al<sup>164</sup> have suggested a possible way to measure the 3 dimensional orientation of collagen fibres, by using linearly polarized light to measure the angle of the fibres in the x-y plane and then combining this with measurements taken using light which is radially polarized in the back aperture of the objective to investigate the orientation of the fibres with respect to the imaging plane. This is possible because radially polarized light becomes polarized parallel to the optical axis in the focal plane.

We have been able to characterise the polarization sensitivity with depth pattern for healthy cartilage tissue and found that this pattern changes at a lesion. Therefore this may prove to

be a useful technique for assessing the amount of disruption to the collagen architecture at lesions sites, in intact tissue samples. For this to be the case a larger number of lesions may need to be investigated and the data acquisition time would need to be greatly reduced, especially if the ultimate aim was to use this technique for assessing lesions in vivo.

## 7 Conclusions and Future Work

---

The first stage of the work described in this thesis was the construction of a simple multi-photon microscope, which could carry out both SHG and TPF imaging in the backscattered direction. It was used to image cartilage and to investigate the SHG and TPF polarization sensitivity effects in both cartilage and tendon. Later in this study the imaging work was transferred to a new multiphoton microscope and laser system which allowed CARS imaging to be combined with TPF and SHG imaging and also allowed simultaneous forward and backscattered detection.

The multi-photon imaging of cartilage has allowed the production of submicron resolution images where the following features can be observed: pericellular matrix (TPF imaging), elastin fibres (TPF imaging), inter-territorial collagen matrix (SHG imaging), cell boundaries within the matrix (CARS imaging) and lipids within the cells (CARS imaging). The combination of the three imaging modalities TPF, SHG and CARS therefore provides a very powerful technique for investigating cartilage.

Other techniques which give cellular resolution images of cartilage are confocal microscopy, transmitted light microscopy and electron microscopy. Confocal microscopy offers comparable resolution to multi-photon microscopy and also shares the advantage of providing 3D data sets. Confocal microscopy has been used to investigate the pericellular matrix and chondrons by immuno-staining for collagen VI<sup>91, 165</sup> however with multi-photon imaging we were able to image both the cells and pericellular matrix in unstained sample. Also the penetration depth for multi-photon imaging is better than for con-focal imaging with the maximum penetration depths being about  $500\mu\text{m}^6$  and  $150\text{-}200\mu\text{m}^{16}$  respectively. Electron microscopy offers much higher resolution images, for example with electron microscopy cellular structures and individual collagen fibres can be clearly resolved whereas these were found to be beyond the resolution of our multi-photon microscope. However it requires a complex sample preparation technique which may result in artefacts. OCT like multi-photon microscopy allows imaging on intact unstained samples with an improved penetration depth into the tissue. Typically the entire depth of cartilage can be

imaged on intact tissue samples using OCT compared to only the superficial and transitional zones with multi-photon microscopy<sup>166, 167</sup>. However OCT images have a lower resolution (typically 1-15 $\mu\text{m}$ )<sup>9</sup> and also rely on contrast due to the differences in refractive index and therefore do not have the advantages of molecular specificity which is provided by multi-photon imaging. This means that feature seen on the multi-photon images such as elastin fibres, cellular lipids and pericellular matrix are not visible with OCT.

One of the most significant results of this work was that TPF imaging of cartilage showed a network of fine elastin fibres in the most superficial 50 $\mu\text{m}$  of the tissue. These fibres were found to be lying parallel with the articular surface and their identity was confirmed by immuno-staining. Multi-photon imaging is the only technique where by these fibres can be observed without any staining of the tissue. Little has been previously reported regarding elastin in cartilage and therefore work was done to map out the distribution of the fibres over the joint surface and to investigate their orientations. Future work needs to be done to characterise this network in more detail using a larger sample size so that variations between horses can be characterised and to investigate the fibre networks in different joints and species. The majority of the elastin fibres appeared long and straight indicating that they may be under tension. Future investigations should be carried out into what contribution these fibres provide to the physical properties of the tissue, this could possibly involve imaging the fibres in tissue subjected to mechanical stretching.

Spectroscopic studies of the TPF from purified matrix components have shown that type II collagen and cross-links from collagen and elastin are sources of TPF in our TPF images. Much of the fluorescence may also be due to AGE (Advanced Glycation Endproduct) crosslinks. If age related crosslinks are an important source of fluorescence then a valuable extension of the present work would be to investigate the changes in fluorescence intensity and spectra involved in ageing and disease especially as these have been correlated in single photon fluorescence studies<sup>125, 126, 129, 130</sup>. The data collected on the two-photon fluorophores did not include a study of the relative quantum efficiencies of the different components and their concentrations within the samples. Therefore it is unknown how large a contribution each fluorophores makes to the overall fluorescence of the intact tissue samples, also it is likely that there are additional fluorophores within the tissues

which are yet to be identified. The multi-photon spectra of intact tissue samples were taken over large imaging areas. These areas contained the following features within the TPF image: elastin fibres, pericellular matrix fluorescence, interterritorial matrix fluorescence and cellular fluorescence. The fluorophores responsible for these features will vary and therefore future work should be to extend this to allow spectrally resolved multi-photon imaging similar to the work done by Palero et al<sup>40</sup> in the dermis.

From the polarization sensitivity of SHG measurements we were able to measure the predominant collagen fibre orientation at the articular surface (most superficial 0-30µm). In these regions the collagen fibres are too fine to be resolved by imaging. At increased depths into the cartilage the polarization sensitivity results were complicated by the optical properties of the overlying material (birefringence and biattenuation) and also by the orientation of the collagen fibres at an angle to the imaging plane in the transitional zone. The advantages of our technique for measuring the collagen fibre orientation is that it can be used on intact tissue samples, and it has the potential for providing high resolution data on the collagen fibre orientations. This was demonstrated by generating ratio images where differences in collagen fibre orientations within a 100 ×100 µm area could be observed. The disadvantages of the technique was that it required long exposure times (although this may be reduced by automating the data collection process) and the difficulties in interpreting the data from deeper zones of cartilage where the polarization has been affected by the overlying tissue. Further work would be required to directly relate the polarization sensitivity with depth patterns to the collagen fibre orientations using computer modelling. The SHG data is also complicated by the fact that the SHG signal and polarization dependence decreases for collagen fibres which are orientated at an angle to the imaging plane. This is discussed in more detail in the appendix. Therefore when collecting polarization sensitivity data it is difficult to identify whether a decrease in polarization sensitivity is due to less ordered collagen fibres or because the collagen fibres are orientated at an angle to the focal plane. Also when imaging some knowledge of the histology is useful to distinguish between regions which have a low SHG signal due to a low collagen fibre content and those where the collagen fibres are orientated perpendicular to the imaging plane.

Other techniques for measuring the collagen fibre orientation are: electron microscopy, small angle X-ray scattering (SAXS), polarized light microscopy and polarization sensitive OCT. Electron microscopy (both SEM and TEM) is the only technique providing high enough resolution to clearly resolve the smallest fibres within the matrix.<sup>162, 168, 169</sup> However electron microscopy techniques require fixation and drying of the samples which may result in artefacts. Also the very high resolution images have a small field of view and therefore are less well suited for investigating large scale patterns of fibre orientation. Small angle X-ray scattering (SAXS) enables the collagen fibres to be determined from the anisotropy of diffraction rings generated when a beam of X-rays is scattered through a sample. The intensity of the scattered X-rays varies around the ring depending on the number of collagen fibres orientated at the azimuth angle. From this the distribution of collagen fibre angles can be measured through the sample at approximately 25 $\mu$ m resolution. The disadvantages of this technique are the need for an X-ray source and that the results require a large amount of data analysis.<sup>12</sup>

Polarized light microscopy and polarization sensitive OCT both rely on the birefringence of the collagen fibres to measure their orientation. In polarized light microscopy a thin section is placed between crossed polarizers, then regions where there is a large amount of birefringence corresponding to an organised collagen structure appear bright, whereas areas which are not birefringent will appear black. If the thickness of the sample is known quantitative data on the birefringence of the sample can be measured.<sup>36</sup> Polarization sensitive OCT measures the birefringence of a material from the separation of the interference bands in the images (interference between light polarized parallel with the fast and slow axes of the birefringent material), these band appear closer with increased birefringence. In PSOCT studies on cartilage the collagen fibre orientation has been estimated in the radial zone by measuring the angle at which the birefringence is minimised.<sup>72, 170, 171</sup> These two techniques have the quickest time for the acquisition of data however they offer the lowest resolution.

Currently only the microscope 1 has been set-up to carry out polarization sensitive experiments. This is the least user friendly of the three microscopes and therefore in the future it would be advantageous to incorporate the necessary wave-plates in the both

microscope 2 and the spectrometer microscope. Microscope 2 allows forwards detection of the SHG signal and therefore it would be possible to measure the polarization of the SHG by placing an analyser in front of the forwards SHG PMT. (It was not possible to do this with the epi detection set-up used in microscope 1 as the wave-plate placed before the objective altered the polarization of the 400nm SHG signal as well as rotating the 800nm laser fundamental). It would also be possible to measure the polarization anisotropy of the TPF signal (if the SHG filter was swapped for a TPF filter). This would be useful when interpreting the TPF polarization sensitivity with depth results presented in chapter 6.

In the CARS work in this thesis only the C-H bond vibrations have been investigated. These predominantly give contrast for lipid molecules. The OPO used for CARS imaging can be tuned to different values of  $(\omega_p - \omega_s)$  which can allow different bond vibrations to be imaged for example the amide I bond vibration can be used to image the protein content within a sample and the O-P-O bond vibration can be used to image the DNA within the sample<sup>61</sup>. Future work would be to investigate these bond vibrations to gain additional information on the chondrocytes. The CARS images in this thesis showed a strong signal from the non-resonant background. This reduces the sensitivity for imaging the resonant bond vibrations and for weaker bond vibrations the signal may be completely swamped by the non-resonant background. In order improve this CARS techniques which reduce the non-resonant background need to be used; for example time resolved CARS<sup>172</sup>, heterodyne CARS<sup>173</sup> and polarization CARS<sup>62</sup>.

Both SHG and CARS are coherent processes and therefore affected by phase matching effects. The ratio of forwards to backwards signal is dependent on the size and distribution of the scatters for both processes.<sup>23, 24, 55, 59</sup> The forwards and epi images may therefore show different features<sup>44, 174</sup>. The ratio of forwards to backwards SHG from a sample contains information on the scatters, for collagen this may provide information on the thickness<sup>175</sup> and organisation of the fibres and the proportion on the fibril generating the SHG<sup>23</sup>. Future work may be to compare forwards and backwards SHG for different collagen types. This would be to investigate how the ratio of forwards to backwards SHG depends on the different amount of organisation and fibre thicknesses in different collagen types, and also how the ratio depends on the chemical environment. This will hopefully

help with the understanding of how SHG is generated in collagen at a fundamental level as it is still under debate as to which level of molecular anisotropy is responsible for the molecules' non-linear properties and whether the SHG originates from the whole fibril or just a cylindrical outer-shell.

We have been able to characterise normal cartilage tissue and observed changes associated with osteoarthritis. Lesion tissue has been investigated using both SHG and TPF imaging and through polarization sensitivity experiments. Through, this cellular changes and changes to the matrix have been observed, and compared to the classical histology taken on the samples after the multi-photon imaging. The multi-photon imaging appeared most promising for investigating the changes which occur with early osteoarthritis. With the multi-photon images degenerative changes were visible at the articular surface of samples which showed no macroscopic lesions. Small "microlesions" have been observed at the articular surface and these can be reconstructed in 3D from the image stacks. 3D data on these microlesions could be important to the understanding of the progression of the disease as once the articular surface has been disrupted the tissue will become more vulnerable to degeneration caused by mechanical wear. The imaging has shown changes surrounding the cells and cell clustering in degenerate tissue. Investigations into degenerate tissue should be repeated in future work to combine with CARS imaging which may reveal structural or metabolic changes occurring within the cells associated with the disease process.

A potential application of multi-photon microscopy in articular cartilage is to gain an increased understanding of the structure of healthy cartilage and the changes which occur in aging and osteoarthritic degeneration. There is a possibility that this may be developed into an in-vivo technique with future developments in the instrumentation. In vivo measurements would be especially important to osteoarthritis research as they would allow longitudinal studies. Recently cartilage has been imaged via an arthroscopy probe using laser scanning confocal microscopy<sup>176</sup>. This procedure was carried on a cadaver as it was not possible for it to be carried out in-vivo as the tissue needed to be stained for the confocal microscopy by infusing the joint capsule with a fluorescent marker. As shown in this chapter multi-photon microscope images can be produced on unstained tissues and therefore if this could be performed via an arthroscopy probe then this would prove more

useful than a confocal arthroscopy. Fibre optic two-photon endoscopes have been developed<sup>177, 178</sup> and the potential for CARS endoscopy is under investigation<sup>179</sup>. If these techniques became available a remaining challenge would be to develop an means of quantifying pathological changes and producing a clinical scale similar to the Mankin scale<sup>180</sup> which is currently the standard technique for assessing the level of cartilage degeneration via histology for clinical purposes.

The work could be extended to investigate the biomechanics of cartilage, this would be done via dynamic studies where the collagen and elastin fibres organisation would be investigated under different loading conditions.

The multi-photon imaging in this thesis has concentrated on tissue samples, however the technique is also very well suited for investigated cultured cells. Other possible applications are to investigate the pericellular matrix of isolated chondrons and cells in culture. Because of the lack of staining the cells could be imaged using time lapse experiments to investigate the assembly of matrix fibres by the cultured cells.

## Appendix:

---

### Polarization sensitivity of collagen fibres at an angle to the imaging plane

The discussion of polarization sensitivity of tendon in the Introduction was limited to the simplest case where the collagen fibres were orientated in the plane perpendicular to the laser propagation. In many biological tissue samples this is unlikely to be the case so here the effects of the angle  $\phi$  between the fibre axis and the imaging plane are investigated. This has previously been discussed by Stoller et al<sup>19</sup>, however their description was not in terms of the polarization curves. In chapter 6 we present results in terms of the polarization sensitivity curves rather than determine the ratio R. Here we have substituted values into the Kleinman D tensor to find the effect of different fibre angles on polarization sensitivity curves. The polarization of the SHG P is calculated from the Kleinman D tensor and the electric field E of the laser excitation light, according to the relationship;

$$\begin{pmatrix} P_x \\ P_y \\ P_z \end{pmatrix} = \epsilon_0 \begin{pmatrix} \chi_{xxx} & \chi_{xyy} & \chi_{xzz} & \chi_{xyz} & \chi_{xxz} & \chi_{xxy} \\ \chi_{yxx} & \chi_{yyy} & \chi_{yzz} & \chi_{yyz} & \chi_{yxz} & \chi_{yyx} \\ \chi_{zxx} & \chi_{zyy} & \chi_{zzz} & \chi_{zyz} & \chi_{zxz} & \chi_{zxy} \end{pmatrix} \begin{pmatrix} E_x^2 \\ E_y^2 \\ E_z^2 \\ 2E_y E_z \\ 2E_x E_z \\ 2E_x E_y \end{pmatrix}$$

The components of the tensor  $\chi_{ijk}$  can be calculated from the following equation,

$$\chi_{ijk} = as_i s_j s_k + bs_i \delta_{jk} + \frac{c}{2} (s_j \delta_{ik} + s_k \delta_{ij})$$

and assuming the fibre to be orientated at an angle  $\phi$  in the x-z plane so that the unit vector becomes.  $s_x = \hat{s} \cos \phi$ ,  $s_y = 0$  and  $s_z = \hat{s} \sin \phi$ . The laser fundamental is taken to be propagating in the z direction with a polarization angle  $\theta$  in the x-y plane and therefore the components of the E field are as follows,  $E_x = E \cos \theta$ ,  $E_y = E \sin \theta$  and  $E_z = 0$ . The intensity of the SHG was evaluated from these equations for a matrix of values of  $\phi$  and  $\theta$ , using a spread sheet. For this we used a value of  $\gamma = -0.83$  (which corresponds to  $\rho = 1.8$ ) as this is an average of the values in the literature. Figure 0-1.a shows that as the angle

### *Appendix*

between the fibre axis and the imaging plane increases the amount of SHG light produced decreases with 4.7 times as much SHG intensity being generated when the collagen fibre axis is in the imaging plane than when it is perpendicular to it. Figure 0-1.b shows the intensity at each angle between the fibre axis and the imaging plane normalised by dividing through by the average intensity at this angle, this figure shows that the visibility of the polarization sensitivity curve also decreases with increased angle between the fibre axis and imaging plane.

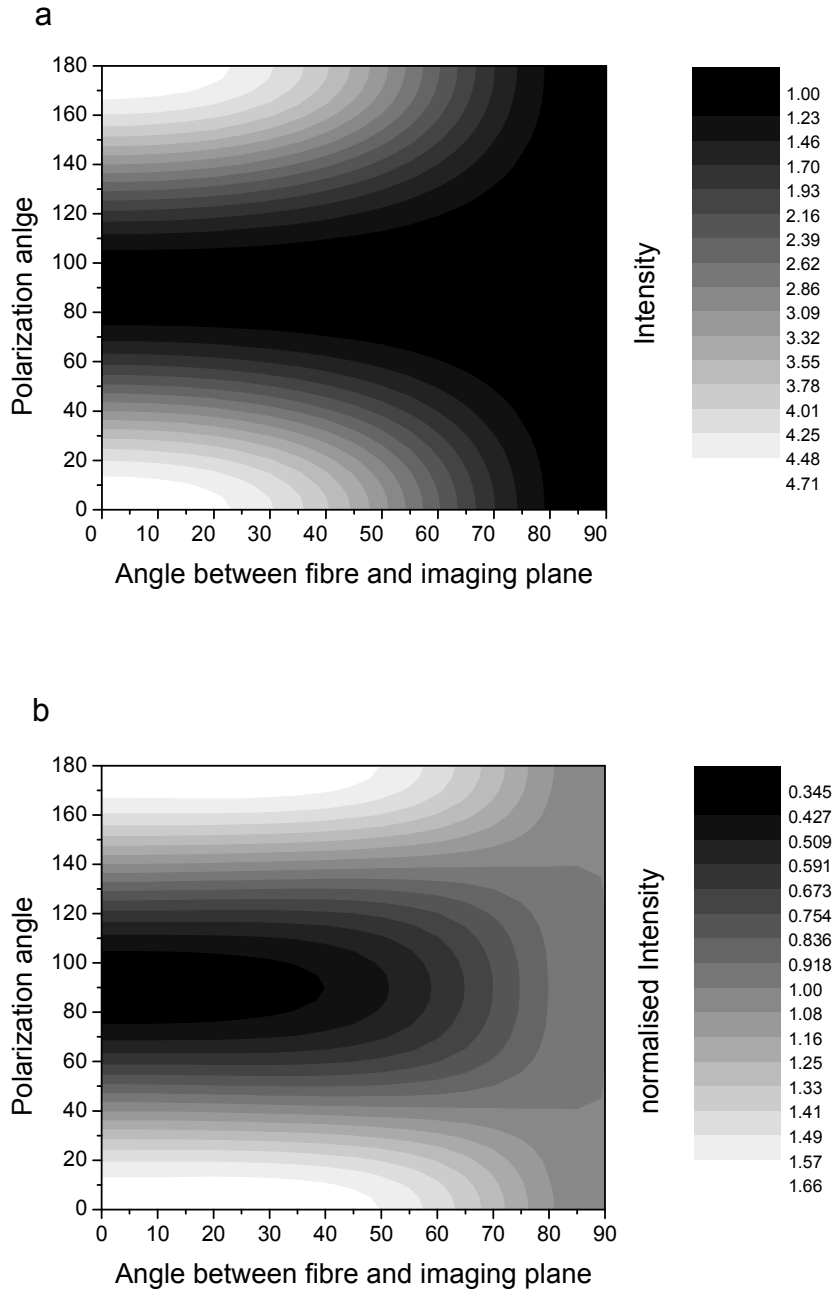


**Figure 0-1 Polarization sensitivity for collagen fibres at an angle to the imaging plane:**  
**The polarization sensitivity of collagen at different angles  $\phi$  between the imaging plane and the collagen fibre axis. The y axis on both graphs represents the polarization angle of the laser fundamental with respect to the component of the collagen fibre axis in the imaging plane. (a) shows the absolute intensity of the SHG (in arbitrary units where the minimum intensity is taken to be 1) where as (b) shows the intensity which has been normalized for each angle by dividing through by the mean intensity at each angle  $\phi$ .**

## References

---

1. C. L. Tang, "Nonlinear Optics," in *Hand Book of Optics II*, (Optical Society of America, 1995).
2. G. S. He, and S. H. Lui, *Physics of Nonlinear Optics* (World Scientific, Singapore, 1999).
3. A. Diaspro, and C. J. R. Sheppard, "Two-Photon Excitation Fluorescence Microscopy," in *Confocal and Two-Photon Microscopy: Foundations, Applications and Advances*, A. Diaspro, ed. (Wiley-Liss Inc., 2002), pp. 39-73.
4. P. T. C. So, "Two-Photon Microscopy of Tissues," in *Handbook of Biomedical Fluorescence*, M.-A. Mycek, and B. W. Pogue, eds. (Marcel Dekker, New York, 2003), pp. 181-209.
5. L. Hsu, K. H. Kim, C. Y. Dong, P. Kaplan, T. Hancewicz, C. Buehler, K. Berland, B. R. Masters, and P. T. C. So, "Two-Photon Imaging of Tissue Physiology Based on Endogenous Fluorophores," in *Confocal and Two-Photon Microscopy: Foundations, Applications and Advances*, A. Diaspro, ed. (Wiley-Liss, New York, 2002), pp. 431-448.
6. P. J. Campagnola, A. C. Millard, M. Terasaki, P. E. Hoppe, C. J. Malone, and W. Mohler, "Three-Dimensional High-Resolution Second Harmonic Generation Imaging of Endogenous Structural Proteins in Biological Tissues," *Biophys. J.* **81**, 493-508 (2002).
7. C. L. Evans, and X. S. Xie, "Coherent Anti-Stokes Raman Scattering Microscopy: Chemical Imaging for Biology and Medicine," *Annual Review of Analytical Chemistry*, 883-909 (2008).
8. Y. C. Guo, P. P. Ho, H. Savage, D. Harris, P. Sacks, S. Schantz, F. Liu, N. Zhadin, and R. R. Alfano, "Second-harmonic tomography of tissues," *Opt. Lett.* **22**, 1323-1325 (1997), <Go to ISI>://A1997XU42500015.
9. J. G. Fujimoto, "Optical coherence tomography for ultrahigh resolution in vivo imaging," *Nature Biotechnology* **21**, 1361-1367 (2003), <Go to ISI>://000186320000039
10. C. Boote, S. Hayes, M. Abahussin, and K. M. Meek, "Mapping collagen organization in the human cornea: Left and right eyes are structurally distinct," *Investigative Ophthalmology & Visual Science* **47**, 901-908 (2006), <Go to ISI>://000235894300020
11. K. M. Meek, S. J. Tuft, Y. F. Huang, P. S. Gill, S. Hayes, R. H. Newton, and A. J. Bron, "Changes in collagen orientation and distribution in keratoconus corneas," *Investigative Ophthalmology & Visual Science* **46**, 1948-1956 (2005), <Go to ISI>://000229504600011
12. C. J. Moger, R. Barrett, P. Bleuet, D. A. Bradley, R. E. Ellis, E. M. Green, K. Knapp, M. P, and C. P. Winlove, "Regional variations of collagen orientation in normal and diseased articular cartilage and subchondral bone determined using small angle X-ray scattering (SAXS)," *Osteoarthritis Cartilage* **15**, 682-687 (2007).
13. I. Shinya, "Foundations of Confocal Scanned Imaging in Light Microscopy," in *Handbook of Biological Confocal Microscopy*, J. B. Pawley, ed. (Plenum Press, New York, 1995), pp. 1-17.
14. E. H. K. Stelzer, "The Intermediate Optical System of Laser-Scanning Confocal Microscopes," in *Handbook of Biological Confocal Microscopy*, J. B. Pawley, ed. (Plenum Press, New York, 1995).

## References

15. J. Squier, and M. Muller, "High resolution nonlinear microscopy: A review of sources and methods for achieving optimal imaging," *Review of Scientific Instruments* **72**, 2855-2867 (2001), <Go to ISI>://000169663500001
16. A. L. Clark, A. M. Gillenwater, T. G. Collier, R. Alizadeh-Naderi, A. K. El-Naggar, and R. R. Richards-Kortum, "Confocal microscopy for real-time detection of oral cavity neoplasia," *Clinical Cancer Research* **9**, 4714-4721 (2003), <Go to ISI>://000186212000009
17. S. Fine, and W. P. Hansen, "Optical Second Harmonic Generation in Biological Systems," *Appl. Optics* **10**, 2350-& (1971), <Go to ISI>://A1971K428400024
18. P. Stoller, B. M. Kim, A. M. Rubenchik, K. M. Reiser, and L. B. Da Silva, "Polarization-dependent optical second-harmonic imaging of a rat-tail tendon," *J. Biomed. Opt.* **7**, 205-214 (2002), <Go to ISI>://000175480500005.
19. P. Stoller, K. M. Reiser, P. M. Celliers, and A. M. Rubenchik, "Polarization-modulated second harmonic generation in collagen," *Biophys. J.* **82**, 3330-3342 (2002), <Go to ISI>://000175802700049.
20. R. Gauderon, P. B. Lukins, and C. J. R. Sheppard, "Optimization of second-harmonic generation microscopy," *Micron* **32**, 691-700 (2001), <Go to ISI>://000168714600007.
21. E. Hecht, *Optics* (Addison Wesley, 1998).
22. J. Mertz, and L. Moreaux, "Second-harmonic generation by focused excitation of inhomogeneously distributed scatterers," *Opt. Commun.* **196**, 325-330 (2001), <Go to ISI>://000170722200040
23. R. M. Williams, W. R. Zipfel, and W. W. Webb, "Interpreting second-harmonic generation images of collagen I fibrils," *Biophys. J.* **88**, 1377-1386 (2005), <Go to ISI>://000226750800055.
24. L. Moreaux, O. Sandre, S. Charpak, M. Blanchard-Desce, and J. Mertz, "Coherent scattering in multi-harmonic light microscopy," *Biophys. J.* **80**, 1568-1574 (2001), <Go to ISI>://000167182100047
25. I. Freund, M. Deutsch, and A. Sprecher, "Connective-Tissue Polarity - Optical 2nd-Harmonic Microscopy, Crossed-Beam Summation, and Small-Angle Scattering in Rat-Tail Tendon," *Biophys. J.* **50**, 693-712 (1986), <Go to ISI>://A1986E309700016.
26. D. A. Dombeck, K. A. Kasischke, H. D. Vishwasrao, M. Ingelsson, B. T. Hyman, and W. W. Webb, "Uniform polarity microtubule assemblies imaged in native brain tissue by second-harmonic generation microscopy," *Proc. Natl. Acad. Sci. U. S. A.* **100**, 7081-7086 (2003), <Go to ISI>://000183493500036
27. S. W. Chu, S. Y. Chen, G. W. Chern, T. H. Tsai, Y. C. Chen, B. L. Lin, and C. K. Sun, "Studies of  $x^{(2)}$ / $x^{(3)}$  tensors in submicron-scaled bio-tissues by polarization harmonics optical microscopy," *Biophys. J.* **86**, 3914-3922 (2004), <Go to ISI>://000222035200051
28. S. V. Plotnikov, A. C. Millard, P. J. Campagnola, and W. A. Mohler, "Characterization of the myosin-based source for second-harmonic generation from muscle sarcomeres," *Biophys. J.* **90**, 693-703 (2006), <Go to ISI>://000234252100030
29. I. Amat-Roldan, I. G. Cormack, P. Loza-Alvarez, and D. Artigas, "Starch-based second-harmonic-generated collinear frequency-resolved optical gating pulse characterization at the focal plane of a high-numerical-aperture lens," *Opt. Lett.* **29**, 2282-2284 (2004), <Go to ISI>://000224193500024.

## References

30. G. Mizutani, Y. Sonoda, H. Sano, M. Sakamoto, T. Takahashi, and S. Ushioda, "Detection of starch granules in a living plant by optical second harmonic microscopy," *Journal of Luminescence* **87-89**, 824-826 (2000).
31. T. Verbiest, S. Van Elshocht, M. Kauranen, L. Hellemaans, J. Snauwaert, C. Nuckolls, T. J. Katz, and A. Persoons, "Strong enhancement of nonlinear optical properties through supramolecular chirality," *Science* **282**, 913-915 (1998), <Go to ISI>://000076727300039.
32. G. Cox, P. Xu, C. J. R. Sheppard, and J. Ramshaw, "Characterisation of the Second Harmonic Signal from Collagen," *Proceedings of SPIE* **4963**, 32-40 (2003).
33. S. Roth, and I. Freund, "Second Harmonic Generation in Collagen," *Journal of Chemical Physics* **70**, 1637-1643 (1978).
34. P. Stoller, P. M. Celliers, K. M. Reiser, and A. M. Rubenchik, "Quantitative second-harmonic generation microscopy in collagen," *Appl. Optics* **42**, 5209-5219 (2003), <Go to ISI>://000184963200029.
35. T. Yasui, Y. Tohno, and T. Araki, "Determination of collagen fiber orientation in human tissue by use of polarization measurement of molecular second-harmonic-generation light," *Appl. Optics* **43**, 2861-2867 (2004), <Go to ISI>://000221340200006.
36. Y. E. Yarker, R. M. Aspden, and D. W. L. Hukins, "Birefringence of Articular-Cartilage and the Distribution of Collagen Fibril Orientations," *Connective Tissue Research* **11**, 207-213 (1983), <Go to ISI>://A1983QX58400012.
37. S. J. Matcher, C. P. Winlove, and S. V. Gangnus, "The collagen structure of bovine intervertebral disc studied using polarization-sensitive optical coherence tomography," *Phys. Med. Biol.* **49**, 1295-1306 (2004), <Go to ISI>://000221109000017.
38. K. Beop-Min, J. Eichler, and L. B. Da Silva, "Frequency doubling of ultrashort laser pulses in biological tissues," *Appl. Optics* **38**, 7145-7150 (1999).
39. T. A. Theodossiou, C. Thrasivoulou, C. Ekwobi, and D. L. Becker, "Second harmonic generation confocal microscopy of collagen type I from rat tendon cryosections," *Biophys. J.* **91**, 4665-4677 (2006), <Go to ISI>://000242339600034.
40. J. A. Palero, H. S. de Bruijn, A. V. van den Heuvel, H. Sterenberg, and H. C. Gerritsen, "Spectrally resolved multiphoton imaging of in vivo and excised mouse skin tissues," *Biophys. J.* **93**, 992-1007 (2007), <Go to ISI>://000247851600027.
41. A. Zoumi, A. Yeh, and B. J. Tromberg, "Imaging cells and extracellular matrix in vivo by using second-harmonic generation and two-photon excited fluorescence," *Proc. Natl. Acad. Sci. U. S. A.* **99**, 11014-11019 (2002), <Go to ISI>://000177606900015.
42. W. R. Zipfel, R. M. Williams, R. Christie, A. Y. Nikitin, B. T. Hyman, and W. W. Webb, "Live tissue intrinsic emission microscopy using multiphoton-excited native fluorescence and second harmonic generation," *Proc. Natl. Acad. Sci. U. S. A.* **100**, 7075-7080 (2003), <Go to ISI>://000183493500035.
43. T. F. Heinz, C. K. Chen, D. Ricard, and Y. R. Shen, "Spectroscopy of Molecular Monolayers by Resonant 2nd-Harmonic Generation," *Physical Review Letters* **48**, 478-481 (1982), <Go to ISI>://A1982NA88900010.
44. F. Legare, C. Pfeffer, and B. R. Olsen, "The role of backscattering in SHG tissue imaging," *Biophys. J.* **93**, 1312-1320 (2007), <Go to ISI>://WOS:000248208800024.
45. K. Konig, "Multiphoton microscopy in life sciences," *Journal of Microscopy-Oxford* **200**, 83-104 (2000), <Go to ISI>://000165557000001.
46. C. Xu, W. Zipfel, J. B. Shear, R. M. Williams, and W. W. Webb, "Multiphoton fluorescence excitation: New spectral windows for biological nonlinear microscopy," *Proc. Natl. Acad. Sci. U. S. A.* **93**, 10763-10768 (1996), <Go to ISI>://A1996VL33300044.

## References

47. F. Bestvater, E. Spiess, G. Stobrawa, M. Hacker, T. Feurer, T. Porwol, U. Berchner-Pfannschmidt, C. Wotzlaw, and H. Acker, "Two-photon fluorescence absorption and emission spectra of dyes relevant for cell imaging," *Journal of Microscopy-Oxford* **208**, 108-115 (2002), <Go to ISI>://000179109700004
48. C. Xu, and W. W. Webb, "Measurement of two-photon excitation cross sections of molecular fluorophores with data from 690 to 1050 nm," *Journal of the Optical Society of America B-Optical Physics* **13**, 481-491 (1996), <Go to ISI>://A1996TW7650001
49. J. R. Lakowicz, *Principles of Fluorescence Spectroscopy* (Kluwer Scientific, New York, 1999).
50. I. Georgakoudi, B. C. Jacobson, M. G. Muller, E. E. Sheets, K. Badizadegan, D. L. Carr-Locke, C. P. Crum, C. W. Boone, R. R. Dasari, J. Van Dam, and M. S. Feld, "NAD(P)H and collagen as in vivo quantitative fluorescent biomarkers of epithelial precancerous changes," *Cancer Research* **62**, 682-687 (2002), <Go to ISI>://000173740600013
51. A. M. Pena, M. Strupler, T. Boulesteix, and M. C. Schanne-Klein, "Spectroscopic analysis of keratin endogenous signal for skin multiphoton microscopy," *Opt. Express* **13**, 6268-6274 (2005), <Go to ISI>://000231109600043
52. P. T. C. So, C. Y. Dong, B. R. Masters, and K. M. Berland, "Two-photon excitation fluorescence microscopy," *Annual Review of Biomedical Engineering* **2**, 399-429 (2000), <Go to ISI>://000089887400015
53. H. J. Koester, D. Baur, R. Uhl, and S. W. Hell, "Ca<sup>2+</sup> fluorescence imaging with pico- and femtosecond two-photon excitation: Signal and photodamage," *Biophys. J.* **77**, 2226-2236 (1999), <Go to ISI>://000083059800042
54. G. H. Patterson, and D. W. Piston, "Photobleaching in two-photon excitation microscopy," *Biophys. J.* **78**, 2159-2162 (2000), <Go to ISI>://000086349500046
55. J. X. Cheng, A. Volkmer, L. D. Book, and X. S. Xie, "An epi-detected coherent anti-stokes raman scattering (E-CARS) microscope with high spectral resolution and high sensitivity," *Journal of Physical Chemistry B* **105**, 1277-1280 (2001), <Go to ISI>://000167130800001
56. J. X. Cheng, and X. S. Xie, "Coherent anti-Stokes Raman scattering microscopy: Instrumentation, theory, and applications," *Journal of Physical Chemistry B* **108**, 827-840 (2004), <Go to ISI>://000188199500005
57. A. Zumbusch, G. R. Holtom, and X. S. Xie, "Three-dimensional vibrational imaging by coherent anti-Stokes Raman scattering," *Physical Review Letters* **82**, 4142-4145 (1999), <Go to ISI>://WOS:000080319900055
58. H. F. Wang, Y. Fu, P. Zickmund, R. Y. Shi, and J. X. Cheng, "Coherent anti-stokes Raman scattering imaging of axonal myelin in live spinal tissues," *Biophys. J.* **89**, 581-591 (2005), <Go to ISI>://000230114500059
59. A. Volkmer, J. X. Cheng, and X. S. Xie, "Vibrational imaging with high sensitivity via epidetected coherent anti-Stokes Raman scattering microscopy," *Physical Review Letters* **87**, (2001), <Go to ISI>://WOS:000169823100015
60. J. R. Ferraro, K. Nakamoto, and C. W. Brown, *Introductory Raman Spectroscopy* (Academic Press, London, 2003).
61. J. X. Cheng, Y. K. Jia, G. F. Zheng, and X. S. Xie, "Laser-scanning coherent anti-stokes Raman scattering microscopy and applications to cell biology," *Biophys. J.* **83**, 502-509 (2002), <Go to ISI>://000176445800043
62. J. X. Cheng, L. D. Book, and X. S. Xie, "Polarization coherent anti-Stokes Raman scattering microscopy," *Opt. Lett.* **26**, 1341-1343 (2001), <Go to ISI>://000170759400011

## References

63. N. Djaker, P. F. Lenne, D. Marguet, A. Colonna, C. Hadjur, and H. Rigneault, "Coherent anti-Stokes Raman scattering microscopy (CARS): Instrumentation and applications," *Nuclear Instruments & Methods in Physics Research Section a-Accelerators Spectrometers Detectors and Associated Equipment* **571**, 177-181 (2007), <Go to ISI>://000244599100042
64. C. L. Evans, E. O. Potma, M. Puoris'haag, D. Cote, C. P. Lin, and X. S. Xie, "Chemical imaging of tissue in vivo with video-rate coherent anti-Stokes Raman scattering microscopy," *Proc. Natl. Acad. Sci. U. S. A.* **102**, 16807-16812 (2005), <Go to ISI>://000233462900051
65. C. L. Evans, X. Y. Xu, S. Kesari, X. S. Xie, S. T. C. Wong, and G. S. Young, "Chemically-selective imaging of brain structures with CARS microscopy," *Opt. Express* **15**, 12076-12087 (2007), <Go to ISI>://000250006400035
66. J. Moger, B. D. Johnston, and C. R. Tyler, "Imaging metal oxide nanoparticles in biological structures with CARS microscopy," *Opt. Express* **16**, 3408-3419 (2008), <Go to ISI>://000254121300064
67. A. Zoumi, X. A. Lu, G. S. Kassab, and B. J. Tromberg, "Imaging coronary artery microstructure using second-harmonic and two-photon fluorescence microscopy," *Biophys. J.* **87**, 2778-2786 (2004), <Go to ISI>://000224129200060.
68. K. Konig, K. Schenke-Layland, I. Riemann, and U. A. Stock, "Multiphoton autofluorescence imaging of intratissue elastic fibers," *Biomaterials* **26**, 495-500 (2005), <Go to ISI>://000224135700004
69. P. M. Gribbon, A. Maroudas, K. H. Parker, and C. P. Winlove, "Water and Solute transport in the extracellular matrix: physical principles and macromolecular determinants," in *Connective Tissue Biology: Integration and Reductionism*, R. K. Reed, and K. Rubin, eds. (Portland Press, London, 1997).
70. S. Weiner, and W. Traub, "Bone-Structure - from Angstroms to Microns," *Faseb J.* **6**, 879-885 (1992), <Go to ISI>://A1992HE39000011.
71. K. E. Kadler, C. Baldock, J. Bella, and R. P. Boot-Handford, "Collagens at a glance," *Journal of Cell Science* **120**, 1955-1958 (2007), <Go to ISI>://WOS:000247024300001
72. N. Ugryumova, D. P. Attenburrow, C. P. Winlove, and S. J. Matcher, "The collagen structure of equine articular cartilage, characterized using polarization-sensitive optical coherence tomography," *J. Phys. D-Appl. Phys.* **38**, 2612-2619 (2005), <Go to ISI>://000231406800013
73. N. J. Kemp, H. N. Zaatari, J. Park, H. G. Rylander, and T. E. Milner, "Form-biattenuance in fibrous tissues measured with polarization-sensitive optical coherence tomography (PS-OCT)," *Opt. Express* **13**, 4611-4628 (2005), <Go to ISI>://000229799200027
74. R. A. Stockwell, *Biology of Cartilage Cells* (Cambridge University Press, 1979).
75. J. M. Davidson, "Elastin structure and biology," in *Connective Tissue Disease: Molecular Pathology of the Extracellular Matrix*, J. Uitto, and A. Perejola, eds. (Dekker, 1987).
76. W. R. Gray, L. B. Sandberg, and J. A. Foster, "Molecular Model for Elastin Structure and Function," *Nature* **246**, 461-466 (1973), <Go to ISI>://A1973R586800024
77. R. P. Mecham, and J. E. Heuser, "the Elastic fibre," in *Cell Biology of the Extracellular Matrix*, E. D. Hay, ed. (Plenum Press, 1991).
78. K. A. Piez, and A. H. Reddi, eds., *Extracellular Matrix Biochemistry* (Elsevier Science Publishing Co, 1984).

## References

79. E. R. Myers, C. G. Armstrong, and V. C. Mow, "Swelling Pressure and Collagen Tension."
80. A. T. Yeh, M. J. Hammer-Wilson, D. C. Van Sickle, H. P. Benton, A. Zoumi, B. J. Tromberg, and G. M. Peavy, "Nonlinear optical microscopy of articular cartilage," *Osteoarthritis Cartilage* **13**, 345-352 (2005), <Go to ISI>://000228216200009.
81. G. J. Tortora, and N. P. Anagnostakos, *Principles of Anatomy and Physiology* (Harper Collins, 1990).
82. Y. C. Fung, *Biomechanics Mechanical Properties of Living Tissues* (Springer-Verlag, New York, 1981).
83. R. A. Stockwell, "Cartilage Failure in Osteoarthritis: Relevance of Normal Structure and Function. A Review," *Clinical Anatomy* **4**, 161-191 (1991).
84. V. Roth, V. Mow, and A. J. Grodzinsky, "Biophysical and Electromechanical Properties of Articular Cartilage," *Skeletal Research*, 301-341 (1979).
85. D. Eyre, "Collagen of articular cartilage," *Arthritis Research* **4**, 30-35 (2002).
86. A. Naumann, J. E. Dennis, A. Awadallah, D. A. Carrino, J. M. Mansour, E. Kastenbauer, and A. I. Caplan, "Immunochemical and mechanical characterization of cartilage subtypes in rabbit," *Journal of Histochemistry & Cytochemistry* **50**, 1049-1058 (2002), <Go to ISI>://WOS:000177068700007
87. I. Hesse, "The Occurrence of Elastic System Fibers in the Matrix of Normal Articular-Cartilage," *Cell and Tissue Research* **248**, 589-593 (1987), <Go to ISI>://A1987H274300015
88. W. Horton, "Morphology of Connective Tissue: Cartilage," in *Connective Tissue and Its Hertiabale Disorders*, (Wiley-Liss, 1993), pp. 73-84.
89. E. B. Hunziker, T. M. Quinn, and H. J. Hauselmann, "Quantitative structural organization of normal adult human articular cartilage," *Osteoarthritis Cartilage* **10**, 564-572 (2002), <Go to ISI>://WOS:000177625700009
90. T. M. Quinn, E. B. Hunziker, and H. J. Hauselmann, "Variation of cell and matrix morphologies in articular cartilage among locations in the adult human knee," *Osteoarthritis Cartilage* **13**, 672-678 (2005), <Go to ISI>://000231213500004
91. I. Youn, J. B. Choi, L. Cao, L. A. Setton, and F. Guilak, "Zonal variations in the three-dimensional morphology of the chondron measured in situ using confocal microscopy," *Osteoarthritis Cartilage* **14**, 889-897 (2006), <Go to ISI>://000239898500007
92. K. D. Jadin, W. C. Bae, B. L. Schumacher, and R. L. Sah, "Three-dimensional (3-D) imaging of chondrocytes in articular cartilage: Growth-associated changes in cell organization," *Biomaterials* **28**, 230-239 (2007), <Go to ISI>://000242310500011
93. K. Arkill, "Mass Transport to Articular Cartilage," in *School of Physics*, (University of Exeter, Exeter, 2005).
94. H. Muir, "Cartilage Structure and Metabolism and Basic Changes in Degenerative Joint Disease," **8**, 1-5 (1978).
95. E. L. Radin, and R. M. Rose, "Role of Subchondral Bone in the Initiation and Progression of Cartilage Damage," 34-40 (1986).
96. L. Sokoloff, "Pathology and Pathogenesis of Osteoarthritis."
97. G. Meachim, and R. Allibone, "Topographical Variation in the Calcified Zone of Upper Femoral Articular-Cartilage," *Journal of Anatomy* **139**, 341-352 (1984), <Go to ISI>://A1984TN65700011
98. J. P. G. Urban, "Solute transport in articular cartilage and the intervertebral disc," in *Connective Tissue Matrix* D. W. L. Hukins, ed. (Macmillian Press, 1990), pp. 44-65.

## References

99. J. Yu, C. P. Winlove, S. Roberts, and J. P. G. Urban, "Elastic fibre organization in the intervertebral discs of the bovine tail," *Journal of Anatomy* **201**, 465-475 (2002), <Go to ISI>://000179862900003
100. N. Bogduk, *Clinical Anatomy of the Lumbar Spine and Sacrum* (Churchill Livingstone, London, 2001).
101. M. Wang, K. M. Reiser, and A. Knoesen, "Spectral moment invariant analysis of disorder in polarization-modulated second-harmonic-generation images obtained from collagen assemblies," *Journal of the Optical Society of America a-Optics Image Science and Vision* **24**, 3573-3586 (2007), <Go to ISI>://000251335100020
102. J. P. G. Urban, and S. Roberts, "Degeneration of the intervertebral disc," *Arthritis Research & Therapy* **5**, 120-130 (2003), <Go to ISI>://WOS:000182395200009
103. A. Prescher, "Anatomy and pathology of the aging spine," *European Journal of Radiology* **27**, 181-195 (1998), <Go to ISI>://WOS:000075380900002
104. D. W. Fawcett, and R. P. Jensch, *Bloom and Fawcetts Consise Histology* (Oxford University Press, London, 2002).
105. B. Young, and J. W. Heath, *Wheater's Functional Histology: a text and colour atlas* (Churchill Livingstone, London, 2000).
106. V. Nikolenko, B. Nemet, and R. Yuste, "A two-photon and second-harmonic microscope," *Methods* **30**, 3-15 (2003), <Go to ISI>://000182506200002
107. R. J. Stanley, Z. J. Hou, A. P. Yang, and M. E. Hawkins, "The two-photon excitation cross section of 6MAP, a fluorescent adenine analogue," *Journal of Physical Chemistry B* **109**, 3690-3695 (2005), <Go to ISI>://000227247100084
108. Mackay-Smith, "Pathogenesis and Pathology of Equine Osteoarthritis," **141**, 1246-1252 (1962).
109. H. Brommer, P. R. van Weeren, P. A. Brama, and A. Barneveld, "Quantification and age-related distribution of articular cartilage degeneration in the equine fetlock joint," *Equine Vet J* **35**, 697-701 (2003).
110. M. Alini, S. M. Eisenstein, K. Ito, C. Little, A. A. Kettler, K. Masuda, J. Melrose, J. Ralphs, I. Stokes, and H. J. Wilke, "Are animal models useful for studying human disc disorders/degeneration?," *European Spine Journal* **17**, 2-19 (2008), <Go to ISI>://000252625400002
111. T. Wakebe, and E. Van Keuren, "The excitation spectra of two-photon induced fluorescence in xanthene dyes," *Japanese Journal of Applied Physics Part 1-Regular Papers Short Notes & Review Papers* **38**, 3556-3561 (1999), <Go to ISI>://000081576500028
112. N. T. Soskel, T. B. Wolt, and L. B. Sandberg, "Isolation and Characterization of Insoluble and Soluble Elastins," *Methods in Enzymology* **144**, 196-214 (1987), <Go to ISI>://A1987M167800010
113. Y. Jiang, I. Tomov, Y. M. Wang, and Z. P. Chen, "Second-harmonic optical coherence tomography," *Opt. Lett.* **29**, 1090-1092 (2004), <Go to ISI>://000221189400016.
114. K. Barnard, S. A. Burgess, D. A. Carter, and D. M. Woolley, "3-Dimensional Structure of Type-Iv Collagen in the Mammalian Lens Capsule," *J. Struct. Biol.* **108**, 6-13 (1992), <Go to ISI>://WOS:A1992HE67500002
115. Y. C. Wu, and J. N. Y. Qu, "Two-photon autofluorescence spectroscopy and second-harmonic generation of epithelial tissue," *Opt. Lett.* **30**, 3045-3047 (2005), <Go to ISI>://000233258800025

## References

116. R. Richards-Kortum, R. Drezek, K. Sokolov, I. Pavlova, and M. Follen, "Survey of Endogenous Biological Fluorophores," in *Handbook of Biomedical Fluorescence*, M.-A. Mycek, and B. W. Pogue, eds. (Marcel Dekker, New York, 2003), pp. 237-264.
117. E. Konova, S. Baydanoff, M. Atanasova, and A. Velkova, "Age-related changes in the glycation of human aortic elastin," *Experimental Gerontology* **39**, 249-254 (2004), <Go to ISI>://WOS:000189124100014
118. C. P. Winlove, K. H. Parker, N. C. Avery, and A. J. Bailey, "Interactions of elastin and aorta with sugars in vitro and their effects on biochemical and physical properties," *Diabetologia* **39**, 1131-1139 (1996), <Go to ISI>://WOS:A1996VK99100001
119. D. R. Eyre, M. A. Paz, and P. M. Gallop, "Cross-Linking in Collagen and Elastin," *Annu. Rev. Biochem.* **53**, 717-748 (1984), <Go to ISI>://A1984SZ66900021
120. D. P. Thornhill, "Separation of a Series of Chromophores and Fluorophores Present in Elastin," *Biochemical Journal* **147**, 215-219 (1975), <Go to ISI>://A1975AA80500004
121. F. Labella, F. Keeley, S. Vivian, and Thornhill, D., "Evidence for Dityrosine in Elastin," *Biochemical and Biophysical Research Communications* **26**, 748-& (1967), <Go to ISI>://WOS:A19679106600020
122. D. A. Malencik, J. F. Sprouse, C. A. Swanson, and S. R. Anderson, "Dityrosine: Preparation, isolation, and analysis," *Analytical Biochemistry* **242**, 202-213 (1996), <Go to ISI>://WOS:A1996VV31800006
123. S. Sajdera, and V. C. Hascall, "Proteinpolysaccharide Complex from Bovine Nasal Cartilage - a Comparison of Low and High Extraction Procedures," *Journal of Biological Chemistry* **244**, 77-& (1969), <Go to ISI>://WOS:A1969C404800013
124. M. G. Xu, E. D. Williams, E. W. Thompson, and M. Gu, "Effect of handling and fixation processes on fluorescence spectroscopy of mouse skeletal muscles under two-photon excitation," *Appl. Optics* **39**, 6312-6317 (2000), <Go to ISI>://000165607300006
125. M. Handl, E. Filova, M. Kubala, Z. Lansky, L. Kolacna, J. Vorlicek, T. Trc, M. Pach, and E. Amler, "Fluorescent advanced glycation end products in the detection of factual stages of cartilage degeneration," *Physiological Research* **56**, 235-242 (2007), <Go to ISI>://WOS:000246657500012
126. G. J. Gibson, J. J. Verner, F. R. T. Nelson, and D. L. Lin, "Degradation of the cartilage collagen matrix associated with changes in chondrocytes in osteoarthritis. Assessment by loss of background fluorescence and immunodetection of matrix components," *Journal of Orthopaedic Research* **19**, 33-42 (2001), <Go to ISI>://WOS:000168179000005
127. C. A. Poole, "Articular cartilage chondrons: Form, function and failure," *Journal of Anatomy* **191**, 1-13 (1997), <Go to ISI>://WOS:A1997XT25700001
128. T. Aigner, and J. Stove, "Collagens - major component of the physiological cartilage matrix, major target of cartilage degeneration, major tool in cartilage repair," *Advanced Drug Delivery Reviews* **55**, 1569-1593 (2003), <Go to ISI>://WOS:000186813500004
129. R. A. Bank, M. T. Bayliss, F. Lafeber, A. Maroudas, and J. M. Tekoppele, "Ageing and zonal variation in post-translational modification of collagen in normal human articular cartilage - The age-related increase in non-enzymatic glycation affects biomechanical properties of cartilage," *Biochemical Journal* **330**, 345-351 (1998), <Go to ISI>://000072441800049
130. A. Uchiyama, T. Ohishi, M. Takahashi, K. Kushida, T. Inoue, M. Fujie, and K. Horiuchi, "Fluorophores from Aging Human Articular-Cartilage," *Journal of Biochemistry* **110**, 714-718 (1991), <Go to ISI>://WOS:A1991GN91200008

## References

131. B. J. F. Wong, V. Wallace, M. Coleno, H. P. Benton, and B. J. Tromberg, "Two-photon excitation laser scanning microscopy of human, porcine, and rabbit nasal septal cartilage," *Tissue Eng.* **7**, 599-606 (2001), <Go to ISI>://000172030300011.
132. C. A. Poole, M. H. Flint, and B. W. Beaumont, "Chondrons in Cartilage - Ultrastructural Analysis of the Pericellular Microenvironment in Adult Human Articular Cartilages," *Journal of Orthopaedic Research* **5**, 509-522 (1987), <Go to ISI>://WOS:A1987L138700005
133. P. G. Bush, and A. C. Hall, "The volume and morphology of chondrocytes within non-degenerate and degenerate human articular cartilage," *Osteoarthritis Cartilage* **11**, 242-251 (2003), <Go to ISI>://000182094800002
134. P. G. Bullough, and A. Jagannath, "The Morphology of the Calcification Front in Articular-Cartilage - Its Significance in Joint Function," *Journal of Bone and Joint Surgery-British Volume* **65**, 72-78 (1983), <Go to ISI>://A1983QA02900018
135. K. P. Arkill, and C. P. Winlove, "Solute transport in the deep and calcified zones of articular cartilage," *Osteoarthritis Cartilage* **16**, 708-714 (2008), <Go to ISI>://000257241700011
136. K. P. Arkill, and C. P. Winlove, "Fatty acid transport in articular cartilage," *Archives of Biochemistry and Biophysics* **456**, 71-78 (2006), <Go to ISI>://000242672800008
137. W. T. Green, G. N. Martin, E. D. Eanes, and L. Sokoloff, "Microradiographic Study of Calcified Layer of Articular Cartilage," *Archives of Pathology* **90**, 151-& (1970), <Go to ISI>://A1970G931100008
138. T. R. Oegema, R. J. Carpenter, F. Hofmeister, and R. C. Thompson, "The interaction of the zone of calcified cartilage and subchondral bone in osteoarthritis," *Microscopy Research and Technique* **37**, 324-332 (1997), <Go to ISI>://A1997XC79300007
139. I. Redler, V. C. Mow, M. L. Zimny, and J. Mansell, "Ultrastructure and Biomechanical Significance of Tidemark of Articular-Cartilage," *Clinical Orthopaedics and Related Research*, 357-362 (1975), <Go to ISI>://A1975AU95500038
140. T. Aigner, A. Hemmel, D. Neureiter, P. M. Gebhard, G. Zeiler, T. Kirchner, and L. McKenna, "Apoptotic cell death is not a widespread phenomenon in normal aging and osteoarthritic human articular knee cartilage - A study of proliferation, programmed cell death (apoptosis), and viability of chondrocytes in normal and osteoarthritic human knee cartilage," *Arthritis and Rheumatism* **44**, 1304-1312 (2001), <Go to ISI>://000171751100011
141. S. Hashimoto, R. L. Ochs, F. Rosen, J. Quach, G. McCabe, J. Solan, J. E. Seegmiller, R. Terkeltaub, and M. Lotz, "Chondrocyte-derived apoptotic bodies and calcification of articular cartilage," *Proc. Natl. Acad. Sci. U. S. A.* **95**, 3094-3099 (1998), <Go to ISI>://000072596200070
142. C. W. McIlwraith, "Current Concepts in Equine Degenerative Joint Disease," *Journal of the American Veterinary Medical Association* **180**, 239-250 (1982), <Go to ISI>://A1982NA01700006.
143. M. Poenie, J. Kuhn, and J. Combs, "Real-time visualization of the cytoskeleton and effector functions in T cell," *Current Opinion in Immunology* **16**, 428-438 (2004), <Go to ISI>://000222919200006
144. S. Hashimoto, R. L. Ochs, S. Komiya, and M. Lotz, "Linkage of chondrocyte apoptosis and cartilage degradation in human osteoarthritis," *Arthritis and Rheumatism* **41**, 1632-1638 (1998), <Go to ISI>://000076066400013

## References

145. A. Mobasher, "Role of chondrocyte death and hypocellularity in ageing human articular cartilage and the pathogenesis of osteoarthritis," *Medical Hypotheses* **58**, 193-197 (2002), <Go to ISI>://000176428300002
146. C. M. Thomas, C. J. Fuller, C. E. Whittles, and M. Sharif, "Chondrocyte death by apoptosis is associated with cartilage matrix degradation," *Osteoarthritis Cartilage* **15**, 27-34 (2007), <Go to ISI>://000244182900004
147. P. T. C. So, H. Kim, and I. E. Kochevar, "Two-photon deep tissue ex vivo imaging of mouse dermal and subcutaneous structures," *Opt. Express* **3**, 339-350 (1998), <Go to ISI>://000076706100006
148. T. Boulesteix, A. M. Pena, N. Pages, G. Godeau, M. P. Sauviat, E. Beaufrepaire, and M. C. Schanne-Klein, "Micrometer scale ex vivo multiphoton imaging of unstained arterial wall structure," *Cytom. Part A* **69A**, 20-26 (2006), <Go to ISI>://000234383700003
149. K. Schenke-Layland, I. Riemann, F. Opitz, K. Konig, K. J. Halbhuber, and U. A. Stock, "Comparative study of cellular and extracellular matrix composition of native and tissue engineered heart valves," *Matrix Biol.* **23**, 113-125 (2004), <Go to ISI>://000222854800005
150. M. T. Butcher, and M. A. Ashley-Ross, "Fetlock joint kinematics differ with age in thoroughbred racehorses," *Journal of Biomechanics* **35**, 563-571 (2002), <Go to ISI>://WOS:000175522300001
151. H. Brommer, R. R. van Weeren, P. A. J. Brama, and A. Barneveld, "Quantification and age-related distribution of articular cartilage degeneration in the equine fetlock joint," *Equine Vet. J.* **35**, 697-701 (2003), <Go to ISI>://000186486500011
152. P. A. J. Brama, D. Karssenbergh, A. Barneveld, and P. R. van Weeren, "Contact areas and pressure distribution on the proximal articular surface of the proximal phalanx under sagittal plane loading," *Equine Vet. J.* **33**, 26-32 (2001), <Go to ISI>://000166432500004.
153. J. Yu, U. Tirlapur, J. Fairbank, P. Handford, S. Roberts, C. P. Winlove, Z. F. Cui, and J. Urban, "Microfibrils, elastin fibres and collagen fibres in the human intervertebral disc and bovine tail disc," *Journal of Anatomy* **210**, 460-471 (2007), <Go to ISI>://000245694100009
154. C. H. Yu, S. P. Tai, C. T. Kung, I. J. Wang, H. C. Yu, H. J. Huang, W. J. Lee, Y. F. Chan, and C. K. Sun, "In vivo and ex vivo imaging of intra-tissue elastic fibers using third-harmonic-generation microscopy," *Opt. Express* **15**, 11167-11177 (2007), <Go to ISI>://WOS:000249339800011
155. Y. Mikawa, H. Hamagami, J. Shikata, and T. Yamamuro, "Elastin in the Human Intervertebral-Disk - a Histological and Biochemical-Study Comparing It with Elastin in the Human Yellow Ligament," *Archives of Orthopaedic and Trauma Surgery* **105**, 343-349 (1986), <Go to ISI>://WOS:A1986E826200006
156. J. A. Foster, C. B. Rich, and M. D. Desa, "Comparison of Aortic and Ear Cartilage Tropoelastins Isolated from Lathyrictic Pigs," *Biochimica Et Biophysica Acta* **626**, 383-389 (1980), <Go to ISI>://WOS:A1980KX03200014
157. P. Keatly, "Time resolved magneto-optical investigations of picosecond magnetisation dynamics in arrays of non-ellipsoidal ferromagnetic nano-elements," in *School of Physics*, (University of Exeter, Exeter, 2007).
158. A. Marchant, B, *Optical Recording- A Technical Overview* (Addison Wesley, 1990).
159. B. Richards, and E. Wolf, "Electromagnetic Diffraction in Optical Systems .2. Structure of the Image Field in an Aplanatic System," *Proceedings of the Royal Society of*

## References

- London Series a-Mathematical and Physical Sciences **253**, 358-379 (1959), <Go to ISI>://A1959WU33300007
160. Y. Sasazaki, R. Shore, and B. B. Seedhom, "Deformation and failure of cartilage in the tensile mode," *Journal of Anatomy* **208**, 681-694 (2006), <Go to ISI>://000237930800003
161. A. K. Jeffery, G. W. Blunn, C. W. Archer, and G. Bentley, "3-Dimensional Collagen Architecture in Bovine Articular-Cartilage," *Journal of Bone and Joint Surgery-British Volume* **73**, 795-801 (1991), <Go to ISI>://A1991GG32900021
162. P. Bullough, and J. Goodfellow, "The Significance of the Fine Structure of Articular Cartilage," *The Journal of Bone and Joint Surgery* **50B**, 852-857 (1968).
163. V. Sankaran, J. T. Walsh, and D. J. Maitland, "Comparative study of polarized light propagation in biologic tissues," *J. Biomed. Opt.* **7**, 300-306 (2002), <Go to ISI>://000177482700004
164. K. Yoshiki, M. Hashimoto, and T. Araki, "Second-harmonic-generation microscopy using excitation beam with controlled polarization pattern to determine three-dimensional molecular orientation," *Japanese Journal of Applied Physics Part 2-Letters & Express Letters* **44**, L1066-L1068 (2005), <Go to ISI>://000232318900009
165. J. B. Choi, I. Youn, L. Cao, H. A. Leddy, C. L. Gilchrist, L. A. Setton, and F. Guilak, "Zonal changes in the three-dimensional morphology of the chondron under compression: The relationship among cellular, pericellular, and extracellular deformation in articular cartilage," *Journal of Biomechanics* **40**, 2596-2603 (2007), <Go to ISI>://000249508900002
166. S. B. Adams, P. R. Herz, D. L. Stamper, M. J. Roberts, S. Bourquin, N. A. Patel, K. Schneider, S. D. Martin, S. Shortkroff, J. G. Fujimoto, and M. E. Brezinski, "High-resolution imaging of progressive articular cartilage degeneration," *Journal of Orthopaedic Research* **24**, 708-715 (2006), <Go to ISI>://000236682700016
167. J. Rogowska, and M. E. Brezinski, "Image processing techniques for noise removal, enhancement and segmentation of cartilage OCT images," *Phys. Med. Biol.* **47**, 641-655 (2002), <Go to ISI>://000174526400008
168. R. J. Minns, and F. S. Steven, "Collagen Fibril Organization in Human Articular-Cartilage," *Journal of Anatomy* **123**, 437-457 (1977), <Go to ISI>://A1977DB82300016
169. M. J. Kaab, K. Ito, J. M. Clark, and H. P. Notzli, "Deformation of articular cartilage collagen structure under static and cyclic loading," *Journal of Orthopaedic Research* **16**, 743-751 (1998), <Go to ISI>://000077786300016.
170. N. Ugryumova, S. V. Gangnus, and S. J. Matcher, "Three-dimensional optic axis determination using variable-incidence-angle polarization-optical coherence tomography," *Opt. Lett.* **31**, 2305-2307 (2006), <Go to ISI>://000239173300021
171. T. Q. Xie, S. G. Guo, J. Zhang, Z. P. Chen, and G. M. Peavy, "Use of polarization-sensitive optical coherence tomography to determine the directional polarization sensitivity of articular cartilage and meniscus," *J. Biomed. Opt.* **11**, (2006), <Go to ISI>://000243968700004
172. A. Volkmer, L. D. Book, and X. S. Xie, "Time-resolved coherent anti-Stokes Raman scattering microscopy: Imaging based on Raman free induction decay," *Appl. Phys. Lett.* **80**, 1505-1507 (2002), <Go to ISI>://WOS:000174181400001
173. E. O. Potma, C. L. Evans, and X. S. Xie, "Heterodyne coherent anti-Stokes Raman scattering (CARS) imaging," *Opt. Lett.* **31**, 241-243 (2006), <Go to ISI>://WOS:000234665000034

## References

174. C. P. Pfeffer, B. R. Olsen, and F. Legare, "Second harmonic generation imaging of fascia within thick tissue block," *Opt. Express* **15**, 7296-7302 (2007), <Go to ISI>://WOS:000248359700027
175. S. W. Chu, S. P. Tai, M. C. Chan, C. K. Sun, I. C. Hsiao, C. H. Lin, Y. C. Chen, and B. L. Lin, "Thickness dependence of optical second harmonic generation in collagen fibrils," *Opt. Express* **15**, 12005-12010 (2007), <Go to ISI>://000250006400027
176. C. W. Jones, D. Smolinski, C. Willers, P. J. Yates, A. Keogh, D. Fick, T. B. Kirk, and M. H. Zheng, "Laser scanning confocal arthroscopy of a fresh cadaveric knee joint," *Osteoarthritis Cartilage* **15**, 1388-1396 (2007), <Go to ISI>://000251322800006
177. L. Fu, and M. Gu, "Fibre-optic nonlinear optical microscopy and endoscopy," *Journal of Microscopy-Oxford* **226**, 195-206 (2007), <Go to ISI>://WOS:000246762200002
178. L. Fu, A. Jain, C. Cranfield, H. Xie, and M. Gu, "Three-dimensional nonlinear optical endoscopy," *J Biomed Opt* **12**, 040501 (2007), <Go to ISI>://MEDLINE:17867789
179. F. Legare, C. L. Evans, F. Ganikhanov, and X. S. Xie, "Towards CARS endoscopy," *Opt. Express* **14**, 4427-4432 (2006), <Go to ISI>://WOS:000237608600024
180. D. Bobinac, J. Spanjol, S. Zoricic, and I. Maric, "Changes in articular cartilage and subchondral bone histomorphometry in osteoarthritic knee joints in humans," *Bone* **32**, 284-290 (2003), <Go to ISI>://000182100900010